

**THREE DIMENSIONAL DYNAMIC RESPONSE OF REINFORCED  
CONCRETE BRIDGES UNDER SPATIALLY VARYING SEISMIC GROUND  
MOTIONS**

by

Carlos Enrique Peña Ramos

---

A Dissertation Submitted to the Faculty of the  
**DEPARTMENT OF CIVIL ENGINEERING AND ENGINEERING MECHANICS**  
To Meet a Requirement for the Degree of  
**DOCTOR OF PHILOSOPHY**  
**WITH MAJOR IN CIVIL ENGINEERING**

In the Graduate College of  
**THE UNIVERSITY OF ARIZONA**

2011

**UNIVERSITY OF ARIZONA  
GRADUATE COLLEGE**

As members of the Dissertation Committee, we certify that we have read the dissertation prepared by Carlos Enrique Peña Ramos entitled “Three Dimensional Dynamic Response of Reinforced Concrete Bridges under Spatially Varying Seismic Ground Motion” and recommend that it be accepted as fulfilling the dissertation requirement for the Degree of Doctor of Philosophy.

\_\_\_\_\_  
Dr, Achintya Haldar Date:

\_\_\_\_\_  
Dr. Mohammad Ehsani Date:

\_\_\_\_\_  
Dr. Chandrakant Desai Date:

Final approval and acceptance of this dissertation is contingent upon the candidate's submission of the final copies of the dissertation to the Graduate College.

I hereby certify that I have read this dissertation prepared under my direction and recommend that it be accepted as fulfilling the dissertation requirement.

\_\_\_\_\_  
Dissertation Director: Dr. Achintya Haldar Date:

**STATEMENT BY AUTHOR**

This dissertation has been submitted in partial fulfillment of requirements for an advanced degree at The University of Arizona and is deposited in the University Library to be available to borrowers under rules of the Library.

Brief quotations from this dissertation are allowed without special permission, providing that accurate acknowledgement of source is made. Request for permission for extended quotation from, or reproduction of this manuscript in whole or in part, may be granted by the author.

SIGNED: \_\_\_\_\_  
Carlos Enrique Peña Ramos

## **ACKNOWLEDGENTS**

The author would like to first express his most sincere appreciation and gratitude to his Dissertation Director Professor Achintya Haldar for his continuous support, assistance, encouragement and patience throughout the development of his doctoral studies and research, as well as his careful review of this manuscript.

Sincere thanks are also extended to Professors Mohammad Ehsani and Chandrakant Desai for their gracious acceptance in serving in the author's PhD Committee and for their time spent in reviewing this manuscript. Special mention is due to Professor Ehsani, whom the author has had the privilege of knowing professionally as a fellow structural engineer at QuakeWrap and who the author is indebted for his mentoring, support and generous time allowance while the author was completing his research.

The author acknowledges gratefully his indebtedness to his parents, brother and sisters for their unconditional love and support. The author is forever indebted to his wife, his partner in life, for her encouragement, support and love and for her most precious gift, his children, whom have always been his first source of inspiration.

Sincere appreciation is also extended to the Ministry of Education of Mexico and to the Universidad de Sonora for the financial support that made it possible for the author to pursue and conclude his doctoral studies.

## **DEDICATION**

**To my loving family: my parents Carlos Enrique and Evelia, my brother Javier and my sisters Etna Aida and Martha Olivia.**

**To my loving wife Vicky.**

**To my children: Carlos Enrique, Manuel Alejandro and Ana Lucia.**

## TABLE OF CONTENTS

<b>LIST OF FIGURES .....</b>	<b>11</b>
<b>LIST OF TABLES .....</b>	<b>19</b>
<b>ABSTRACT .....</b>	<b>21</b>
<b>1. INTRODUCTION .....</b>	<b>23</b>
1.1 General Remarks .....	23
1.2 Causes of Spatially Variability in Seismic Waves .....	35
1.3 Objectives .....	40
1.4 Organization .....	42
<b>2. LITERATURE REVIEW .....</b>	<b>43</b>
2.1 Introduction .....	43
2.2 Modeling Spatial Variation in Seismic Waves using Stochastic Approach .....	43
2.3 Modeling Spatial Variation in Seismic Waves using Deterministic Approach .....	44
2.4 Coherence Functions .....	45
2.4.1 Empirical Coherence Functions .....	46
2.4.1.1 The HV Coherence Function .....	46
2.4.1.2 The Abrahamson Coherence Function .....	47
2.4.2 Analytical Coherence Functions .....	50
2.4.2.1 The LW Coherence Function .....	51
2.4.3 Structural Response using the HV and LW Coherence Functions .....	52

## **TABLE OF CONTENTS - Continued**

2.4.4 Anisotropic Coherence Functions .....	53
2.5 Structural Response under Spatially Variable Seismic Waves .....	54
2.5.1 Structural Response Using Frequency Domain Analysis .....	55
2.5.2 Structural Response Using Time Domain Analysis .....	61
2.6 Concluding Remarks .....	68
<b>3. PROPOSED METHODOLOGY .....</b>	<b>73</b>
3.1 Introduction .....	73
3.2 Stochastic Model for Spatially Varying Acceleration Time Histories .....	73
3.2.1 Acceleration Time Histories Modeled as a Random Process of Uncorrelated Random Variables .....	74
3.2.2 Acceleration Time Histories Modeled as a Random Process of Correlated Random Variables .....	76
3.2.3 Cross Spectral Density Matrix of a Spatially Variable Random Process .....	77
3.2.4 Simulation of a Stationary Spatially Variable Random Process .....	78
3.2.5 Simulation of a Non-Stationary Spatially Variable Random Process ..	80
3.2.6 Simulation of a Non-Stationary and Non-Homogeneous Spatially Variable Random Process .....	84
3.2.7 Generation of Acceleration Time Histories of a Multi-Component Seismic Shear Wave using Non-Stationary and Non-Homogeneous Random Processes .....	87
3.2.8 Generation of Displacement Time Histories of a Multi-Component Seismic Shear Wave .....	90
3.2.8.1 Methodology to Determine the Displacement Time History Set under Each Bridge Support .....	94

### **TABLE OF CONTENTS - Continued**

3.2.9 Use of the Stochastic Model to Generate Spatially Varying Acceleration Time Histories .....	96
3.3 Analytical Model for Bridge Structure .....	100
3.4 Analytical Model for the Soil-Foundation Interface .....	115
3.4.1 General Remarks .....	115
3.4.2 Soil-Foundation Dynamic Stiffness Model .....	116
3.4.3 Soil Type Characterization Model .....	118
3.4.4 Soil Response Spectrum Characterization Model .....	120
3.4.4.1 Determination of Dynamic Shear Modulus of the Soil .....	120
3.4.4.2 Determination of Soil Response Spectrum Curves .....	122
3.5 Implementation of Spatially Variable Displacement Time Histories and Finite Element Bridge Model in the SAP2000 Computer Program .....	126
3.6 Monte Carlo Simulation Scheme .....	127
3.7 General Algorithm of the Proposed Methodology .....	129
3.8 Concluding Remarks .....	133
<b>4. EFFECT OF SPATIAL VARIABILITY OF SEISMIC EXCITATION AND VARIABILITY OF SOIL CONDITIONS ON PIER DUCTILITY DEMANDS OF MULTI-SPAN BRIDGES .....</b>	<b>136</b>
4.1 Introduction .....	136
4.2 Modeling Methodology .....	136
4.2.1 Multi-Span Highway Bridge Models .....	137
4.2.2 Soil Cases .....	139
4.3 Results for Bridge Pier Ductility Demands .....	141



## TABLE OF CONTENTS - Continued

4.3.1 Short Multi-Span Bridge Models .....	142
4.3.2 Medium Multi-Span Bridges Models .....	152
4.3.3 Long Multi-Span Bridges Models .....	162
4.3.4 Design Limitations on Pier Ductility Demands .....	173
4.4 Concluding Remarks .....	174
<b>5. EFFECT OF SPATIAL VARIABILITY OF SEISMIC EXCITATION ON DUCTILITY DEMANDS OF MULTI-SPAN BRIDGES WITH UNIFORM SOIL CONDITIONS AND VARIABLE SPAN LENGTHS AND PIER HEIGHTS .....</b>	<b>179</b>
5.1 Introduction .....	179
5.2 Modeling Methodology .....	180
5.3 Three-Span Bridge Models with Variable Lengths .....	186
5.4 Six-Span Bridge Models with Variable Lengths.....	192
5.5 Two-Span Bridge Models with Constant Length ( $L = 3a$ ) .....	198
5.6 Two-Span to Four-Span Bridge Models with Constant Length ( $L = 6a$ ) ...	201
5.7 Concluding Remarks .....	206
<b>6. EFFECT OF SPATIAL VARIABILITY OF SEISMIC EXCITATION WITH A STRONG VERTICAL ACCELERATION COMPONENT AND VARIABILITY OF SOIL CONDITIONS ON PIER DUCTILITY DEMANDS OF MULTI-SPAN BRIDGES .....</b>	<b>209</b>
6.1 Introduction .....	209
6.2 Modeling Methodology .....	210
6.2.1 Pier Axial Load Amplification Factor .....	211
6.3 Results for Bridge Pier Ductility Demands .....	216

## **TABLE OF CONTENTS - Continued**

6.3.1 Short Multi-Span Bridge Models .....	217
6.3.2 Medium Multi-Span Bridge Models .....	219
6.3.3 Long Multi-Span Bridge Models .....	222
6.4 Concluding Remarks .....	226
<b>7. SUMMARY, CONCLUSIONS AND RECOMMENDATIONS .....,.....</b>	<b>229</b>
7.1 Summary .....	229
7.2 Conclusions .....	231
7.3 Recommendations for Further Research .....	237
<b>APPENDIX A. REPRESENTATIVE ACCELERATION, VELOCITY AND DISPLACEMENT TIME HISTORY GRAPHS IN SHORT MULTI-SPAN BRIDGES .....</b>	<b>240</b>
A.1 Time History Graphs for Short Multi-Span Bridge Model Supported on Hard Soil Case .....	241
A.2 Time History Graphs for Short Multi-Span Bridge Model Supported on Medium Soil Case .....	245
A.3 Time History Graphs for Short Multi-Span Bridge Model Supported on Soft Soil Case .....	249
<b>APPENDIX B. BASIC CONCEPTS OF PROBABILITY THEORY AND RANDOM PROCESSES .....</b>	<b>253</b>
B.1 Basic Concepts of Probability Theory .....	253
B.2 Random Processes .....	254
<b>APPENDIX C. NOTATION .....</b>	<b>256</b>
<b>REFERENCES .....</b>	<b>263</b>

## LIST OF FIGURES

Figure 1.1 Typical Reinforced Concrete Highway Bridge Structures .....	24
Figure 1.2 Correlated Point Specific Acceleration Time Histories Generated under Abutment and Pier Foundations of a Typical Multi-Span Highway Bridge Model .....	26
Figure 1.3 SMART-1 Array Accelerometer Configuration. The Dots Represent Accelerometer Locations in Three Concentric Rings .....	28
Figure 1.4 Superimposed Shear Wave Time Histories for SMART-1 Array Accelerometers.....	29
Figure 1.5 Typical Acceleration Response Spectra Curves Generated for Soil Classes C (Hard Soils: Very Dense Soils or Soft Rocks), D (Medium Stiff Soils) and E (Soft Soils) Considering 5% Damping in Accordance with the 2009 Edition of the International Building Code Criteria. ....	31
Figure 1.6 Illustrations of the Wave Passage, Incoherence and Local Site Effects in Acceleration Time Histories .....	39
Figure 2.1 Variation of the HV Coherence Function with Frequency and Separation Distance between Stations.....	48
Figure 2.2 Variation of the Abrahamson Coherence Function with Frequency and Separation Distance between Stations .....	50
Figure 2.3 Variation of the LW Coherence Function with Frequency and Separation Distance between Stations for $\alpha = 2.5 \times 10^{-4} \text{ sec/m}$ .....	52
Figure 3.1 Modulation Function $M_j(t)$ given by Jennings et al (1968) .....	82
Figure 3.2 Effect of a Wave Amplitude Modulation Function on a Stationary Acceleration Time History .....	83
Figure 3.3 Multi-Component Shear Wave Traveling in a Horizontal Plane and Acting with an Angle of Incidence $\beta$ with respect to a Highway Bridge Longitudinal Axis.....	87

### LIST OF FIGURES – Continued

Figure 3.4 Decomposition of the Multi-Component $S$ Wave into a Multi-Component Longitudinal Shear Wave $S_X$ and a Multi-Component Transverse Shear Wave $S_Y$ .....	88
Figure 3.5 Cross Spectral Density Curves Generated from the Acceleration Time History Records shown in Figure 1.3(a) .....	91
Figure 3.6 Acceleration, Velocity and Displacement Time Histories Generated on Hard Soils for the Right Bent of the Highway Bridge Model Shown in Figure 3.4 due to the Horizontal Component of the $S_X$ Shear Wave .....	93
Figure 3.7 Application of Unique Displacement Time History Sets ( $D_X$ , $D_Y$ , $D_Z$ ) Under Bridge Pier Supports of a Three-Span Bridge Model .....	95
Figure 3.8 Effect of Spatial Variability in the X Direction on Acceleration Time Histories of the Horizontal Component of the $S_X$ Wave for Bridge Supports Located on Hard Soils .....	96
Figure 3.9 Effect of Spatial Variability in the Y Direction on Acceleration Time Histories of the Horizontal Component of the $S_Y$ Wave for Bridge Supports Located on Hard Soils .....	98
Figure 3.10 Response Spectra Compatibility of the $A_X$ Acceleration Time History at Bent 1 Supports for the Highway Bridge Model under Different Soil Conditions .....	99
Figure 3.11 Highway Bridge Structural System .....	102
Figure 3.12 Finite Element Model of Highway Bridge Showing Location of Plastic Hinges and Rotational and Translational Spring Sets Representing Soil Dynamic Stiffness Model .....	105
Figure 3.13 Three-Dimensional Finite Element Representation of a Typical Three Span Highway Bridge Structural System .....	106
Figure 3.14 Plastic Hinge Model .....	108
Figure 3.15 Moment Curvature Relationship for Piers .....	111
Figure 3.16 Local Axes of Plastic Hinges in Bridge Piers Referred to Bridge Global Axes .....	113

### LIST OF FIGURES – Continued

Figure 3.17 Rigid Footing Spring Constants .....	118
Figure 3.18 Soil Response Spectrum Curve .....	122
Figure 3.19 Response Spectrum Curve for Hard Soils .....	124
Figure 3.20 Response Spectrum Curve for Medium Soils .....	125
Figure 3.19 Response Spectrum Curve for Soft Soils .....	125
Figure 4.1 Multi-Span Highway Bridge Models .....	138
Figure 4.2 Typical Cross-Section (Bent Frame) of the Multi-Span Bridge Models .....	139
Figure 4.3 Pier Ductility Demand Statistics for Short Multi-Span Bridge Model Supported on Hard Soil Case .....	143
Figure 4.4 Pier Ductility Demand Statistics for Short Multi-Span Bridge Model Supported on Medium Soil Case .....	143
Figure 4.5 Pier Ductility Demand Statistics for Short Multi-Span Bridge Model Supported on Soft Soil Case .....	143
Figure 4.6 Mean Pier Ductility Demands on Short Multi-Span Bridge Model as a Function of the Soil Case .....	144
Figure 4.7 Mean Pier Ductility Index Values for Short Multi-Span Bridge Model .....	148
Figure 4.8 Longitudinal ( $R_2$ ) and Transverse ( $R_3$ ) Mean Pier Ductility Demands in Short Multi-Span Bridge Model Supported on Hard Soil Case .....	149
Figure 4.9 Longitudinal ( $R_2$ ) and Transverse ( $R_3$ ) Mean Pier Ductility Demands in Short Multi-Span Bridge Model Supported on Medium Soil Case .....	149
Figure 4.10 Longitudinal ( $R_2$ ) and Transverse ( $R_3$ ) Mean Pier Ductility Demands in Short Multi-Span Bridge Model Supported on Soft Soil Case .....	150
Figure 4.11 Pier Ductility Demand Statistics for Medium Multi-Span Bridge Model Supported on Hard Soil Case .....	154
Figure 4.12 Pier Ductility Demand Statistics for Medium Multi-Span Bridge Model Supported on Medium Soil Case .....	154

### LIST OF FIGURES – Continued

Figure 4.13 Pier Ductility Demand Statistics for Medium Multi-Span Bridge Model Supported on Soft Soil Case .....	154
Figure 4.14 Mean Pier Ductility Demands on Medium Multi-Span Bridge Model as a Function of Soil Case .....	155
Figure 4.15 Mean Pier Ductility Indexes for Medium Multi-Span Bridge Model .....	157
Figure 4.16 Longitudinal ( $R_2$ ) and Transverse ( $R_3$ ) Mean Pier Ductility Demands in Medium Multi-Span Bridges Model Supported on Hard Soil Case .....	160
Figure 4.17 Longitudinal ( $R_2$ ) and Transverse ( $R_3$ ) Mean Pier Ductility Demands in Medium Multi-Span Bridges Model Supported on Medium Soil Case .....	160
Figure 4.18 Longitudinal ( $R_2$ ) and Transverse ( $R_3$ ) Mean Pier Ductility Demands in Medium Multi-Span Bridges Model Supported on Soft Soil Case .....	161
Figure 4.19 Pier Ductility Demand Statistics for Long Multi-Span Bridge Model Supported on Hard Soil Case .....	165
Figure 4.20 Pier Ductility Demand Statistics for Long Multi-Span Bridge Model Supported on Medium Soil Case .....	165
Figure 4.21 Pier Ductility Demand Statistics for Long Multi-Span Bridge Mode Supported on Soft Soil Case .....	166
Figure 4.22 Mean Pier Ductility Demands on Long Multi-Span Bridge Models as a Function of Soil Case .....	166
Figure 4.23 Mean Pier Ductility Indexes for Long Multi-Span Bridge Models .....	168
Figure 4.24 Longitudinal ( $R_2$ ) and Transverse ( $R_3$ ) Mean Pier Ductility Demands in Long Multi-Span Bridges Models on Supported Hard Soil Case .....	171
Figure 4.25 Longitudinal ( $R_2$ ) and Transverse ( $R_3$ ) Mean Pier Ductility Demands in Long Multi-Span Bridges Models on Supported Medium Soil Case .....	171
Figure 4.26 Longitudinal ( $R_2$ ) and Transverse ( $R_3$ ) Mean Pier Ductility Demands in Long Multi-Span Bridges Models on Supported Soft Soil Case .....	172
Figure 5.1 Three-Span Bridge Models with Variable Lengths .....	181

### LIST OF FIGURES – Continued

Figure 5.2 Six-Span Bridge Models with Variable Lengths .....	182
Figure 5.3 Two-Span to Four-Span Bridge Models with Constant Length ( $L = 6a$ ) ...	183
Figure 5.4 Two-Span Bridge Models with Constant Length ( $L = 3a$ ) .....	184
Figure 5.5 Mean Pier Ductility Indexes for Bridge 3SC1 .....	187
Figure 5.6 Mean Pier Ductility Indexes for Bridge 3SC2 .....	187
Figure 5.7 Mean Pier Ductility Indexes for Bridge 3SC3 .....	187
Figure 5.8 Mean Pier Ductility Indexes for Bridge 3SC4 .....	188
Figure 5.9 Mean Pier Ductility Indexes for Bridge 3SC5 .....	188
Figure 5.10 Mean Pier Ductility Indexes for Bridge 3SC6 .....	188
Figure 5.11 Mean Pier Ductility Indexes for Bridges 3SC1 and 3SC6 .....	190
Figure 5.12 Mean Pier Ductility Indexes for Bridge 6SC1 .....	193
Figure 5.13 Mean Pier Ductility Indexes for Bridge 6SC2 .....	193
Figure 5.14 Mean Pier Ductility Indexes for Bridge 6SC3 .....	193
Figure 5.15 Mean Pier Ductility Indexes for Bridge 6SC4 .....	194
Figure 5.16 Mean Pier Ductility Indexes for Bridge 6SC5 .....	194
Figure 5.17 Mean Pier Ductility Indexes for Bridge 6SC6 .....	194
Figure 5.18 Mean Pier Ductility Indexes for Bridges 6SC1 and 6SC6 .....	196
Figure 5.19 Mean Pier Ductility Index Values for Bridges 3SC1, 3SC6, 2S3aC1 and 2S3aC2 Plotted as Bent Ductility Index Lines .....	199
Figure 5.20 Mean Pier Ductility Index Values for Bridges 6SC1, 6SC6, 4S6a, 3S61C1, 3S81C2, 3S6aC3, 2S6aC1, 2S6aC2 and 2S6aC3 Plotted as Bent Ductility Index Lines .....	202
Figure 6.1 Bridge Pier Moment-Curvature Relationship for $Z = 1.0$ .....	212

### LIST OF FIGURES – Continued

Figure 6.2 Bridge Pier Moment-Curvature Relationships for $Z = 0.67$ and $Z = 1.0$ ....	213
Figure 6.3 Mean $Z$ Indexes for Short Multi-Span Bridge Models .....	218
Figure 6.4 Mean $Z$ Indexes for Medium Multi-Span Bridge Models .....	222
Figure 6.5 Mean $Z$ Indexes for Long Multi-Span Bridge Models .....	226
Figure A.1 Left Abutment Acceleration Component Time History for Hard Soils .....	241
Figure A.2 Left Abutment Velocity Component Time History for Hard Soils .....	241
Figure A.3 Left Abutment Displacement Component Time History for Hard Soils ...	241
Figure A.4 Bent 1 (Piers 1&2) Acceleration Component Time History for Hard Soils.	242
Figure A.5 Bent 1 (Piers 1&2) Velocity Component Time History for Hard Soils .....	242
Figure A.6 Bent 1 (Piers 1&2) Displacement Component Time History for Hard Soils .....	242
Figure A.7 Bent 2 (Piers 3&4) Acceleration Component Time History for Hard Soils .....	243
Figure A.8 Bent 2 (Piers 3&4) Velocity Component Time History for Hard Soils .....	243
Figure A.9 Bent 2 (Piers 3&4) Displacement Component Time History for Hard Soils .....	243
Figure A.10 Right Abutment Acceleration Component Time History for Hard Soils.	244
Figure A.11 Right Abutment Velocity Component Time History for Hard Soils .....	244
Figure A.12 Right Abutment Displacement Component Time History for Hard Soils.	244
Figure A.13 Left Abutment Acceleration Component Time History for Hard Soils ...	245
Figure A.14 Left Abutment Velocity Component Time History for Hard Soils .....	245
Figure A.15 Left Abutment Displacement Component Time History for Hard Soils ...	245



### LIST OF FIGURES – Continued

Figure A.16 Bent 1 (Piers 1&2) Acceleration Component Time History for Medium Soils .....	246
Figure A.17 Bent 1 (Piers 1&2) Velocity Component Time History for Medium Soils .....	246
Figure A.18 Bent 1 (Piers 1&2) Displacement Component Time History for Medium Soils .....	246
Figure A.19 Bent 2 (Piers 3&4) Acceleration Component Time History for Medium Soils .....	247
Figure A.20 Bent 2 (Piers 3&4) Velocity Component Time History for Medium Soils .....	247
Figure A.21 Bent 2 (Piers 3&4) Displacement Component Time History for Medium Soils .....	247
Figure A.22 Right Abutment Acceleration Component Time History for Hard Soils ..	248
Figure A.23 Right Abutment Velocity Component Time History for Hard Soils .....	248
Figure A.24 Right Abutment Displacement Component Time History for Hard Soils.	248
Figure A.25 Left Abutment Acceleration Component Time History for Hard Soils ....	249
Figure A.26 Left Abutment Velocity Component Time History for Hard Soils .....	249
Figure A.27 Left Abutment Displacement Component Time History for Hard Soils ...	249
Figure A.28 Bent 1 (Piers 1&2) Acceleration Component Time History for Soft Soils	250
Figure A.29 Bent 1 (Piers 1&2) Velocity Component Time History for Soft Soils ....	250
Figure A.30 Bent 1 (Piers 1&2) Displacement Component Time History for Soft Soils .....	250
Figure A.31 Bent 2 (Piers 3&4) Acceleration Component Time History for Soft Soils .....	251
Figure A.32 Bent 2 (Piers 3&4) Velocity Component Time History for Soft Soils ....	251

**LIST OF FIGURES – Continued**

Figure A.33 Bent 2 (Piers 3&4) Displacement Component Time History for Soft Soils .....	251
Figure A.34 Right Abutment Acceleration Component Time History for Hard Soils ..	252
Figure A.35 Right Abutment Velocity Component Time History for Hard Soils .....	252
Figure A.36 Right Abutment Displacement Component Time History for Hard Soils.	252

## LIST OF TABLES

Table 3.1 Soil Stiffness Coefficients Based on Soil Type .....	117
Table 3.2 Soil Type Characterization and Shear Wave Velocity Values .....	119
Table 3.3 Relevant Static Soil Properties .....	119
Table 3.4 IBC 2009 Code Site Coefficient $F_a$ .....	121
Table 3.5 Effective Shear Modulus Ratio $G/G_o$ .....	122
Table 3.6 Summary of Soil Dynamic Properties .....	121
Table 3.7 IBC 2009 Code Site Coefficient $F_V$ .....	124
Table 3.8 Response Spectrum Curve Parameter Calculations .....	124
Table 4.1 Dimensions of Short, Medium and Long Multi-Span Bridge Models .....	139
Table 4.2 Soil Type Variation Cases for Short Multi-Span Bridge Models .....	140
Table 4.3 Soil Type Variation Cases for Medium Multi-Span Bridge Models .....	141
Table 4.4 Soil Type Variation Cases for Long Multi-Span Bridge Models .....	141
Table 4.5 Resultant Pier Ductility Demand on Short Multi-Span Bridge Models Subjected to Spatially Varying Seismic Excitation .....	142
Table 4.6 Resultant Pier Ductility Demand on Short Multi-Span Bridge Models Subjected to Uniform Seismic Excitation .....	146
Table 4.7 Mean Pier Ductility Index Values for Short Multi-Span Bridge Model .....	148
Table 4.8 Resultant Pier Ductility Demand on Medium Multi-Span Bridge Models Subjected to Spatially Varying Seismic Excitation .....	153
Table 4.9 Resultant Pier Ductility Demand on Medium Multi-Span Bridge Models Subjected to Uniform Seismic Excitation .....	156

### LIST OF TABLES-Continued

Table 4.10 Mean Pier Ductility Index Values for Medium Multi-Span Bridge Modes.	158
Table 4.11 Resultant Pier Ductility Demand on Long Multi-Span Bridge Models Subjected to Spatially Varying Seismic Excitation .....	164
Table 4.12 Resultant Pier Ductility Demand on Long Multi-Span Bridge Models Subjected to Uniform Seismic Excitation .....	167
Table 4.13 Mean Pier Ductility Index Values for Long Multi-Span Bridge Modes ....	170
Table 6.1 Pier Axial Load Amplification Factors on Short Multi-Span Bridge Models Subjected to Spatially Varying Seismic Excitation under the $Z = 1.0$ Condition .....	213
Table 6.2 Pier Axial Load Amplification Factors on Medium Multi-Span Bridge Models Subjected to Spatially Varying Seismic Excitation under the $Z = 1.0$ Condition .....	214
Table 6.3 Pier Axial Load Amplification Factors on Long Multi-Span Bridge Models Subjected to Spatially Varying Seismic Excitation under the $Z = 1.0$ Condition .....	215
Table 6.4 Resultant Pier Ductility Demand on Short Multi-Span Bridge Models Subjected to Spatially Varying Seismic Excitation with a Strong Vertical Acceleration Component ( $Z = 1.0$ Condition) .....	217
Table 6.5 Mean $Z$ Index Values for Short Multi-Span Bridge Models .....	218
Table 6.6 Resultant Pier Ductility Demand on Medium Multi-Span Bridge Models Subjected to Spatially Varying Seismic Excitation with a Strong Vertical Acceleration Component ( $Z = 1.0$ Condition) .....	220
Table 6.7 Mean $Z$ Index Values for Medium Multi-Span Bridge Models .....	221
Table 6.8 Resultant Pier Ductility Demand on Long Multi-Span Bridge Models Subjected to Spatially Varying Seismic Excitation with a Strong Vertical Acceleration Component ( $Z = 1.0$ Condition) .....	224
Table 6.9 Mean $Z$ Index Values for Long Multi-Span Bridge Models .....	225

## ABSTRACT

A new methodology is proposed to perform nonlinear time domain analysis on three-dimensional reinforced concrete bridge structures subjected to spatially varying seismic ground motions. A stochastic algorithm is implemented to generate unique and correlated time history records under each bridge support to model the spatial variability effects of seismic wave components traveling in the longitudinal and transverse direction of the bridge. Three-dimensional finite element models of highway bridges with variable geometry are considered where the nonlinear response is concentrated at bidirectional plastic hinges located at the pier end zones. The ductility demand at each pier is determined from the bidirectional rotations occurring at the plastic hinges during the seismic response evaluation of the bridge models. Variability of the soil characteristics along the length of the bridge is addressed by enforcing soil response spectrum compatibility of the generated time history records and of the dynamic stiffness properties of the spring sets modeling soil rigidity at the soil-foundation interface at each support location.

The results on pier ductility demand values show that their magnitude depends on the type of soil under the pier supports, the pier location and the overall length and geometry of the bridge structure. Maximum ductility demand values were found to occur in piers supported on soft soils and located around the mid span of long multi-span bridges. The results also show that pier ductility demand values in the transverse direction of the bridge can be significantly different than the values in the longitudinal

direction and in some instances, the maximum value occurs in the transverse direction. Moreover, results also show that ignoring the effects of spatial variability of the seismic excitation, the pier ductility demand can be severely underestimated.

Finally, results show that increasing the vertical acceleration component in the seismic wave will generate an increase in the pier axial loads, which will reduce the ductility range of the pier plastic zones. As result, even though the increase in pier ductility demand associated with the increase in the vertical acceleration component was found to be relatively small, the number piers exhibiting significant structural damage increased.

## **1. INTRODUCTION**

### **1.1 General Remarks**

It is a common practice in the seismic design of structures to consider that all ground supports are subjected simultaneously to identical acceleration time histories. Implicit in this consideration are the following assumptions: (a) seismic waves have infinite velocity, (b) the waves propagate through an infinite depth homogeneous soil media and (c) the geotechnical characteristics of the soil supporting the foundation are the same in all supports. Most buildings have structural dimensions that allow the use of these assumptions without introducing significant error. However, some long multi-span bridge structures can have very large dimensions in the direction of traffic and the use of these assumptions may introduce significant error to the predictions of their structural response. As a result of a finite velocity seismic wave traveling long distances through a heterogeneous soil media, the differences in phase (arrival times), amplitude and frequency content of the seismic wave exciting each ground support may no longer be insignificant for these types of structures. Also, many bridges of considerable lengths are required to direct traffic over bodies of water, such as rivers or lakes, and the geotechnical characteristics of the soil under the abutments may be very different than the characteristics present under the submerged pier foundations located on the river or lake bed. Therefore, significant variations in the soil types under the supports may occur even for bridges with relatively short lengths.

Figure 1.1 shows typical highway bridge structures where the foundations of the exterior supports of the bridges (i.e. abutments) are resting on well graded engineered soils and the foundations of the internal supports (i.e. bents) are resting usually on naturally occurring soils. The bents shown in Figure 1.1 are structural frames that support the bridge superstructure and consist of two or more vertical piers and a horizontal cap beam, which may be hidden in the superstructure or exposed.



(a) Highway Bridge with Bents Consisting of Exposed Cap Beams and Five Piers



(b) Highway Bridge with Bents Consisting of Hidden Cap Beams and Two Piers

Figure 1.1 Typical Reinforced Concrete Highway Bridge Structures



Many bridge engineers assume fully rigid soil conditions under the supports, disregarding the differences in load-deformation characteristics that the soil may exhibit under such support. For example, well graded and compacted engineered soils used on bridge approaches can provide relatively more support stiffness to the abutment foundation than natural soils to the pier foundations. Support stiffness modeling based on the soil characteristics will be discussed in more detail in Chapter 3.

Although actual site specific acceleration time history records are always preferable than synthetically generated ones, such records are rarely available. For long multi-span bridges, point specific records at pier support locations would be ideal to capture the effects of the finite velocity seismic wave, but they are usually nonexistent; therefore, most bridge engineers use seismic records from other sites or design code seismic data to provide the information required to generate reliable earthquake excitation loads, failing to capture any significant differences in the seismic wave characteristics under each pier support. An analytical procedure that generates point specific synthetic earthquake acceleration time histories is therefore highly desirable. This procedure should be able to generate statistically independent seismic waves with amplitude variation in the horizontal and vertical direction to simulate the three components of an earthquake acceleration time history record at any point along the path of wave propagation. Also, for a given direction of wave propagation, this procedure should be able to correlate the acceleration time histories between consecutive points on the path of the wave, capturing the expected differences in phase, amplitude and frequency content of the wave as it travels through a heterogeneous soil media.

Figure 1.2 shows a typical multi-span highway bridge model with a superstructure made of a box girder supported on abutments at the ends and on bent frames (each bent frame consisting of piers and a cap beam integrated into the superstructure). If the abutments and pier foundations are assumed excited by a finite velocity seismic wave propagating through a heterogeneous soil media in the longitudinal direction of the bridge, the acceleration time history records shown under each abutment and pier foundation are expected to be unique (point specific) and partially correlated. As will be shown in Chapter 3, the degree of correlation will depend on the distance between supports, the velocity of the wave and the soil characteristics.

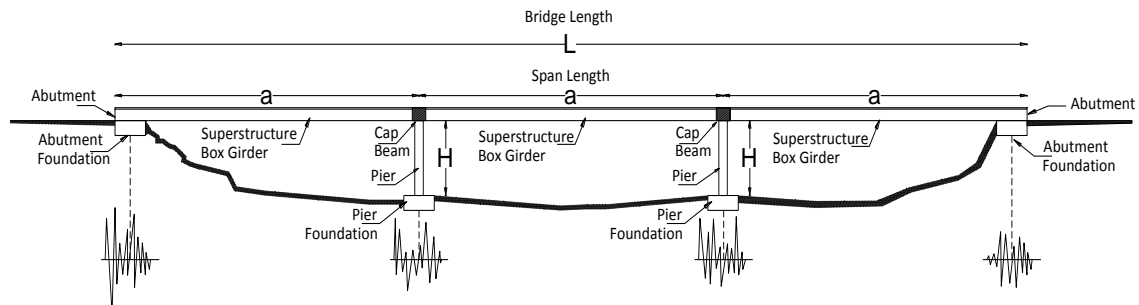


Figure 1.2 Correlated Point Specific Acceleration Time Histories Generated under Abutment and Pier Foundations of a Typical Multi-Span Highway Bridge Model.

A variety of options are available to engineers to estimate the seismic response of structural systems; including equivalent linear static analysis, response spectra analysis, and linear and nonlinear time domain dynamic analysis. For strategically important structures such as large bridges, nuclear power plants, dams, etc., nonlinear time domain dynamic analysis is often the preferred option, since it provides for a more realistic response scenario. In this case, it is common practice to select design earthquake

acceleration time histories that best represent the seismic activity at the site to generate the earthquake excitation data, along with a structural model that considers all relevant structural features and inherent material and geometric nonlinearities. Even under this complex analytical scenario, simplifying assumptions such as uniform seismic excitation, where all supports are assumed excited by the same earthquake time history record, as well as fully rigid soil conditions under the supports are often used. Moreover, in the instances where changes in the soil type below the supports are considered in the analytical model, these changes are typically assumed captured by the corresponding soil type response spectra information prescribed in design codes.

The analysis of time history records from dense arrays of accelerometers located around the world have shown that seismic ground motions can vary significantly in amplitude, phase and frequency content at distances well within the dimensions of long engineering structures. One such array that has been used extensively to study the spatial variation of seismic waves is the Strong Motion Array in Taiwan-Phase 1 (SMART 1), located in Lotung, in northeastern Taiwan. Figure 1.3 shows the configuration of the SMART-1 array. This array consists of three concentric rings, each ring having twelve equally spaced accelerometers, and an accelerometer placed on the center of all three rings. Locations of accelerometers on outer ring (stations O01 to O12) and middle ring (stations M01 to M12) are shown in Figure 1.3, but for the purpose of clarity, only the locations of every third accelerometer are shown for the inner ring (stations I03, I06, I09 and I12).

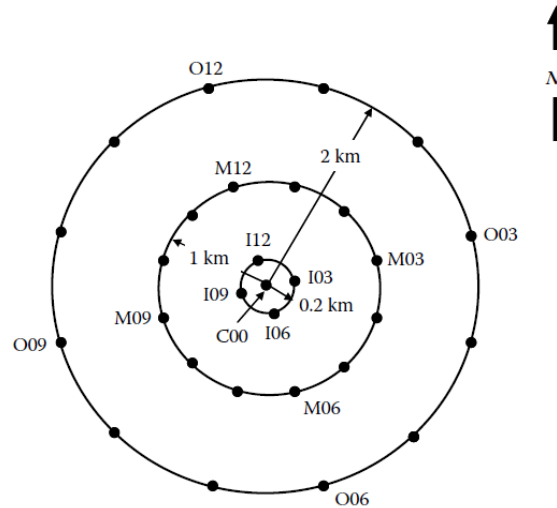
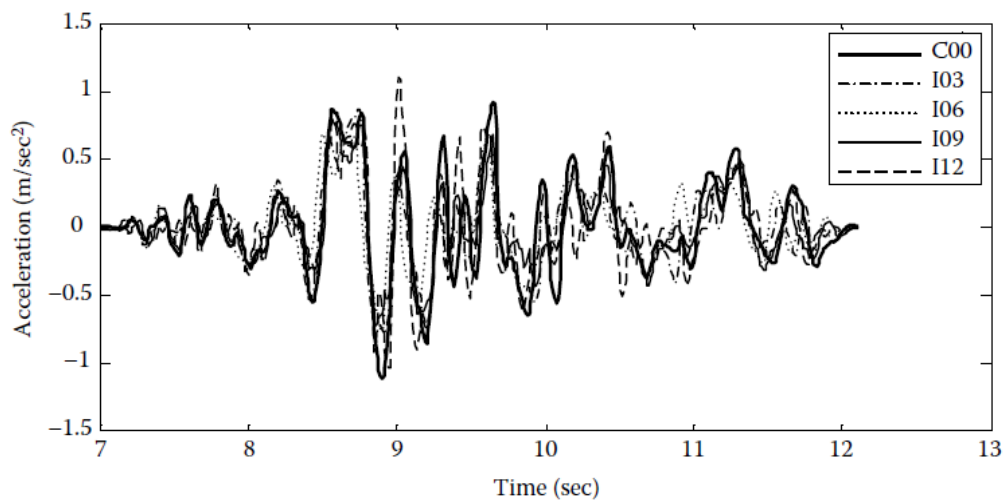


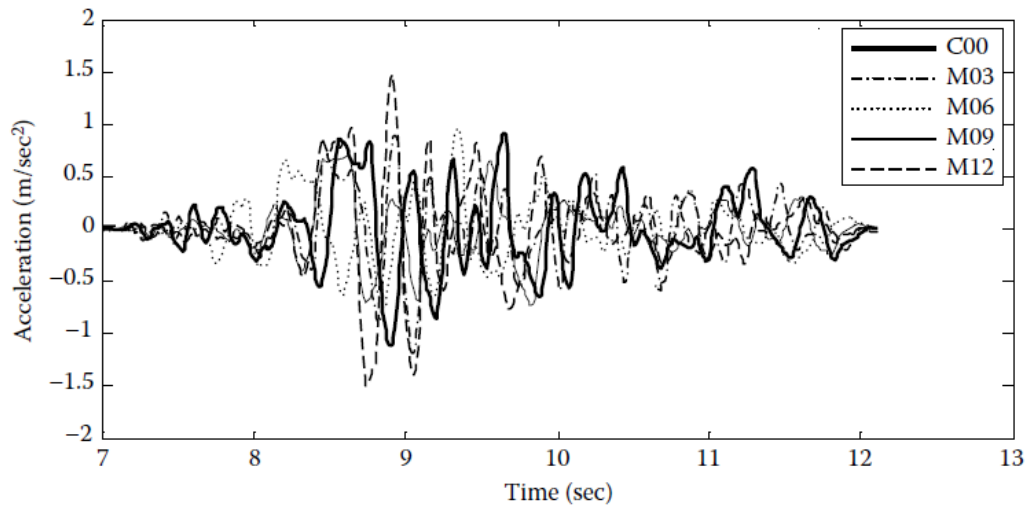
Figure 1.3 SMART-1 Array Accelerometer Configuration. The Dots Represent Accelerometer Locations in Three Concentric Rings [after Zerva (2009)].

Figure 1.4 shows superimposed time histories recorded at different accelerometer locations at the SMART 1 array during the strong motion phase of an earthquake. The epicentral direction of the earthquake almost coincided with the diameter passing through stations O06 and O12; thus, the seismic waves propagated in the North-South direction. Evidence of the spatial variability of the superimposed seismic waves can be clearly observed in the differences in phase (horizontal shifting of the peaks), amplitude (height variations of the peaks) and frequency (number of peaks occurring in a given time interval) of the acceleration time history records. Moreover, such differences are observed to be a function of the distance between accelerometers. For example, in Figure 1.4(a), where the distance between accelerometers does not exceed 0.2 km, these differences are observed to be relatively small. However, in Figure 1.4(b), where the distance between the accelerometers increases to 1 km, significant differences between the acceleration time history records can be observed. Since many long engineering

structures, such as bridges and pipelines, can exceed 1 km in length, the differences in the acceleration time histories exciting each support could be similar to the ones exhibited in Figure 1.4. These differences may induce additional internal forces and deformations in the structure that may not be properly accounted for in the design of the structure if the uniform seismic excitation assumption is used.



(a) Superimposed time histories for center and inner ring accelerometers



(b) Superimposed time histories for center and middle ring accelerometers

Figure 1.4 Superimposed Shear Wave Time Histories for SMART-1 Array Accelerometers [after Zerva (2009)].

The assumption of fully rigid soil conditions under the bridge supports must be looked at carefully in a case by case basis since it may disregard structure-soil interaction (SSI) and soil flexibility. The bridge foundations and surrounding soil can be flexible and kinematic interaction may not be negligible in some cases, which could cause filtering of the seismic waves at the pier supports, further modifying the seismic ground motion characteristics below and around the supports. Moreover, inertial interaction can be significant and may provide a path for dissipating seismic energy back into the surrounding soil media increasing the structural damping and as a result, reducing the internal forces induced on the bridge structure by the seismic excitation. Thus, many structural engineers disregard the SSI effects at the bridge supports under the assumption that it will lead to an acceptable conservative design of the bridge structure. However, in some instances, which sometimes might not be recognized in advance, the bridge structural response may increase when considering the SSI effects. In Section 2.2 more detailed discussion will be presented on the instances when SSI was found to have a detrimental effect on structural response.

The seismic response characteristics of a homogeneous soil media are usually modeled using soil response spectrum curves. These curves provide the maximum response as a function of frequency or time period of a single degree of freedom oscillator representing a particular soil type having defined damping and stiffness characteristic. Existing design codes usually set the damping ratio at 5% regardless of the soil type. Figure 1.5 shows typical response spectra curves for three different soil types.

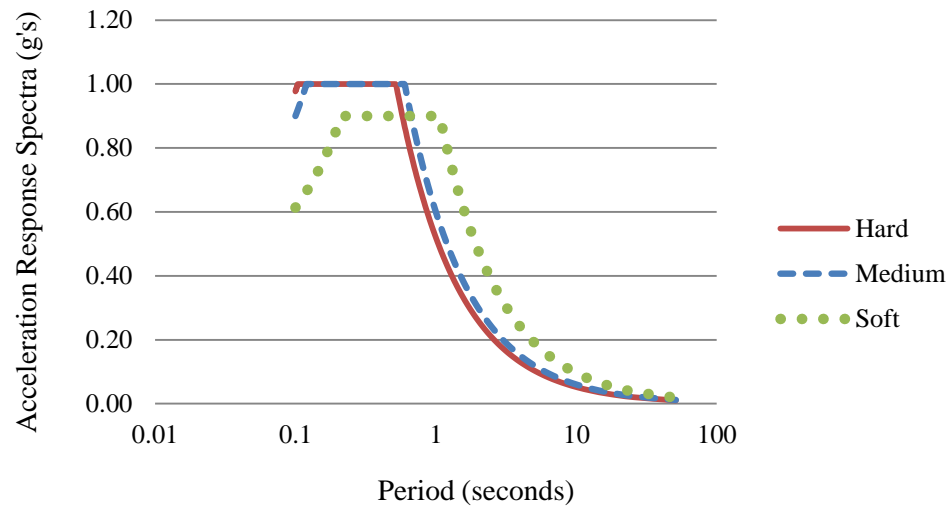


Figure 1.5 Typical Acceleration Response Spectra Curves Generated for Soil Classes C (Hard Soils: Very Dense Soils or Soft Rocks), D (Medium Stiff Soils) and E (Soft Soils) Considering 5% Damping in Accordance with the 2009 Edition of the International Building Code Criteria [IBC (2009)].

However, soil response spectrum curves may not be suitable for modeling the seismic response of multi-layered soil media, where the soil type varies with depth. In these cases, the generation of site specific soil response spectra data obtained from actual records of accelerometers positioned at expected foundation locations may provide a more reliable methodology. Such an elaborate accelerometer set up is typically cost effective only for a very limited number of projects and other less costly analytical models are available to describe the dynamic response of multilayered soil. However, many of the soil parameters that define such analytical models are frequency dependent and thus, not suitable to be used when evaluating structural response under time domain analysis. Although some attempts have been made to generate time dependent

expressions for these soil parameters, many restrictions and simplifications are required. More discussions on this matter are presented in Section 3.4.

The effects of the spatial variability of seismic ground motions act on the overall length of the structure and should not be disregarded even when the distance between adjacent supports is relatively short, since the distance between the first and last supports may be the relevant factor. For example, consider a long multi-span bridge structure where the first and last supports are 1 km apart and all intermediate supports are 0.2 km apart. Assuming that the differences in the seismic excitation at the bridge supports are given by the superimposed acceleration time histories in Figures 1.4(a) and 1.4(b), then the larger the difference in the acceleration time history records between end support locations, the more relevant is the spatial variability of the records on the overall structural response of the bridge; this is true even when the difference in the acceleration time histories between adjacent supports may be relatively small [see Figure 1.4(a)].

When the structural response under a severe earthquake excitation is expected to occur within the nonlinear range, the horizontal (transverse and longitudinal) and vertical acceleration components of the spatially varying seismic wave must be considered simultaneously in order to obtain a realistic structural response. In fact, the application of the principle of superposition, where the dynamic response under each individual component of the spatially varying seismic wave can be superimposed, is only valid when evaluating linear elastic structural response. Moreover, two dimensional (plane frame) simplifications of nonlinear structural response under spatially varying seismic



excitation fail to consider the effect of the transverse (out of plane) component of the horizontal acceleration.

Modern bridge design philosophies restrict the nonlinear response of the bridge to plastic zones occurring at both ends of the bridge piers. These plastic zones are typically modeled as plastic hinges with prescribed flexural moment-rotational behavior based on the yield and ultimate moment capacity of the pier cross sections. Thus, a ductility range of the pier plastic zones can be established by determining the difference in the yield and ultimate rotation values. Since plastic hinges are activated only when the yield rotation is reached or exceeded during the structural response, the ductility demand of the pier can be calculated by dividing the maximum rotation at the plastic hinge by the yield rotation. The plastic hinge model used in this study allows for rotations to exceed the ultimate rotation value, as long as the corresponding flexural strength at the plastic zone drops to a residual value equal to 20% of the yield flexural strength, in accordance with FEMA 365 (2000) criteria. This feature of the plastic hinge model allows the engineer to estimate the degree of the structural damage at the piers plastic zones by keeping track of how much the plastic hinge rotations exceed the ultimate rotation value.

Multi-span bridges structures with significant variations in pier heights and span lengths within the bridge total length are often required in highway intersections or when spanning over canyons with abrupt variations in topography. These variations can generate structural systems with considerable asymmetry that may exhibit complex three-dimensional responses even under uniform seismic excitation. It is to be expected that the degree of complexity of the response of such structural systems will increase when

considering the effects of spatially variability of the seismic excitation. Thus, the nonlinear response of the piers should be determined considering both the variability of the bridge geometry and of the seismic excitation; otherwise, unrealistic estimations of the pier ductility demand may result.

It is an established fact that strong vertical accelerations have been experienced in the past by bridges located at relatively short distances to an earthquake epicenter. In some cases, the magnitude of the vertical acceleration can be similar or greater than the horizontal acceleration. Given the fact that current design codes assume the vertical component of the seismic loading to be a fixed percentage of the horizontal component, there is in general no explicit account for the effect of the magnitude of the vertical component on the bridge structural response. The presence of a strong vertical acceleration component will tend to generate a significant increase in the axial load of the bridge piers and as a result, could lead to a considerable reduction of the flexural ductility range of such piers. Therefore, this reduction must be considered when modeling the nonlinear response of the piers in order to avoid overestimating their ultimate flexural capacity. A reliable methodology is thus required to determine the pier axial load amplification due to the presence of a strong vertical acceleration component. The reduction of the ductility range of the pier plastic zones as a function of the pier axial load magnitude also needs to be addressed, along with modeling considerations of the pier plastic hinges to accounts for such reduction.

It is highly unlikely that the seismic waves arriving at a certain bridge location will have a direction parallel to the bridge longitudinal or transverse axis. Thus, it is

reasonable to expect that the seismic waves will arrive with a certain incidence angle with respect to the bridge longitudinal axis. However, the angle of incidence of the arriving seismic wave is often ignored when estimating the structural response of bridges. Typically, seismic waves are assumed arriving either parallel or perpendicular to the bridge longitudinal axis, producing as a result a simplified two dimensional response of the bridge and unidirectional responses on the bridge piers. The arriving seismic wave can be modeled as a multi-component acceleration vector, with a magnitude given by its horizontal and vertical acceleration components and a direction given by its incidence angle; thus, vector decomposition of the horizontal (transverse and longitudinal) acceleration components, along with algebraic addition of the vertical acceleration components, can be performed in order to distribute the wave effects along the longitudinal and transverse directions of the bridge. As a result, a more realistic three dimensional response of the bridge and bidirectional responses of the bridge piers will be achieved. Although unidirectional or bidirectional responses of the piers are due mainly to the bending and shearing effect of the horizontal acceleration components of the wave, the vertical acceleration components will induce axial loading effects on the piers, which can become significant if the vertical component is particularly strong.

## **1.2 Causes of Spatial Variability in Seismic Waves**

It is generally accepted that spatial variability in the seismic waves is mainly due to the following causes [Saxena (2000), Sextos et al (2003)]:

- 1) *Wave passage effect*, due to the difference in arrival times of the seismic wave at the different pier support locations.
- 2) *Incoherence effect* or loss of coherence of the seismic wave due to the multiple reflections, refractions and/or superposition of the propagating wave as it travels through a heterogeneous soil media.
- 3) *Local soil effect*, due to the change in amplitude, frequency content and/or propagation velocity of the seismic wave as it encounters changes in soil type and,
- 4) *Attenuation of motion effect*, due to the geometrical spread of the wave front and the loss of kinetic energy, which is a function of the epicentral distance.

The attenuation of motion effect may be disregarded if consideration is given to the fact that the dimensions of the structure are usually small compared to the epicentral distance, which implies that all pier supports are practically equidistant to the epicenter.

The wave passage effects may be accounted for by a properly derived deterministic function that induces a phase shift on the wave equation. The phase shift accounts for the difference in the wave arrival times at each pier support location and it depends on wave propagation velocity and the distance between pier supports along the path of the wave.

The incoherence effect may be accounted for more conveniently using a stochastic approach, where the seismic waves are modeled as stochastic vector processes [Shinozuka (1972, 1988), Deodatis (1996)]. The incoherence effect can then be described by a stochastic function, typically known as coherence function, which accounts for the degree of correlation of the acceleration time histories exciting adjacent support. Many

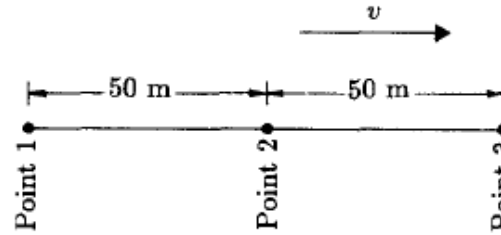
coherence functions are available in the literature [Harichandran and Vanmarke (1986), Luco and Wong (1986), Abrahamson et al (1991)] and some of them have been derived from analytical stochastic models, but most of them have an empirical basis and have been derived from the study of recorded data within dense arrays (mainly from the SMART-1 dense array). A more detailed presentation of some of the most commonly used analytical and empirical coherence functions is made in Section 2.4 of this study.

Empirical coherence functions are site and event dependent, since they are derived from data within a specific dense array using a particular seismic event. Some empirical coherence functions have been shown to have a broader application range when their validity has been verified in other arrays, or within the same array but with different seismic events. Currently, coherence functions are not directly associated with a conceptual understanding of a particular physical mechanism which causes loss of coherency of the wave; they are simply a ratio of convenient parameters that seem to model appropriately the incoherence effects. Therefore, choosing a particular coherence function is mostly based on personal preference, but since one should expect some differences in the generated stochastic waves when using different coherence functions, it is recommended to use coherence functions that have proven to show reliable and consistent behavior for a particular site. The Abrahamson coherence function [Abrahamson et al (1991)], which was selected in this study to model the incoherence effects, was empirically derived. This coherence function is presented in Section 2.4 and compared with other commonly used coherence functions and discussion is made on the criteria used for its selection.

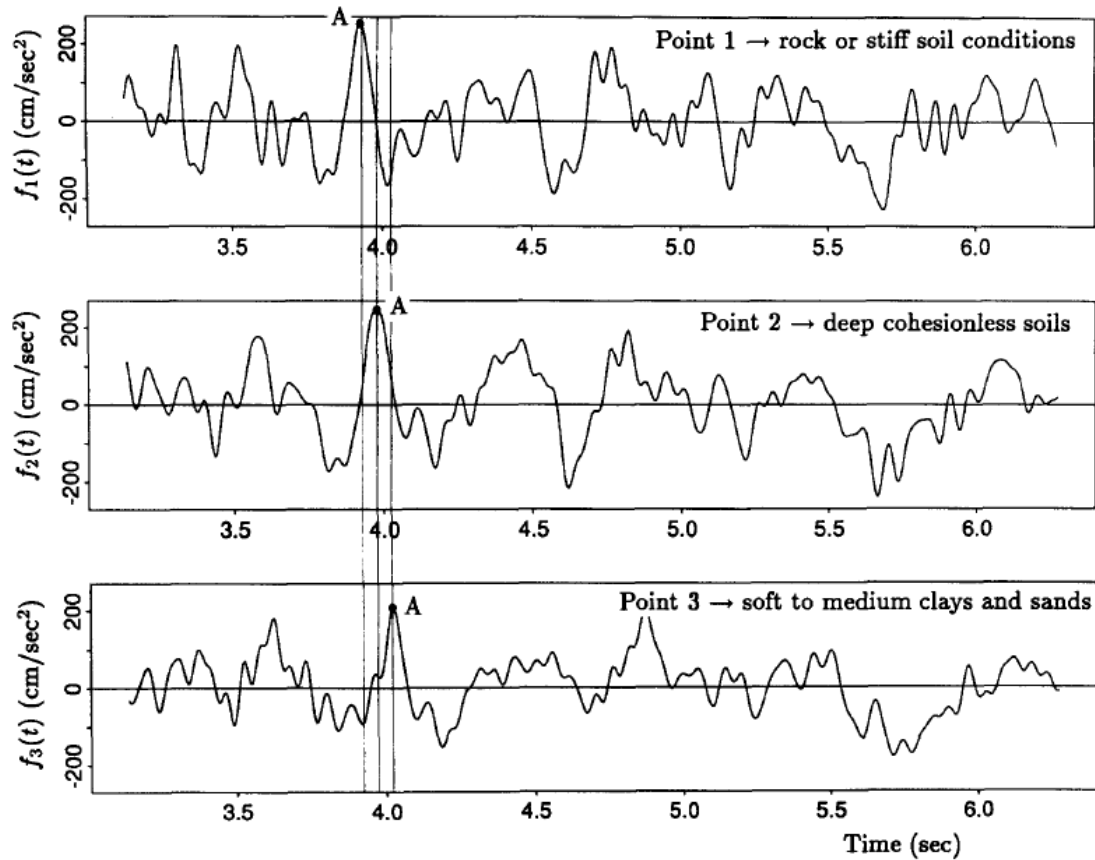
Analytical coherence functions are not based on actual recording within dense arrays and are therefore in principle independent of array location and seismic event. These functions can be attractive alternatives when the use of empirical coherence functions is questionable at a particular site. More discussions on analytical coherence functions will be made in Section 2.1.

The wave passage, incoherence and local soil effects can be illustrated with a simple example. Figure 1.6 shows three acceleration time histories corresponding to three points on the path of a wave traveling at 1000 meters/second. Each point is assumed located on different soil types of infinite depth to account for local soil effects (i.e., the variations of soil type properties are assumed to occur only in the direction of wave propagation and not with depth). The distance between points and the direction of propagation is shown in Figure 1.6(a). The behavior of each soil type is assumed captured by soil response spectrum curves similar to the ones shown in Figure 1.4. The deterministic function that accounts for the wave passage effect generates the horizontal shift in time of peak A shown in Figure 1.6(b) and is consistent with the fact that the wave arrives first at point 1 and last at point 3. The changes in the amplitude and frequency content of the time history curves are consistent with the changes of the soil type under each point, as described by their corresponding response spectrum curves. The degree of correlation is clearly visible in the similarities exhibited by the three time history curves, which accounts for the fact that the incoherence effect is low since the points are separated by relatively short distances. The stochastic procedure to generate

synthetic acceleration time history curves that accounts for all the effects illustrated in the above example is presented in Section 3.2.



(a) Location of points and direction of wave propagation.



(b) Phase shift in peak A accounting for different arrival times of the wave

Figure 1.6 Illustrations of the Wave Passage, Incoherence and Local Soil Effect in Acceleration Time Histories [after Deodatis (1996)].

### 1.3 Objectives

The general objective of this study is to consider the three dimensional response of typical reinforced concrete highway bridges under the effects of spatially varying seismic ground motions. Reinforced concrete is usually the structural material of choice for the superstructure and piers of many existing highway bridges. Although structural steel is sometimes used instead of reinforced concrete in the superstructure of highway bridges, reinforced concrete is still the predominant material of choice for the piers, where the nonlinear behavior is considered in this study. In fact, if the superstructure is allowed to behave linearly in accordance to modern bridge design procedures, many structural engineers model the structural steel sections using equivalent concrete sections [Priestley et al (1996)].

In order to meet with the general objective of this study, the following specific objectives have been identified:

*Objective 1: Develop a methodology to incorporate the effects of spatial variability in seismic waves when evaluating the three dimensional response of reinforced concrete highway bridges.* A point specific stochastic model is presented that can generate synthetic multi-component acceleration time histories. Nonlinear dynamic analysis in the time domain is performed on bridge finite element models with variable number of spans, span lengths and pier heights. Material nonlinearity is focused on plastic hinges located on the end of the bridge piers and the pier ductility demand is identified as the relevant structural response variable.



*Objective 2: Study the effects of the variation of soil characteristics under the bridge supports on the ductility demand of the piers considering spatially varying and uniform seismic waves.* Uniform seismic wave response is achieved by applying identical seismic time history records under each pier support. A parametric study is implemented using a Monte Carlo Simulation scheme based on multiple realizations of seismic time histories and relevant statistical parameters (mean value, standard deviation and coefficient of variation) on pier ductility demands are obtained.

*Objective 3: Study the effects of the variation in bridge structure geometry on the ductility demand of the piers considering spatially varying and uniform seismic waves.* Variations in the span length and pier heights are considered to obtain several symmetric and asymmetric bridge structural configurations. Each structural configuration is subjected to spatially varying and uniform seismic excitation. A parametric study using a Monte Carlo Simulation scheme is implemented and relevant statistical parameters on pier ductility demand variations are obtained.

*Objective 4: Study the effects of a strong vertical acceleration component in the spatially variable seismic wave on the ductility demand of piers.* A pier axial load amplification factor is derived to account for a strong vertical acceleration component using a Monte Carlo Simulation scheme. The ductility range at the pier plastic zones is reduced accordingly by updating the plastic hinge model. A Monte Carlo Simulation scheme is again implemented on the updated bridge models and relevant statistical parameters are obtained for the pier ductility demands.

## **1.4 Organization**

In Chapter 2 a literature review is carried out on relevant published research addressing modeling of spatially varying seismic excitation and structural response under such excitation. The coherence functions used by most researchers to model wave incoherence are discussed at some length. Then, in Chapter 3, the methodologies to generate spatially varying acceleration time histories and the analytical models for the bridge and soil are presented. In Chapter 4, the parameters defining the bridge and soil models are discussed in detail and the effects on pier ductility demands under variable soil characterizations are evaluated. In Chapter 5, the effects on pier ductility demands under variable bridge geometries are evaluated. In Chapter 6, the effects on pier ductility demands due to strong vertical acceleration components in the seismic wave are evaluated. Finally, in Chapter 7, the conclusions of this study are presented and recommendations for further research are outlined.

## **2. LITERATURE REVIEW**

### **2.1 Introduction**

In this chapter relevant published research on modeling of spatial variation in seismic waves and on the response of building and bridge structural systems under such waves are presented. In order to limit the discussion to the relevant conceptual contributions of the research findings, the mathematical procedures are omitted. In depth presentation of the mathematical framework of such findings is given in the publications referenced in this Chapter.

### **2.2 Modeling Spatial Variation in Seismic Waves using Stochastic Approach**

Shinozuka and Deodatis (1988) presented an overview on the main stochastic methods used in modeling seismic waves propagating at any given direction. The stochastic approach in general uses frequency domain analysis to generate spatially varying seismic waves. Stochastic methods are mathematically complex and have at best a weak physical meaning, but they provide acceptable results and are widely used.

Probably one of the more commonly used stochastic techniques to model spatially variability in seismic waves is the spectral representation method. This method is based on simulation techniques of non-stationary vector processes and was pioneered by Shinozuka (1972, 1988) and updated by Deodatis (1996). Deodatis presented an algorithm that simulates spatially varying acceleration time histories accounting for wave propagation, incoherence and local site effect. His procedure is based on a stationary

stochastic vector process that is made non-stationary by the introduction of a modulating function that allows for the control of the seismic wave amplitude time variation and for the overall duration of the strong motion phase of the earthquake. The procedure uses an iterative algorithm that updates the spectral density matrix in order to generate acceleration time histories compatible to prescribed response spectra criteria satisfying local geotechnical conditions. Saxena (2000) improved Deodatis algorithm by incorporating numerical smoothing procedures on the updated spectral density functions and by restricting the number of iterations of the updating algorithm, leading to simulated acceleration time histories that better reflected the prescribed coherence function.

### **2.3 Modeling Spatial Variation in Seismic Waves using Deterministic Approach**

Mylonakis et al (2001) presented a deterministic methodology for structures subjected to spatially varying seismic excitation. The effects of wave passage, local soil conditions and SSI were considered and some qualitative agreement was found with results of the stochastic methods just described above. However, it did not consider the incoherence effect, which restricted its applicability.

Zerva and Zhang (1990) developed a deterministic method for modeling spatial variability in seismic waves using recorded data from seismic events occurring at the SMART-1 dense array. They used a least square minimization technique that minimized the residual between the actual recorded motion and analytical motions modeled as a series of superimposed sinusoidal waves, described by their amplitude, frequency, wavelength and phase. They identified a common coherent component for all time

histories recorded at different stations, which exhibit sinusoidal characteristics, and a variable component that captures the change in amplitude and phase inherent in spatially variable seismic waves. They also found that the changes in amplitude and phase are correlated. Moreover, they discovered through signal processing techniques that seismic waves propagating vertically through the soil strata cause spatially variable wave arrival time delays at the stations, in addition to the delays caused by the horizontally propagating seismic waves.

## 2.4 Coherence Functions

Coherence functions are fundamentally important in modeling the spatial variability of seismic excitations since they capture the correlation of the acceleration time histories at adjacent stations as the seismic waves propagates through these stations. The wave passage and incoherence effects are usually integrated into one expression called the complex coherence function and given by the following expression:

$$\Gamma_{jk}(\omega) = \gamma_{jk}(\omega) \exp\left(\frac{-i\omega\xi}{v}\right) \quad (2.1)$$

Where:  $\gamma_{jk}(\omega)$  = Coherence function correlating stations  $j$  and  $k$

$\exp\left(\frac{-i\omega\xi}{v}\right)$  = Wave passage function (complex term)

$v$  = Wave velocity

$\xi$  = Distance between stations  $j$  and  $k$

$\omega$  = Frequency in rad/sec and  $i = \sqrt{-1}$

The wave velocity  $v$  in Eq. 2.1 is typically given in terms of the shear wave velocity and its magnitude will depend on the characteristics of soil media through which the shear wave propagates. More discussion on this subject will be made in Section 3.4.

As mentioned in Section 1.2, there are several empirical and analytical coherence functions available in the literature and Zerva (2009) provides an in depth overview of the some of these coherence functions. Some of the most widely used coherence functions are discussed in some detail next.

### 2.4.1 Empirical Coherence Functions

Empirical coherence functions are generated from the analysis and processing of recorded time history data at dense array locations. Since different researchers use different processing techniques, the expressions for the coherence functions are in general different, even when the same dense array acceleration time history data is used.

#### 2.4.1.1 The HV Coherence Function

The HV coherence function was developed by Harichandran and Vanmarke (1986) from the analysis and processing of recorded time histories of the SMART-1 dense array and is one of the most widely used empirical coherence functions. The HV coherence function correlating stations  $j$  and  $k$  is given by the following expression:

$$\gamma_{jk}(f) = A \exp\left(-\frac{2B\xi}{av(f)}\right) + (1 - A) \exp\left(-\frac{2B\xi}{v(f)}\right) \quad (2.2)$$

Where: 
$$v(f) = \kappa \left[1 + \left(\frac{f}{f_o}\right)^b\right]^{-1/2}$$

$$B = (1 - A + \delta A)$$

$$\xi = \text{Distance between stations } j \text{ and } k$$

$f$  = Cyclic frequency in Hz =  $\omega/2\pi$  and

$A, \delta, b, \kappa, f_o$  = Parameters to be determined from a specific seismic event.

Using the recorded time history data at the SMART-1 dense array due to a nearby earthquake named “Event 20”, the following values for the function parameters were determined:  $A = 0.736$ ,  $\delta = 0.147$ ,  $\kappa = 5210$  m,  $f_o = 1.09$  Hz and  $b = 2.78$ . Figure 2.1 shows the variation of the HV coherence function using the values of the parameters given above. It can be observed in Figure 2.1 that for a given frequency value the coherence is the greatest when the distance between stations is the shortest and vice versa. Also, regardless of the distance between stations, the coherence is lowest at the highest frequency range. A disadvantage of this coherence function is that it does not predict fully coherent time histories (coherence of 1.0) at zero frequency. This may introduce some error in the incoherence effect prediction in the low frequency range. Since some soft soils can have low fundamental frequencies, the prediction error will be most likely transmitted to the structural response of bridges supported on soft soils. In this study, soft soil supports are considered under bridge piers and thus, the HV coherence function was not selected to avoid introducing such error.

#### 2.4.1.2 The Abrahamson Coherence Function

Abrahamson et al (1991) proposed an empirical coherence function using nonlinear regression analysis of 15 seismic events recorded at the SMART-1 array. They found that their coherence function gave compatible results to the coherence computed at the EPRI Parkway dense array, indicating some degree of site and seismic event independence of their coherence function.

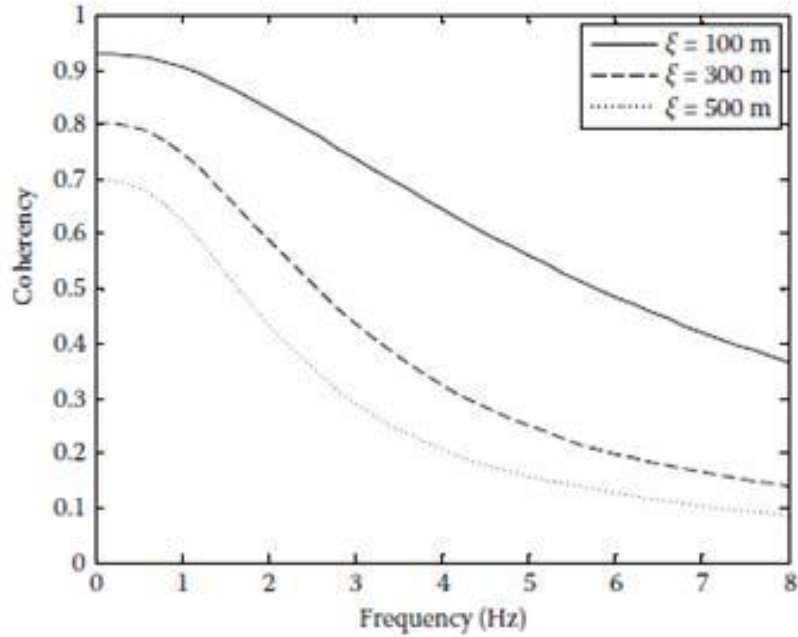


Figure 2.1 Variation of the HV Coherence Function with Frequency and Separation Distance between Stations [after Zerva (2009)].

Abrahamson (1993) gathered and integrated additional time history data recorded at other dense array sites and proposed a more refined version of his empirical coherence function. His coherence function for waves propagating horizontally is given by the following expression:

$$\gamma_{jk}(\omega) = \tanh \left\{ \frac{c_1(\xi)}{1 + c_2(\xi)\omega/(2\pi) + c_4(\xi)[\omega/(2\pi)]^2} + (4.8 - c_1(\xi)) \exp[c_3(\xi)\omega/(2\pi)] + 0.35 \right\} \quad (2.3)$$

Where:

$\xi$  = Distance between stations  $j$  and  $k$

$$c_1(\xi) = \frac{3.95}{1 + 0.0077\xi + 0.000023\xi^2} + 0.85\exp(-0.00013\xi)$$

$$c_2(\xi) = \frac{0.4 \left\{ 1 - \left[ 1 + \left( \frac{\xi}{5} \right)^3 \right]^{-1} \right\}}{\left[ 1 + \left( \frac{\xi}{190} \right)^8 \right] \left[ 1 + \left( \frac{\xi}{180} \right)^3 \right]}$$



$$c_3(\xi) = 3[\exp(-0.05\xi) - 1] - 0.0018\xi$$

$$c_4(\xi) = -.589 + 0.106 \ln(\xi + 325) - 0.015\exp(-0.6\xi)$$

Figure 2.2 shows the variation of the Abrahamson coherence function as a function of the cyclic frequency  $f = \omega/(2\pi)$ . It can be observed from Figure 2.2 that unit coherency is enforced at zero frequency, eliminating the source of error at the low frequency range that appeared in the HV coherence function (see Figure 2.1). Abrahamson's coherence function is considered the most complete model for coherency estimation of waves propagating in soil media, since it was derived considering predominantly time history records obtained at soil sites. It is also site independent, since the records were obtained from multiple dense arrays such as the EPRI LSST, EPRI Parkfield, Chiba, USGS Parkfield, El Centro Differential, Hollister Differential, Stanford, Coalinga, UCSG ZAYA, among others [Zerva (2009)]. Moreover, Abrahamson took special care in separating the terms of the coherence function dealing with shorter and longer station separations, since the shorter and longer separation coherence components were found to be subjected to different exponential decay functions; thus, the model is equally applicable to short and long engineering structures. Since in this study short, medium and long multi-span bridges are assumed supported on variable soil types, Abrahamson's coherence function was chosen to account for the incoherence effects of the spatially variable seismic excitation on these bridges.

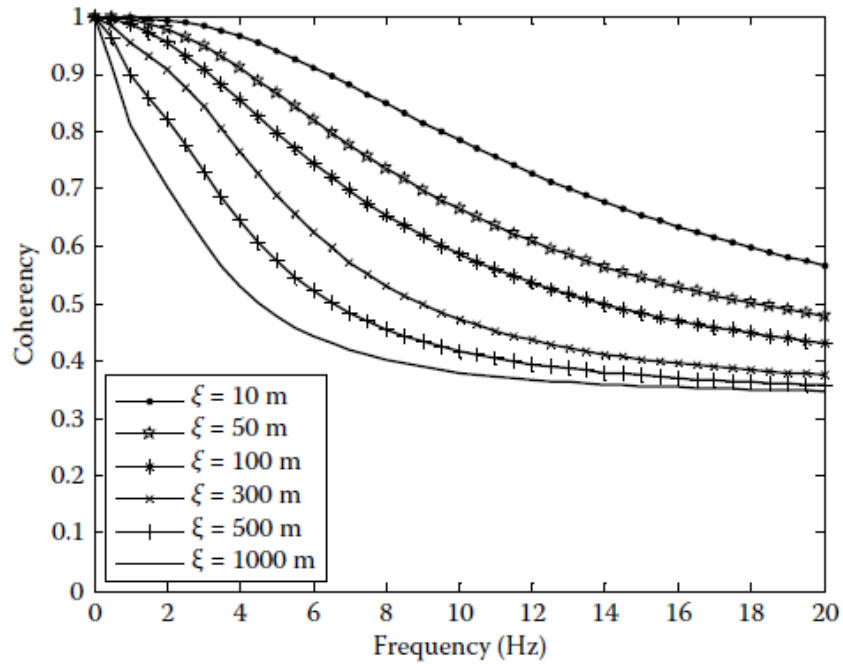


Figure 2.2 Variation of the Abrahamson Coherence Function with Frequency and Separation Distance between Stations [after Zerva (2009)].

#### 2.4.2 Analytical Coherence Functions

Analytical coherence functions are developed from stochastic wave theory and are in principle, site independent. These coherence functions can be subdivided into semi-empirical and purely analytical functions. The semi-empirical functions have an analytical basis, but can be adjusted to fit recorded time history data. Most of the analytical coherence functions reported in the literature fall into this category. For example, Der Kiuregian (1996) derived a semi-empirical coherence function from random processes theory that considered the effects of wave passage, incoherence and local site conditions. Laouami and Labbe (2001) developed an analytical coherence function using a combination of a wave propagation effect (coherent component) and a

zero mean randomizing factor (incoherence effect). The model was compared with Abrahamson's model, showing good results.

#### *2.4.2.1 The LW Coherence Function*

Luco and Wong (1986) developed the semi-empirical LW coherence function from a wave model propagating through random media. Perhaps in part due to its simplicity, the LW coherence function is the most widely used among the semi-empirical types and is given by the following expression:

$$\gamma_{jk}(\omega) = \exp(-\alpha^2 \omega^2 \xi^2) \quad (2.4)$$

Where  $\alpha$  = exponential decay parameter and  $\xi$  = distance between stations  $j$  and  $k$ . When the value of  $\alpha$  is chosen properly, the function has been shown to acceptably model the spatial variation of recorded time histories. Figure 2.3 shows the variation of the LW coherence function for  $\alpha = 2.5 \times 10^{-4} \text{ sec/m}$ , which is one of the values recommended by Luco and Wong. It can be observed from Figure 2.3 that, similarly to the Abrahamson empirical coherency function, the LW coherence function also exhibits unit coherency at a zero frequency value. Moreover, the analytical nature of the LW coherence function also makes it site independent. However, when comparing Figures 2.2 and 2.3, for the same station separation distance, it can be observed that the LW coherence function predicts a much steeper decay of the wave coherence with increasing frequency than the Abrahamson coherence function. Also, the use of a single exponential decay parameter to define the incoherence effect for short and long distances between stations in the LW coherence function may introduce an unnecessary source of error when modeling the correlation of spatially variable acceleration time histories occurring at such distances.

Since the Abrahamson model does consider different exponential decay parameters for short and long distances between stations, the Abrahamson coherence function was considered the better model in this study.

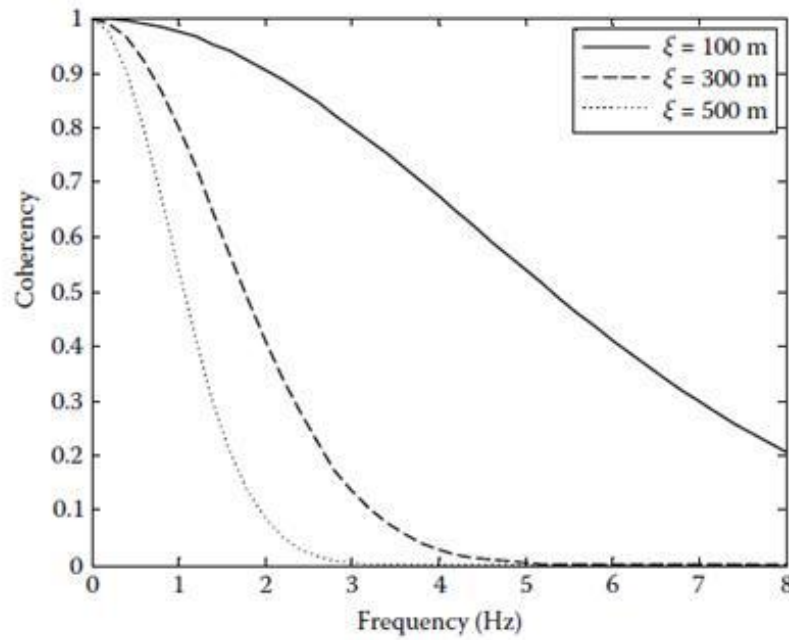


Figure 2.3 Variation of the LW Coherence Function with Frequency and Separation Distance between Stations for  $\alpha = 2.5 \times 10^{-4} \text{ sec/m}$  [after Zerva (2009)].

#### 2.4.3 Structural Response using the HV and LW Coherence Functions

Zerva (1994) compared the structural response of long span structures using simulated spatially varying seismic shear waves based on the HV and LW coherence functions. Zerva did not make a recommendation of which coherence function to use in practical situations, but made the following important observations, which have also been corroborated by other researchers:

- a) For low velocity of propagation of the seismic wave, the wave effect is more predominant than the incoherence effect.

- b) For high velocity of propagation of the seismic wave, the incoherence effect is more predominant than the wave effect.

Soyluk and Domanoglu (2004) also compared the HV and the LW coherence functions and observed that the former predicts larger structural responses than the later for a given seismic excitation, due to the difference in behavior of both models in the low frequency range. The results of this research support the arguments provided in Section 2.4.1.2 for not choosing the HV function in this study.

#### **2.4.4 Anisotropic Coherence Functions**

Most researchers assume the coherence functions to be isotropic; that is, they assume that the same coherence function can model acceleration time history correlations between stations regardless of the direction of propagation of the wave. However, Loh and Lin (1990) analyzing the SMART-1 dense array found that the coherence of horizontally propagating waves to be a function of directionality as well as frequency. A mathematical model for anisotropic coherence was proposed and a process to simulate non-stationary stochastic waves was presented. Hao et al (1989) also proposed an anisotropic coherence function for horizontally propagating waves based on time history records for points located in a horizontal two dimensional array.

Researchers have also expressed interest in studying the coherence of seismic waves propagating in a vertical plane, since they can provide insight into the effects on its coherency as the wave propagates vertically through layered soil media. Zendagui et al (1999) presented an analytical model to predict the statistical characteristics of seismic motions at any point within the soil strata from the statistical characteristics of the free

surface motions. They showed that the reduction in intensity of SH (shear horizontal) waves is more pronounced in layered media than in a homogeneous half-space. They also showed that greater coherence is present in P (primary compression) waves than in SH waves. Zendagui and Berrah (2002) considered coherency studies of seismic waves traveling through stratified soils containing SH, SV (shear vertical waves) and P waves. They concluded that the coherencies of SH and SV waves are different in general and that coherency is greater at some depth than at the free surface. However, no explicit coherency functions were proposed. Lui et al (2004) using Hao's (1989) coherence function proposed a vertical coherence function and studied its relationship with space and frequency. They also concluded that the coherence function is anisotropic. Abrahamson (1993) also recognized the anisotropic property of the coherence function and developed a coherence function for vertically propagating waves.

Since in this study the incoherence effect is modeled using only Abrahamson's coherence function for horizontally propagating waves (see Eq. 2.3), it is implicitly assumed that wave coherence isotropy will exist. More discussion of this assumption is made in Section 3.2.

## **2.5 Structural Response under Spatially Variable Seismic Waves**

There are mainly two types of approaches used by researchers when calculating the structural response under spatially variable seismic waves: frequency domain analysis and time domain analysis. Frequency domain analysis is mathematically and conceptually more complex, but more computationally efficient when Fast Fourier

Transform (FFT) algorithms are implemented. However, it operates under the assumptions of stationary input motion and linear structural behavior, which restrict their practical use. Nevertheless, it is still widely used since spatial variability in seismic waves is usually modeled as frequency dependent stochastic waves, which facilitate the calculation of structural response under a common frequency domain framework. Also, dynamic soil response parameters, such as stiffness and damping, have been found to be frequency dependent and are better modeled in the frequency domain, providing for a rigorous treatment of SSI effects.

Time domain analysis is less computationally efficient than frequency domain analysis, but it is not restricted by the assumptions of stationary input motion and linear behavior, giving it a broader range of applicability. The computational inefficiency of the time domain analysis has become only a secondary concern, given the significant increase in computational power exhibited by modern computers. Moreover, modern design philosophies, such as limit states and capacity design, as well as reliability estimations of structural performance may require nonlinear response consideration, which makes time domain analysis the preferable choice.

### **2.5.1 Structural Response Using Frequency Domain Analysis**

Structural response under spatially varying seismic waves using frequency domain analysis has been studied by many researchers. Ettouney et al (2001) performed frequency domain analysis of long span bridges subjected to spatially varying seismic waves considering effects of wave passage, loss of coherence, local soil conditions and SSI. They observed that non-uniform seismic motions may result in large shifting of

resonant frequencies and significant redistributions of internal forces in the bridge structure, when compared to uniform motions (due to seismic waves that exhibit no spatial variability).

Harichandran et al (1991) analyzed a multi-span suspension bridge (the Golden Gate Bridge in San Francisco, California) and two multi-span arch bridges using frequency domain analysis. They did a parametric study considering spatial variability of the seismic waves, where both the wave passage and incoherence effects were considered, and compared the results obtained when considering only wave passage effect and uniform motion. They made the following observations:

For long multi-span bridges under lateral spatially varying seismic waves and for shorter span of multi-span arch bridges under both longitudinal and transverse spatially varying seismic waves, the following conclusions can be drawn:

- a) The use of uniform motion is generally unacceptable for long multi-span bridges.
- b) The use of only the wave passage effect is acceptable for the longitudinal response of short multi-span arch bridges and the transverse response of the shorter spans of short multi-span suspension bridges.
- c) The use of only the wave passage effect is generally unacceptable for the longitudinal response of the long multi-span arch bridges and the transverse response of short and long multi-span arch bridges and the main spans of long multi-span suspension bridges.



When considering the seismic response of a structural system, the total displacements of the system, measured from a fixed reference point, is the sum of the support displacements and the displacements caused by the deformations of the system. These support displacements, which will be independent of the inertial and damping effects of the structural system, are usually called quasi static or pseudo static displacements. If the structural system is under uniform seismic excitation, all support displacements will be identical at a given time and as a result, the structure will exhibit no deformations (rigid body movement) due to support displacements. However, under spatially varying seismic waves, the support movement will no longer be identical at all supports and the differences in support movements will cause deformations of the structure (quasi static response) and the internal forces generated as a result can sometimes be significant, when compared to the inertial forces caused by the dynamic response. Zerva (1994) performed frequency domain analysis of long span structures and concluded that seismic ground motions that are partially correlated at low frequencies generate the highest quasi static response and that seismic ground motions with slow decaying incoherence generate the highest dynamic response. Soylik and Domanoglu (2004) also observed the relevance in the quasi static component of the total response of long span cable-stayed bridges.

Price and Eberhard (1998) studied the transverse response of two short span bridges under spatially varying seismic waves using frequency domain analysis. They observed that spatial variability effect increases the contribution of the asymmetric vibration modes and decreases the contribution of the symmetric modes. This caused the

dynamic components of the end reactions of the bridge to exceed by about 60% of the values obtained when uniform ground motion was considered. In contrast, the reactions of the middle support were found to be lower by 20% with respect to the reactions obtained by uniform ground motion. They presented a method based on the uniform ground motion assumption which modifies the mode factor participation to account for the spatial variability effect. The increase in the participation of asymmetric modes and the decrease in participation of symmetric modes have also been observed for long span bridges [Abdel-Ghaffar and Rubin (1982), Ettouney et al (2001), Harichandran et al (1996), Nazmy and Abdel-Ghaffar (1990), Sextos et al (2003)].

Zembaty (1997) considered the case of a bridge under spatially varying seismic waves with an oblique angle of propagation. He found that the displacement response caused by the longitudinal and transverse wave components is in general reduced when compared to uniform excitation, but the force response may increase, depending on the velocity and angle of propagation of the wave. This later finding was attributed to the predominant role of the quasi static forces when low propagation velocities were considered.

Several researchers have studied the local soil effect in the frequency domain seismic response of long span bridges [Berrah and Kausel (1993), Saadeghuaziri et al (2000), Saxena (2000), Sextos et al (2003), Soyuluk and Dumanoglu (2004), Wang and Wei (1999)] and most of them arrived basically to the same conclusion: not accounting for local soil effect may significantly underestimate the structural response of short and long multi-span bridges under the effect of spatially variable seismic waves.

Der Kuirghian and Neuenhofer (1996) developed a response spectrum method for structures under the effects of spatially variable seismic waves. They used the coherence function developed by Der Kuirghian (1992) and derived response spectra information which could be used in a design scenario. However, given that the response spectra information was derived using frequency domain analysis its usefulness was limited to structures behaving linearly and subjected to stationary input motion. Loh and Ku (1995) proposed simplified techniques for the frequency domain integrals that need to be solved in the response spectrum method proposed by Der Kuirghian and Neuenhofer.

Lin and Li (2004) presented the Pseudo Excitation Method (PEM) as a viable method for random vibration structural analysis, although only linear analysis was considered. PEM is mainly a mathematical technique to solve stochastic differential equations that includes wave passage effects, incoherence effects and cross-correlations terms of participating modes. In PEM random stationary analysis is transformed into harmonic analysis and non-stationary random analysis is transformed into deterministic transient analysis. This method showed some potential since it simplified the complexity of frequency domain analysis and eliminated the requirement of stationary input excitation, but it could only be applied to linear elastic systems.

Long multiple-span simply supported bridges under the effects of spatially varying seismic excitation present special challenges that have been addresses by some researchers. Hao (1998) studied the required seating length of girders to avoid loss of support during a seismic event. He showed that the largest seating length is required when the natural frequency of the ground motion and the bridge coincide (resonant

response). A larger seating length was required if the spatially varying ground motions were less correlated and if the ground motion phase shift (wave passage effect) was out of phase with the bridge vibration mode. The difference in vibration response of adjacent spans was found to be the dominant factor in determining the required seating length, since such difference caused significant differential displacements when the natural frequencies of the two spans differed noticeably. However, when the two spans exhibited similar natural frequencies, the ground motion spatial variability became the dominant factor. The loss of support of bridge decks under the effects of spatially varying seismic waves has been mentioned as the most probable cause of the partial failure of the San Francisco-Oakland Bay Bridge in California during the Northridge Earthquake and for several highway bridges in Japan during the Kobe Earthquake. Zanardo (2002) studied the pounding of decks under spatially varying seismic excitation. He showed that pounding between adjacent segments of multiple-span simply supported bridge when subjected to spatially varying seismic wave effects increases up to 3 to 4 times the values obtained under uniform ground motion.

Most of the research results mentioned to this point deals mainly with structural response of bridges. However, there is also research that has focused on buildings subjected to spatially varying seismic waves. Hao et al (1995, 1997 and 1998) and Heredia-Zavoni and Barranco (1996) have studied the torsional response of buildings under the effects of spatially varying seismic waves. They concluded that such effects reduced seismic shear response in columns but increased the torsional response of the building. In asymmetric buildings, where there is typically a significant torsional

response due to structural eccentricity, they found that the increase in response due to the effects of spatial variability in the seismic wave may place the building in violation of design code requirements; thus, generating unconservative designs. Hao made some recommendations on new code requirements for coupled torsional response due to eccentricity and spatial variability of the seismic wave. Behnamfar and Sigimura (1999) studied the soil-structure interaction (SSI) of buildings under spatial variability of seismic waves and the cross SSI for two adjacent buildings. Wave passage and incoherence effects were considered. The following conclusions were obtained: i) structural resonant frequency increases with closeness between adjacent structures and ii) depending on the distance between adjacent structures, the structural response may also increase. These findings may also have practical applications to bridge design given the fact that bridges structures are placed in close proximity in highway interchanges.

### **2.5.2 Structural Response Using Time Domain Analysis**

Time domain analysis of the structural response of bridges under spatially variable seismic excitation has also been reported in the literature. Monti et al (1996) conducted a parametric study on the nonlinear response of three bridge models with varying stiffness using a Monte Carlo Simulation scheme. They used the LW coherence function, included the wave passage and incoherence effects, but disregarded the local soil effects by assuming identical soil conditions in all their bridge models. They used the spectral representation method and the Kanai-Tajimi spectral density functions to develop spatially variable acceleration time histories (the use of spectral density functions to generate such time histories is described in Section 3.2). The nonlinear response of the

bridge was modeled with Takeda-type elements at the base of the piers, where plastic hinges or zones were expected to form. These elements are typically modeled in finite element theory as nonlinear link elements with a prescribed hysteretic behavior based on the plasticity model developed by Takeda et al. (1970). The pier ductility demand, which is defined as the ratio of maximum to yield rotation at the plastic hinge location, was considered as the response variable of interest (see Section 3.3 for the mathematical definition of pier ductility demand used in this study). They concluded that in almost all the cases considered the ductility demands of the central piers decreased and increased for the end piers due to the wave incoherence effect. They also concluded that the influence of the wave passage effect on the structural response under spatially variable seismic excitation can be neglected if wave incoherence is dominant.

Saxena (2000) considered nonlinear time history analysis of seven reinforced concrete (RC) bridges using SAP2000 and Monte Carlo Simulation. Non-stationary acceleration time histories were developed using the algorithm developed by Deodatis (1996) and modified by Saxena. Spatial variability of the seismic waves was considered only in the longitudinal direction of the bridges. Saxena used the HV coherence function and the soil response spectra curves were obtained from the 1994 Uniform Building Code (UBC) for soil Type I (stiff), II (medium) and III (soft). 5% damping was assumed for all bridges. A Monte Carlo Simulation scheme was used and the maximum ductility demand of each bridge pier was obtained. Only two-dimensional finite element models of the bridges were considered. Support conditions were assumed pinned (roller supports) at abutment locations and fixed at pier supports, therefore neglecting soil stiffness and SSI

effects. The piers were considered the only elements capable of developing nonlinear behavior and their nonlinear characteristics were assumed to be captured by plastic zones located at both pier ends. The plastic zones were modeled by rigid link elements and nonlinear rotational springs. Some of the significant results observed were:

- a) The maximum ductility demand increases substantially compared to the case of uniform ground motion when considering the effects spatial variability of seismic waves and supports located on hard, medium or soft soil conditions. Ductility ratios (ductility demand under spatial variable seismic waves divided by ductility demand under uniform seismic waves) range from 1.5 to 2.5 for short and medium span bridges and for long span bridges, the ratio may increase to 2.7.
- b) If supports are located on same soil conditions, the maximum ductility demands are reduced. Typical ductility ratios range from 1.0 to 1.5 for short to medium span bridges. For long span bridges, the ratios may increase to 2.2.
- c) The uniform ground motion assumption seems to be generally unconservative, especially when piers are located in different soil conditions. For very long, multiple-span bridges, severe underestimation of maximum ductility demands may be expected even for piers located on same soil conditions.
- d) Wave passage and incoherence effects, as well as the effect of the variation of soil conditions under the pier supports must be taken into account when modeling time histories, since their omission may lead to unrealistic responses

(more discussion on how such effects are incorporated into an acceleration time history generation model is presented in Section 3.2).

Kim and Feng (2003) extend the work of Saxena (2000) by considering both longitudinal and transversal spatially varying seismic waves in two-dimensional RC bridge models. Their conclusions again stress the fact that ignoring differential support ground motions leads in general to un-conservative results.

A comprehensive study of RC bridges under spatially varying seismic waves was performed by Sextos et al (2003). They developed a methodology for the nonlinear time history analysis of two-dimensional RC bridge models that considers wave passage, incoherence and local site effects, as well as soil-foundation-superstructure interaction. Using frequency domain analysis, they went beyond the prescribed soil response spectra approach for defining the local site effect by considering multilayered damped soil media over elastic bedrock. Also, they considered a modification of the SSI kinematic effects by adjusting the dynamic flexibility matrix of the foundation to account for pier base yielding. Subsequently, a parametric study of 20 RC bridges was performed using SAP2000 under the following scenarios: Uniform seismic excitation, spatially variable seismic excitation considering the effects of wave passage, loss of coherence and changes in soil conditions under pier supports, fixed base supports, elastic and inelastic response of bridge piers and kinematic and inertial SSI effects. Pier plastic hinges were assumed occurring only at the pier-foundation interface. Some of their conclusions were:



- a) Significant coupling exists between spatial variability, effects of local soil conditions and SSI effects and their relative importance cannot be easily assessed in advance.
- b) Bridges subjected to spatially varying seismic waves are characterized by the excitation of higher modes of vibration which are mainly asymmetric. Symmetric structures no longer respond symmetrically and their dynamic behavior cannot adequately be reproduced by any combination of uniform motions.
- c) The effect of wave passage and loss of coherence in terms of the absolute displacement and pier base bending moments is generally beneficial for short single span bridges, but also strongly related to the total bridge length.
- d) A tentative total bridge length threshold value of 400 m may be established for rendering consideration of spatial variability of the seismic excitation indispensable.
- e) In general, SSI effects are beneficial since such effects tend to reduce the internal forces developed; however, an increase in the absolute and relative displacements should be expected. Nevertheless, the interaction of the soil with the foundation and the structure is dependent on the modified dynamic characteristics of the structure and the earthquake motion and hence, its impact cannot be assessed in advance.

- f) Ground motion variation between supports is not only due to arrival delay and loss of coherence. Local soil amplification, kinematic SSI and asynchronous pier yielding are all sources of input motion variability.
- g) Ignoring the interrelations between spatial variability of the seismic excitation, local soil characteristics and SSI effects, the ductility demand in bridge piers could be underestimated by 25% on average and up to a factor of 3 in an extreme case, which could lead to un-conservative pier designs.
- h) Even for a constant set of earthquake motions, bridge structural properties (fundamental period, symmetry, abutment conditions, pier to deck connections, etc.), as well as its dimensions (span and overall length) modify the relative effect of the above phenomena.

Sextos et al (2004) also considered the case of a horizontally curved bridge under spatially varying seismic waves with a varying angle of incidence of the wave direction with respect to the bridge cord. They assumed that the coherence function was valid in all directions (isotropic coherence) and that vertical and horizontal shear waves were statistically independent (although vertical shear waves were not considered in their study). They found that the angle of incidence only plays an important role on the structural response when the incoherence effects were disregarded. When incoherence effects were considered they found in general that the structural response was reduced when compared to the uniform earthquake excitation.

Allam and Datta (2004) studied the two-dimensional response of a cable-stayed bridge deck under three-component spatially varying seismic waves. They considered

various ratios for the magnitudes of the two horizontal and vertical components and also considered the variation of the incidence angle of the seismic waves. For incidence angles of 0, 30, 45, 75 and 90 degrees with respect to the bridge longitudinal axis, they found that for a given point on the bridge deck, the minimum displacement occurs when the incidence angle is 90 degrees and the maximum displacement does not occur when the incidence angle is zero (wave traveling parallel to the bridge longitudinal axis). They obtained the displacements at nine points along the bridge deck and found that maximum displacements along the bridge deck occur at incidence angles of 30 or 45 degrees, depending on the location along the bridge deck where the displacement was measured. However, the difference in maximum displacement values at a given point on the bridge deck for incidence angles of 30 and 45 degrees did not exceed 10% and at seven out of the nine points where displacements were obtained, the maximum values occurred when the incidence angle was 45 degrees.

Lupoi et al (2005) evaluated the response of a series of equal length multi-span two-dimensional bridge models with different pier heights under the effects of spatially variable seismic waves applied in the transverse direction only. All piers were assumed connected rigidly to the deck. Nonlinear behavior was assumed occurring only at the pier bases and a parametric study under a probabilistic framework (fragility analysis) was performed to study the effect of wave passage, incoherency and local site conditions. They found that the probability of failure of the bridge increased when piers were of different heights and when the spatial variability effect was considered. They also found that the probability of failure was most sensitive to the local site effect. They considered a

stiffness index (SI) to account for the relative stiffness of the piers with respect to the deck and found that the effect of spatial variability of the seismic excitation was reduced when the SI was increased. This can be explained by noticing that the higher the value of SI, the smaller the deck stiffness is with respect to the pier stiffness; since the deck ties the piers together, the lower deck stiffness reduces the constraining effects on the piers, which will tend to generate decoupled responses for each pier as the deck stiffness is reduced. They also proposed a correction factor  $\rho$  that described the ratio of ductility demand for spatially varying ground motions to the ductility demand for uniform ground motion. They found that SI and  $\rho$  were linearly related. Using a probabilistic procedure, they found that  $\rho = 2$  could be used to account for the effect of spatial variability of the seismic wave. In other words, increasing the ductility demand by 100% or reducing by 50% the Q factor (ductility factor of seismic forces used in the IBC code) in a uniform ground motion seismic analysis could adequately account for spatial variability effects.

## 2.6 Concluding Remarks

Most of the reviewed published literature on structural response of bridges excited by a spatially varying seismic wave considered stochastic methods for the generation of the acceleration time history records, where the spectral representation method seems to be the preferred approach. Most researchers agreed that in order to properly model the spatial variability of the seismic wave, the effects of wave passage, wave incoherence and variations of local soil conditions must all be considered. In this study a stochastic algorithm was developed based on the spectral representation method and the work of

Deodatis (1996) to generate synthetic spatially variable acceleration time history records. The algorithm incorporated the convergence criteria suggested by Saxena (2000) and soil response spectra information given in the 2009 IBC code was used to model the local soil effects.

The HV and LW coherence function were found to be the most popular choice among researchers to model the incoherence effect of the spatially varying seismic waves. However, these coherence functions had deficiencies that introduced unnecessary sources of error to the modeling of the incoherence effect. The Abrahamson coherence function was found to be best suited for the types of soil and bridge length variability considered in this study and thus, was incorporated into the stochastic algorithm.

The literature review shows that bridge dynamic response under spatially varying seismic waves has been studied by many researchers using frequency and time domain approaches. The time domain approach was chosen in this study since it allows for the consideration of nonlinear response of the bridge piers. Most of the published research reviewed considered only two-dimensional seismic response of the bridge structure and thus ignored the bidirectional response of the piers. Since typical bridge structural systems tend to be long and narrow, their response under spatially varying seismic waves is expected to be three-dimensional. Moreover, significant out of plane (transverse) seismic excitation can be expected as a result of a seismic wave arriving with an angle of incidence with respect to the bridge longitudinal axis. Given that one of the main objectives of modern bridge design philosophies is to generate bridge pier designs capable of sustaining significant plastic deformations in order for the bridge to remain in

service after severe earthquakes, then three-dimensional bridge response should be considered in order to obtain more realistic bidirectional nonlinear responses at the piers. Otherwise, underestimation of the pier ductility demand may result.

Except for Sextos et al (2003), who considered flexible soils under the support of his two dimensional bridge models, the rest of the published research reviewed ignored soil flexibility and thus, assumed that soil under the bridge supports had infinite rigidity. This disregards the fact that the dynamic shear modulus of the soil is in general smaller than the static shear modulus. It also disregards the fact that the dynamic and static shear modulus values are dependent on the soil type. Since changes in the soil type are likely under the supports of many bridges, explicitly accounting for the corresponding changes in the soil shear modulus allows for a more rigorous treatment of the local soil effects.

Limited consideration was found in the published literature on the effects of variations in bridge geometry on the nonlinear response of the bridges under spatially varying seismic waves. Variations on the pier heights and span lengths are likely to occur in bridges due to topographic limitations or due to project requirements at highway interchanges. The three-dimensional bridge response should be considered when variations in bridge geometry exist, especially when asymmetric structural configurations occur as a result.

The vertical component of the seismic wave was rarely considered explicitly in the reviewed published research and no study was found where the nonlinear response of the bridge piers were studied under spatially varying seismic waves with a strong vertical component. Strong vertical acceleration components typically occur in bridges near the

epicenter of a severe earthquake and since a strong vertical acceleration component is expected to generate a significant increase in the pier axial loads, the ductility range of the piers is expected to decrease accordingly. Not accounting for such a decrease may generate an overestimation of the ultimate rotation capabilities at the pier plastic zones.

This study addresses the above weaknesses in the current state of the art by incorporating in the proposed methodology the following relevant features:

1. Three-dimensional finite element modeling of the bridge structural configuration that allows for variations in the bridge geometry.
2. Three-dimensional nonlinear response of the bridge piers captured by bidirectional plastic hinge models.
3. Stochastic generation of point specific and correlated acceleration time history records of spatially varying seismic shear waves traveling parallel and perpendicular to the bridge longitudinal axis.
4. Allowance for the incorporation of scaling factors to the time history records to consider strong vertical acceleration components of the seismic shear wave.
5. More rigorous treatment of variations in the geotechnical characteristics under the bridge foundations by defining a soil stiffness model at each foundation node.
6. Incorporation of updated seismic data by using the IBC 2009 code spectral acceleration maps and procedures to generate soil response spectrum curves.

Using the above relevant features of the proposed methodology each one of the objectives of this study presented in Section 1.3 is developed in the subsequent chapters.

In the next chapter, the mathematical framework of these features is presented in some detail.



### **3. PROPOSED METHODOLOGY**

#### **3.1 Introduction**

In this Chapter the conceptual framework of the stochastic algorithm used to generate spatially variable acceleration time history records under the bridge supports is presented. Also presented is the three-dimensional finite element model of the bridge, including the bidirectional plastic hinge model used to capture the nonlinear response of the bridge pier plastic zones, and the three-dimensional soil spring model used capture the dynamic response of the soil under the pier supports.

Finally, general discussion is made on the implementation of the time history data, bridge and soil models in SAP 2000 under a Monte Carlo Simulation scheme and a general algorithm is provided illustrating the proposed methodology.

#### **3.2 Stochastic Algorithm to Generate Spatially Variable Acceleration Time Histories**

The stochastic algorithm developed in this study to generate spatially variable acceleration time history records for each of the three components of the seismic wave model is based on the spectral representation method originally developed by Shinosuka (1972, 1988) and updated by Deodatis (1996) and Saxena (2000). The conceptual framework of the stochastic algorithm is presented in this section. A brief presentation of the basic concepts of probability theory and random processes used in this section is given in Appendix B.

### 3.2.1 Acceleration Time Histories Modeled as a Random Process of Uncorrelated Random Variables.

Acceleration time histories recorded on the ground surface can be modeled as random vectors  $a_j(t)$ , where  $j$  defines the position on the ground where the acceleration time history is required. Thus, a random process can be generated considering  $n$  points on the ground as  $a_j(t)$ ,  $j = 1, \dots, n$ . In this case, each realization of the random process will represent independently generated acceleration time histories at any station  $j$  with no correlation with the time histories generated at any other stations on the ground surface.

The stochastic descriptors of the random process occurring at any station  $j$  will be characterized by its mean value and autocovariance function (see Appendix B) and given respectively by the following expressions:

$$\mu_j(t) = E[a_j(t)] \quad (3.1)$$

$$R_j(t_1, t_2) = E[a_j(t_1)a_j(t_2)] - \mu_j(t_1)\mu_j(t_2) \quad (3.2)$$

Although the correlation of the acceleration time histories is required to properly model the effects of spatially varying seismic waves, the stochastic descriptors of the uncorrelated process will be required when the correlation effect is considered, as will be shown in Section 3.2.2.

When modeling actual recorded acceleration time histories as a random process, it is convenient to assume that the process is Gaussian, stationary and ergodic. A random process is Gaussian if it can be assumed to be fully characterized by its stochastic descriptors. A random process is stationary, if the stochastic descriptors are not functions of absolute time  $(t_1, t_2)$ , but of a time difference  $\tau = t_2 - t_1$ ; thus, due to its independence

of absolute time, a Gaussian stationary process will be perpetual (without a beginning or an end) with the same stochastic characteristics throughout its infinite duration. By definition, Gaussian stationary processes have a constant mean value and for processes modeling acceleration time histories, such value is generally set at zero. Therefore, the stochastic descriptors of a Gaussian stationary process at any station  $j$  become:

$$\mu_j(t) = 0 \quad (3.3)$$

$$R_j(t_1, t_2) = R_j(\tau) \quad (3.4)$$

A stationary process is ergodic if the stochastic information contained in each realization of the process is sufficient to fully describe the process; thus, to determine the stochastic characteristics of a stationary ergodic process, one only needs to analyze a single realization of the process.

To this point the stochastic descriptors have been defined in the time domain. However, it is usually more convenient to define them in the frequency domain. Fourier transform functions are used to change the variable domain from time to frequency, as shown below:

$$X(\omega) = \frac{1}{2\pi} \int_{-\infty}^{+\infty} x(t) e^{-i\omega t} dt \quad (3.5)$$

The power spectral density function  $S_j(\omega)$  of the stationary process is obtained by Fourier transforming the autocovariance function (Eq. 3.4) as shown below:

$$S_j(\omega) = \frac{1}{2\pi} \int_{-\infty}^{+\infty} R_j(\tau) e^{-i\omega\tau} d\tau \quad (3.6)$$

Where  $\omega$  is the frequency of the process in rad/sec.

### 3.2.2 Acceleration Time Histories Modeled as a Random Process of Correlated Random Variables.

When comparing acceleration time histories recorded at different stations arranged in dense array patterns, such as SMART-1, they show similarities in amplitude and frequency variations [see Figure 1.4]; this is particularly evident when the distances between the stations are relatively short [see Figure 1.4(a)]. Therefore, acceleration time histories recorded at dense arrays are obviously correlated and if a random process is used to realistically describe them, then the process must account for such correlation.

Random processes considering multiple correlated random variables are called multivariate random processes. For simplicity, a bivariate random process, which involves only two correlated random variables, will be considered to present the relevant stochastic descriptors. The extension to a multivariate process will be shown to be straight forward.

Consider two stationary zero mean acceleration time histories  $a_j(t_1)$  and  $a_k(t_2)$ , which are defined as correlated random variables and recorded at stations  $j$  and  $k$ , respectively. The time domain stationary stochastic descriptor of the corresponding bivariate random process is given by the following expression:

$$R_{jk}(t_1, t_2) = R_{jk}(\tau) \quad (3.7)$$

Where  $R_{jk}(\tau)$  is the cross covariance function and accounts for the correlation between  $a_j(t_1)$  and  $a_k(t_2)$ . The corresponding frequency domain stochastic descriptor is the cross spectral density function, which is given by the following expression:

$$S_{jk}(\omega) = \frac{1}{2\pi} \int_{-\infty}^{+\infty} R_{jk}(\tau) e^{-i\omega\tau} d\tau \quad (3.8)$$

Consider now a multivariate random process with  $n$  random variables, representing  $n$  stations on the ground where acceleration time histories are recorded. The cross spectral density of the  $n$ th-variate random process becomes an  $n \times n$  cross spectral density matrix as shown below:

$$S(\omega) = \begin{bmatrix} S_{11}(\omega) & \cdots & S_{1n}(\omega) \\ \vdots & \ddots & \vdots \\ S_{n1}(\omega) & \cdots & S_{nn}(\omega) \end{bmatrix} \quad (3.9)$$

Where the diagonal terms:  $S_{jj}(\omega) = S_j(\omega)$ ,  $j = 1, \dots, n$  are given by Eq. 3.6, and the off diagonal terms:  $S_{jk}(\omega)$ ,  $j, k = 1, \dots, n; j \neq k$  are given by Eq. 3.8.

### 3.2.3 Cross Spectral Density Matrix of a Spatially Variable Random Process

In order to properly account for the incoherence and wave passage effects in the correlation between the acceleration time histories recorded at stations  $j$  and  $k$  due a propagating spatially variable seismic wave, the coherency of the wave must be considered. The wave coherency function  $\Gamma_{jk}(\omega)$  can be evaluated in terms of the spectral density and cross spectral density functions of the acceleration time histories recorded at stations  $j$  and  $k$  using the following expression:

$$\Gamma_{jk}(\omega) = \frac{S_{jk}(\omega)}{\sqrt{S_j(\omega)S_k(\omega)}} \quad (3.10)$$

Where  $S_j(\omega)$  and  $S_k(\omega)$  are the spectral density functions of the uncorrelated acceleration time histories at stations  $j$  and  $k$ , respectively (given by Eq. 3.6) and  $S_{jk}(\omega)$  is the cross spectral density function that correlates the acceleration time histories at stations  $j$  and  $k$  (given by Eq. 3.8). From Eq. 3.10 it can be shown that the wave coherency function at a single station  $j$  will be unity [ $\Gamma_{jj}(\omega) = 1$ ]. Therefore, updating the coefficients of the

cross spectral density matrix given in Eq. 3.9 to account for wave coherency effects requires:

$$S_{jj}(\omega) = \Gamma_{jj}(\omega)S_j(\omega) = S_j(\omega), \quad j = 1, \dots, n \quad (3.11)$$

$$S_{jk}(\omega) = \Gamma_{jk}(\omega)\sqrt{S_j(\omega)S_k(\omega)}, \quad j, k = 1, \dots, n; j \neq k \quad (3.12)$$

For practical purposes, the wave coherence is expressed in terms of the complex coherence function given in Eq. 2.1. As can be observed from Eq. 3.12, the coefficients of the cross spectral density matrix of a spatially variable random process can be determined from the spectral density function coefficients evaluated from the uncorrelated acceleration time histories recorded at each station.

### 3.2.4 Simulation of a Stationary Spatially Variable Random Process

From Eqs. 3.11 and 3.12 it can be observed that the coefficients in the cross spectral density matrix are functions of frequency only; thus, the random process that it describes is stationary in time and homogeneous in space. A random process is homogeneous in space if the station locations are not expressed in terms of absolute spatial locations, but in terms of relative distance between stations.

In order to simulate the acceleration time histories by an  $n$ th-variate stationary random process  $a_j(t)$ ,  $j = 1, 2, 3, \dots, n$ , the cross spectral density matrix given in Eq. 3.9 is decomposed into the following matrix factoring operation:

$$S(\omega) = H(\omega)[H^*(\omega)]^T \quad (3.13)$$

Where  $H(\omega)$  is a factor matrix,  $H^*(\omega)$  is the complex conjugate of the factor matrix and the superscript  $T$  denotes the transpose of  $H^*(\omega)$ . When Cholesky decomposition is used, the factor matrix becomes a lower triangular matrix of the form:

$$H(\omega) = \begin{bmatrix} H_{11}(\omega) & \cdots & 0 \\ \vdots & \ddots & \vdots \\ H_{n1}(\omega) & \cdots & H_{nn}(\omega) \end{bmatrix} \quad (3.14)$$

The diagonal coefficients  $H_{jj}(\omega)$  are real and non-negative functions of  $\omega$  and the off-diagonal coefficients  $H_{jk}(\omega)$  are generally complex functions of  $\omega$  given by:

$$H_{jk}(\omega) = |H_{jk}(\omega)| \exp[i\theta_{jk}(\omega)]; \quad j > k \quad (3.15)$$

Where: 
$$\theta_{jk}(\omega) = \tan^{-1} \left( \frac{\text{Im}[H_{jk}(\omega)]}{\text{Re}[H_{jk}(\omega)]} \right) \quad (3.16)$$

and “Im” and “Re” represent the imaginary and real part of  $H_{jk}(\omega)$ , respectively.

Once the  $S(\omega)$  matrix is decomposed according to Eqs. 3.14 and 3.15, the  $n$ th-variate homogeneous stationary random process  $a_j(t)$ ,  $j = 1, \dots, n$  can be simulated by the following series as  $N \rightarrow \infty$  [Deodatis (1996)]:

$$A_j(t) = 2 \sum_{m=1}^n \sum_{q=1}^N |H_{jm}(\omega_q)| \sqrt{\Delta\omega} \cos[\omega_q t - \theta_{jm}(\omega_q) + \Phi_{mq}]; \quad j = 1, \dots, n \quad (3.17)$$

where:

$$\omega_q = q\Delta\omega; \quad q = 1, \dots, N \quad (3.18)$$

$$\Delta\omega = \frac{\omega_u}{N} \quad (3.19)$$

$$\theta_{jk}(\omega) = \tan^{-1} \left( \frac{\text{Im}[H_{jk}(\omega_q)]}{\text{Re}[H_{jk}(\omega_q)]} \right) \quad (3.20)$$

and  $A_j(t)$ ,  $j = 1, \dots, n$  is the simulation of the homogeneous stationary random process  $a_j(t)$ ,  $j = 1, \dots, n$ . In Eq. 3.19,  $\omega_u$  represents a constant upper cut-off frequency for which the coefficients of the  $S(\omega)$  matrix may be assumed to be zero for any time  $t$ . Therefore,  $\Delta\omega \rightarrow 0$  as  $N \rightarrow \infty$ , so that  $N\Delta\omega = \omega_u$ . Also, as  $N \rightarrow \infty$  the simulated process given by Eq. 3.17 is asymptotically Gaussian because of the Central Limit Theorem. In this study, the

value of the upper cut-off frequency was set at  $\omega_u = 62.83$  rad/sec, following the criterion established by Shinozuka et al (1991). Such cut-off value was established by Shinozuka based on the fact that typical structural systems respond in the cyclic frequency range of  $0 \leq f \leq 10$  Hz; thus,  $\omega_u = 2\pi f = 2\pi(10) = 62.83$  rad/sec.

The expression  $\Phi_{mq}$ ,  $m = 1, \dots, n$ ,  $q = 1, \dots, N$  represents  $n$  sequences of independent random phase angles distributed uniformly over the interval  $[0, 2\pi]$ . In order to generate the  $i$ -th realization of the simulated stationary process given by Eq. 3.17, the  $i$ -th realization of the random phase angle given by  $\phi_{mq}^{(i)}$ ,  $m = 1, \dots, n$ ,  $q = 1, \dots, N$  is substituted into Eq. 3.17 giving:

$$A_j^{(i)}(t) = 2 \sum_{m=1}^n \sum_{q=1}^N |H_{jm}(\omega_q)| \sqrt{\Delta\omega} \cos[\omega_q t - \theta_{jm}(\omega_q) + \phi_{mq}^{(i)}]; \quad j = 1, \dots, n \quad (3.21)$$

where  $A_j^{(i)}(t)$ ,  $j = 1, \dots, n$  is the  $i$ -th realization of the simulation  $A_j(t)$ ,  $j = 1, \dots, n$ . Notice that for any given time  $t$ , Eq. 3.21 is a function of the frequency only; therefore, it can be efficiently solved in the frequency domain using the Fast Fourier Transform (FFT) method. The complete stationary time history can be simulated by starting at  $t = 0$  and choosing an appropriate time step  $\Delta t$ . It is recommended to choose a time step that complies with  $\Delta t \leq \pi/\omega_u$  in order to avoid numerical difficulties during the simulation process.

### 3.2.5 Simulation of a Non-Stationary Spatially Variable Random Process

As established in Section 3.2.1 a stationary random process is perpetual (has infinite duration) and thus it cannot provide a realistic representation of a seismic wave. In



general, a seismic wave has finite duration with frequency and amplitude variations; therefore, the random process describing such a wave should be non-stationary.

A modulation function  $M_j(t)$  can be considered to provide the non-stationary property to the simulated stationary random process  $A_j(t), j = 1, \dots, n$ . The modulation function can be made to provide simultaneous modulation of wave amplitude and frequency, but this is rarely required in practice; except maybe when modeling abrupt changes in the frequency content occurring during soil liquefaction phenomena. Therefore, in this study only wave amplitude modulation was considered. Amplitude modulation provides the means to control the strong motion phase duration of the seismic excitation, as well as the time variation of the amplitude, thus providing for a more realistic model of a seismic wave.

In this study, the amplitude modulation function provided by Jennings et al (1968) was used (See Figure 3.1). Therefore, the simulated non-stationary random process  $F_j(t), j = 1, \dots, n$  will be given by the following expression:

$$F_j(t) = M_j(t)A_j(t), j = 1, \dots, n \quad (3.22)$$

Where  $A_j(t), j = 1, \dots, n$  is given by Eq. 3.17. The  $i$ -th realization of the simulated non-stationary random process will be given by:

$$F_j^{(i)}(t) = M_j(t)A_j^{(i)}(t), j = 1, \dots, n \quad (3.23)$$

Where  $A_j^{(i)}(t), j = 1, \dots, n$  is given by Eq. 3.21.

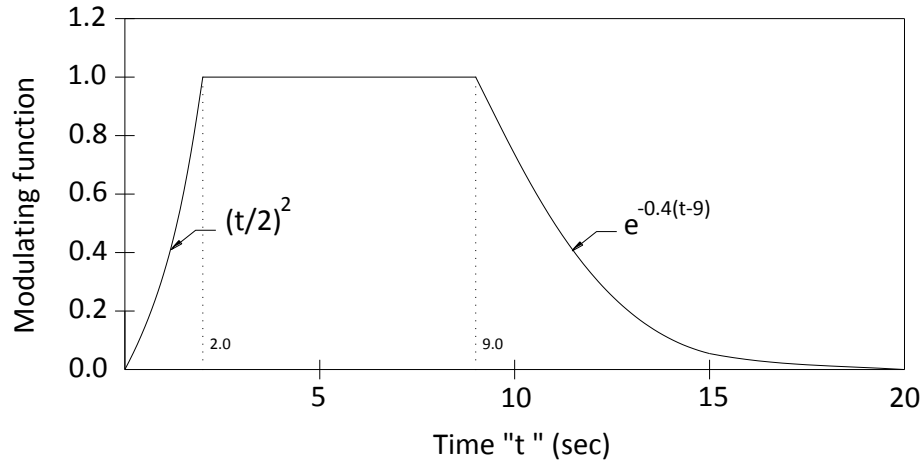
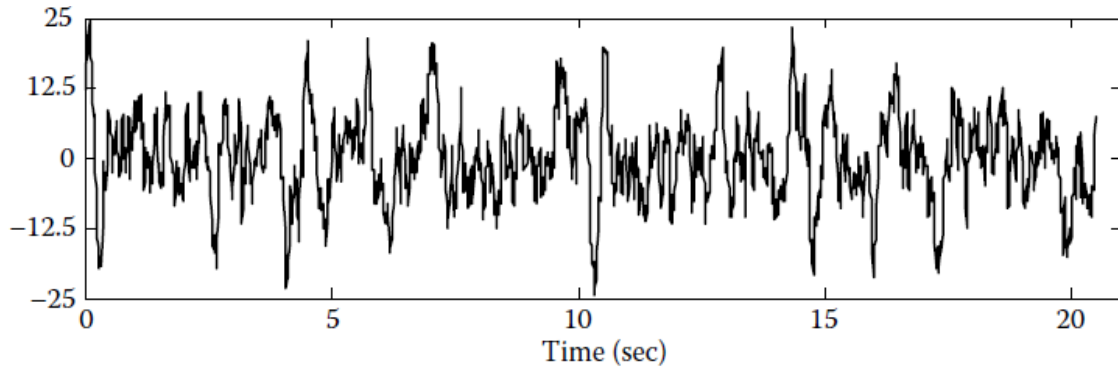


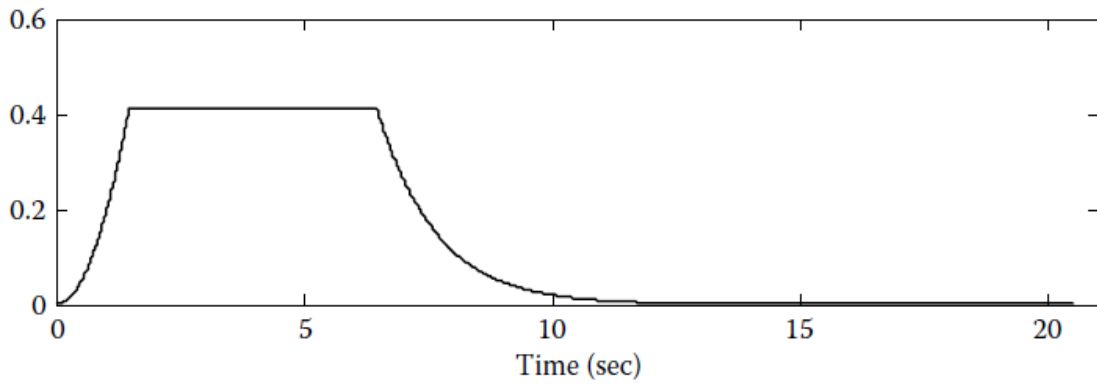
Figure 3.1 Modulation Function  $M_j(t)$  given by Jennings et al (1968)

The effect of the amplitude modulation on a stationary acceleration time history is illustrated in Figure 3.2. Figure 3.2(a) represents a realization of the stationary random process given by Eq. 3.21 and Figure 3.2(c) represents a realization of the non-stationary random process given by Eq. 3.23.

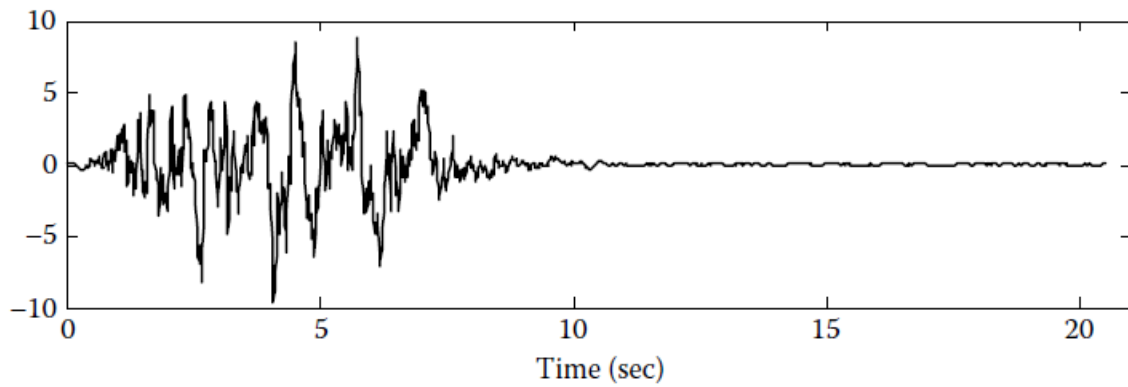
Additional realizations of the simulated non-stationary random process can be obtained by simply considering additional realizations of the random phase angle (obtained from a random number generating algorithm) and all the realizations will be statistically independent of each other. This is a highly desirable feature, since a significant number of simulated acceleration time histories are required when Monte Carlo Simulation procedures are implemented.



(a) Stationary Acceleration Time History  $A_j^{(i)}(t)$  (cm/sec<sup>2</sup>)



(b) Wave Amplitude Modulation Function  $M_j(t)$



(c) Amplitude Modulated Acceleration Time History  $F_j^{(i)}(t)$  (cm/sec<sup>2</sup>)

Figure 3.2 Effect of a Wave Amplitude Modulation Function on a Stationary Acceleration Time History [after Zerva (2009)].

### **3.2.6 Simulation of a Non-Stationary and Non-Homogeneous Spatially Variable Random Process.**

When uniform soil conditions exist between stations, the stochastic characteristics of the cross spectral density matrix  $S(\omega)$  correlating the acceleration time histories at such stations are not expected to vary significantly. However, it may not be realistic to assume uniform soil conditions when analyzing the spatial variability effects of seismic waves on highway bridges. For example, for highway bridges spanning over rivers, the abutments may be supported on well compacted base soils while many of the piers may be supported on river bed soils. In these instances, differences in the soil conditions, also called local site effects, should be expected when generating the simulated non-stationary random process. The incorporation of the local site effects may cause the stochastic characteristics of the  $S(\omega)$  matrix to vary significantly between stations, making the random process non-homogeneous.

The simulated non-stationary random process given by Eq. 3.22 can consider local site effects and become non-homogeneous if the prescribed cross-spectral density matrix  $S(\omega)$  coefficients are functions of the soil type characteristics at any given station. For example, Clough and Penzien (1993) provide such coefficients. However, only a few of these matrix coefficients are available in the literature. A more practical alternative consists of updating the  $S(\omega)$  matrix until compatibility with the response spectra characteristics of soil is achieved, since response spectra information for different soil types is readily available in many design codes.

In this study, the iterative algorithm proposed by Deodatis (1996) was used to generate a response spectra compatible  $S(\omega)$  matrix. The procedure starts by initializing the  $S(\omega)$  matrix by setting the coefficients equal to arbitrary nonzero values for the entire frequency range. Then, the  $i$ -th realization of the non-stationary random process is calculated using Eq. 3.23 and the corresponding response spectrum  $RSA_j^{(i)}(\omega)$ ,  $j = 1, \dots, n$  is generated. A target response spectrum  $RSA_j(\omega)$ ,  $j = 1, \dots, n$  is generated that represents the soil type characteristics at station  $j$ . Finally, the  $S(\omega)$  matrix is updated using the following equation:

$$S_j^{k+1}(\omega) = S_j^k(\omega) \left[ \frac{RSA_j(\omega)}{RSA_j^k(\omega)} \right]^2 \quad (3.24)$$

Where:

$S_j^k(\omega) = S(\omega)$  updated during the  $k^{th}$  iteration at station  $j$ .

$S_j^{k+1}(\omega) = S(\omega)$  updated during the  $(k+1)^{th}$  iteration at station  $j$ .

$RSA_j^k(\omega) = RSA_j^{(i)}(\omega)$  generated during the  $k^{th}$  iteration at station  $j$ .

$RSA_j(\omega) =$  target response spectrum at station  $j$ .

The iteration process is continued until the ratio of the generated response spectra of the  $k$  and the  $k+1$  iteration is close to one.

In this study, Saxena's (2000) recommendation to keep only the realizations of the non-stationary random process that take no more than four iterations to convergence was followed. The limitation in the number of iterations of the updating process of  $S(\omega)$  is intended to minimize the randomness introduced into the amplitudes of the non-stationary random process given by Eq. 3.22 via the  $H_{jm}(\omega_q)$  amplitude term of Eq. 3.17,

since such amplitude term is generated by the factorization of  $S(\omega)$  (see Eq. 3.13). An increase in randomness of the  $H_{jm}(\omega_q)$  term with each iteration of the updating process of  $S(\omega)$  may cause the non-stationary random process to gradually lose its ability to capture the prescribed wave coherence (Saxena, 2000).

Deodatis (1996) generated the target response spectrum for a given soil type using the procedure provided in the 1994 Edition of the Uniform Building Code (UBC 1994). In this study, the target response spectrum was generated using the procedure provided in the 2009 Edition of the International Building Code (IBC 2009). Although both the UBC 1994 and IBC 2009 specify the same general shape of the soil response spectrum curve, the UBC 1994 is more limited in the number of soil types considered and on the degree of precision for the determination of the spectral acceleration values generated from mapped information. For example, the UBC 1994 considers the entire coast of California under a single seismic zone (Zone 4) and thus, the spectral acceleration values of the response spectrum curve for a given soil type will be constant for the entire region.

The IBC 2009 provides spectral acceleration contour maps, where each contour line represents points of equal spectral acceleration value. Since around active seismic fault regions, more variation in spectral acceleration values are expected, the contour lines are accordingly more closely spaced. For example, considering again the coast of California, the San Andres Fault causes the occurrence of closely spaced contour lines, where multiple values of spectral acceleration are possible in the region surrounding the fault; thus, multiple response spectrum curves for a given soil type are possible for the entire region, where the spectral acceleration values of the curves will depend on the

proximity to the San Andres Fault. Therefore, the IBC 2009 allows for the generation of response spectrum curves for a given soil type that are more representative of the expected ground accelerations based on the recorded seismic activity of the region. The procedure to generate response spectrum curves for the soil types considered in this study is given in Section 3.4.4.2.

### 3.2.7 Generation of Acceleration Time Histories of a Multi-Component Seismic Shear Wave using Non-Stationary and Non-Homogeneous Random Processes.

A multi-component seismic shear wave  $S$  traveling in a horizontal plane was assumed acting at a certain angle of incidence  $\beta$  with respect to the bridge model longitudinal axis. Figure 3.3 shows a model of a three-span highway bridge subjected to such a wave, where the  $S$  wave is represented as a sinusoidal displacement time history for clarity purposes. The  $S$  wave is made of two components: a vertical component with amplitude variation  $D_V$  and a horizontal component with amplitude variation  $D_H$ .

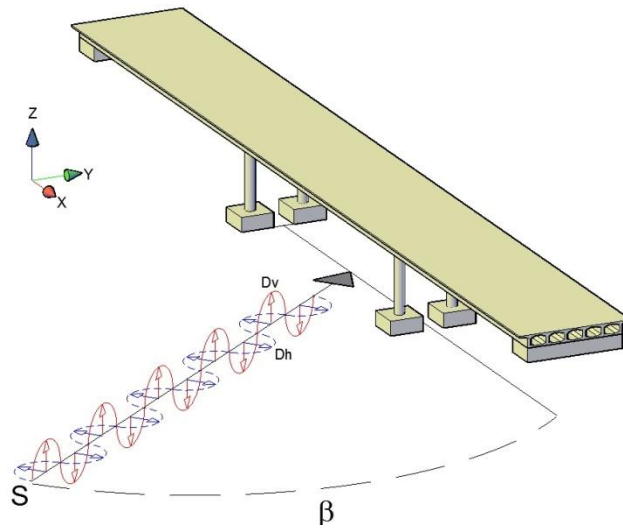


Figure 3.3 Multi-Component Shear Wave Traveling in a Horizontal Plane and Acting with an Angle of Incidence  $\beta$  with respect to a Highway Bridge Longitudinal Axis.

In this study, the  $S$  wave was assumed to have vector properties (i.e. a shear wave with velocity magnitude  $v$  and a direction defined by the angle of incidence  $\beta$ ) and thus it can be decomposed into  $S_X$  and  $S_Y$  waves, with directions parallel and perpendicular to the longitudinal axis of the bridge as shown in Figure 3.4. Therefore, the  $S_X$  wave is a multi-component longitudinal shear wave with a shear wave velocity of  $v_X = v \cos \beta$ , with vertical amplitude variation  $D_Z$  and horizontal amplitude variation  $D_Y$ . Similarly, the  $S_Y$  wave is a multi-component shear wave with a shear wave velocity of  $v_Y = v \sin \beta$ , with vertical amplitude variation  $D_Z$  and horizontal amplitude variation  $D_X$ . An angle of incidence of  $\beta = 45^\circ$  was used in this study. This angle was found by Allam and Datta (2004) to maximize the three-dimensional displacement response of bridges (see Section 2.4.2) and it also allows for the  $S_X$  and  $S_Y$  shear wave velocities to have the same magnitude (i.e.,  $v_X = v_Y$ ).

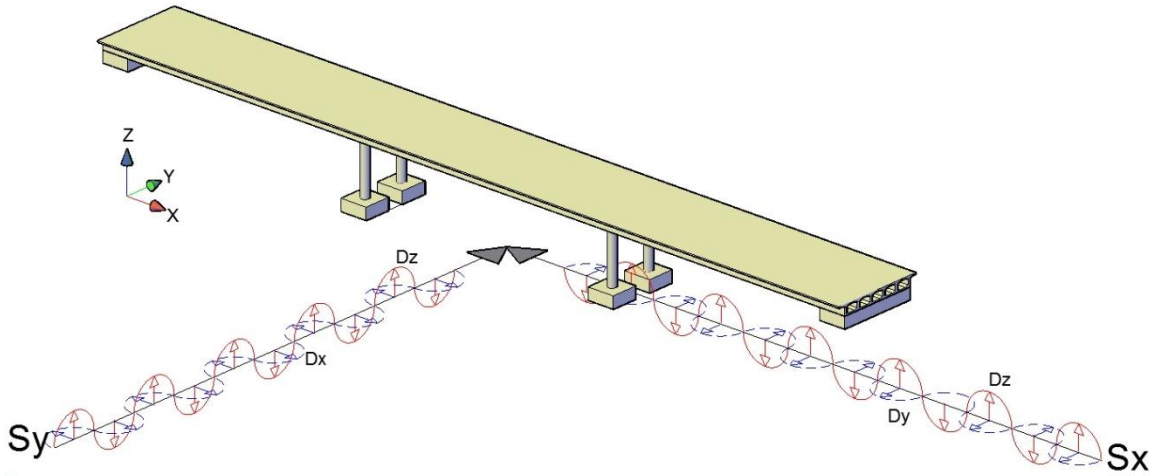


Figure 3.4 Decomposition of a Multi-Component Shear Wave  $S$  into a Multi-Component Longitudinal Shear Wave  $S_X$  and a Multi-Component Transverse Shear Wave  $S_Y$ .



Since the bridge structure in Figure 3.4 is symmetric with respect to both of its centroidal axis, the center of gravity and shear center of the bridge coincide. The shear center is the geometric location on the bridge where the resultant of horizontal forces must pass in order not to induce torsional response. It is assumed that the  $S$  wave passed through the projection on the ground of the bridge shear center location. As a result, the direction  $S_X$  and  $S_Y$  wave components also passed through the projection on the ground of the shear center.

To generate the acceleration time histories of the multi-component  $S$  wave, each horizontal and vertical component of the  $S_X$  and  $S_Y$  waves was modeled as a non-stationary random process and the desired non-homogeneous property was introduced by generating response spectra compatible cross spectral density matrices. Moreover, it was assumed that acceleration time histories generated for the horizontal and vertical component of the  $S_X$  and  $S_Y$  waves were statistically independent with respect to each other and that the same coherence function could be used to generate such components (i.e. isotropic coherence function). These assumptions were also used by Sextos (2003).

The Monte Carlo Simulation (MCS) scheme implemented in this study required a significant number of realizations of the random process describing each horizontal and vertical component of the  $S_X$  and  $S_Y$  waves. Statistical independence was enforced for all realizations by varying the seed number of the random number generator each time a realization (i.e. an acceleration time history record) was generated. In this study, the number of realizations generated for a particular wave component was established at twenty, following the recommendations of Saxena (2000), who determined such number

based on a study of the variation of the statistical parameters (mean, standard deviation, etc.) for an increasing number of realizations. Saxena (2000) found that these statistical parameters ceased to show significant variations when the number of realizations used to generate such parameters exceeded twenty. Saxena's observations were corroborated in this study and therefore, multiple sets of twenty acceleration time history records were prepared for each vertical and horizontal component of the  $S_X$  and  $S_Y$  waves to account for variations in the bridge span length and in the type of soil under the bridge supports.

### **3.2.8 Generation of Displacement Time Histories of a Multi-Component Seismic Shear Wave.**

The SAP2000 computer program was used to perform nonlinear time domain analysis on the highway bridge models. SAP2000 requires that the spatially varying seismic loading be introduced at the bridge supports as displacement time histories instead of acceleration time histories. This required performing numerical double integration on the acceleration time history data. The cumulative trapezoidal rule was used to perform numerical integration using a 0.012 second time step. The following post-processing techniques suggested by Vo and Haldar (2003) were used to eliminate potential sources of error in generating the displacement time history data:

- a) Filtering of very low and very high frequency content. Actual cross spectral density curves generated from recorded acceleration time histories at the inner circle accelerometers of the SMART-1 array (see Figure 3.5) show that cross spectral density amplitudes are nonzero for a frequency range of approximately  $0.1\text{Hz} \leq f \leq 8\text{Hz}$ , which is similar to Shinozuka's range

of  $0\text{Hz} \leq f \leq 10\text{Hz}$ . Therefore, in order better reflect the frequency content of actual time history records, Low-Pass and High-Pass Butterworth Filters were applied to the generated time history data to remove frequencies below 0.1Hz and above 8.0 Hz.

- b) Minimization of slope and offset. The offset is a nonzero value of the displacement and/or velocity time history at zero time and the slope is a linear trend in the time history curve with respect to the time axis. Both are consequences of numerical integration error, since the acceleration time history curve does not contain offset or slope. Curve fitting on the time history data using linear regression analysis was used to minimize these errors.

These techniques were applied when integrating acceleration time histories to obtain velocity time histories and also when integrating velocity time histories to obtain displacements time histories. Numerical integration and post-processing was done using an algorithm prepared within the MATHLAB environment.

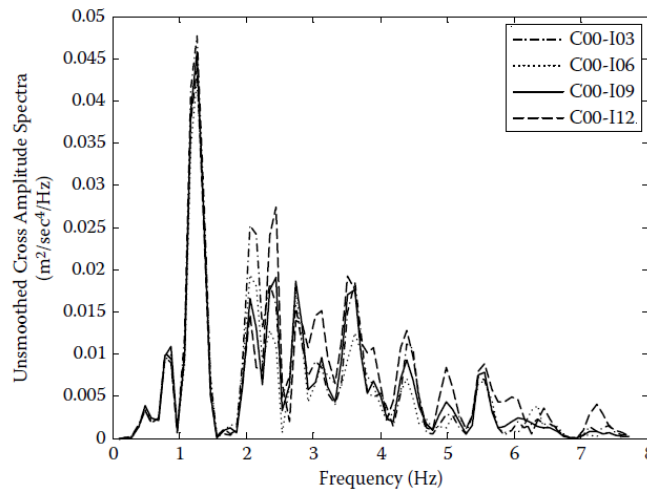
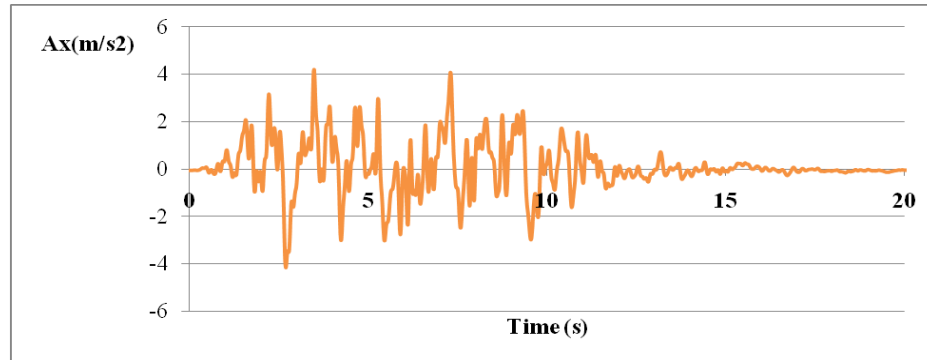


Figure 3.5 Cross Spectral Density Curves Generated from the Acceleration Time History Records shown in Figure 1.3(a). [after Zerva (2009)].

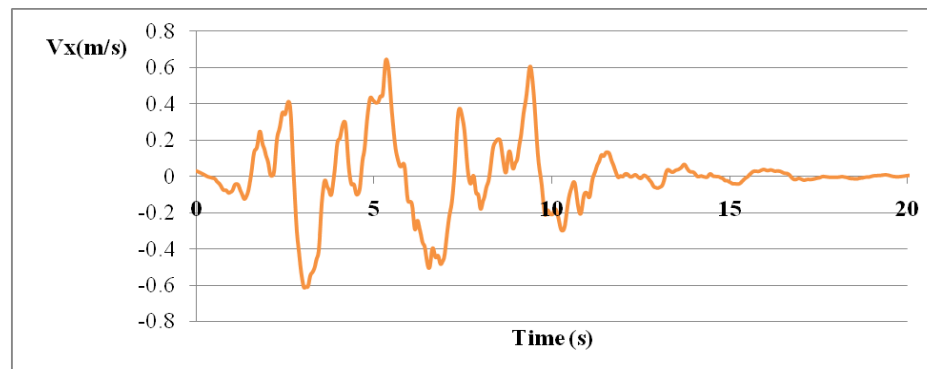
Figure 3.6 shows acceleration, velocity and displacement time history records for the horizontal component of the  $S_X$  shear wave generated for hard soils at the right bent location of the highway bridge model shown in Figure 3.4. Figure 3.6(a) shows an amplitude modulated acceleration time history record generated from a non-stationary and non-homogeneous random process as described in Section 3.2.7. Figure 3.6(b) and 3.6(c) are the velocity and displacement time history records, respectively, obtained by numerical integration of the acceleration time history. There is no visible offset or linear trend in neither the displacement nor the velocity time history curves, which shows the effectiveness of the minimization of the offset and slope post-processing techniques used in this study.

Appendix A shows acceleration, velocity and displacement time histories generated on hard, medium and soft soil cases for the horizontal component of the  $S_X$  shear wave for all the supports of the highway bridge model shown in Figure 3.4. Notice that in this highway bridge model, the offset of the displacement time histories is visible for piers on medium soils (see Figures A.15, A.18, A.21 and A.24). Since displacement time histories are used as seismic input data in SAP 2000, the offset would represent an initial support displacement at zero time. This offset value was very similar for all supports and was always in the same direction, which could be interpreted as a fictitious rigid body motion caused by numerical integration error. Rigid body motions do not produce deformations on the highway bridge model and as a result, the offset caused by integration error did not affect the seismic response of the bridge. For hard soils, the offset is visible, with similar value and with the same direction in the velocity time

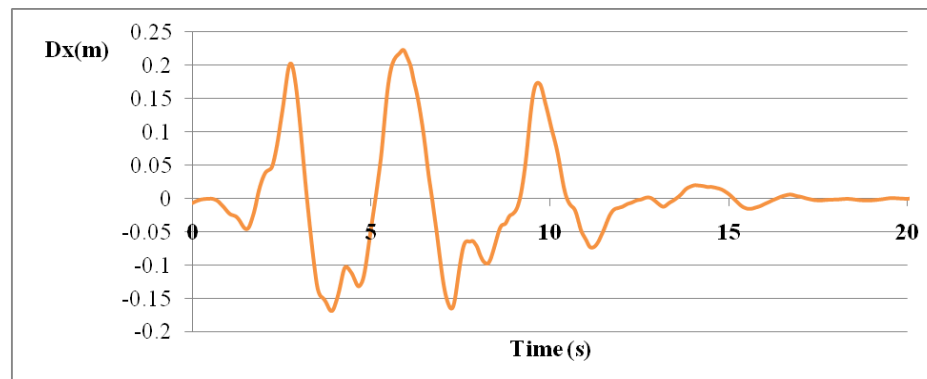
history curves (see Figures A.2, A.5, A.8 and A.11), but practically disappears in the displacement time histories.



(a) Acceleration time history



(b) Velocity time history



(c) Displacement time history

Figure 3.6 Acceleration, Velocity and Displacement Time Histories Generated on Hard Soils for the Right Bent of the Highway Bridge Model Shown in Figure 3.4 due to the Horizontal Component of the  $S_X$  Shear Wave.

### *3.2.8.1 Methodology to Determine the Displacement Time History Set under each Bridge Support.*

As the  $S_X$  wave travels along the longitudinal ( $X$ ) direction of the highway bridge model (as shown in Figure 3.4) it will encounter first the right abutment, followed by Bent 2, Bent 1 and finally the left abutment (see also Figure 3.7). Since spatial variability effects of the  $S_X$  wave occur in the  $X$  direction, each bridge support with a unique  $X$  coordinate will have a unique acceleration time history set ( $A_X, A_{XZ}$ ); where  $A_X$  and  $A_{XZ}$  are the horizontal and vertical components of the  $S_X$  wave, respectively. Similarly, as the  $S_Y$  wave travels in the transverse ( $Y$ ) direction of the bridge (as shown in Figure 3.4) it will encounter first the left side of the abutments along with the left piers of Bents 1 and 2, followed by the right side of the abutments along with the right piers of Bents 1 and 2. Since spatial variability effects of the  $S_Y$  wave occur in the  $Y$  direction, each bridge support with a unique  $Y$  coordinate will have a unique acceleration time history set ( $A_Y, A_{YZ}$ ); where  $A_Y$  and  $A_{YZ}$  are the acceleration time histories of the horizontal and vertical component of the  $S_Y$  wave, respectively.

Since each bridge support has a unique position in the ground surface ( $X, Y$ ), it follows that each bridge support will be subjected to a unique set of acceleration time histories ( $A_X, A_Y, A_Z$ ); where  $A_Z$  is obtained by adding algebraically the vertical components of the  $S_X$  and  $S_Y$  waves (i.e.  $A_Z = A_{XZ} + A_{YZ}$ ). After numerically integrating twice the ( $A_X, A_Y, A_Z$ ) acceleration time history set, a unique displacement time history set ( $D_X, D_Y, D_Z$ ) was generated for each bridge pier support as shown in Figure 3.7.

Before applying the displacement time history sets as seismic input data within the SAP2000 environment, the  $D_Z$  displacement time histories were multiplied by a scaling factor  $Z$ , to account for the fact that the magnitude of vertical component is generally less than the magnitude of the horizontal components. Existing seismic design codes typically assume a value for the  $Z$  factor of  $Z = 0.67$ , which was used in Chapters 4 and 5 to evaluate the seismic response of the highway bridge model consistent with such codes. In Chapter 6, the  $Z$  factor was increased to  $Z = 1.0$  to account for the presence of a particularly strong vertical component; this occurs in seismic excitations near the earthquake epicenter and the seismic response of the highway bridge model was evaluated for such case.

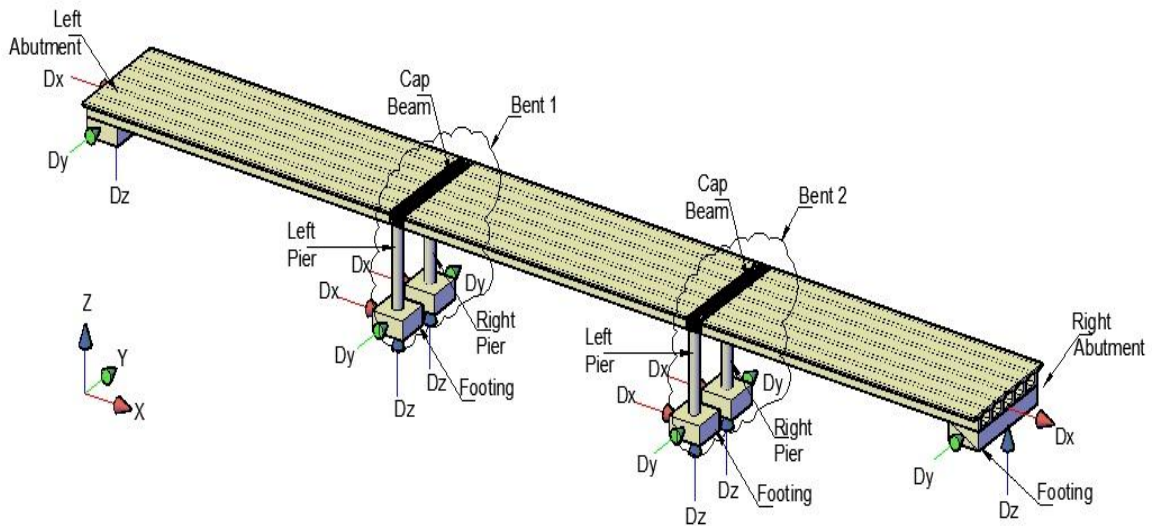


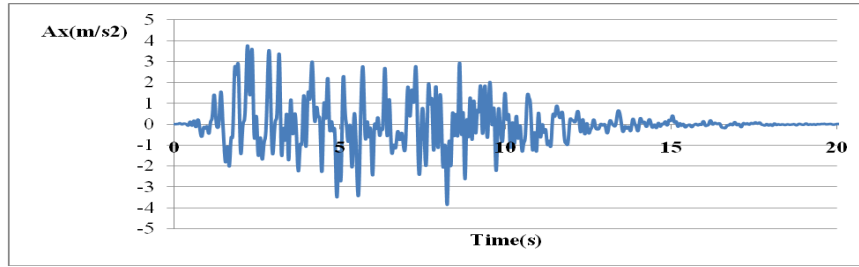
Figure 3.7 Application of Unique Displacement Time History Sets ( $D_x$ ,  $D_y$ ,  $D_z$ ) under Pier Supports of a Three-Span Bridge Model.

### 3.2.9 Use of the Stochastic Model to Generate Spatially Varying Acceleration Time Histories.

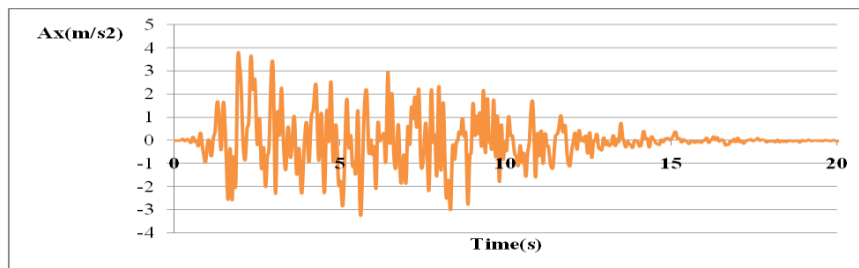
The highway bridge model shown in Figure 3.7 is used to demonstrate the capabilities of the proposed stochastic model to account for the spatial variability of a shear wave in the  $X$  and  $Y$  direction, the strong motion phase of the wave, as well as the local site effects by enforcing response spectra compatibility of the  $S(\omega)$  matrix. The  $S_X$  and  $S_Y$  shear waves were assumed traveling in the positive  $X$  and  $Y$  direction, respectively.

Appendix A shows the spatially variable acceleration time histories generated under the supports of this bridge model for different soil conditions due the horizontal component of the  $S_X$  wave (see Figures A.1, A.4, A.7, A.10, A.13, A.16, A.19, A.22, A.25, A.28, A.31 and A.34). The non-stationary characteristic of these time histories, which defined the duration of strong motion phase of the wave, was introduced by the amplitude modulation function discussed in Section 3.2.6 and shown in Figure 3.1. To illustrate the effect of spatial variability in the  $X$  direction on the acceleration time histories, Figures A.1, A.4, A.7 and A.10 are compared in Figure 3.8. All bridge supports sharing the same  $X$  coordinate, such as the left and right piers of the bents, are subjected to the same acceleration time histories generated by the horizontal and vertical component of the  $S_X$  wave. The effect of spatial variability in the  $Y$  direction on the acceleration time history curves is illustrated in Figure 3.9 for the horizontal component of the  $S_Y$  wave. All bridge supports sharing the same  $Y$  coordinate, such as the left piers or right piers of each bent, are subjected to the same acceleration time histories generated by the horizontal and vertical component of the  $S_Y$  wave.

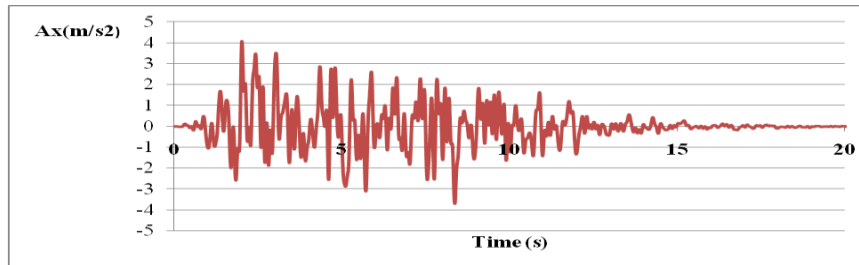




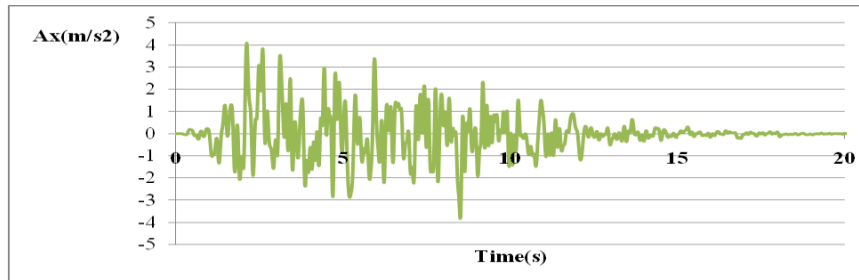
(a) Acceleration time history  $A_X$  at Left Abutment



(b) Acceleration time history  $A_X$  at Bent 1 (left and right piers)

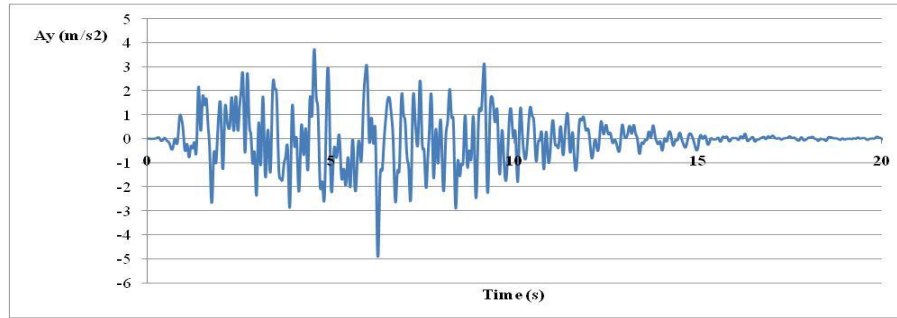


(c) Acceleration time history  $A_X$  at Bent 2 (left and right piers)

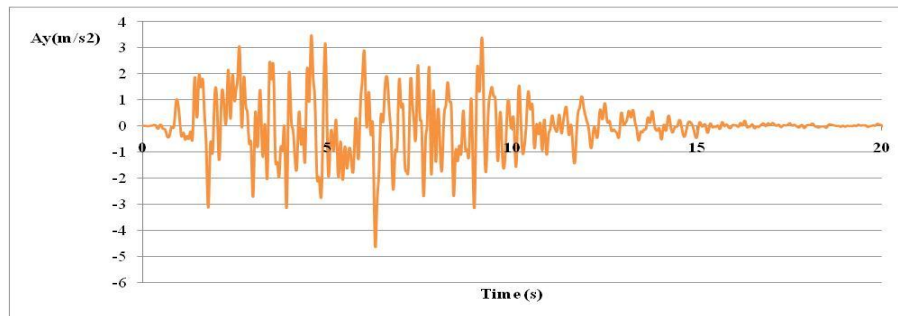


(d) Acceleration time history  $A_X$  at Right Abutment

Figure 3.8 Effect of Spatial Variability in the X Direction on Acceleration Time Histories of the Horizontal Component of the  $S_X$  Wave for Bridge supports Located on Hard Soils.



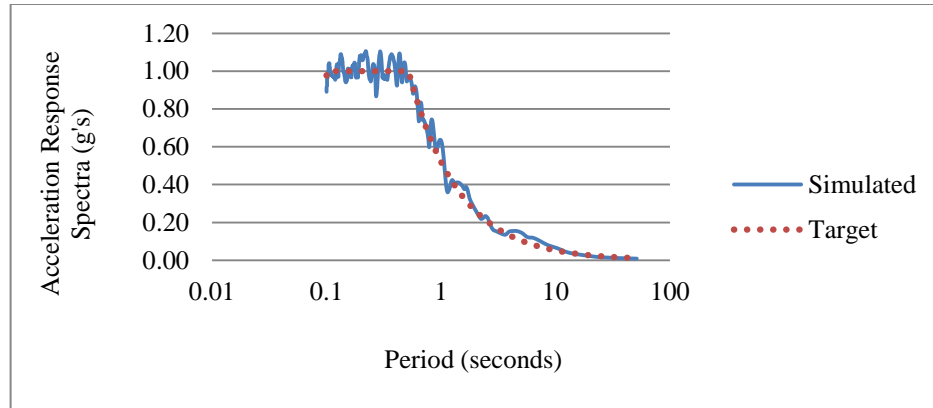
(a) Acceleration time history  $A_Y$  at left pier of Bent 1 and 2



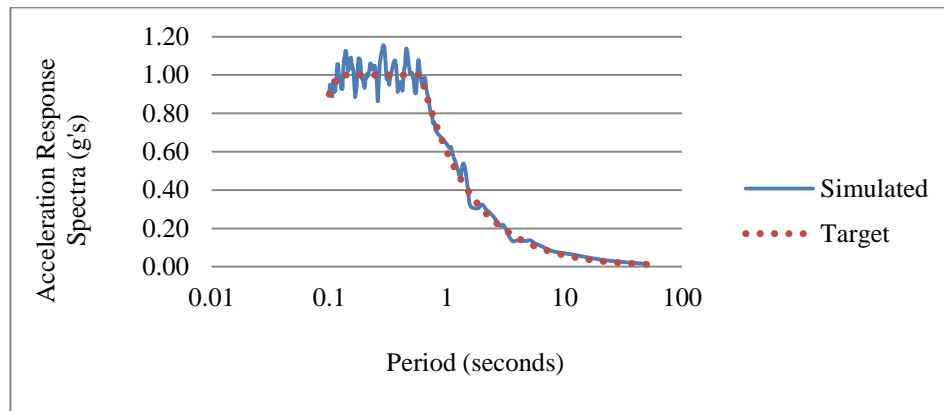
(a) Acceleration time history  $A_Y$  at right pier of Bent 1 and 2

Figure 3.9 Effect of Spatial Variability in the  $Y$  Direction on Acceleration Time Histories of the Horizontal Component of the  $S_Y$  Wave for Bridge Supports Located on Hard Soils.

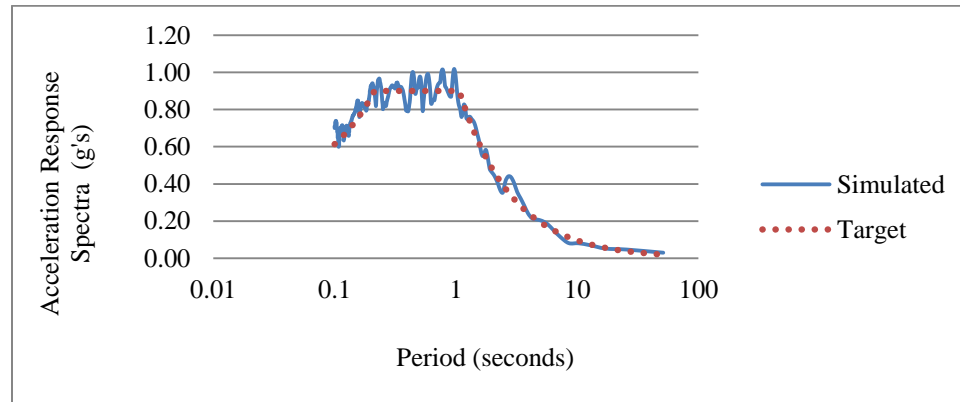
The non-homogeneous characteristics of the acceleration time histories given in Appendix A are introduced by updating the  $S(\omega)$  matrix using the iterative procedure described in Section 3.2.6 (see Eq. 3.24) until response spectra compatibility is achieved for a given soil type. Target response spectrum curves, as shown in Figure 1.5, were developed for hard, medium and soft soil types using the information given in the 2009 IBC code (see Section 3.4.4.2). Figure 3.10 shows the degree of response spectrum compatibility achieved by the  $A_X$  time histories generated at Bent 1 supports for hard, medium and soft soil types.



(a) Response spectra compatibility for hard soil type



(b) Response spectra compatibility for medium soil type



(c) Response spectra compatibility for soft soil type

Figure 3.10 Response Spectra Compatibility of the  $A_x$  Acceleration Time History at Bent 1 Supports for the Highway Bridge Model under Different Soil Conditions.

When comparing the acceleration time histories in Figure 3.8, it is evident that there are differences that make each of them unique. Such differences are due to the spatial variability effects caused by the shear wave traveling in the longitudinal direction of the bridge. The acceleration time histories given in Figure 3.9, where spatial variability effects occur due to the shear wave traveling in the transverse direction of the bridge, are also unique, but their differences decrease significantly. The stochastic model predicts this effect: the wave incoherence and wave passage effects decrease with decreasing distance between supports. As a result, the spatial variability effects on the acceleration time histories also decrease, minimizing the differences in the acceleration time histories at these supports.

Figure 3.10 shows that the degree of response spectra compatibility achieved by the acceleration time histories is acceptable for the three soil types considered. Figure 3.10 also shows that the degree of compatibility is similar for all soil types and that compatibility increases with increasing period of the soil.

Finally, from the evidence provided by Figures 3.8, 3.9 and 3.10, it can be observed that the stochastic model used in this study achieves the objective of generating realistic acceleration time history data at each bridge supports that accounts for spatial variability effects of a shear wave traveling in the short and long direction of the bridge.

### **3.3 Analytical Model for Bridge Structure**

The structural systems of highway bridges are typically relatively simple, with minor use of nonstructural elements and limited structural redundancy when compared to the

structural systems of buildings. The simplicity of the bridge structure has the advantage of facilitating the analytical modeling of the structural system, providing for a more realistic representation of its response; however, the typical redundancies present during the seismic response of building structures, such as additional sources of damping provided by friction between structural and nonstructural elements and the generation of multiple alternative load paths (should a main structural member fail), will have limited presence in bridge structure. Therefore, the required bridge analytical model may be relatively simple, but must be as realistic as possible in order to properly predict its seismic response. In this study, the three-dimensional seismic response of the bridge is of interest, since such a response will be induced when the  $S_X$  and  $S_Y$  shear waves act simultaneously on the bridge structure; thus, a three-dimensional analytical model for the bridge was developed and is presented in some detail next.

Figure 3.11 shows one of the highway bridge structural systems considered in this study. The bridge consists of a multi-span girder superstructure supported on uniformly separated two pier bents. The bridge was assumed supported at the ends on abutment foundations and on isolated footings at the pier locations. The cap beams of the bents were assumed integrated to the superstructure as shown in Figure 3.11(b) and the embedment depth of the footings was assumed equal to the footing thickness. The same bridge structural system was also considered by Priestley et al (1996).

The bridge was assumed made of reinforced concrete, with given concrete compressive strength  $f'_c$  and steel reinforcement yield strength  $f_y$ . Typical steel reinforcement details for the piers are shown in Figure 3.11(b).

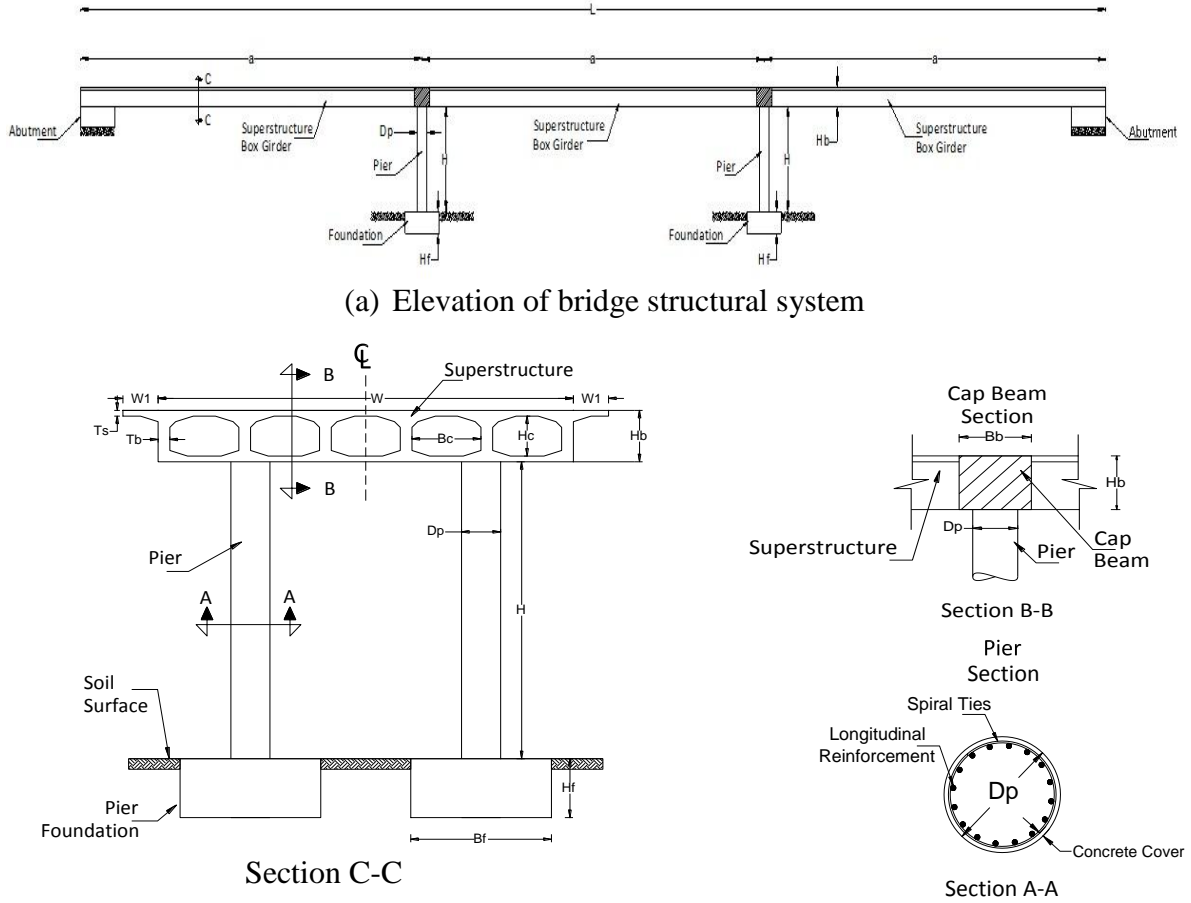


Figure 3.11 Highway Bridge Structural System

All cross sectional dimensions of cap beams, box girder and piers, as well as the overall dimensions of abutments and pier foundations, were assumed to remain constant. Changes in the bridge structural geometry, such as variations in the number of spans, span lengths and pier heights were considered with the objective of studying the effects of spatial variability of the seismic excitation on bridges with variable geometry. In Chapter 4, short, medium and long multi-span bridges with equal span length and pier height are considered. In Chapter 5, variations in span length and pier height are considered resulting in symmetric and asymmetric bridge structure configurations.

Modern design philosophies allow the structural engineer to predetermine the locations of inelastic response (plastic zones) of the structural system by proportioning the other parts of the system, where inelastic behavior is undesirable, so that these parts respond elastically under a given loading condition (Priestley, 1996). For bridges, the pier end zones (at the foundation and superstructure connection points) are typically selected as the plastic zone locations [see Figure 3.12(b)]. The steel reinforcement in the plastic zones is detailed so that proper confinement of the concrete core is achieved, which is necessary to develop the high strain levels required for plastic zone formation. Since in this study the flexural response of the piers is of interest, the relevant strains in the plastic zone will be rotational in nature. Thus, the plastic zone is typically modeled as a hinge (plastic hinge) that is activated once the rotational yield strains are exceeded during the flexural response of the piers. The bridge structural system shown in Figure 3.11(b) was defined by Priestley et al (1996) in compliance with such modern design philosophies. Therefore, the pier zones outside of the plastic hinge locations, along with the cap beams, superstructure and foundation were designed to respond elastically under the seismic loads considered in this study.

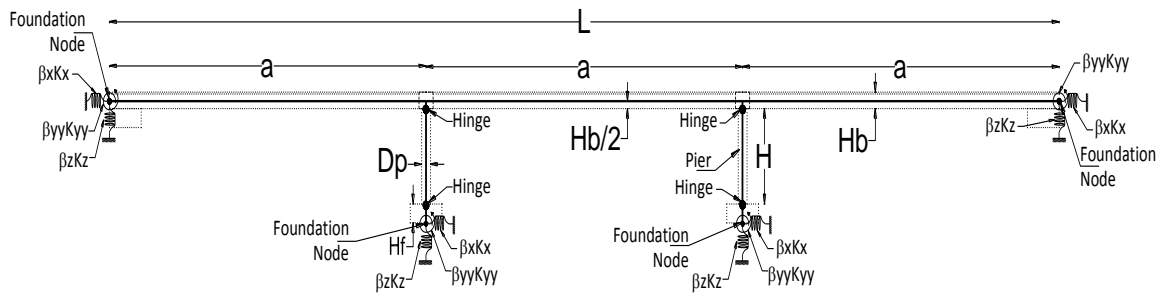
The bridge foundations at the abutment and pier locations were assumed mounted on spring supports to account for soil stiffness. Movement joints in the superstructure were not considered in the bridge layout, since modern bridge design requires them typically at every 1000 ft and none of the bridge models considered in this study exceeded that length. However, the proposed bridge analytical model could easily

consider movement joints by specifying a node at the joint location and releasing the corresponding nodal degrees of freedom.

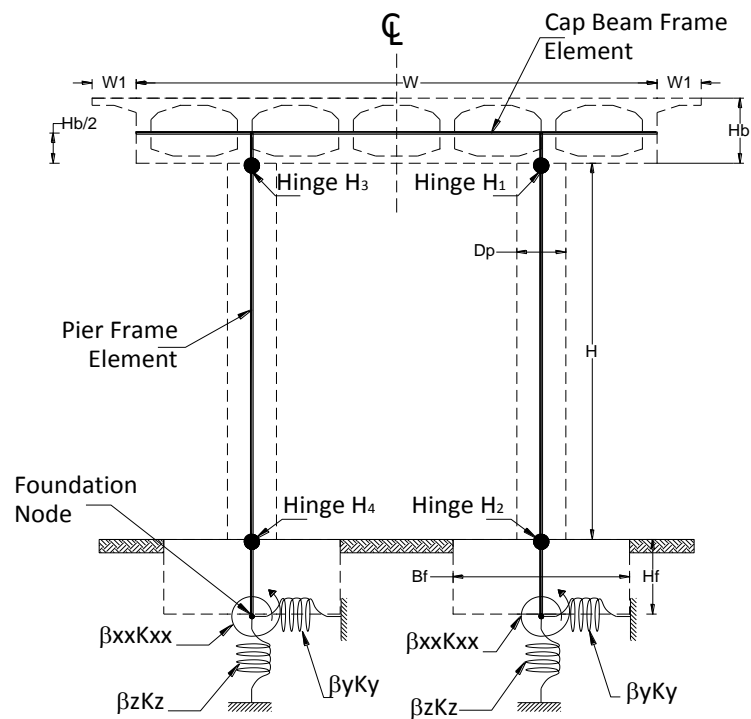
For the purpose of defining soil response spectrum acceleration values based on IBC 2009 code seismic zone maps, all bridge models were assumed located in the San Francisco, California geographical area. Such location was chosen due the high spectral acceleration values specified in the IBC 2009 code, given its proximity to the San Andres Fault. As a result, relatively large design seismic loads would be generated, which would increase the likelihood of inelastic flexural response of the bridge piers.

The finite element model of a typical three-span highway bridge structural system along with the soil dynamic stiffness model is shown in Figure 3.12 and Figure 3.13 shows a three-dimensional representation of the finite element model. The bridge piers were modeled using frame elements with plastic hinge locations coinciding with the lower elevation of the connection to the superstructure and the upper elevation of the connection to the foundation. The cap beams and superstructure were modeled using frame element with the superstructure element spanning continuously in between bents as shown in Figure 3.13. Relevant structural properties of the cap beam section and box girder section of the superstructure, such as flexural and torsional stiffness, cross sectional area, etc., were calculated automatically within the SAP 2000 environment based on their geometrical configuration. Gross cross sectional properties were considered for the box girder superstructure since it is typically designed as a pre-stressed concrete element and it was designed to behave elastically under seismic excitation. The spring coefficients of the soil dynamic stiffness model are determined in Section 3.4.2.





(a) Elevation of the highway bridge finite element model with soil dynamic stiffness model represented by translational springs with stiffness  $\beta_z K_z$  and  $\beta_x K_x$  and rotational springs with stiffness  $\beta_{yy} K_{yy}$  at foundation nodes.



(b) Cross section of the highway bridge finite element model (bridge bent) with soil dynamic stiffness model represented by translational springs with stiffness  $\beta_z K_z$  and  $\beta_y K_y$  and rotational springs with stiffness  $\beta_{xx} K_{xx}$  at foundation nodes.

Figure 3.12 Finite Element Model of Highway Bridge Showing Locations of Plastic Hinges and Rotational and Translational Spring Sets Representing Soil Dynamic Stiffness Model.

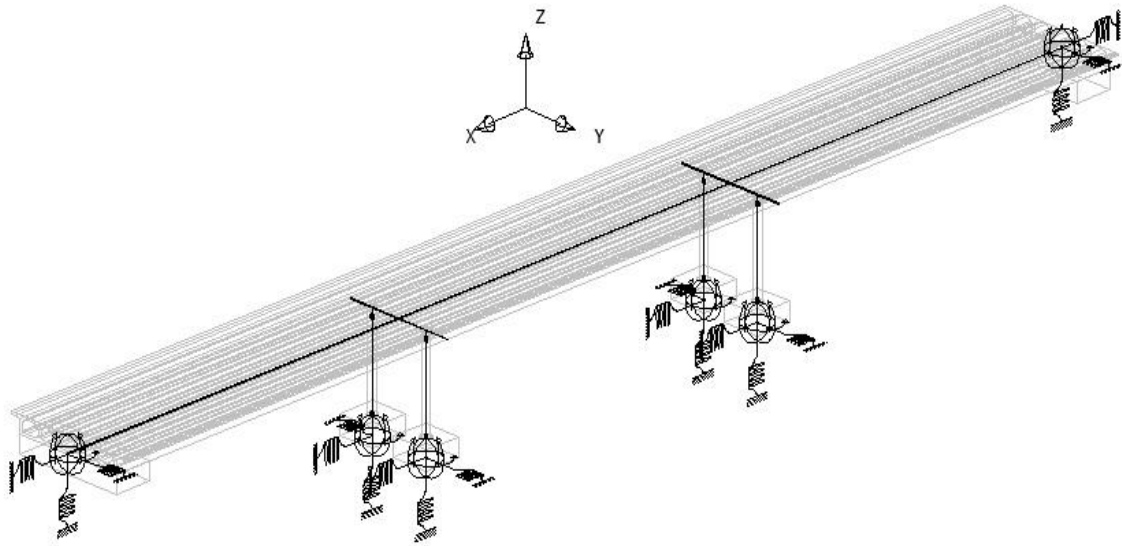


Figure 3.13 Three-Dimensional Finite Element Representation of a Typical Three-Span Highway Bridge Structural System (stiffness coefficients of the six degree of freedom spring set at foundation nodes not shown for clarity).

Figure 3.11(b) shows that the cap beam depth is  $H_b$  and the horizontal frame element representing the cap beam is shown in Figure 3.12(b). Such frame element is assumed located at the centerline (longitudinal axis) of the cap beam and the upper plastic hinges are assumed located at the interface of the piers and cap beam, with the pier vertical frame elements extending past the hinge until they reach the cap beam horizontal frame element. Therefore, the upper plastic hinge locations will be at half the cap beam depth, or  $0.5H_b$ . Similarly, Figure 3.11(b) shows that the depth of the footings is  $H_f$  and since the lower plastic hinges are assumed located at the interface of the piers and the footings, the depth of the footing defines the location of these plastic hinges [see Figure 3.12(b)] . The pier vertical frame elements are assumed extending past these hinges until they reach the foundation node (foundation-soil interface), where the spring set system modeling the soil dynamic stiffness is located.

The spring set system shown in Figure 3.12 considers elastic rotational and translational springs to model soil dynamic response due to the three-dimensional response of the bridge model. The translational spring stiffness coefficients in the  $X$ ,  $Y$  and  $Z$  bridge axis directions are given by  $K_X$ ,  $K_Y$  and  $K_Z$ , respectively, and these are modified to account for foundation embedment by the corresponding factors  $\beta_X$ ,  $\beta_Y$  and  $\beta_Z$ . The rotational spring coefficients with rotations with respect to the  $X$  and  $Y$  bridge axis are given by  $K_{XX}$  and  $K_{YY}$ , respectively, and the corresponding foundation embedment factors are given by  $\beta_{XX}$  and  $\beta_{YY}$ . The translational and rotational spring coefficients and the corresponding embedment factors are determined in accordance to FEMA 356 (2000) criteria, as shown in Figure 3.17. The support at the end of the translational springs shown in Figure 3.12 is only symbolic and it is meant to show a “reaction base” for the springs. More discussion on the spring support system, including the determination of the spring stiffness coefficients is made in Section 3.4.

Each plastic hinge was assumed to have a length  $L_p$  equal to 90% of the pier diameter, which is consistent with commonly accepted criteria. This length can be interpreted physically as the depth of the plastic zones at the pier ends. The plastic hinge element behavior was modeled using FEMA 356 (2000) criteria as shown in Figure 3.14. The smallest rotation  $\theta$  for which the plastic hinge model is defined (point A in Figure 3.14) is given by  $\theta = \theta_y$ , where  $\theta_y$  is the yield rotation (the rotation at which the yield moment  $M_y$  of the pier section is reached). Thus, the plastic hinge is not activated for elastic rotations ( $\theta < \theta_y$ ) and becomes part of the pier elements while such elements respond elastically. Point B in Figure 3.14 is defined at  $\theta = \theta_u$ , where  $\theta_u$  is the ultimate

rotation (the rotation at which the ultimate moment  $M_u$  of the pier section is reached). The values for yield and ultimate rotations and moments, as well as the slope of the  $BC$  segment of Figure 3.14, are obtained from moment-curvature relationships generated for each pier (as will be shown later in this Section). The residual flexural strength ratio (point  $D$  in Figure 3.14) was established at  $M_R/M_y = 0.20$  as recommended by FEMA 356. In this study, the residual flexural strength ratio of the bridge piers and the corresponding segment  $DE$  of Figure 3.14 were established to allow for plastic hinge rotations greater than the ultimate rotation ( $\theta > \theta_u$ ). Since plastic hinge rotational values exceeding the ultimate rotation can be expected to cause significant structural distress at the pier plastic zones, the plastic hinge model used allow for the prediction of which bridge piers were expected to suffer significant structural damage as a result of severe earthquake excitation.

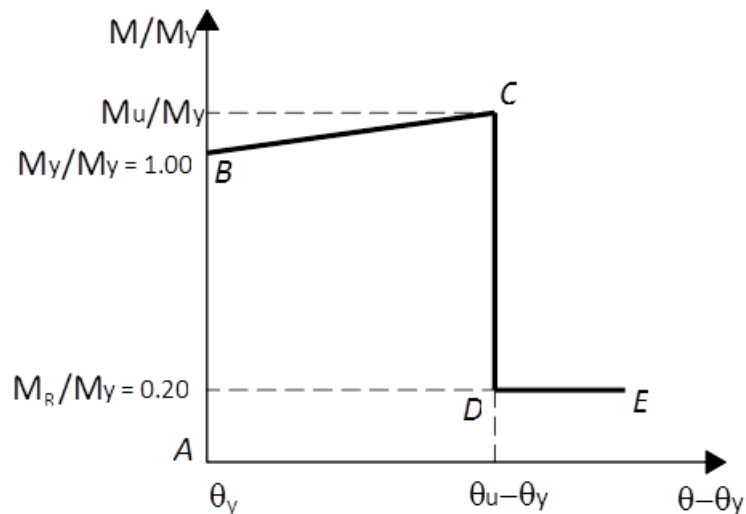


Figure 3.14 Plastic Hinge Model [FEMA 356 (2000)]

Since under the three-dimensional seismic response of the bridge model the piers are expected to be subjected to biaxial bending, the plastic hinge element must be defined for rotations along the longitudinal and transverse axis of the piers (bidirectional rotational response). Given the circular geometry of the pier cross section and the symmetry in the arrangement of the steel reinforcement, the plastic hinge element moment-rotational properties, as defined by Figure 3.14, were assumed identical in the longitudinal and transverse rotational directions.

The pier moment-curvature relationships are expected to be sensible to the pier axial load magnitude and ideally, the value of pier flexural stiffness should be continuously updated reflecting the variation of the axial load time history caused by the seismic excitation during nonlinear dynamic analysis. The range of sensibility to variations of the axial load for the elastic portion of the moment curvature relationship typically occurs for axial load ratios of  $P/(f'_c A_g) \leq 0.4$ , where  $P$  is the axial load and  $A_g$  is the gross cross sectional area of the pier, and bridge piers under combined gravity and seismic loads typically fall within this range. Since continuous updating of the moment-curvature relationship due to variations in the pier axial loads is not readily available in most commercial structural analysis software, Priestley et al (1996) suggested the alternative of using constant pier axial loads calculated from the plastic analysis of the two-dimensional bent frame given in Figure 3.11(b) under the effect of lateral seismic loads to determine the moment-curvature relationships. In this study, the constant pier axial load approach was used and thus only one moment-curvature relationship was assumed required to define the plastic hinge model.

Priestley's methodology assumed a vertical to horizontal seismic acceleration component ratio of 0.67, which is the ratio considered in most design codes. Therefore, moment-curvature relationships based on the implementation of Priestley's constant pier axial load alternative are only valid for such ratio. However, a methodology is presented in Chapter 6 that can be used to address the effects on the pier axial load due to different vertical to horizontal seismic acceleration component ratios.

The moment-curvature relationships for the pier cross section given in Figure 3.11(b) were calculated using the COLx Column Ductility Program developed by the California Department of Transportation (1993), which was also used by Saxena (2000). This program calculates the yield and ultimate moment capacity of the piers, their corresponding yield and ultimate curvature values and the effective (cracked) moment of inertia of the pier section. Since the piers are expected to respond in the inelastic range under seismic excitation, it is reasonable to assume that the pier section in the plastic zone region will exhibit more cracking than pier sections outside such region; therefore, the effective moment of inertia was used to model the frame elements of the pier. Figure 3.15 shows the moment curvature relationship obtained for the pier sections using the COLx program, as well as the bilinear approximation used to define the plastic hinge model.

The linear-elastic portion of the moment-curvature relationship was not considered in the plastic hinge model given in Fig 3.14, since the plastic hinge only accounts for plastic rotations (i.e.  $\theta - \theta_y \geq 0$ ). The values of the yield and ultimate

rotations of the plastic hinge model were obtained by multiplying the corresponding curvature values by the plastic hinge length; thus:  $\theta_y = L_p \phi_y$  and  $\theta_u = L_p \phi_u$ .

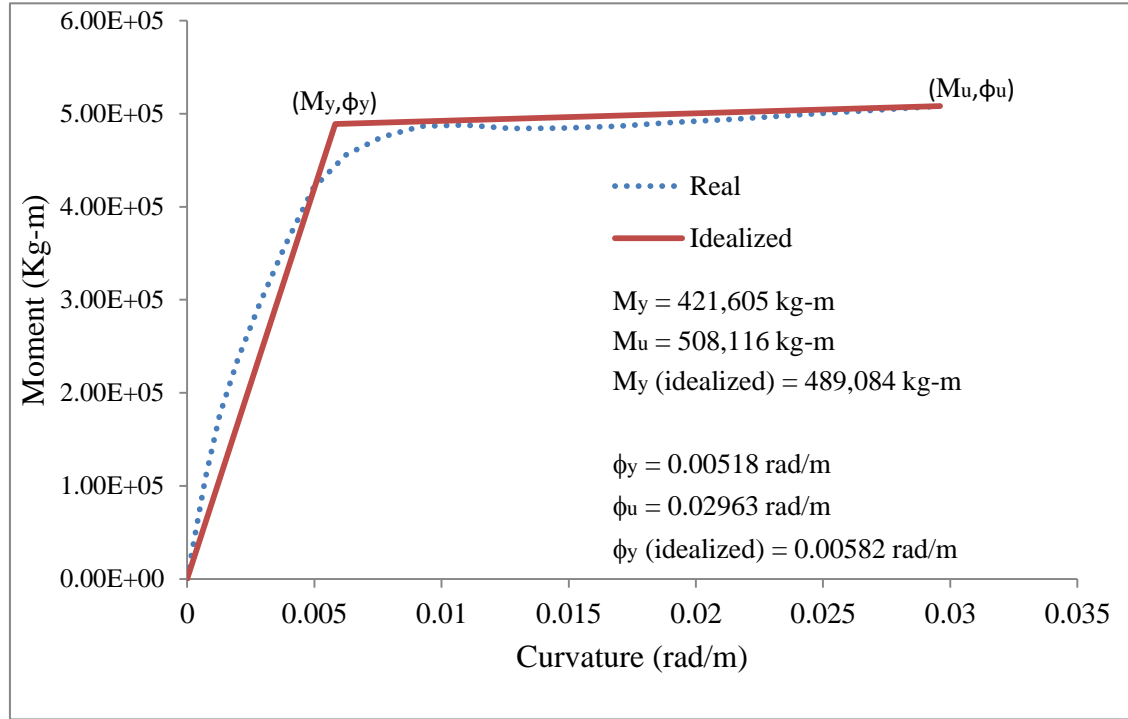


Figure 3.15 Moment Curvature Relationship for the Bridge Piers

In this study, the response variable of interest is the pier rotational ductility demand. The pier rotational ductility demand is a measure of the plastic rotational deformation that the pier must withstand at the plastic hinge locations for a given seismic loading condition. If  $\theta_{max}$  is the maximum rotation of a plastic hinge obtained from a nonlinear three-dimensional time domain analysis of the bridge model using three component spatially varying seismic time histories, and  $\theta_y$  is the yield rotation at the plastic hinge, then the maximum rotational ductility demand  $R$  on the plastic hinge can be conveniently expressed as the following ratio:

$$R = \frac{\theta_{max}}{\theta_y} \quad (3.25)$$

It is reasonable to expect different rotational ductility demands in the transverse and longitudinal direction to occur at each plastic hinge location given the differences in transverse and longitudinal structural arrangement considered in the bridge model. For non-circular pier sections, these ductility demand components will be coupled and the resultant ductility demand would have to be determined from axial load and biaxial bending yield surfaces. However, for circular pier sections, these components can be decoupled and the resultant ductility demand can be determined as discussed next.

Consider a plastic hinge located on a circular pier section with local axis 3 and 2 parallel to the bridge longitudinal  $X$  direction and transverse  $Y$  directions, respectively, as shown in Figure 3.16. Let  $M_3$  and  $M_2$  be the moments applied with respect to these axes and assume that both moments exceed the corresponding yield moments  $M_{3y}$  and  $M_{2y}$  for each axis. Thus, the corresponding plastic rotations can be obtained from the curvature values given in Fig 3.15 as  $\theta_3 = L_p \phi_3$  and  $\theta_2 = L_p \phi_2$ , and the yield rotations as  $\theta_{3y} = L_p \phi_{3y}$  and  $\theta_{2y} = L_p \phi_{2y}$ . Given the symmetry in the reinforcement arrangement and the circular pier cross section, it is reasonable to assume that the yield curvatures and moments with respect to axis 3 and 2 will be identical. Therefore, the rotational ductility demand for the longitudinal and transverse axis can be calculated using Eq. 3.25 as:

$$R_2 = \frac{\theta_2}{\theta_{2y}} = \frac{M_2}{M_{2y}} \quad (3.26)$$

$$R_3 = \frac{\theta_3}{\theta_{3y}} = \frac{M_3}{M_{3y}} \quad (3.27)$$



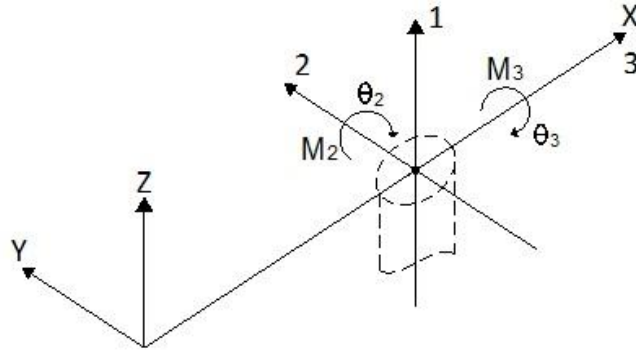


Figure 3.16 Local Axes of Plastic Hinges in Bridge Piers referred to Bridge Global Axes

Since in a circular pier cross section any axis is a principal axis, then it follows that a resultant axis can be determined at the plastic hinge location that transforms the existing bidirectional plastic rotations given by  $\theta_2$  and  $\theta_3$  into a unidirectional resultant plastic rotation given by  $\theta_R$ . Therefore, for piers with circular cross section the resultant plastic rotation, the angle of inclination  $\alpha$  of the resultant axis with respect to axis 3, and the resultant rotational ductility demand  $R$  are given by:

$$\theta_R = \sqrt{\theta_2^2 + \theta_3^2} \quad (3.28)$$

$$\alpha = \tan^{-1} \left( \frac{\theta_2}{\theta_3} \right) \quad (3.29)$$

$$R = \frac{\theta_R}{\theta_y} = \frac{\sqrt{\theta_2^2 + \theta_3^2}}{\theta_y} = \sqrt{\left( \frac{\theta_2}{\theta_y} \right)^2 + \left( \frac{\theta_3}{\theta_y} \right)^2} \quad (3.30)$$

It is also reasonable to assume that for piers with circular cross section with symmetric arrangement of the longitudinal steel reinforcement that the same yield rotation and yield moment values apply on any axis, including the resultant axis (i.e.  $\theta_y = \theta_{2y} = \theta_{3y}$  and

$M_y = M_{2y} = M_{3y}$ ). Therefore, substituting Eq. 3.26 and Eq. 3.27 into Eq. 3.30, the following expression can be obtained:

$$R = \sqrt{R_2^2 + R_3^2} \quad (3.31)$$

Eq. 3.31 is the resultant rotational ductility demand at a plastic hinge location where  $R_2 = \theta_2/\theta_y$  and  $R_3 = \theta_3/\theta_y$  are the uncoupled rotational ductility demands in the transverse and longitudinal axis, respectively.

Since  $\theta_2$  and  $\theta_3$  are response variables obtain at the plastic hinge during three-dimensional time domain analysis of the bridge model, they will be functions of time; thus, the determination of  $R_2$  and  $R_3$  must consider the values of  $\theta_2$  and  $\theta_3$  evaluated at the same time step in order to determine  $R$  from Eq. (3.31). The maximum value of  $R$  obtained from the complete time history was identified and selected as the resultant rotational ductility demand for each plastic hinge. Since each pier considered a plastic hinge at both ends, the maximum resultant rotational ductility demand of both plastic hinges was identified and selected as the rotational ductility demand for the pier.

A pier ductility index is proposed in this study to highlight the differences in rotational ductility demands of the piers when the bridge structure is subjected to spatially variable and uniform seismic excitation. The ductility index for any given pier is determined by dividing the rotational ductility demand caused by the spatially seismic excitation by the rotational ductility demand caused by the uniform seismic excitation. Thus, ductility indexes greater than one would indicate that the spatially variability of the seismic excitation increased the rotational ductility demand of the pier under consideration.

### **3.4 Analytical Model for the Soil-Foundation Interface**

#### **3.4.1 General Remarks**

Most of the results obtained when considering the effects of soil-structure interaction (SSI) have been generated by modeling the structure and the soil in the frequency domain, since the parameters that define the dynamic soil behavior are typically frequency dependent. Some of these results are discussed in Chapter 2. Detailed presentations can also be found in Wolf (1985) and Clough and Penzein (1993). As mentioned previously, frequency domain analysis has the disadvantage that nonlinear behavior cannot be properly considered.

Some researchers such as Wolf (1988) and Sextos (2003) have presented indirect procedures that allow the consideration of SSI in time domain analysis. Wolf presented a hybrid frequency domain procedure, in which nonlinearities are modeled as a series of linear analyses performed in the frequency domain with pseudo-loads recalculated in the time domain after each linear analysis. Wolf also presented an alternative where he considered the generation of discrete stiffness and dashpot models, and equations for dynamic soil parameters (stiffness, damping and mass participation) were obtained by curve fitting the actual frequency dependent behavior of the parameters in the low and medium frequency range. However, given the difficulty of obtaining good curve fits, Wolf restricted their applicability to one particular value of the soil's Poisson Ratio. Sextos (2003) used a similar approach and evaluated SSI effects in the frequency domain and decoupled the inertial and kinematic interaction effects in order to generate equivalent stiffness and viscous damping properties that were assigned to discrete springs

and dashpots, respectively, which were connected to foundation nodes. A nonlinear time domain analysis could then be performed on the structure. Both procedures could be implemented into computer codes and Sextos (2003) discussed such a code. However, no other studies could be found in the published literature that validated Wolf or Sextos procedures. Sextos compared his results with more rigorous analytical procedures, obtaining good agreement when modeling elastic behavior in soils, but some error was present when modeling nonlinear soil behavior.

Therefore, it seems evident that the current state of the art on nonlinear time domain analysis has yet to produce widely accepted procedures that properly incorporate the SSI effects. As a consequence, only equivalent static soil stiffness was considered in this study, where the dynamic properties of the soil were indirectly accounted for as established in FEMA 356 (2000).

### **3.4.2 Soil-Foundation Dynamic Stiffness Model**

FEMA 356 (2000) considers three methods for calculating foundation stiffness based on the degree of rigidity of the foundation. The simplest method (FEMA 365 Method 1) assumes a rigid foundation supported on a flexible soil. The other two methods assume a Winkler spring model which allows for the deformation of the footing slab. The massive dimension of typical bridge footings, allows for the assumption of a rigid foundation supported on a flexible soil and Method 1 was considered in this study.

Method 1 considers a foundation node at the footing-soil interface where the soil dynamic stiffness is modeled by linear discrete springs for translational, rocking and torsional degrees of freedom at the node. Coupling between horizontal and rocking

stiffness was disregarded in this study in accordance with FEMA 356 (2000) criteria. The formulas to calculate each of the individual soil dynamic stiffness coefficients are given in Fig 3.17. These values depend on typical soil properties such dynamic shear modulus  $G$  and Poisson Ratio  $\nu$ , as well as the dimensions of the footing and depth of embedment. The procedure to calculate the dynamic shear modulus  $G$  is given in Sections 3.4.3 and 3.4.4.

In this study, the depth of embedment of the pier footings was assumed equal to the thickness of the footing, as shown in Figure 3.11(b). All pier footings were assumed having a square footprint with dimensions as given in Figure 3.11(b). The abutments were modeled as rectangular footings with the short dimension identical to the dimensions of the pier footings and the long dimension equal to the superstructure width.

Since the dynamic soil stiffness model will be a function of the soil type, then by using the expressions given in Figure 3.17, a unique set of six spring stiffness coefficients was calculated for each soil type considered in this study as shown in Table 3.1 and Figure 3.12. Finally, depending on the soil type defined under each pier location, the corresponding spring stiffness coefficient set was assigned at the pier foundation node as shown in Figure 3.12.

Table 3.1 Soil Stiffness Coefficients Based on Soil Type

Soil Type	$K_x$ (kg/m)	$K_y$ (kg/m)	$K_z$ (kg/m)	$K_{xx}$ (kg-m)	$K_{yy}$ (kg-m)	$K_{zz}$ (kg-m)
Hard	$1.565 \times 10^9$	$1.565 \times 10^9$	$1.360 \times 10^9$	$1.475 \times 10^9$	$7.453 \times 10^9$	$1.298 \times 10^{10}$
Medium	$7.979 \times 10^7$	$7.979 \times 10^7$	$6.936 \times 10^7$	$3.810 \times 10^8$	$3.800 \times 10^8$	$6.620 \times 10^8$
Soft	$3.664 \times 10^6$	$3.664 \times 10^6$	$3.185 \times 10^6$	$1.750 \times 10^7$	$1.744 \times 10^7$	$3.040 \times 10^7$

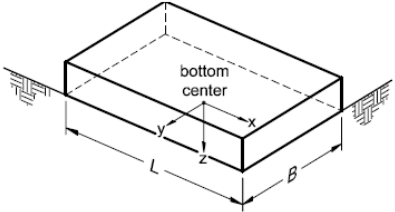
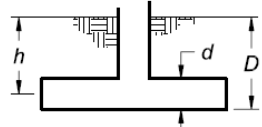
Degree of Freedom	Stiffness of Foundation at Surface	Note
Translation along x-axis	$K_{x, sur} = \frac{GB}{2-v} \left[ 3.4 \left( \frac{L}{B} \right)^{0.65} + 1.2 \right]$	 <p>Orient axes such that <math>L \geq B</math></p>
Translation along y-axis	$K_{y, sur} = \frac{GB}{2-v} \left[ 3.4 \left( \frac{L}{B} \right)^{0.65} + 0.4 \frac{L}{B} + 0.8 \right]$	
Translation along z-axis	$K_{z, sur} = \frac{GB}{1-v} \left[ 1.55 \left( \frac{L}{B} \right)^{0.75} + 0.8 \right]$	
Rocking about x-axis	$K_{xx, sur} = \frac{GB^3}{1-v} \left[ 0.4 \left( \frac{L}{B} \right) + 0.1 \right]$	
Rocking about y-axis	$K_{yy, sur} = \frac{GB^3}{1-v} \left[ 0.47 \left( \frac{L}{B} \right)^{2.4} + 0.034 \right]$	
Torsion about z-axis	$K_{zz, sur} = GB^3 \left[ 0.53 \left( \frac{L}{B} \right)^{2.45} + 0.51 \right]$	
Degree of Freedom	Correction Factor for Embedment	Note
Translation along x-axis	$\beta_x = \left( 1 + 0.21 \sqrt{\frac{D}{B}} \right) \cdot \left[ 1 + 1.6 \left( \frac{hd(B+L)}{BL^2} \right)^{0.4} \right]$	 <p><math>d</math> = height of effective sidewall contact (may be less than total foundation height)  <math>h</math> = depth to centroid of effective sidewall contact</p> <p>For each degree of freedom, calculate  <math>K_{emb} = \beta K_{sur}</math></p>
Translation along y-axis	$\beta_y = \beta_x$	
Translation along z-axis	$\beta_z = \left[ 1 + \frac{1}{21} \frac{D}{B} \left( 2 + 2.6 \frac{B}{L} \right) \right] \cdot \left[ 1 + 0.32 \left( \frac{d(B+L)}{BL} \right)^{2/3} \right]$	
Rocking about x-axis	$\beta_{xx} = 1 + 2.5 \frac{d}{B} \left[ 1 + \frac{2d}{B} \left( \frac{d}{D} \right)^{-0.2} \sqrt{\frac{B}{L}} \right]$	
Rocking about y-axis	$\beta_{yy} = 1 + 1.4 \left( \frac{d}{L} \right)^{0.6} \left[ 1.5 + 3.7 \left( \frac{d}{L} \right)^{1.9} \left( \frac{d}{D} \right)^{-0.6} \right]$	
Torsion about z-axis	$\beta_{zz} = 1 + 2.6 \left( 1 + \frac{B}{L} \right) \left( \frac{d}{B} \right)^{0.9}$	

Figure 3.17 Rigid Footing Spring Constants [FEMA 356 (2000)]

### 3.4.3 Soil Type Characterization Model

Table 3.2 shows the soil type characterizations and shear wave velocity ranges given in the IBC 2009 code and the corresponding soil type and shear wave velocity values assumed in this study. Such values were selected to approximate the midpoint value of the velocity ranges provided by the IBC 2009 code for each soil type.

Table 3.2 Soil Type Characterization and Shear Wave Velocity Values

Soil Class (IBC 2009)	Description	Soil Type	$v_s$ range (ft/sec)	$v_s$ assumed (ft/sec)	$v_s$ assumed (m/sec)
C	Very Dense Soil and Soft Rock	Hard	$1200 < v_s \leq 2500$	1968	600
D	Stiff Soil	Medium	$600 \leq v_s \leq 1200$	984	300
E	Soft Soil	Soft	$v_s < 600$	492	150

( $v_s$  is the shear wave velocity)

The dynamic shear modulus  $G$  and Poisson ratio  $\nu$  required to calculate the soil stiffness coefficients are variables that depend on the soil type characterization. FEMA 356 provides the following equation to calculate the static shear modulus  $G_o$  of the soil:

$$G_o = \frac{\gamma v_s^2}{g} \quad (3.32)$$

Where  $\gamma$  = unit weight of the soil and  $g = 9.81 \text{ m/sec}^2$  is the acceleration of gravity. Table 3.3 provides values of unit weight  $\gamma$  and Poisson ratio  $\nu$  for the soil types considered, as well as the calculated value of the static shear modulus  $G_o$  based on Eq. 3.32 and the value of the assumed shear wave velocity given in Table 3.2.

Table 3.3 Relevant Static Soil Properties

Soil Type	Unit Weight $\gamma$ ( $\text{kg/m}^3$ )	Poisson's Ratio $\nu$	$G_o$ ( $10^7 \text{ kg/m}^2$ )
Hard	2500	0.30	9.1743
Medium	1800	0.35	1.6514
Soft	1600	0.40	0.3670

In this study, variation in the soil characteristics was considered only along the longitudinal direction of the bridge; thus, the soil type was assumed constant along the transverse direction of the bridge. In other words, changes in the soil type were defined only at bent and abutment locations and the piers at any given bent were assumed located on the same soil type. This may be considered a valid assumption, since the likelihood of large variations in the geotechnical characteristics of the soil decreases with decreasing distance between bridge supports.

### **3.4.4 Soil Response Spectrum Characterization Model**

#### *3.4.4.1 Determination of Dynamic Shear Modulus of the Soil*

In order to calculate the proper value of the dynamic shear modulus of the soil, response spectrum information needed to be gathered first. From the IBC 2009 code maps for the San Francisco, California coast line (assumed location of the bridges), the following spectral response accelerations were obtained:  $S_s$  = mapped short period (0.2 sec) spectral response acceleration =  $1.5g$  and  $S_l$  = mapped 1.0 sec period spectral response acceleration =  $0.6g$ , where  $g$  = acceleration of gravity. Spectral acceleration maps in the IBC 2009 code assume 5% of critical system damping, which is consistent with the system damping assumed for all bridge models.

Table 1613.5.3(1) of the IBC 2009 code, which is partially reproduced in Table 3.4, provides the means to determine the site coefficients  $F_a$  based on the site classifications. In accordance to the IBC 2009 code, the maximum earthquake spectral response acceleration for short period is given by  $S_{MS} = F_a S_s$ . Thus from Table 3.4,  $S_{MS} = 1.5g$  for Hard and Medium Soils and  $S_{MS} = 1.35g$  for Soft Soils.



Table 3.4 IBC 2009 Code Site Coefficient  $F_a$ 

Site Class	Soil Type	$S_s \leq 0.25g$	$S_s = 0.50g$	$S_s = 0.75g$	$S_s = 1.00g$	$S_s \geq 1.25g$
C	Hard	1.2	1.2	1.1	1.0	1.0
D	Medium	1.6	1.4	1.2	1.1	1.0
E	Soft	2.5	1.7	1.2	0.9	0.9

Table 4.7 given in FEMA 365 (2000), which is partially reproduced here in Table 3.5, was used to calculate the dynamic shear modulus of the soil  $G$  based on the soil type, the value of the static shear modulus  $G_o$  and the value of  $S_{MS}$ . Thus, for Hard and Medium Soils,  $S_{MS}/2.5 = 1.5g/2.5 = 0.60g$  and for Soft Soils,  $S_{MS}/2.5 = 1.35g/2.5 = 0.54g$ . FEMA 365 defines the term  $S_{MS}/2.5$  as the “effective peak acceleration”. Using linear interpolation considering the calculated values of  $S_{MS}/2.5$ , the value of  $G/G_o$  was determined from Table 3.4. Table 3.6 provides a summary of the calculation of the soil dynamic properties.

Table 3.5 Effective Shear Modulus Ratio  $G/G_o$ 

Soil Type	$S_{MS}/2.5 = 0$	$S_{MS}/2.5 = 0.1g$	$S_{MS}/2.5 = 0.4g$	$S_{MS}/2.5 = 0.8g$
Hard	1.0	0.95	0.75	0.60
Medium	1.0	0.90	0.50	0.10
Soft	1.0	0.60	0.05	Not req.

Table 3.6 Summary of Soil Dynamic Properties

Soil Type	$G_o$ (kg/m <sup>2</sup> )	$S_{XS}/2.5$	$G/G_o$	$G$ (kg/m <sup>2</sup> )
Hard	$9.174 \times 10^7$	0.6g	0.675	$6.193 \times 10^7$
Medium	$1.651 \times 10^7$	0.6g	0.300	$4.954 \times 10^6$
Soft	$3.670 \times 10^6$	0.54g	0.050	$1.835 \times 10^5$

#### 3.4.4.2 Determination of Soil Response Spectrum Curves

In Section 3.2.6 a procedure was presented where the spectral density matrix  $S(\omega)$  was updated to reflect local site conditions by using a target response spectra  $RSA_j(\omega)$  that defined the dynamic response characteristics of the soil. The target response spectrum curve used in this study for Hard, Medium and Soft Soils was given in the IBC 2003 code as shown in Figure 3.18. The IBC 2009 code did not include such curve, but did include all the parameters required to generate the curve.

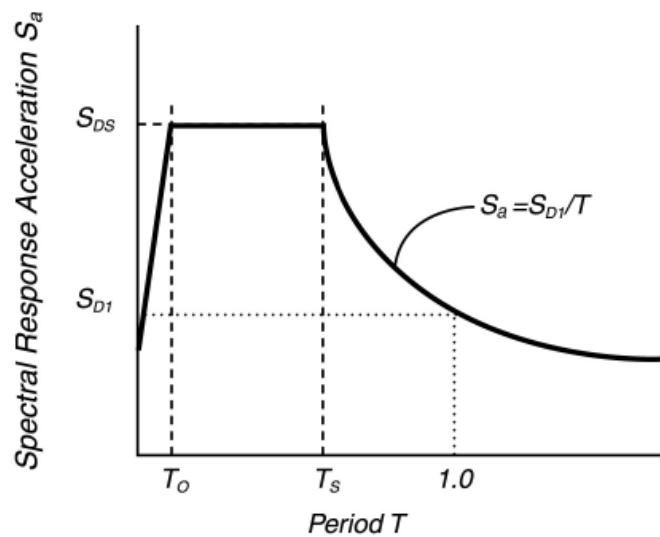


Figure 3.18 Soil Response Spectrum Curve

The equations that define the response spectrum curve shown in Figure 3.18 are given by the following expressions:

$$\text{For } T \leq T_o: \quad S_a = 0.60 \left( \frac{S_{DS}}{T_o} \right) T + 0.40 S_{DS} \quad (3.33)$$

$$\text{For } T_o < T \leq T_s: \quad S_a = S_{DS} \quad (3.34)$$

$$\text{For } T > T_s: \quad S_a = \frac{S_{D1}}{T} \quad (3.35)$$

Where:

$S_{DS} = \frac{2}{3} S_{MS}$  is the 5% damped design spectral response acceleration at short periods.

$S_{D1} = \frac{2}{3} S_{M1}$  is the 5% damped design spectral response acceleration at 1.0 sec. periods.

$S_{M1} = F_V S_1$  is the max. considered earthquake response acceleration at 1.0 sec. periods.

$S_{MS} = F_a S_s$  is the max. considered earthquake response acceleration at short periods.

$S_s$  = mapped spectral response acceleration at short periods.

$S_1$  = mapped spectral response acceleration at 1.0 sec. periods.

$T_o = 0.2 \left( \frac{S_{D1}}{S_{DS}} \right)$  and  $T_s = \frac{S_{D1}}{S_{DS}}$  are period values defined in Figure 3.18

The values of  $S_s$ , and  $S_1$  were defined in Section 3.4.4.1 as  $1.5g$  and  $0.6g$ , respectively. The values of  $S_{MS}$  were also defined in Section 3.4.4.1 as  $1.5g$  for Hard and Medium Soils and  $1.35g$  for Soft Soils. The site coefficient  $F_V$  can be determined from Table 1613.5.3(2) of the IBC 2009 code, which is partially reproduced in Table 3.7. The calculated values of all the parameters that define Eqs. 3.33, 3.34 and 3.35 are given in Table 3.8. The corresponding response spectrum curves for Hard, Medium and Soft Soils generated from these parameters are given in Figures 3.19, 3.20 and 3.21.

Table 3.7 IBC 2009 Code Site Coefficient  $F_V$ 

Site Class	Soil Type	$S_I \leq 0.10g$	$S_I = 0.20g$	$S_I = 0.30g$	$S_I = 0.40g$	$S_I \geq 0.50g$
C	Hard	1.7	1.6	1.5	1.4	1.3
D	Medium	2.4	2.0	1.8	1.6	1.5
E	Soft	3.5	3.2	2.8	2.4	2.4

Table 3.8 Response Spectrum Curve Parameter Calculations

Soil Type	$S_{MS}$ (g's)	$S_{M1}$ (g's)	$S_{DS}$ (g's)	$S_{D1}$ (g's)	$T_s$ (sec)	$T_o$ (sec)
Hard	1.50	0.78	1.00	0.52	0.52	0.10
Medium	1.50	0.90	1.00	0.60	0.60	0.12
Soft	1.35	1.44	0.90	0.96	1.07	0.21

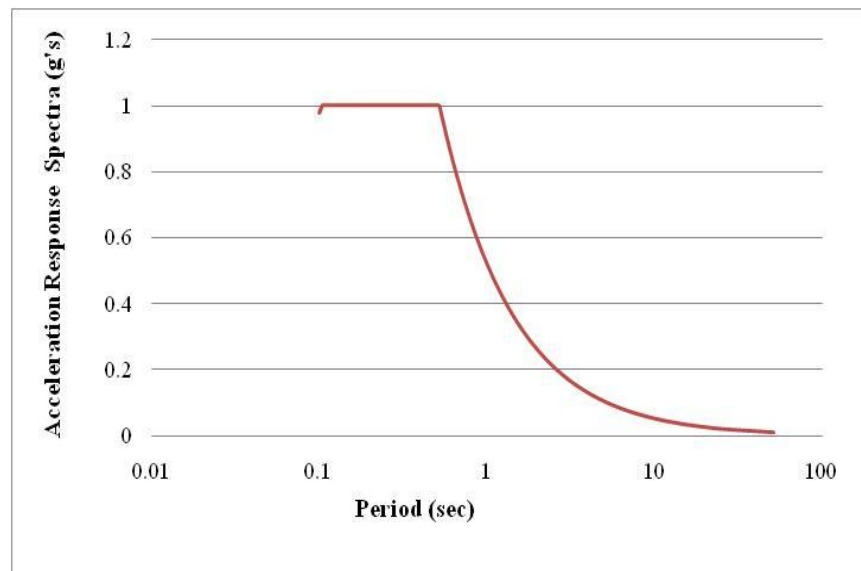


Figure 3.19 Response Spectrum Curve for Hard Soils

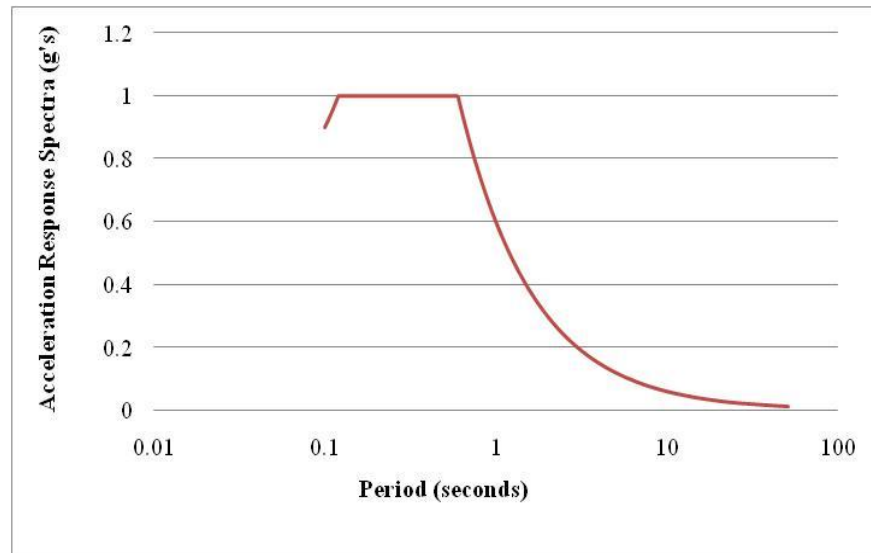


Figure 3.20 Response Spectrum Curve for Medium Soils

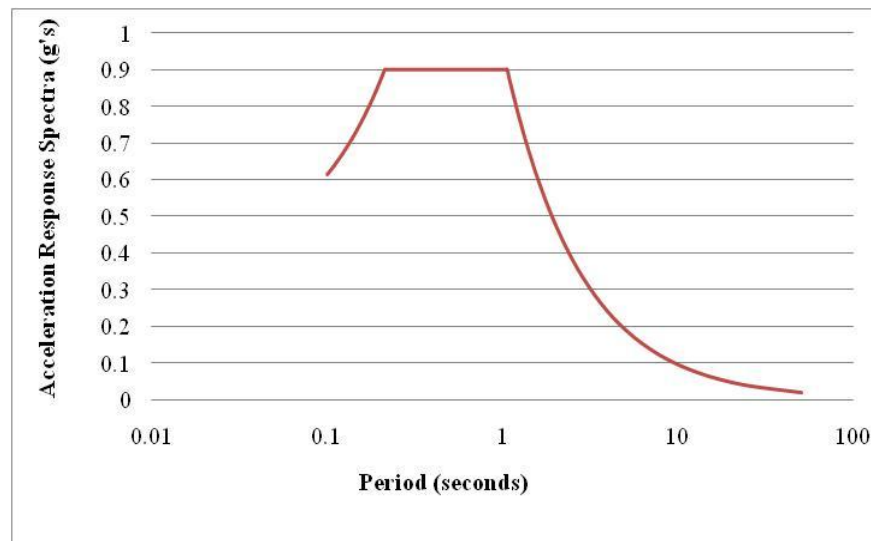


Figure 3.21 Response Spectrum Curve for Soft Soils

### **3.5 Implementation of Spatially Variable Displacement Time Histories and Finite Element Bridge Models in the SAP2000 Computer Program.**

The three-dimensional finite element models for all bridge structural configurations, as well as the soil dynamic stiffness spring sets and spatially variable displacement time history sets were implemented in SAP 2000, which is a commercially available finite element program used by many researchers, such as Saxena (2000), Kim (2003) and Sextos (2003) among others.

Spatially variable displacement time history sets ( $D_X$ ,  $D_Y$ ,  $Z*D_Z$ ) were applied at abutment and pier support locations defining a particular seismic load case as shown in Figure 3.7. Where  $Z$  is the scaling factor used to account for typical ( $Z = 0.67$ ) and strong ( $Z = 1.00$ ) vertical seismic motions. The soil stiffness coefficient sets given in Table 3.1 were assigned to the foundation nodes at abutment and pier locations in accordance to the applicable soil type and soil case. The soil case defined the variation of the soil type under each abutment and pier in the longitudinal direction of the bridge (see Section 4.2.2). Since the magnitude of each  $D_X$ ,  $D_Y$  and  $D_Z$  component of the displacement time history set generated at any given support is a function of the support location, the soil type response spectrum information and the soil case, a seismic load case was conveniently defined for each soil case.

The relevant structural properties, such as cross sectional area, gross torsional and flexural moments of inertia of the pier, cap beam and superstructure frame elements were generated automatically within the SAP 2000 environment based on their geometric configuration. SAP 2000 also provided automatic generation into sub-elements for the

superstructure frame element in order to improve the accuracy of the finite element model. Bidirectional plastic hinges were located near the ends of the pier frame elements as shown in Figure 3.12.

Once the three-dimensional finite element model of the bridge structure was completely defined within the SAP 2000 environment, a seismic load case was implemented, along with typical gravitational bridge loading (see Chapter 4 for the discussion on bridge gravitational loading). Nonlinear time domain analysis was applied to the loaded bridge model and the bidirectional rotations of the plastic hinges of all bridge piers were obtained as the relevant response variables. Post processing of the plastic hinge rotations allowed for the determination of the rotational ductility demand and ductility index of each pier in accordance with Section 3.3.

### **3.6 Monte Carlo Simulation Scheme**

Since in general seismic loading is inherently random, the bridge response variables obtained from the nonlinear time domain analysis will also be random in nature. Thus, very little insight may be gained on the understanding of the dynamic response of the bridge under a single seismic load case. Rational treatment of random response variables usually requires the consideration of multiple possible values of the random response variables so that relevant statistical information can be extracted. As a result, multiple statistically independent seismic load cases must be generated and nonlinear time domain analysis performed on the bridge model for each seismic load case in order to develop a sample space of the random response variable. In this study, the sample space size was

set at twenty statistically independent values of the random response variable following the criteria established in Section 3.2.7.

The process of developing a sample space for a random output variable from the response of a system subjected to a sample space of random input variables and generating the statistical information that describes the random output variable is called Monte Carlo Simulation. In this study, Monte Carlo Simulation was used to develop the sample space for the pier rotational ductility demand (random output variable) for a given bridge model (system) under a given soil case subjected to spatially varying seismic excitation (random input variable). A similar sample space was developed for the pier rotational ductility demand for a given bridge model under a given soil case subjected to uniform seismic excitation. From the data contained in these sample spaces, mean, standard deviation and coefficient of variation values were obtained for the rotational ductility demand of each pier of a bridge model subjected to spatially varying and uniform seismic excitation. Ductility indexes for each pier were then calculated by dividing the mean values of the rotational ductility demands obtained under spatially varying seismic excitation by the mean values of the rotational ductility demands obtained under uniform seismic excitation.

Since a significant number of different bridge structural configurations under a given soil case were considered in this study, then a significant number of different sample spaces for the pier rotational ductility demand needed to be generated. Also, since each value in the sample space was obtained from the results of a nonlinear time domain analysis of the bridge model, then considerable computer time was required to run all the



required time domain analysis within the SAP 2000 environment. SAP 2000 batch file programming features were used for automatically running the next seismic load case once the previous seismic load case run was completed in order to minimize computer time.

The analysis of results of the SAP 2000 runs, along with presentation of relevant statistical information on the variation of the pier rotational ductility demands due to variations of soil conditions under bridge supports, variations in bridge structural geometry and under the presence of strong vertical seismic acceleration components are presented in Chapters 4, 5 and 6, respectively.

### **3.7 General Algorithm of the Proposed Methodology**

The proposed methodology requires prior knowledge of the structural arrangement of the bridge, including the dimensions of the main structural elements (superstructure, cap beams, piers, abutments and foundations), as well as the structural properties of the concrete and steel reinforcement. For the case of the piers, the steel reinforcement details are also required. The general algorithm of the methodology follows:

#### *Step I. Determine General Site Conditions for the Bridge*

1. Generate applicable soil case by defining geotechnical characteristics of the soil under piers and abutment foundations and determine unit weight, Poisson's ratio and static shear modulus and the corresponding Soil Class from the IBC 2009 code for each type of soil identified.

2. Determine shear wave velocity corresponding to the predominant soil class from the IBC 2009 code.
3. Determine spectral response accelerations from IBC 2009 code maps based on the geographical location of the bridge. Generate IBC 2009 code response spectrum information and dynamic shear modulus values for each type of soil.
4. Determine vertical acceleration component scaling factor  $Z$  and angle of incidence  $\beta$  of the seismic wave based on records of seismic activity around the bridge location.

*Step II. Generate Spatially Varying Seismic Excitation Data*

1. Determine location on the ground surface where point specific and correlated acceleration time history records are required (locations will usually coincide with the center of footings for piers and abutments).
2. Determine response spectra data for each soil type using spectral acceleration data gathered in Step I and IBC 2009 code criteria.
3. Generate spatially variable response spectra compatible acceleration time history records for each of the three components of seismic wave (two horizontal, corresponding to the longitudinal and transverse bridge axis and one vertical) using proposed stochastic algorithm.
4. Perform numerical double integration of acceleration time history record to obtain the displacement time history sets for each pier and abutment support.

*Step III. Generate Three-Dimensional Finite Element Model of the Bridge Structure*

1. Based on structural plans of existing bridge or bridge design proposal generate the three-dimensional finite element model of the bridge structure using frame elements.
2. Based on pier cross sectional dimensions and longitudinal reinforcement arrangement, generate moment-curvature relationship for the piers. Using these relationships generate bidirectional plastic hinge models using FEMA 356 criteria. Place plastic hinges near the ends of the pier frame elements at the locations coinciding with the interface of the superstructure and footing connections.

*Step IV. Generate Dynamic Soil Stiffness Spring Sets under Bridge Supports*

1. Determine dynamic shear modulus for each soil type using the geotechnical and spectral acceleration information gathered in Step I.
2. Based on soil case definition (Step I.1), determine spring stiffness set and foundation embedment factor at the foundation node of each pier and abutment in accordance with FEMA 356 criteria.

*Step V. Perform Nonlinear Time Domain Analysis on the Bridge Model*

1. Implement bridge finite element model in SAP 2000 or other computer program with nonlinear time domain analysis capabilities and apply seismic load case (displacement time history sets) on bridge supports and other required gravitational loads.

2. Identify the response variable of interest. For determining pier rotational ductility demands, the variable of interest are the rotations at the bidirectional plastic hinges.

*Step VI. Determine Rotational Ductility Demands on Bridge Piers*

1. Determine pier rotational ductility demands from plastic hinge rotational response in longitudinal and transverse bridge direction, as well as resultant rotational ductility demand using decoupling procedure provided in Section 3.3.
2. If the pier rotational ductility demand is considered a random response variable, then generate a sample space for the variable using Monte Carlo Simulation. A minimum sample space of twenty statistically independent values of the rotational pier ductility demand is recommended. Thus, Steps II.3 and II.4 must be repeated twenty times varying each time the random number generator of the stochastic algorithm to ensure the statistical independence of the generated seismic load cases. Run Step V for each seismic load case and go to Step VI.1 to obtain the corresponding pier rotational ductility demand values. Finally, determine mean, standard deviation and coefficient of variation values of the sample space.

### 3.8 Concluding Remarks

The proposed methodology presented in this chapter and summarized in the general algorithm given in Section 3.7 improves the state of the art in highway bridge design and analysis by incorporating the following unique features:

1. Three-dimensional response of bridge finite element models excited by multi-component spatially varying seismic waves. Since the bridge structure is modeled with frame finite elements, the three-dimensional variations of the bridge geometry can be captured with relative ease.
2. The seismic waves are modeled as multi-component acceleration vectors of variable magnitude with a direction defined by the angle of incidence of the arriving wave with respect to the bridge longitudinal axis. Vector decomposition of the arriving wave is used to distribute the vertical and horizontal wave components in the longitudinal and transverse directions of the bridge.
3. The spatial variability of the vertical and horizontal acceleration components of the wave is captured by using a stochastic algorithm that generates unique and correlated acceleration time history records under each bridge support that account for the wave passage, wave incoherence and local soil effects. Since the acceleration time history records of each component of the seismic wave are independently generated, the magnitude of each record can be scaled independently (using Z scaling factors), allowing for the explicit consideration of strong vertical acceleration components.

4. Bidirectional plastic hinge models that capture the in plane and out of plane plastic rotations at the pier plastic zones occurring during three-dimensional bridge response. The moment-rotation behavior of the plastic hinge is generated from moment-curvature relationships obtained from the pier structural characteristics. Thus, the reduction in the flexural ductility range of the piers under the increase in axial load generated by strong vertical acceleration components can be explicitly accounted for. By incorporating FEMA 356 (2000) criteria, plastic rotations beyond the ultimate value predicted by the pier moment-curvature relationships can be considered by the bidirectional plastic hinge model. By keeping track of such rotations, the plastic hinge model allows for the detection of piers that will exhibit significant structural damage at their plastic zone under a particularly strong earthquake.
5. The soil dynamic stiffness is considered under each bridge support by incorporating a six degree of freedom soil spring set model at the foundation node. Using FEMA 365 criteria, a unique three dimensional soil spring set model is generated under each bridge foundation by determining the stiffness coefficients of each spring as a function of the soil dynamic shear modulus and Poisson's ratio, as well as the dimensions and depth of embedment of the foundation. Thus, changes in the soil conditions and/or the foundation system in the longitudinal and transverse direction of the bridge can be accounted for by adjusting the soil spring set model accordingly.

6. The soil response spectrum information used to update the cross spectral density matrix during the generation of the spatially variable acceleration time history records and to define the soil dynamic stiffness under the bridge foundations is obtained from the IBC 2009 code spectral acceleration maps. This achieves a more precise correlation between the bridge geographical location and the expected level of earthquake excitation, based on the seismic risk analysis of the region.

## **4. EFFECTS OF SPATIAL VARIABILITY OF SEISMIC EXCITATION AND VARIABILITY OF SOIL CONDITIONS ON PIER DUCTILITY DEMANDS OF MULTI-SPAN BRIDGES**

### **4.1 Introduction**

As discussed in Chapter 2, many researchers have considered the influence of the effects of the wave passage, incoherence and local soil conditions, either independently or in combination, when studying structural response of bridges under spatially varying seismic waves. There seems to be a consensus among researchers that the ductility demand on the piers is most sensible to the variation of soil conditions. In this Chapter, this sensibility is studied under three-dimensional nonlinear time domain response of short, medium and large multi-span bridge models under spatially varying and uniform seismic excitation.

### **4.2 Modeling Methodology**

The general methodology followed in this study for modeling spatial variability of the seismic wave, the bridge structure and the soil dynamic stiffness, as well as their implementation in the SAP 2000 computer program was presented in Chapter 3. Modeling specifics that cover the objectives of this chapter are mentioned next.

Seismic load case sets considering spatially varying displacement time histories were generated as described in Section 3.5. For the uniform seismic excitation case, the seismic load case sets were prepared in similar fashion, except that each of the twenty



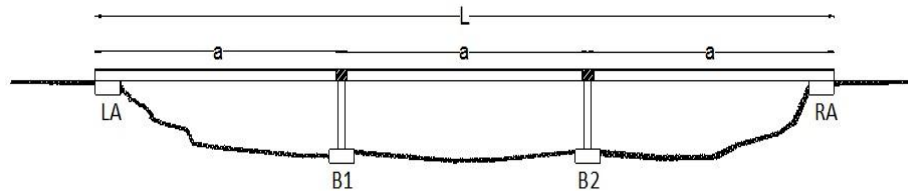
statistically independent seismic load cases included in each seismic load case set considered only one unique displacement time history set generated at the first pier location and the same set was applied to the rest of the pier and abutment locations. In this Chapter, the ratio of the vertical to horizontal acceleration component was set at  $Z = 0.67$ , which is the assumed ratio considered in most seismic design codes.

#### **4.2.1 Multi-Span Highway Bridge Models**

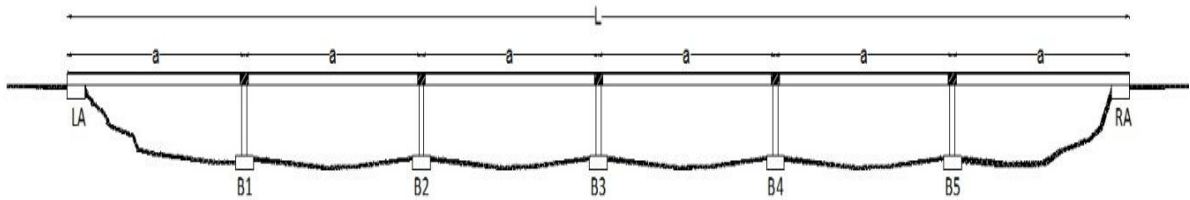
The longitudinal and cross sectional dimensions of the multi-span bridge models considered in this Chapter are given in Figures 4.1 and 4.2, respectively. The bridges were assumed made of reinforced concrete with design compressive strength of  $f'_c = 4$  ksi (27.6 MPa) and steel reinforcement yield strength of  $f_y = 60$  ksi (413.7 MPa). The gravitational loading on bridge piers was assumed to be dead and live axial compressive loads of 900 kips (408.6 metric tons) and 300 kips (136.2 metric tons), respectively, and 25% of the live load was assumed to be sustained when used in combination with seismic loads. A typical 5% damping ratio was assumed for all bridge models. The same bent frame given in Figure 4.1 was considered by Priestley et al (1996), along with the pier gravitational loading defined above. Priestley performed plastic analysis of the bent frame under the  $Z = 0.67$  condition and obtained an amplified constant pier compressive axial load of 1776 kips (806.3 metric tons), which was used to generate the moment-curvature relationship of the piers (see Figure 3.15).

All multi-span bridge models were assumed to have the same individual span length and the same bridge bent cross section given in Figure 4.1 and thus, the only

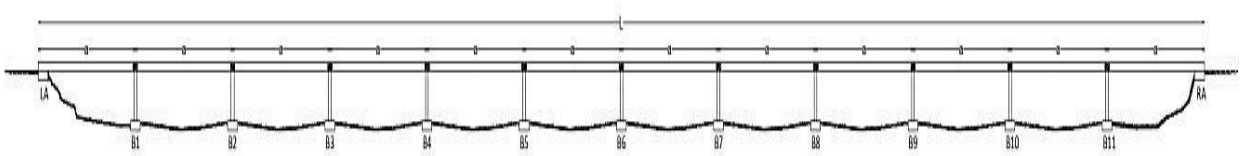
variation considered was the number of spans. This allowed for the generation of short, medium and long multi-span bridge models by simply increasing the number of spans.



(a) Small Multi-Span Bridge Model



(b) Medium Multi-Span Bridge Model



(c) Large Multi-Span Bridge Model

Figure 4.1 Multi-Span Highway Bridge Models

Table 4.1 shows the overall dimensions of the short, medium and long multi-span bridge models considered in this Chapter.

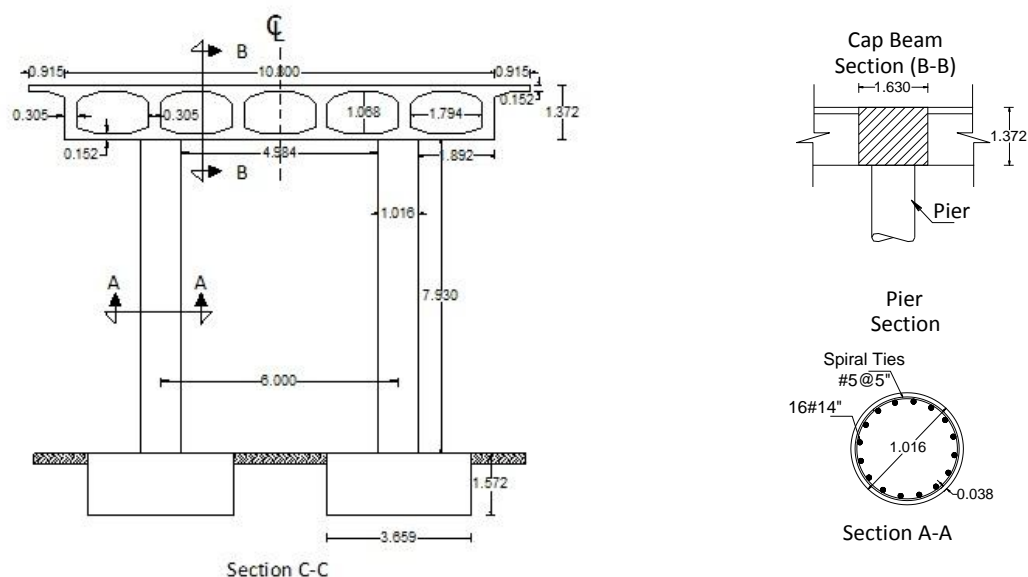


Figure 4.2 Typical Cross Section (Bent Frame) of the Multi-Span Bridge Models (all dimensions shown given in meters).

Table 4.1 Dimensions of Short, Medium and Long Multi-Span Bridge Models

Bridge Type	Spans	Bents	Piers	a (meters)	H (meters)	L (meters)
Short	3	2	4	36.58	7.93	109.73
Medium	6	5	10	36.58	7.93	219.46
Long	12	11	22	36.58	7.93	438.91

#### 4.2.2 Soil Cases

Considering that all the multi-span bridge models in this Chapter have an abutment at each end with a specific number of equally spaced two pier bents, then from Table 4.1,

the short, medium and long multi-span bridge models have 4, 7 and 13 locations, respectively, along the longitudinal direction where changes in the soil type can be defined. Since abutments are typically built over well compacted and properly graded materials that are used to construct the approaches to the bridge, these were assumed supported on Hard Soils. Three cases of soil type variation at bent and abutment locations were assumed in this Chapter as indicated in Tables 4.2, 4.3 and 4.4. In these tables H, M, and S stand for Hard, Medium and Soft soils, respectively, and are represented by 6 degree of freedom spring sets applied at the foundation nodes as illustrated in Figure 3.12 with dynamic stiffness coefficients calculated as described in Section 3.4. The longitudinal locations where the soil types are defined in Figure 4.1 as LA (Left Abutment), RA (Right Abutment) and Bi (Bent i). Since each bent has two piers, this means that both piers are assumed supported on the same soil type. These variations were intended to provide different realistic geotechnical scenarios for highway bridges going through abrupt changes in topography, such as when spanning over bodies of water or canyons.

Table 4.2 Soil Type Variation Cases for Short Multi-Span Bridge Models

Soil Case	LA	B1	B2	RA
Hard	H	H	H	H
Medium	H	M	M	H
Soft	H	S	S	H

Table 4.3 Soil Type Variation Cases for Medium Multi-Span Bridge Models

Soil Case	LA	B1	B2	B3	B4	B5	RA
Hard	H	H	H	H	H	H	H
Medium	H	M	M	M	M	M	H
Soft	H	M	S	S	S	M	H

Table 4.4 Soil Type Variation Cases for Long Multi-Span Bridge Models

Soil Case	LA	B1	B2	B3	B4	B5	B6	B7	B8	B9	B10	B11	RA
Hard	H	H	H	H	H	H	H	H	H	H	H	H	H
Medium	H	M	M	M	M	M	M	M	M	M	M	M	H
Soft	H	M	M	S	S	S	S	S	S	S	M	M	H

### 4.3 Results for Bridge Pier Ductility Demands

The structural response variables of interest obtained from the SAP 2000 runs were the maximum bidirectional rotations  $\theta_2$  and  $\theta_3$  occurring at the plastic hinge locations as shown in Figure 3.16, from which the corresponding rotational ductility demands  $R_2$  and  $R_3$  were calculated using Eq. 3.26 and Eq. 3.27, respectively. Then, the maximum resultant rotational ductility demand  $R$  at each plastic hinge was calculated using Ec. 3.31. The pier rotational ductility demand was defined as the larger of the resultant rotational ductility demands occurring at any of the two plastic hinge locations in each

pier. For convenience, from this point forward pier rotational ductility demand and pier ductility demand will be considered analogous.

Piers were identified within a bridge model as a function of the bent where they are located and bents were counted from left to right along the longitudinal axis of the bridge; thus Bent 1 includes Piers 1 and 2, Bent 2 includes Piers 3 and 4, etc. For example, considering the short multi-span bridge model illustrated in Figure 3.7, Piers 1 and 2 are located on the left bent (Bent 1) and Piers 3 and 4 are located on the right bent (Bent 2).

#### 4.3.1 Short Multi-Span Bridge Models

Table 4.5 shows the mean, standard deviation (SD) and coefficient of variation (COV) values of the resultant pier ductility demands of short multi-span bridge models subjected to spatially varying seismic excitation. The mean and SD data in Table 4.5 is shown graphically for each soil case in Figures 4.3 to 4.4.

Table 4.5 Resultant Pier Ductility Demand on Short Multi-Span Bridge Models Subjected to Spatially Varying Seismic Excitation.

Bent	Pier	Hard Soil Case			Medium Soil Case			Soft Soil Case		
		Mean	SD	COV	Mean	SD	COV	Mean	SD	COV
B1	1	2.488	0.508	0.204	2.951	0.468	0.159	5.239	0.931	0.178
	2	2.491	0.497	0.200	2.962	0.452	0.153	5.197	0.966	0.186
B2	3	3.899	0.441	0.113	4.496	0.507	0.113	7.245	1.145	0.158
	4	3.873	0.458	0.118	4.496	0.447	0.099	7.156	1.089	0.152

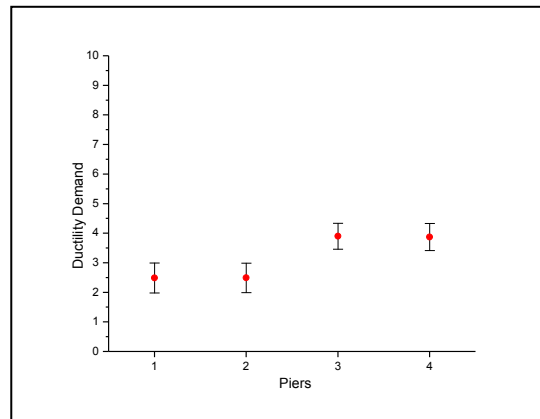


Figure 4.3 Pier Ductility Demand Statistics for Short Multi-Span Bridge Model Supported on Hard Soil Case.

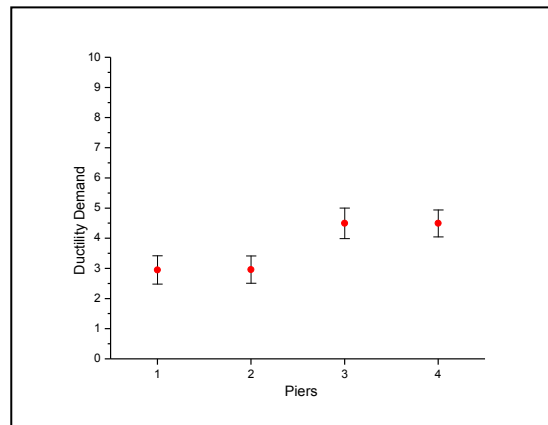


Figure 4.4 Pier Ductility Demand Statistics for Short Multi-Span Bridge Model Supported on Medium Soil Case.

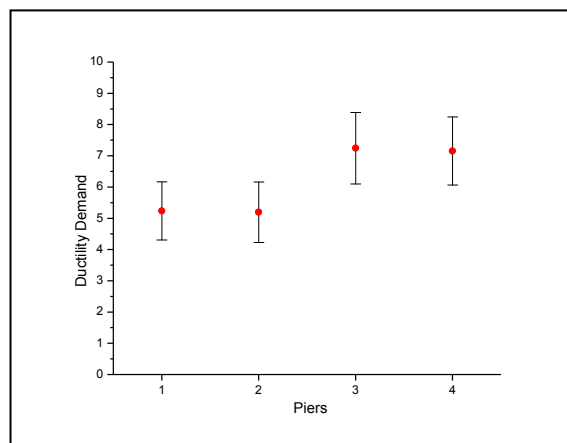


Figure 4.5 Pier Ductility Demand Statistics for Multi-Span Short Bridge Model Supported on Soft Soil Case.

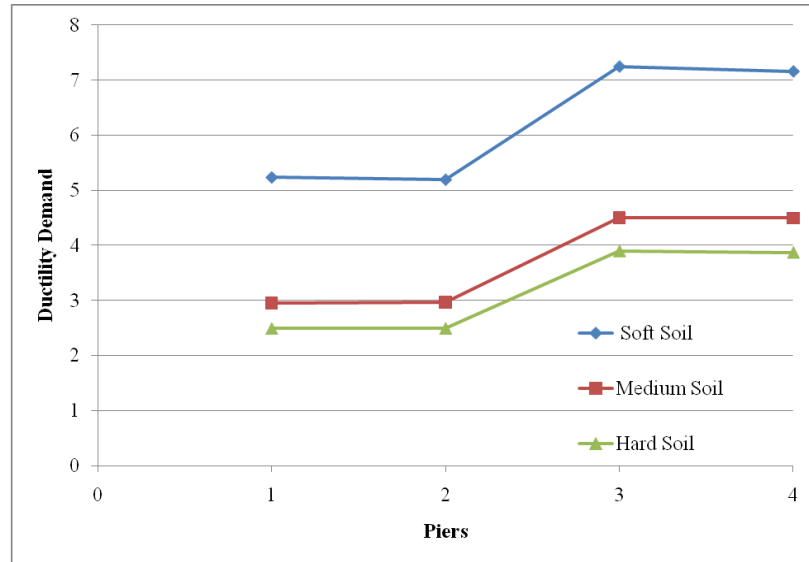


Figure 4.6 Mean Pier Ductility Demands on Short Multi-Span Bridge Model as a Function of the Soil Case.

Saxena (2000) generated similar graphs to the ones shown in Figures 4.3 to 4.5. Although she also considered a three-span bridge to generate such figures, the piers were skewed walls instead of circular columns and the superstructure was made of variable section steel girders instead of pre-stressed concrete box girders. Moreover, she considered only fully rigid soil conditions under the pier foundations and two soil case variations for soil response spectra compatibility purposes of the spatially variable time history records: constant Medium Soil conditions on all bridge supports and variable Medium to Soft Soil conditions. Despite the significant differences between Saxena's bridge and soil model and the bridge and soil model considered in this Chapter for short multi-span bridges, there is general agreement on the magnitude of the mean pier ductility demands for Saxena's constant Medium Soil conditions and the Medium Soil Case considered in this Chapter. For variable Medium to Soft Soil conditions, Saxena's pier ductility demand values are similar to the ones obtained in this Chapter for the Soft Soil Case.



From Table 4.5 it can be noticed that the SD values of the pier ductility demand exhibit a significant increase for the Soft Soil Case when compared to Hard and Medium Soil Cases; however, the COV values do not show similar increases. COV values vary in the range of 15% to 20% and 10% to 16% for Bents B1 and B2, respectively, with the maximum COV value occurring for the Hard Soil Case in Pier 1 of Bent B1 and for the Soft Soil Case in Pier 3 of Bent B2. Therefore, the uncertainty ranges in the prediction of the pier ductility demand values for a given bent remain practically invariant regardless of the soil case considered. Figure 4.6 shows mean values of the pier ductility demands for a short multi-span bridge as a function of the soil case. It can be observed that the relative difference between pier ductility demands for Hard and Medium Soil Cases is not significant when compared with the difference in pier ductility demands between Medium and Soft Soil Cases.

The maximum ductility demand that the pier can withstand at the plastic hinge, before reaching the residual flexural strength level (segment DE in Figure 3.14), can be obtained from Figure 3.15 by taking the ratio of the ultimate to idealized yield value of curvature (that is,  $0.02963/0.00582 = 5.091$ ). From Figure 4.6 it can be observed that only the ductility demands for piers supported on soft soils exceed the 5.091 threshold and thus significant structural distress at pier plastic zone locations is predicted for this case. From the practical standpoint, this finding identifies the need to modify the pier design given in Figure 4.2 in order to lower its ductility demand and improve its performance under the expected earthquake excitation if soft soil conditions are present under the pier foundation. From Figure 4.6 it can also be observed that the line segments

joining Piers 1 and 2 and Piers 2 and 3 are practically horizontal in the three graphs. This means that piers belonging to the same bent exhibit practically the same ductility demands regardless of the soil case considered.

Table 4.6 shows mean, SD and COV values of the pier ductility demands of short multi-span bridges subjected to uniform seismic excitation. Comparing the values in Tables 4.5 and 4.6, it can be observed that the mean pier ductility demands are higher when spatial variability of the seismic wave is considered, regardless of the soil case. However, the difference in the pier ductility demands of piers belonging to the same bent remains practically negligible. Therefore, for the case of short multi-span bridges, the similarity in pier ductility demands for piers belonging to the same bent may have little to do with the effects of spatial variability of the seismic excitation and more to do with how the piers interact within the three-dimensional response of the bridge model.

Table 4.6 Resultant Pier Ductility Demand on Short Multi-Span Bridge Models Subjected to Uniform Seismic Excitation.

Bent	Pier	Hard Soil Case			Medium Soil Case			Soft Soil Case		
		Mean	SD	COV	Mean	SD	COV	Mean	SD	COV
B1	1	2.248	0.490	0.218	2.598	0.450	0.173	3.902	0.453	0.116
	2	2.236	0.463	0.207	2.618	0.481	0.184	3.903	0.468	0.120
B2	3	3.674	0.286	0.078	4.230	0.470	0.111	5.706	0.856	0.150
	4	3.669	0.298	0.081	4.232	0.465	0.110	5.702	0.857	0.150

To study the differences in nonlinear response of bridge piers subjected to spatially varying and uniform seismic excitation, the concept of pier ductility index was

introduced in Section 3.3. Such index is obtained by dividing the mean values of the pier ductility demands caused by spatially variable seismic excitation by the mean values of the pier ductility demands caused by uniform seismic excitation. The values of pier ductility indexes for short multi-span bridges are shown in Table 4.7. It can be observed that all the pier ductility indexes are greater than 1.0, regardless of the soil case and that the pier ductility indexes are the greatest for short multi-span bridges when the piers are supported on soft soil. It can also be observed that the ductility indexes are very similar for piers supported on hard and medium soils. Therefore, ignoring spatial variability in the seismic waves, even in short multi-span bridges can cause an underestimation of up to 36% on the pier ductility demand if the piers are located on soft soils. For piers located on hard and medium soils the underestimation of the pier ductility demand can be as high as 21% if spatial variability in the seismic wave is ignored. Sextos et al (2003) reported an average underestimation of 25% of the pier ductility demand when spatial variability of the seismic excitation is ignored, which is in agreement with these results. The data in Table 4.7 is shown graphically in Figure 4.7.

It can be observed in Figure 4.7 that the ductility index values are practically the same when the bridge piers are supported on hard and medium soils and that the ductility index values are the highest when the piers are supported on soft soils. Saxena (2000) reported typical ductility indexes in the range of 1.0 to 1.5 for short and medium span bridges for piers supported on the same soil type, which is in agreement with the ductility index values shown in Figure 4.7.

Table 4.7 Mean Pier Ductility Index Values for Short Multi-Span Bridge Models.

Bent	Pier	Hard Soil Case	Medium Soil Case	Soft Soil Case
B1	1	1.127	1.149	1.357
	2	1.186	1.197	1.345
B2	3	1.167	1.162	1.283
	4	1.214	1.213	1.269

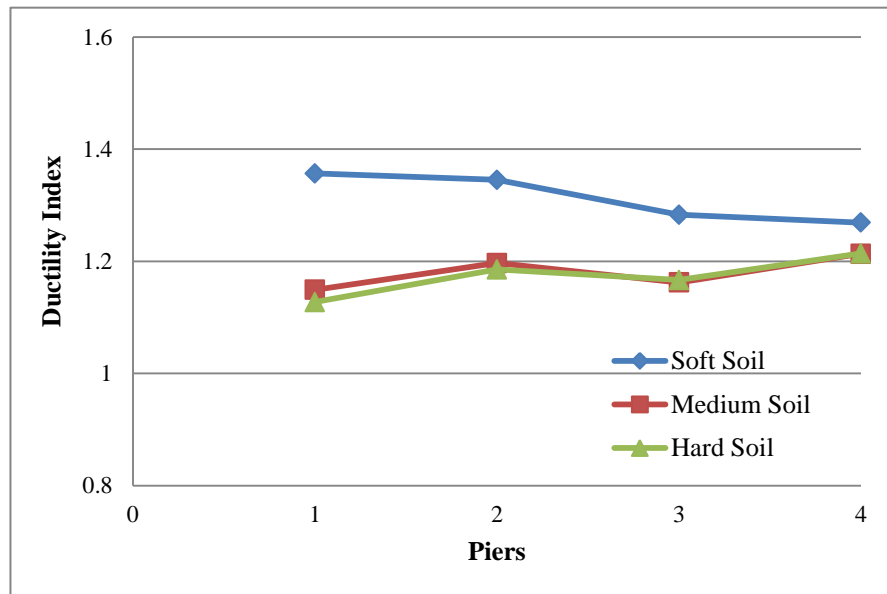


Figure 4.7 Mean Pier Ductility Indexes for Short Multi-Span Bridge Model

Up to this point, only resultant pier ductility demand results have been presented, as defined by Eq. 3.31. In order to obtain a better understanding of the biaxial bending behavior of the piers and thus the three-dimensional response of the bridge, the mean values of the ductility demands in the longitudinal ( $R_2$ ) and transverse directions ( $R_3$ ) of the bridge for piers supported on hard, medium and soft soils, respectively are plotted in Figures 4.8 to 4.10. It can be observed in these figures that regardless of the soil case, the ductility demands in the transverse direction are negligible for Piers 1 and 2 (Bent B1),

while the longitudinal ductility demand remains practically invariant for Bents B1 and B2. However, the ductility demands in the transverse direction become significant in Piers 3 and 4 (Bent B2). In fact, the pier ductility demands in the transverse and longitudinal are practically the same in Bent B2, when considering Hard and Medium Soil Cases and the transverse ductility demand becomes significantly larger than the longitudinal ductility demand when considering the Soft Soil Case.

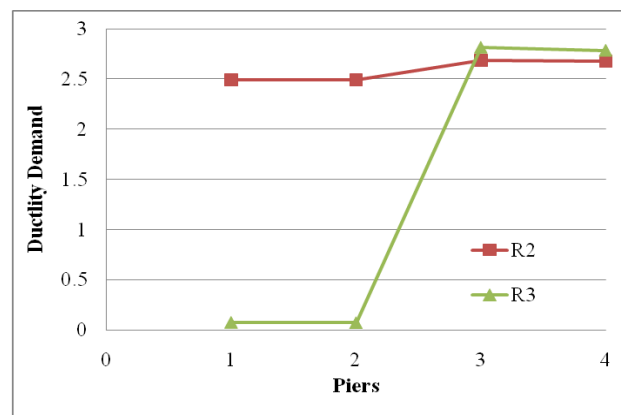


Figure 4.8 Longitudinal ( $R_2$ ) and Transverse ( $R_3$ ) Mean Pier Ductility Demand Values in Short Multi-Span Bridge Model Supported on Hard Soil Case.

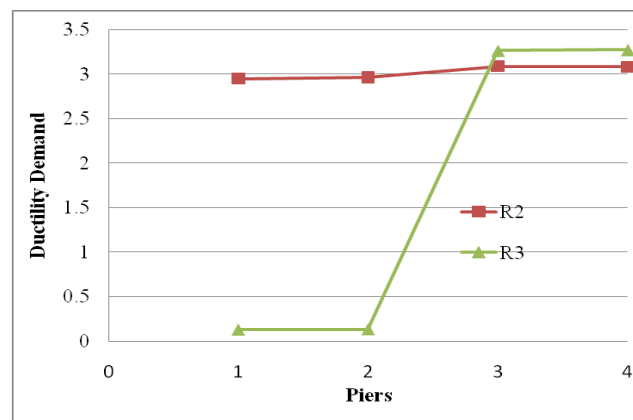


Figure 4.9 Longitudinal ( $R_2$ ) and Transverse ( $R_3$ ) Mean Pier Ductility Demand Values in Short Multi-Span Bridge Model Supported on Medium Soil Case.

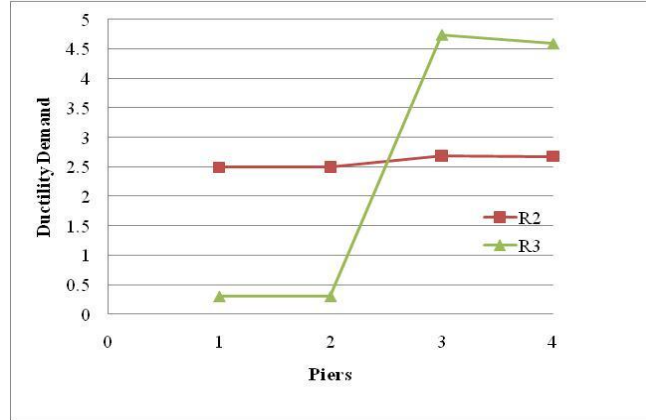


Figure 4.10 Longitudinal ( $R_2$ ) and Transverse ( $R_3$ ) Mean Pier Ductility Demand Values in Short Multi-Span Bridge Model Supported on Soft Soil Case.

The negligible transverse ductility demand in Bent B1 together with the practically invariant longitudinal ductility demand in Bents B1 and B2 was observed only in short multi-span bridge models. One possible reason is the significant difference in the lateral bending stiffness between the superstructure and the bents. The bridge superstructure was assumed to remain elastic in all bridge models and thus its lateral bending stiffness remains constant under seismic response. Moreover, for a given superstructure cross section, the shorter the span, the larger the lateral bending stiffness. As plastic hinges develop on the ends of the bridge piers, the lateral bending stiffness of each bent decreases, therefore further increasing the relative difference between the lateral bending stiffness of the superstructure and the bents. Thus, the superstructure will tend to behave as a shear diaphragm subjected to rigid body translations and rotations when excited by the multi component seismic wave. Under this possible scenario, the negligible transverse ductility demand in Bent B1 could be due to its proximity to the shear center of the diaphragm.

As established in Section 3.3, the bridge pier models considered two plastic hinge locations: one at the bottom (coinciding with the pier-foundation interface) and one at the

top (coinciding with the pier- cap beam interface). In this section, only the maximum ductility demand between these two plastic hinges was reported per pier; however, up to this point no information was given of which of the two hinges exhibited the maximum value. Such information can be summarized in the following facts:

1. When considering the Soft Soil Case, the top plastic hinges of the piers exhibited the largest resultant ductility demand, regardless of whether the seismic excitation was uniform or spatially varying.
2. When considering the Hard Soil Case, the bottom plastic hinges of the piers exhibited the largest ductility demands, regardless of whether the seismic excitation was uniform or spatially varying.
3. When considering the Medium Soil Case, the top or bottom hinge exhibited the largest ductility demand, depending on the seismic load case considered, regardless of whether the seismic excitation was spatially variable or uniform.

Saxena (2000) and Kim and Feng (2003) also considered bridge pier models with plastic hinges located at both end zones. However, their published research did not provide results on the differences in pier ductility demands exhibited by the plastic hinges located in the same pier as a function of the soil type and the type of seismic excitation (spatially varying vs. uniform).

Finally, based on the results of this section, the following general conclusions can be observed for short multi-span bridge models:

1. The pier ductility demands are highest when considering the Soft Soil Case and lowest when considering the Hard Soil Case, regardless of the pier location within the bridge or the type of seismic excitation (spatially variable or uniform).
2. Spatial variable seismic excitation generates higher pier ductility demands than uniform seismic excitation, regardless of the soil case considered.

#### **4.3.2 Medium Multi-Span Bridge Models**

Table 4.8 shows the statistics on pier ductility demands for medium multi-span bridge models. The mean and SD data is shown graphically for each soil case in Figures 4.11 to 4.13. It can be observed in Table 4.8 that the SD values are similar to the short multi-span bridge model values when considering the Hard Soils Case. It can also be observed in Table 4.8 that the SD and COV values are the greatest for piers located near the midspan of the bridge regardless of the soil case. Therefore, the uncertainty on the ductility demand values is the greatest for piers at such locations. Table 4.8 also shows that piers belonging to the same bent exhibit practically identical pier ductility demands, regardless of the soil case.

Figure 4.14 shows mean values of the pier ductility demands for medium multi-span bridges models as a function of the soil case. It can be observed that pier ductility demand variation along the span of the bridge is not significant, regardless of the soil case under consideration. It can also be observed that pier ductility demands are highest when considering the Soft Soil Case and that the relative difference between pier ductility demands for the Hard and Medium Soil Cases is small when compared to the relative difference between the Medium and Soft Soil cases. However, when compared to the



response of short multi-span bridge models (see Figure 4.7) the relative difference in pier ductility demands for bridges considering Hard and Medium Soil cases is greater for the bridge models with more spans. It can also be observed that ductility demands on all piers for the Soft Soil Case exceed the 5.09 threshold value and thus, significant structural damage is predicted at the pier plastic zone locations if the piers are not redesigned to reduce their ductility demand. This also occurred for piers supported on soft soils in short multi-span bridges.

Table 4.8 Resultant Pier Ductility Demand on Medium Multi-Span Bridge Models Subjected to Spatially Varying Seismic Excitation.

Bent	Pier	Hard Soil Case			Medium Soil Case			Soft Soil Case		
		Mean	SD	COV	Mean	SD	COV	Mean	SD	COV
B1	1	3.873	0.461	0.119	4.533	0.601	0.133	5.907	0.857	0.145
	2	3.828	0.483	0.126	4.522	0.597	0.132	5.796	0.773	0.133
B2	3	3.669	0.539	0.147	4.250	0.791	0.186	5.851	0.759	0.130
	4	3.693	0.571	0.155	4.305	0.744	0.173	5.653	0.757	0.134
B3	5	3.733	0.466	0.125	4.258	0.883	0.207	5.679	1.062	0.187
	6	3.724	0.515	0.138	4.225	0.992	0.235	5.510	0.911	0.165
B4	7	3.687	0.426	0.116	4.298	0.926	0.215	5.686	1.008	0.177
	8	3.674	0.462	0.126	4.354	0.845	0.194	5.435	0.878	0.162
B5	9	3.982	0.547	0.137	4.475	0.698	0.156	5.902	0.724	0.123
	10	3.952	0.547	0.138	4.516	0.737	0.163	5.804	0.716	0.123

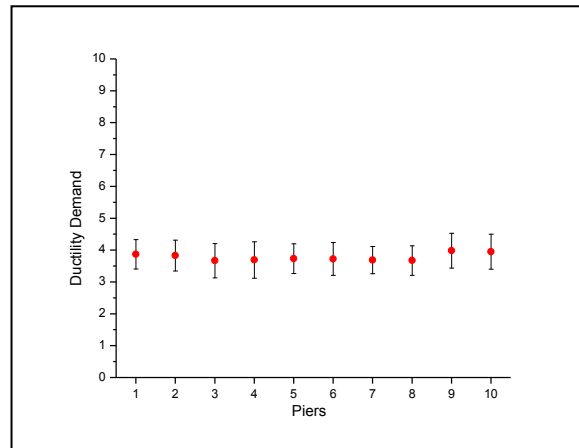


Figure 4.11 Pier Ductility Demand Statistics for Medium Multi-Span Bridge Model Supported on Hard Soil Case.

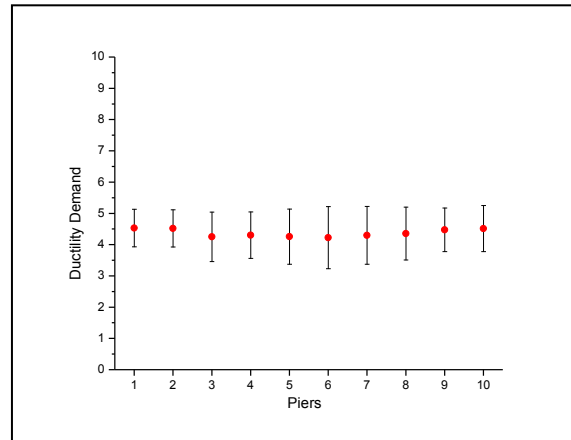


Figure 4.12 Pier Ductility Demand Statistics for Medium Multi-Span Bridge Model Supported on Medium Soil Case.

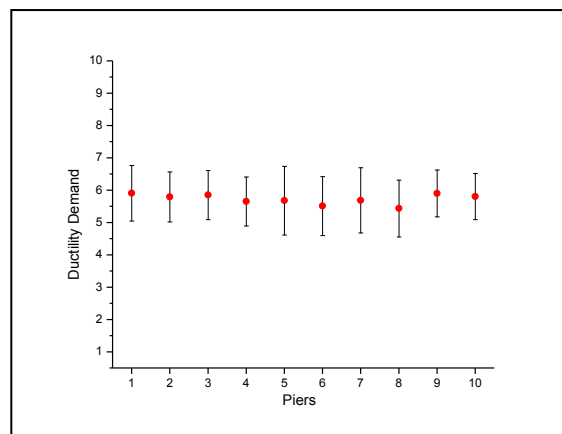


Figure 4.13 Pier Ductility Demand Statistics for Medium Multi-Span Bridge Model Supported on Soft Soil Case.

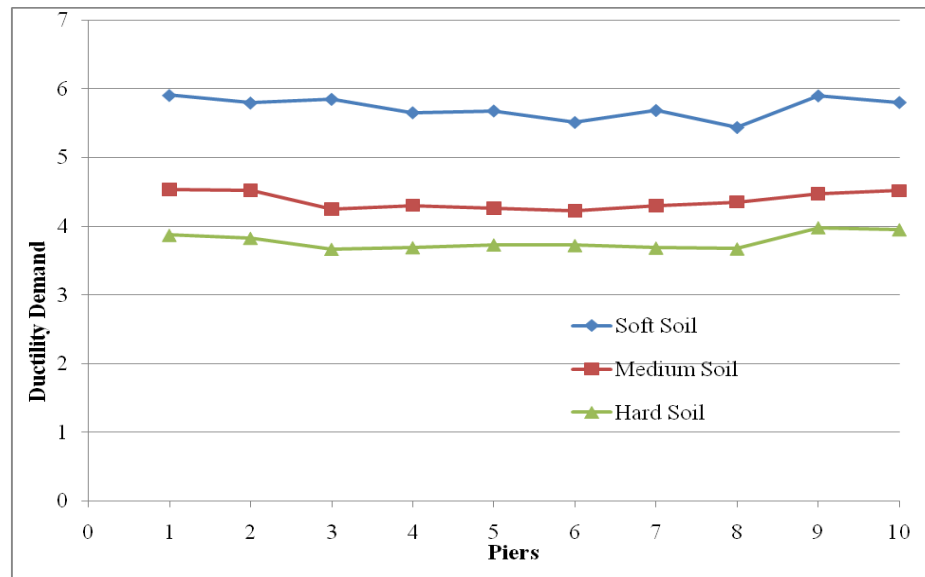


Figure 4.14 Mean Pier Ductility Demands on Medium Multi-Span Bridge Model as a Function of Soil Case.

Table 4.9 shows the pier ductility demand statistics for medium multi-span bridge models under uniform seismic excitation. It can be observed that the pier ductility demand also remains practically the same for piers belonging to the same bent, which was also the case when considering spatial variability of the seismic excitation (see Table 4.8). Moreover, Table 4.9 shows lower pier ductility demands in interior Bents B2 to B4 and higher pier ductility demands for exterior Bents B1 and B5 when compared to the values exhibited in Table 4.8, the effects of which can better be visualized using ductility indexes. It can also be observed that the 5.09 ductility demand threshold is exceeded only on the piers of exterior Bents B1 and B5 when considering the Soft Soil Case.

Table 4.9 Resultant Pier Ductility Demand on Medium Multi-Span Bridge Models Subjected to Uniform Seismic Excitation.

Bent	Pier	Hard Soil Case			Medium Soil Case			Soft Soil Case		
		Mean	SD	COV	Mean	SD	COV	Mean	SD	COV
B1	1	4.393	0.744	0.169	4.965	0.619	0.125	5.497	0.594	0.108
	2	4.374	0.746	0.171	4.952	0.625	0.126	5.524	0.595	0.108
B2	3	3.144	0.584	0.186	3.365	0.951	0.283	4.095	0.773	0.189
	4	3.155	0.577	0.183	3.414	0.954	0.279	4.091	0.777	0.190
B3	5	3.086	0.612	0.198	3.104	0.813	0.262	4.005	0.750	0.187
	6	3.070	0.603	0.196	3.100	0.814	0.263	3.999	0.753	0.188
B4	7	3.121	0.421	0.135	3.302	0.733	0.222	4.168	0.767	0.184
	8	3.150	0.482	0.153	3.318	0.714	0.215	4.159	0.772	0.186
B5	9	4.369	0.599	0.137	4.892	0.895	0.183	5.446	0.961	0.176
	10	4.379	0.629	0.144	4.904	0.877	0.179	5.441	0.965	0.177

Figure 4.15 shows mean values of the mean pier ductility indexes for a medium multi-span bridge model as a function of the soil case (see also Table 4.10). Mean pier ductility index values less than one can be observed for piers located in exterior bents, which means that pier ductility demand predicted for spatially varying seismic excitation is less than the one predicted by uniform seismic excitation. However, for pier located in interior bents the reverse is true. Therefore, neglecting the spatial variation of the seismic wave will produce conservative effects on piers located on exterior bents and un-conservative effects for all other piers. The underestimation on the pier ductility demand when ignoring spatial variability of the seismic wave can be as high as 24%, 44% and 47% when considering Hard, Medium and Soft Soil Cases, respectively. It can also be

observed in Figure 4.15 that the ductility index range of 1.0 to 1.5 reported by Saxena (2000) is still valid for medium multi-span bridge models.

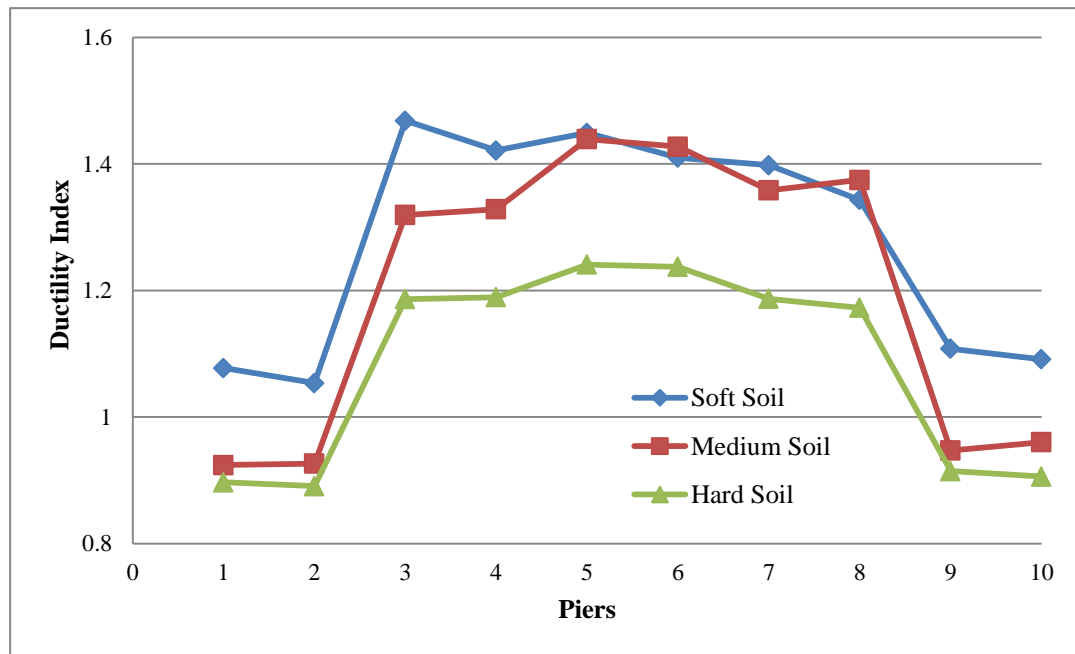


Figure 4.15 Mean Pier Ductility Indexes for Medium Multi-Span Bridge Model

When compared to short multi-span bridge models (see Figure 4.7), it can be observed that the increase in bridge length generates an increase in the ductility index for piers in interior bents only and that the relative difference in the ductility indexes for Hard and Medium Soil Cases remains small only on pier located on exterior bents, with the difference becoming significant for piers located in interior bents. In fact, although the maximum pier ductility index still occurs under the Soft Soil Case, the relative difference between ductility indexes for medium multi-span bridge models for Medium and Soft Soil Cases becomes small for piers located around the midspan. For the case of short multi-span bridge models, this relative difference remained high in all piers, which

points to the fact that ignoring the effects of spatial variability of the seismic excitation as the span of the bridge increases will generate similar un-conservative effects for medium multi-span bridges under Soft and Medium Soil Cases.

Table 4.10 Mean Pier Ductility Index Values for Medium Multi-Span Bridge Models.

Bent	Pier	Hard Soil Case	Medium Soil Case	Soft Soil Case
B1	1	0.897	0.924	1.077
	2	0.891	0.926	1.054
B2	3	1.186	1.319	1.468
	4	1.189	1.328	1.421
B3	5	1.241	1.439	1.449
	6	1.237	1.427	1.410
B4	7	1.187	1.358	1.398
	8	1.173	1.375	1.343
B5	9	0.915	0.947	1.108
	10	0.906	0.960	1.091

Figures 4.16 to 4.18 present mean values of the pier ductility demands in the longitudinal ( $R_2$ ) and transverse directions ( $R_3$ ) of the medium multi-span bridge models for Hard, Medium and Soft Soil Cases, respectively. A sharp contrast with the behavior exhibited by short multi-span bridge models (see Figures 4.8 to 4.10) can be observed as a result of the increase in the bridge length and on the number of bents. As the length of the bridge increased, the lateral bending stiffness of the superstructure was reduced proportionally, while the individual bents increased in number and continued to exhibit loss in their lateral bending stiffness due to the formation of plastic hinges at the pier

ends. As a result, the difference in lateral bending stiffness between the superstructures and bents was reduced as the bridge length increased and thus, the shear diaphragm effect of the superstructure observed in short multi-span bridge models practically vanishes in medium multi-span bridge models, allowing for a full engagement of the transverse plastic hinge action on all the piers, as the bridge model was excited by the longitudinal and transverse multi-component seismic wave.

Figure 4.16 shows the variation of  $R_2$  and  $R_3$  for piers in medium multi-span bridge models on Hard Soil Case. Little variation in  $R_2$  is observed along the length of the bridge, which was also the case for small multi-span bridge models; however, the value of  $R_3$  is no longer insignificant and such value is now on the same order of magnitude as  $R_2$  and exhibits similar degree of variation along the span. The variation of  $R_2$  and  $R_3$  for medium multi-span bridge models on Medium Soil Case is shown in Figure 4.17. Except for the fact that the ductility demand increases, both  $R_2$  and  $R_3$  show similar variation along the span when compared to medium bridge models with piers on hard soil case.

Figure 4.18 shows the variation of  $R_2$  and  $R_3$  for a medium multi-span bridge model with piers on Soft Soil Case. It can be observed that the maximum ductility demand value occurs in the longitudinal direction, which was also the case for piers on Hard and Medium Soil Cases, although the location of such value varied depending on the soil case. Maximum ductility demand in the transverse direction was observed in short multi-span bridge models with piers on Soft Soil Case (see Figure 4.10).

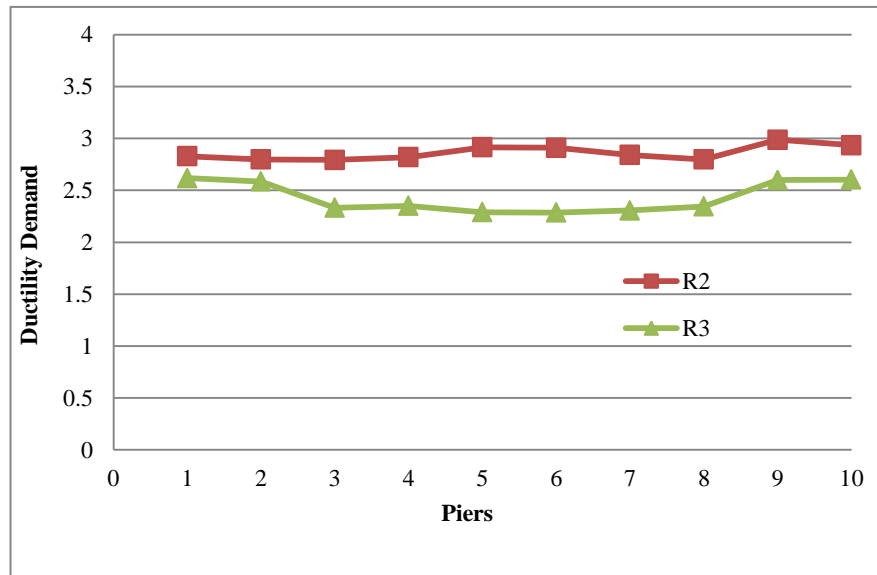


Figure 4.16 Longitudinal ( $R_2$ ) and Transverse ( $R_3$ ) Mean Pier Ductility Demands in Medium Multi-Span Bridges Model Supported on Hard Soil Case.

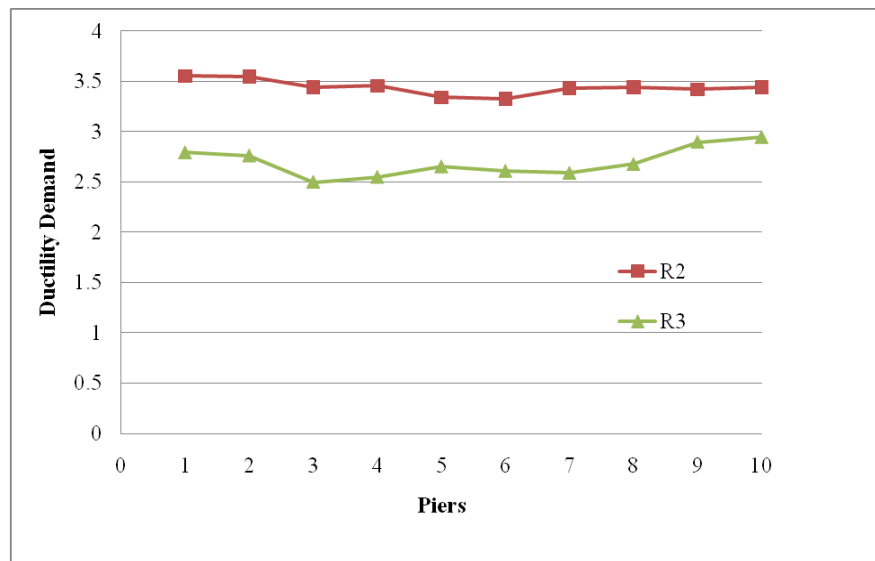


Figure 4.17 Longitudinal ( $R_2$ ) and Transverse ( $R_3$ ) Mean Pier Ductility Demands in Medium Multi-Span Bridge Model Supported on Medium Soil Case.



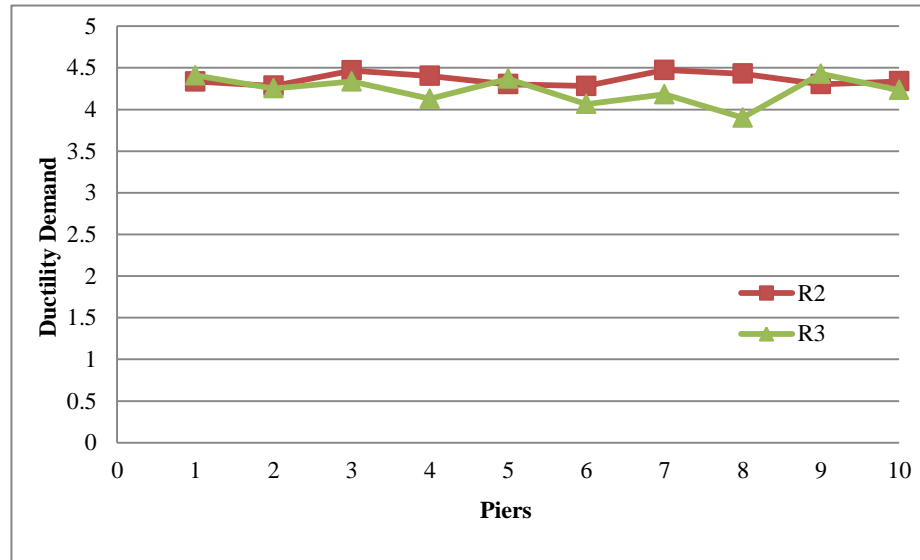


Figure 4.18 Longitudinal ( $R_2$ ) and Transverse ( $R_3$ ) Mean Pier Ductility Demands in Medium Multi-Span Bridge Model Supported on Soft Soil Case.

In regards to the identification of the plastic hinge that exhibited the maximum ductility demand within a given pier, Facts 1 to 3 established in page 151 for short multi-span bridges were also found to apply to medium multi-span bridges. Thus, the location of the plastic hinge that exhibits the maximum ductility demand within a given pier seems to be a function of the soil case and not the bridge length.

Finally, based on the results of this section, the following general conclusions can be observed for medium multi-span bridge models:

1. Pier ductility demands are in general higher than the ones occurring in short multi-span bridge models, regardless of the type of seismic excitation (spatially varying or uniform) and the soil case.

2. Except for piers located in interior bents, the spatially variable seismic excitation generates higher pier ductility demands than uniform seismic excitation, regardless of the soil case considered.

### 4.3.3 Long Multi-Span Bridge Models

Table 4.11 shows the statistics on pier ductility demands for long bridge models. The same data is shown graphically for each soil case in Figures 4.19 to 4.21. It can be observed that the pier ductility demand and SD values increase significantly and the COV values exhibit relatively little variability, regardless of the soil case, when compared to the short and medium multi-span bridge model values. It can also be observed that the SD and ductility demand values are the greatest for piers located near the mid span of the bridge. The COV value ranges are observed to be 15% to 28%, 16% to 36% and 12% to 24% for the Hard, Medium and Soft Soil Cases, respectively. Therefore, the degree of uncertainty on the pier ductility demand values exhibit relatively little change due to the increase in length of the bridge and changes in the soil conditions. Moreover, ductility demands for piers belonging to the same bent exhibit significant differences, where the smallest difference occurs under the Hard Soil Case and the greatest under the Soft Soil Case. This is a departure from the behavior observed by short and medium multi-span bridges models, where such difference was insignificant, regardless of the soil case.

Figure 4.22 shows mean values of the pier ductility demands for long multi-span bridge models as a function of the soil case. It can be observed that the degree of variation of the pier ductility demand along the length of the bridge depends on the soil case. The degree of variation is smallest when the bridge is on Hard and Medium Soil

Cases and largest when the bridge is on the Soft Soil Case. In fact, for long multi-span bridge models under spatially variable seismic excitation the pier ductility demands exhibit small differences in values when the bridge is on Medium and Hard Soil Cases. As was the case for short and medium multi-span bridge models, the highest ductility demand in long multi-span bridge models occurs when the piers are on the Soft Soil Case and the lowest ductility demand occurs when the piers are on the Hard Soil Case. However, the relative difference in the pier ductility demands for medium and long multi-span bridge models on Hard and Medium Soil Cases is small, compared to difference that is observed when such bridges are on the Soft Soil Case. It can also be observed that the maximum ductility demands in long multi-span bridge models occur in the piers located around the mid span of the bridge, regardless of the soil case.

Table 4.12 shows the pier ductility demand statistics for long multi-span bridge models under uniform seismic excitation. It can be observed that the pier ductility demand remains practically the same for piers belonging to the same bent, which was not the case when considering spatial variability of the seismic excitation (see Table 4.11). Thus, spatial variability of the seismic excitation affects the ductility demand distribution for piers located on the same bent for long multi-span bridge models, regardless of the type of soil. Moreover, uniform seismic excitation will generate maximum ductility demands on the piers close to the mid span, as was the case for spatially varying seismic excitation. The degree of the uncertainty on the pier ductility demand measured from the COV values is observed to exhibit relatively little change, regardless of the soil case considered, as was the case when considering spatially varying seismic excitation.

Table 4.11 Resultant Pier Ductility Demand on Long Multi-Span Bridge Models Subjected to Spatially Varying Seismic Excitation.

Bent	Pier	Hard Soil Case			Medium Soil Case			Soft Soil Case		
		Mean	SD	COV	Mean	SD	COV	Mean	SD	COV
B1	1	3.849	0.650	0.169	4.257	0.692	0.163	6.187	0.971	0.157
	2	3.895	0.613	0.157	4.285	0.692	0.161	6.002	0.986	0.164
B2	3	3.643	1.008	0.277	4.005	1.459	0.364	4.548	1.065	0.234
	4	3.673	0.996	0.271	4.093	1.400	0.342	4.572	0.950	0.208
B3	5	3.397	0.879	0.259	3.507	0.663	0.189	5.919	1.025	0.173
	6	3.520	0.912	0.259	3.574	0.638	0.179	6.191	1.122	0.181
B4	7	3.903	0.828	0.212	3.950	0.805	0.204	6.730	1.364	0.203
	8	4.015	0.891	0.222	3.970	0.775	0.195	7.222	1.334	0.185
B5	9	4.482	0.676	0.151	4.760	1.193	0.251	7.658	1.456	0.190
	10	4.551	0.710	0.156	4.794	1.152	0.240	8.052	1.481	0.184
B6	11	4.891	0.965	0.197	4.884	1.023	0.209	8.098	1.722	0.213
	12	4.895	0.899	0.184	4.977	1.032	0.207	8.480	1.715	0.202
B7	13	4.696	0.784	0.167	4.575	1.024	0.224	7.791	1.432	0.184
	14	4.774	0.890	0.186	4.698	1.060	0.226	8.175	1.402	0.171
B8	15	3.847	0.668	0.174	4.253	1.428	0.336	6.707	1.368	0.204
	16	3.814	0.686	0.180	4.407	1.536	0.349	7.087	1.328	0.187
B9	17	3.343	0.613	0.183	3.616	0.855	0.236	5.637	1.342	0.238
	18	3.451	0.625	0.181	3.709	0.881	0.238	5.920	1.210	0.204
B10	19	3.379	0.681	0.202	3.791	1.004	0.265	5.966	1.081	0.181
	20	3.415	0.656	0.192	3.848	0.972	0.253	5.996	0.969	0.162
B11	21	4.005	0.671	0.168	4.241	0.984	0.232	7.238	0.940	0.130
	22	3.997	0.667	0.167	4.355	0.948	0.218	7.139	0.840	0.118

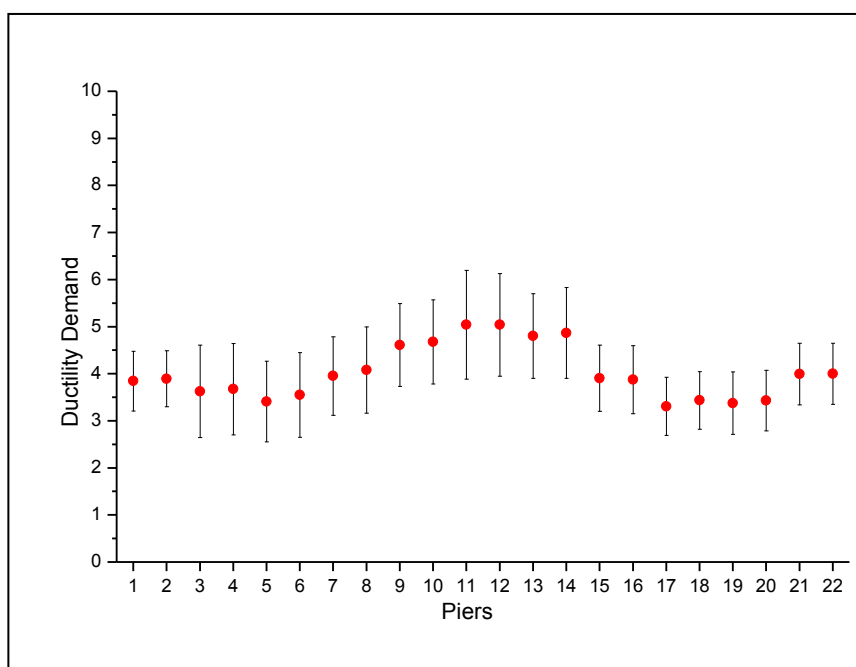


Figure 4.19 Pier Ductility Demand Statistics for Long Multi-Span Bridge Model Supported on Hard Soil Case.

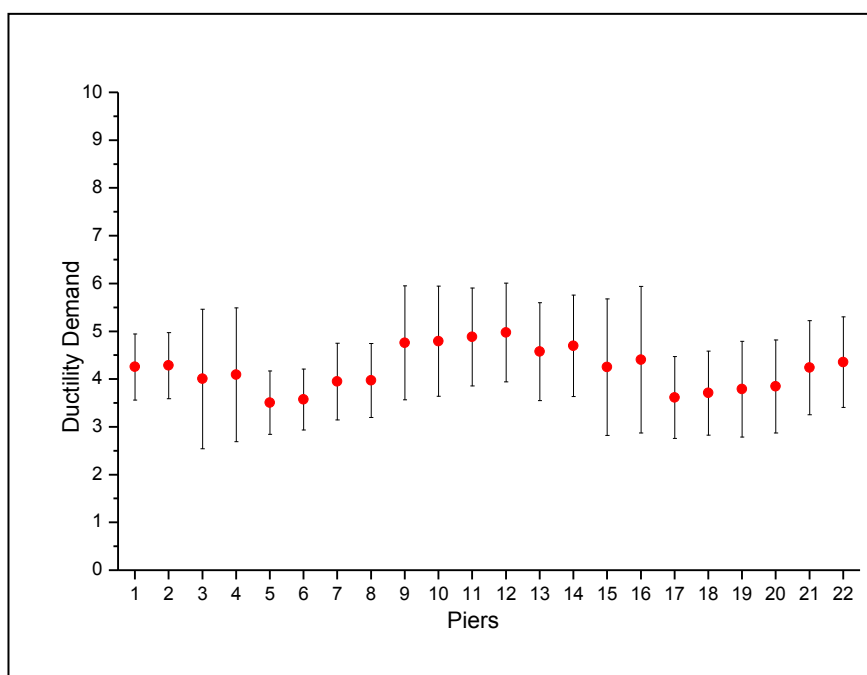


Figure 4.20 Pier Ductility Demand Statistics for Long Multi-Span Bridges Model Supported on Medium Soil Case.

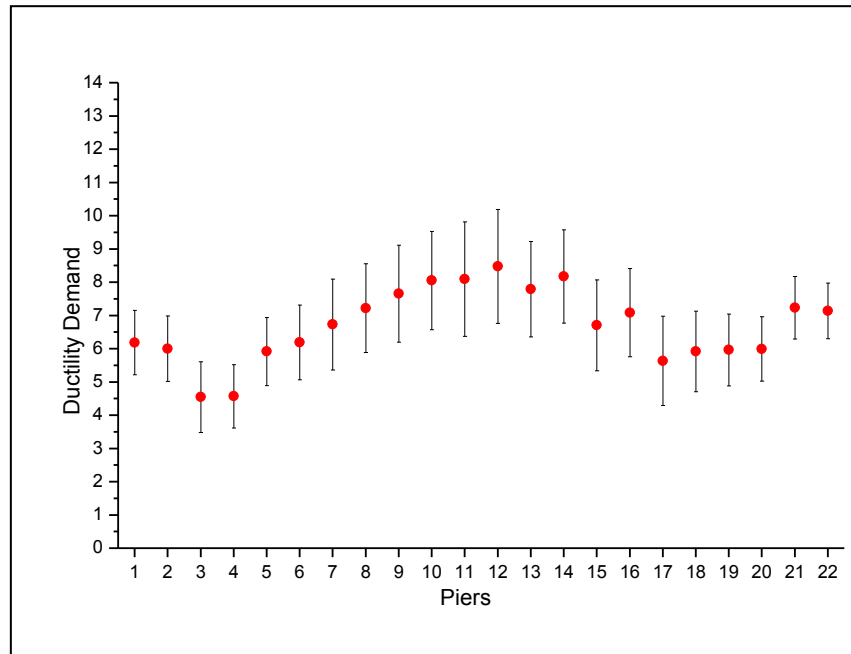


Figure 4.21 Pier Ductility Demand Statistics for Long Multi-Span Bridge Model Supported on Soft Soil Case.

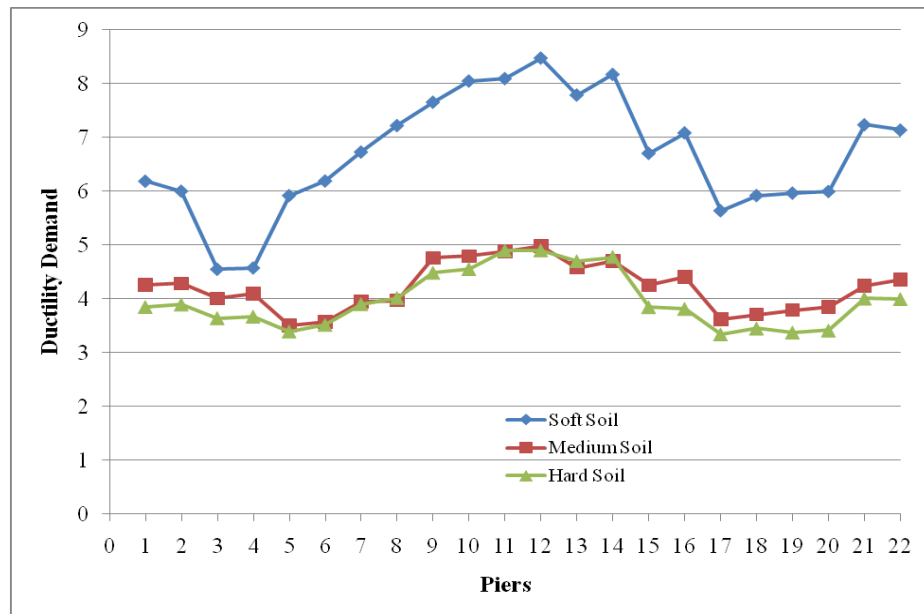


Figure 4.22 Mean Pier Ductility Demands on Long Multi-Span Bridge Models as a Function of Soil Case.

Table 4.12 Resultant Pier Ductility Demand on Long Multi-Span Bridge Models Subjected to Uniform Seismic Excitation.

Bent	Pier	Hard Soil Case			Medium Soil Case			Soft Soil Case		
		Mean	SD	COV	Mean	SD	COV	Mean	SD	COV
B1	1	3.470	0.740	0.213	3.852	0.662	0.172	5.364	0.915	0.171
	2	3.505	0.741	0.211	3.837	0.648	0.169	5.346	0.882	0.165
B2	3	2.899	0.690	0.238	3.354	0.486	0.145	3.818	0.841	0.220
	4	2.936	0.701	0.239	3.310	0.512	0.155	3.783	0.788	0.208
B3	5	2.965	0.617	0.208	3.353	0.560	0.167	3.981	0.780	0.196
	6	3.012	0.678	0.225	3.346	0.557	0.166	3.988	0.750	0.188
B4	7	3.492	0.596	0.171	3.898	0.518	0.133	5.255	0.966	0.184
	8	3.499	0.648	0.185	3.859	0.502	0.130	5.246	0.998	0.190
B5	9	4.099	0.640	0.156	4.595	0.677	0.147	6.640	1.346	0.203
	10	4.085	0.651	0.159	4.587	0.675	0.147	6.639	1.375	0.207
B6	11	4.338	0.633	0.146	4.996	0.830	0.166	7.310	1.405	0.192
	12	4.366	0.649	0.149	4.996	0.825	0.165	7.306	1.415	0.194
B7	13	4.091	0.615	0.150	4.585	0.687	0.150	6.595	1.321	0.200
	14	4.069	0.612	0.150	4.598	0.685	0.149	6.593	1.311	0.199
B8	15	3.511	0.630	0.179	3.880	0.495	0.128	5.238	0.964	0.184
	16	3.495	0.590	0.169	3.910	0.493	0.126	5.247	0.928	0.177
B9	17	2.996	0.631	0.211	3.211	0.609	0.190	3.943	0.745	0.189
	18	3.003	0.590	0.196	3.275	0.557	0.170	3.926	0.755	0.192
B10	19	2.972	0.742	0.250	3.355	0.604	0.180	3.805	0.747	0.196
	20	2.943	0.737	0.250	3.407	0.585	0.172	3.835	0.795	0.207
B11	21	3.468	0.707	0.204	3.842	0.507	0.132	5.565	1.038	0.187
	22	3.426	0.707	0.206	3.860	0.506	0.131	5.596	1.082	0.193

Figure 4.23 and Table 4.13 shows mean values of the pier ductility indexes for a long multi-span bridge models as a function of the soil case. Pier ductility indexes are all greater than one, which means that pier ductility demand predicted for spatially varying seismic excitation is greater than the one predicted by uniform seismic excitation for all piers, regardless of the soil case considered. Therefore, neglecting the spatial variation of the seismic wave will produce un-conservative effects for all piers. The underestimation on the pier ductility demand when ignoring spatial variability of the seismic wave can be as high as 29%, 26% and 64% when the bridge was on Hard, Medium and Soft Soil Cases, respectively. In all cases, the largest underestimation occurred in piers located away from the midspan, regardless of the soil case. This is a departure of the behavior observed in medium multi-span bridge models, where the largest underestimation of the pier ductility demand occurred in piers located near the midspan. A possible reason for this departure is the change in the superstructure lateral stiffness, as will be discussed in some detail next.

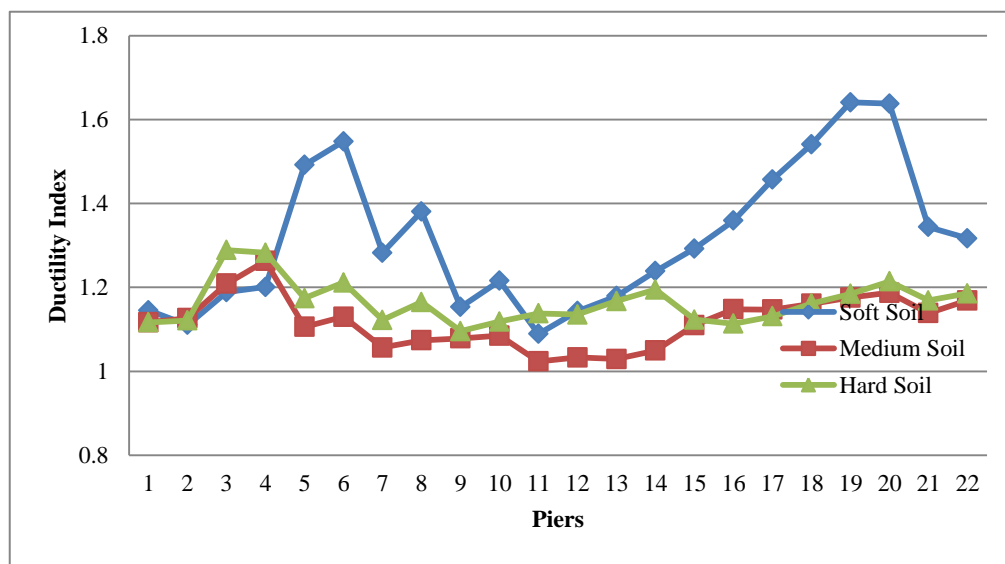


Figure 4.23 Mean Pier Ductility Indexes for Long Multi-Span Bridge Models



Figures 4.24 to 4.26 show the relative variation of the pier ductility demands in the longitudinal ( $R_2$ ) and transverse ( $R_3$ ) direction along the span of the bridge as a function of the soil case. It can be observed in these figures that the degree of variability of  $R_2$  depends on the soil case, where maximum and minimum degree of variability occur when the bridge is on Soft and Hard Soil Cases, respectively. The degree of variability of  $R_3$  is relatively less dependent on the soil case. Maximum ductility demand occurs in the transverse direction on the piers located around the midspan of the bridge, regardless of the soil case. This is a departure of the behavior observed in medium multi-span bridge models, where maximum ductility demand occurred in the longitudinal direction. One probable reason for the predominance of the transverse ductility demand in long multi-span bridge models is the fact that the lateral bending stiffness of the superstructure decreases as the length of the bridge increases. Thus, long multi-span bridge models present the least lateral bending stiffness when compared to the short and medium multi-span bridge models and as a result, transverse response is maximized under a multi-component seismic wave.

As can be observed in Figures 4.24 and 4.26 there is very little difference in the degree of variability and the values of the ductility demands in the transverse and longitudinal direction for long multi-span bridge models supported on Hard and Medium Soil Cases. Maximum degree of variability and maximum values of the ductility demands in the transverse and longitudinal direction occurred when piers are supported on Soft Soil Case.

Finally, it can be observed in Figure 4.22 that the 5.09 pier ductility demand threshold is exceeded only when the long multi-span bridge models were supported on the Soft Soil Case and subjected to spatially varying seismic excitation.

Table 4.13 Mean Pier Ductility Index Values for Long Multi-Span Bridges Models.

Bent	Pier	Hard Soil Case	Medium Soil Case	Soft Soil Case
B1	1	1.116	1.117	1.145
	2	1.121	1.126	1.110
B2	3	1.289	1.209	1.189
	4	1.283	1.263	1.201
B3	5	1.174	1.106	1.492
	6	1.212	1.130	1.548
B4	7	1.122	1.057	1.283
	8	1.165	1.074	1.381
B5	9	1.096	1.079	1.153
	10	1.119	1.085	1.216
B6	11	1.138	1.024	1.089
	12	1.135	1.033	1.144
B7	13	1.168	1.029	1.179
	14	1.195	1.050	1.239
B8	15	1.123	1.110	1.292
	16	1.114	1.148	1.359
B9	17	1.131	1.147	1.457
	18	1.162	1.161	1.541
B10	19	1.185	1.176	1.641
	20	1.214	1.187	1.638
B11	21	1.169	1.139	1.344
	22	1.186	1.169	1.317

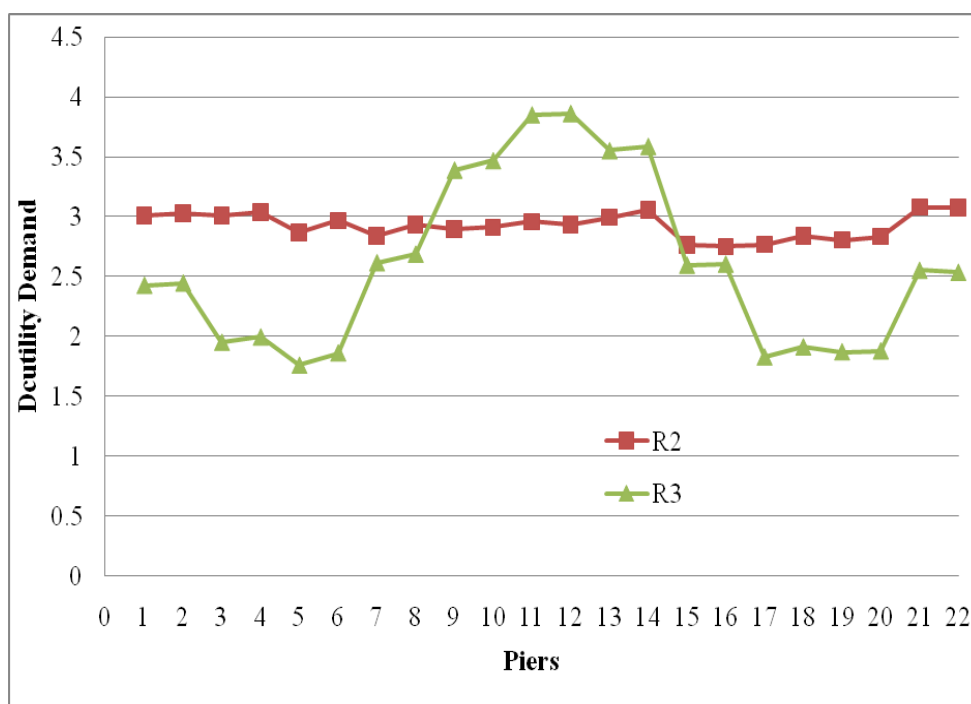


Figure 4.24 Longitudinal ( $R_2$ ) and Transverse ( $R_3$ ) Mean Pier Ductility Demands in Long Multi-Span Bridges Models Supported on Hard Soil Case.

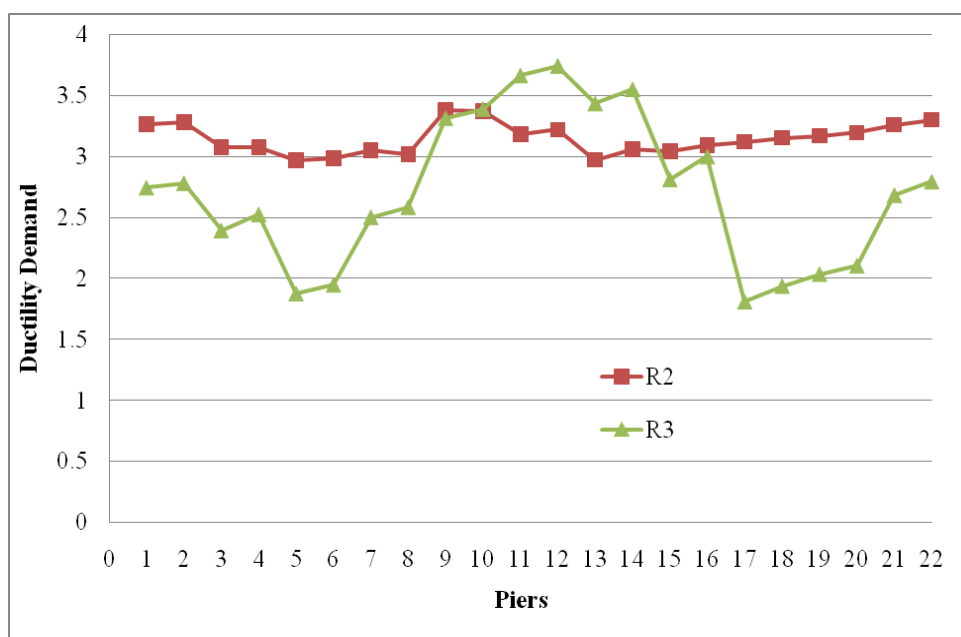


Figure 4.25 Longitudinal ( $R_2$ ) and Transverse ( $R_3$ ) Mean Pier Ductility Demands in Long Multi-Span Bridges Models Supported on Medium Soil Case.

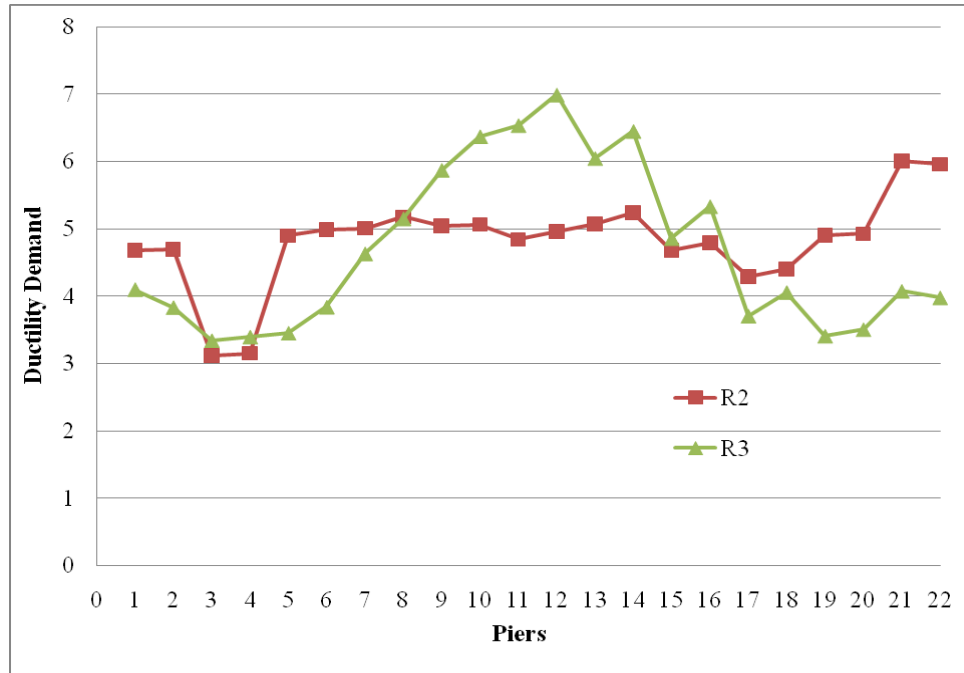


Figure 4.26 Longitudinal ( $R_2$ ) and Transverse ( $R_3$ ) Mean Pier Ductility Demands in Long Multi-Span Bridges Models Supported on Soft Soil Case.

Long multi-span bridges were observed to follow the same behavior as short and medium multi-span bridges in regards to the identification of the plastic hinge that exhibited the maximum ductility demand within a given pier. This further corroborates the fact that the location of the plastic hinge that exhibits the maximum ductility demand within a given pier was observed to be a function of the soil case and not the bridge length.

Finally, based on the results of this section, the following general conclusions can be observed for long multi-span bridge models:

1. The pier ductility demands are in general higher than the ones occurring in short and medium multi-span bridge models, regardless of the type of seismic excitation (spatially varying or uniform).

2. The spatially variable seismic excitation generates higher ductility demands than uniform seismic excitation for all piers, regardless of the soil case considered.

#### 4.3.4 Design Limitations on Pier Ductility Demands

The pier rotational ductility demand threshold of 5.09 calculated from the moment-curvature relationship given in Figure 3.15 is used in this study as a limit state that indicates that the ultimate rotation value of the plastic hinge model has been reached (Point C of Figure 3.14). If such a threshold value is exceeded, then the plastic hinge will enter the reserve flexural capacity region (segment DE of Figure 3.14) and as a result, significant structural distress at the pier end zones should be expected. However, no design limitations were found in the literature based on pier rotational ductility demands.

AASHTO (2011) requires for the seismic design of bridges that the maximum displacement ductility demand of the piers in multiple-pier bents be  $\mu_D \leq 6.0$ . AASHTO defines the displacement ductility demand using the following expression:

$$\mu_D = 1 + \frac{\Delta_{pd}}{\Delta_{yi}} \quad (4.1)$$

$$\text{Where: } \Delta_{pd} = \theta_{max} \left( L_c - \frac{L_p}{2} \right) \quad (4.2)$$

$$\Delta_{yi} = \frac{\phi_y L_c^2}{3} = \frac{\phi_y L_p L_c^2}{3L_p} = \frac{\theta_y L_c^2}{3L_p} \quad (4.3)$$

$L_c$  = length of pier from the maximum moment location to the point of moment contraflexure.

All other variables in Equations (4.2) and (4.3) were defined for the plastic hinge model in Section 3.3. Substituting Equations (4.2) and (4.3) in (4.1) and solving for  $\theta_{max}/\theta_y$  an

expression for the rotational ductility demand can be obtained in terms of the displacement ductility demand as follows:

$$R = \frac{\theta_{max}}{\theta_y} = (\mu_D - 1) \left[ \frac{L_c^2}{3L_p(L_c - \frac{L_p}{2})} \right] \quad (4.4)$$

Considering that in Section 3.3 the value of  $L_p$  was established as 90% of the pier diameter and assuming that the point of moment contraflexure occurs around the pier mid height, then from Eq. (4.4) and  $\mu_D \leq 6.0$ , the maximum value of  $R$  according to AASHTO design criteria is  $R \leq 8.0$ .

The displacement ductility demand provided by AASHTO was developed for two-dimensional bridge structures; thus,  $R \leq 8.0$  must be checked separately in the longitudinal ( $R_2$ ) and transverse ( $R_3$ ) direction of the three-dimensional bridge models. It can be observed in Figures 4.8 to 4.10, 4.16 to 4.18 and 4.24 to 4.26 for short, medium and long multi-span bridge models, respectively, that none of the piers have mean values of  $R_2$  and  $R_3$  exceeding 8.0, regardless of the soil type under the pier supports. Therefore, all piers are in compliance with maximum pier ductility demand design criteria, as established by AASHTO.

#### 4.4 Concluding Remarks

Based on the results on pier ductility demands for the multi-span bridge models analyzed in this chapter, the following general conclusions can be established:

1. Regardless of the length of the bridge and the type of soil under the piers, ignoring the spatial variability of the seismic excitation will result in the

underestimation of the pier ductility demands. Evidence of this fact is that the ductility index of practical all piers exceeded 1.0 (the only exception being the piers at the first and last bent of medium multi-span bridges when supported on the Hard and Medium Soil Cases).

2. A pier ductility index range of 1.0 to 1.4 was found for small multi-span bridges. For medium and long multi-span bridges, the pier ductility index range was found to be 0.9 to 1.5 and 1.0 to 1.7, respectively. This means that up to 40%, 50% and 70% underestimation of the pier ductility demand is possible for small, medium and long multi-span bridges, respectively, if the spatial variability of the seismic excitation is ignored.
3. The pier ductility demand was found to be more sensible to variations of the type of soil under the piers than variations of the length of the bridge. The maximum pier ductility demand values were found to occur in bridges supported on the Soft Soil Case, regardless of their length.
4. The degree of uncertainty in the pier ductility demand values exhibits relatively little change, regardless of the soil case and the length of the bridge.
5. The piers will exhibit significant bidirectional (transverse and longitudinal) response when the bridge is subjected to seismic excitation with an angle of incidence with respect to the bridge longitudinal axis. For small and large multi-span bridges, the transverse response of the pier plastic hinges was found to exceed the longitudinal response for a significant number of piers. For medium multi-span bridges, the longitudinal and transverse responses were found to be of

similar magnitude, with the longitudinal response typically exceeding the transverse response.

6. All piers, regardless of the length of the bridge and type of soil under the pier supports, exhibit mean values of rotational ductility demand in the transverse and longitudinal direction that are in compliance with maximum design values established by AASHTO (2011).

Results show that the effect of the spatial variability of the seismic excitation increases with the length of the bridge; however, the type of soil also played a fundamental roll. In fact, the ductility indexes of piers in small multi-span bridges supported on the Soft Soil Case were greater than the ductility indexes of piers in large multi-span bridges supported on Hard and Medium Soil Cases. Saxena (2000), Kim and Feng (2003) and Sextos et al (2003) also observed similar results, although they obtained greater mean values for the pier ductility index for the two-dimensional idealizations of the long multi-span bridges models they considered. It should also be mentioned that significant differences existed in the type of piers and structural arrangement in the two-dimensional bridge models used by these researchers and the three-dimensional bridge models considered in this chapter. For example, Sextos et al (2003) considered bents made of a single variable section pier with a plastic zone occurring at the pier-foundation connection zone only. Saxena (2000) and Kim and Feng (2003) considered many types of bridge structures with piers having plastic zones occurring at the pier-foundation and pier-cap beam connection zones. The pier types varied from single variable section pier, wall piers, as well as bents with circular and noncircular piers. Therefore, pier ductility



indexes obtained from significantly different pier models under unidirectional flexural response should be expected to exhibit different ductility indexes when compared to circular piers under bidirectional flexural response.

The significance of the transverse response of the piers observed in this study indicates that two-dimensional idealizations of the bridge response may introduce significant error in the estimation of pier ductility demands. As the bridge length increases, the lateral (transverse) stiffness of the superstructure decreases. This effect is compounded by the loss of lateral stiffness of the bents when plastic hinges form at the pier end zones. As a result, significant transverse response is expected to occur, especially when a strong transverse seismic excitation component is present. Therefore, the three-dimensional response of the bridge structure should be considered in order to properly capture these effects. Studies on three-dimensional modeling and analysis of highway bridges under spatially varying seismic excitation could not be found in the published literature.

Results also show that piers on short, medium and large multi-span bridge models consistently exhibited the largest ductility demands on the top plastic hinge (at the pier-cap beam interface) when supported on the Soft Soil Case and on the bottom plastic hinge (at the pier-foundation interface) when the bridges were supported on the Hard Soil Case. This fact can be better explained in the context of general structural mechanics theory: rigid bent frames on simple supports will have the highest moment demand at the cap beam-pier connection zone, given the inability of the simple support to take moments. If support fixity increases, then the moment demand at such connection zone

decreases, and if full fixity is assumed at the support, the maximum moments will usually occur at the pier-foundation connection zone.

The soil spring set stiffness coefficients at the pier foundation nodes were determined based on the type of soil considered, thus the degree of fixity at the support was a function of the soil type. Since the dynamic stiffness values of soft soils are lower than the hard soil dynamic stiffness values, the degree of fixity at the supports was the lowest for soft soils and the highest for hard soils. Moreover, the plastic hinges only measured rotational ductility generated by the moment demands at the pier-cap beam and pier-foundation interfaces; therefore, the bottom plastic hinges exhibited the highest ductility demand when the support fixity was the highest. When the support fixity was the lowest, top plastic hinges exhibited the highest ductility demand. This fact could also explain why no consistency was observed on the location of the plastic hinge with the highest ductility demand when the bridges were supported on the medium soil case. The inherent uncertainty within the seismic excitation model coupled with the partial fixity conditions at the support could have caused such inconsistency. No published research could be found that studied the effect of the dynamic soil stiffness under the pier supports on the pier ductility demand for bridges subjected to spatially varying seismic excitation.

## **5. EFFECT OF SPATIAL VARIABILITY OF SEISMIC EXCITATION ON DUCTILITY DEMANDS OF MULTI-SPAN BRIDGES WITH UNIFORM SOIL CONDITIONS AND VARIABLE SPAN LENGTHS AND PIER HEIGHTS**

### **5.1 Introduction**

Bridge structures are typically used when highways must span over canyons or bodies of water. To deal with the irregular topography prevalent in canyons and at river, lake and sea beds, bridge engineers often design multi-span bridges with variable pier heights and spans with variable lengths. Highway interchange projects are another example where the bridge engineer must consider piers of different heights and spans of different lengths in order to provide clearance for bridges dealing with intersecting highways. In many instances, the resulting structural configuration of the bridge will be asymmetric requiring three-dimensional finite element modeling in order to properly predict the response under spatially varying seismic excitation.

In Chapter 4 multi-span bridge models of variable lengths, but equal span lengths and pier heights were considered as shown in Figure 4.1. Pier ductility demands and ductility indexes for these bridge models were determined under spatially variable seismic excitation for Hard, Medium and Soft Soil Cases, as defined by Tables 4.2, 4.3 and 4.4. In this Chapter, all bridge models are assumed supported on the Hard Soil Case; thus, it is assumed that no variability in the soil conditions occurs while variations in the bridge geometry are being considered. In order to study the effects of such variations on

the nonlinear response of the piers, pier ductility indexes are determined for bridge models with significant differences in their structural arrangements, including asymmetric arrangements. As defined in Chapter 3, the pier ductility index is obtained by dividing the pier ductility demand under spatially varying seismic excitation by the pier ductility demand under uniform seismic excitation.

## **5.2 Modeling Methodology**

Since there are an infinite number of possible structural arrangements for multi-span bridge models with variations in span lengths and pier heights, in this Chapter only a few representative cases of two-span to six-span bridge models are considered as shown in Figures 5.1 to 5.4. Figures 5.1 and 5.2 consider three-span and six-span bridge models with variable span lengths and total bridge lengths and constant pier heights, as well as three-span and six-span bridge models with constant span lengths and variable pier heights. Figure 5.3 show two-span to four-span bridge models with variable span lengths and constant pier heights where the total length is set equal to the length of the medium multi-span bridge model illustrated in Figure 4.1(b). Figure 5.4 show two-span bridge models with variable span lengths and constant pier heights where the total bridge length is set equal to the length of the short multi-span bridge model illustrated in Figure 4.1(a). In all multi-span bridge models considered in this Chapter the structural asymmetry is assumed caused by variable span lengths and not by variable pier heights. Many typical bridge structural configurations are not represented in these figures; however, the objective of this Chapter is to study the effects of variations of span lengths and pier heights and not variations of particular bridge structural configurations.

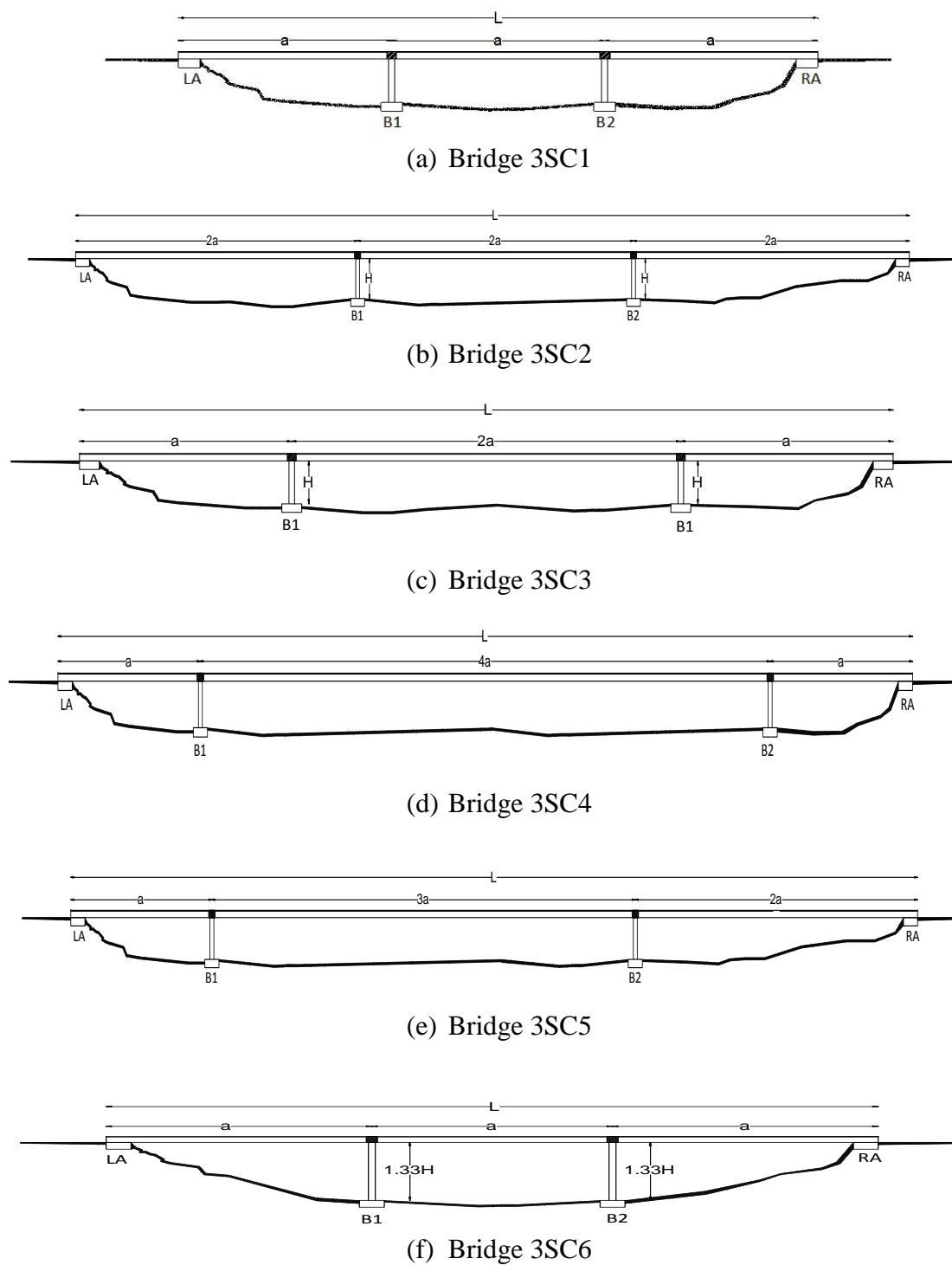
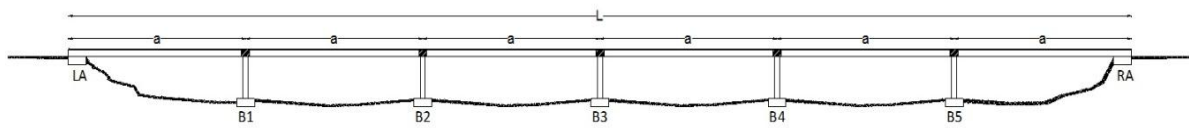
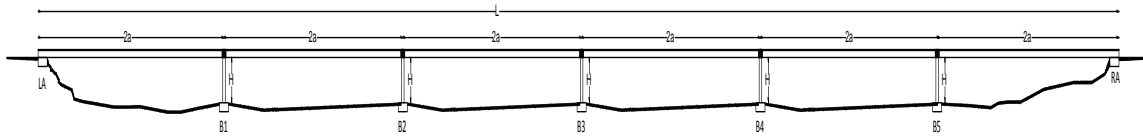


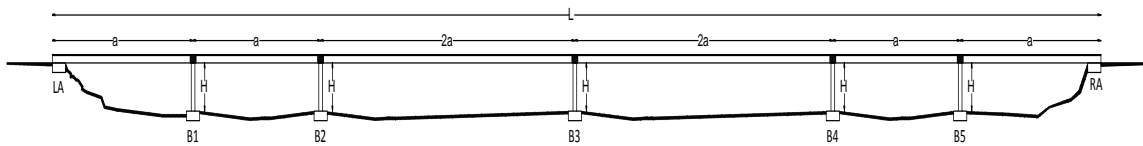
Figure 5.1 Three-Span Bridge Models with Variable Bridge Lengths



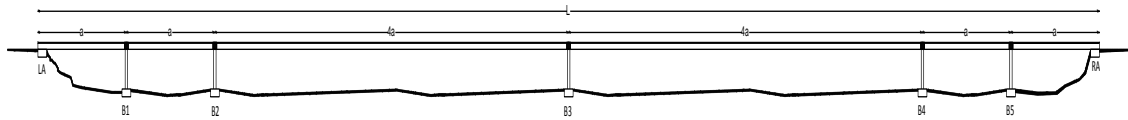
(a) Bridge 6SC1



(b) Bridge 6SC2



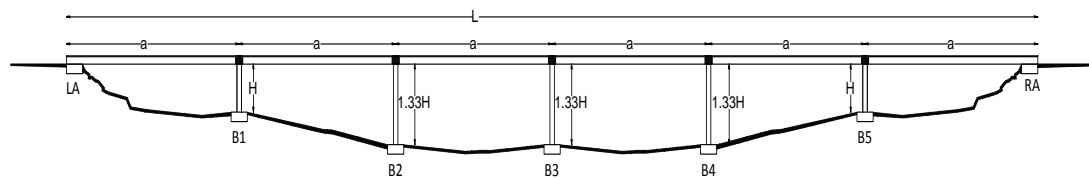
(c) Bridge 6SC3



(d) Bridge 6SC4

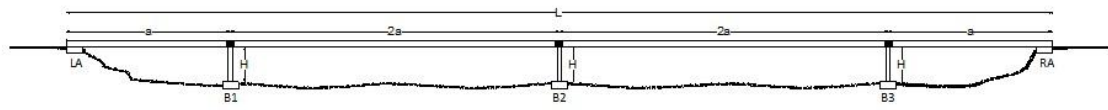


(e) Bridge 6SC5

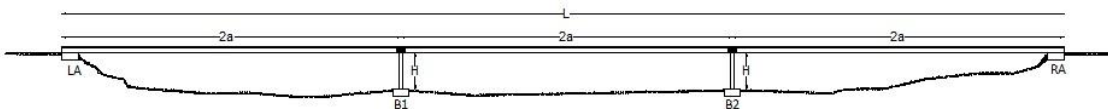


(f) Bridge 6SC6

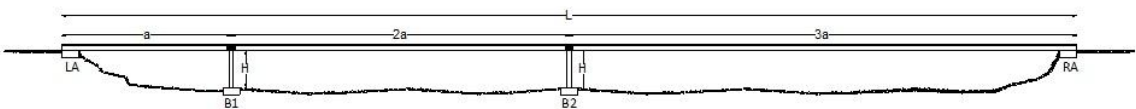
Figure 5.2 Six-Span Bridge Models with Variable Bridge Lengths



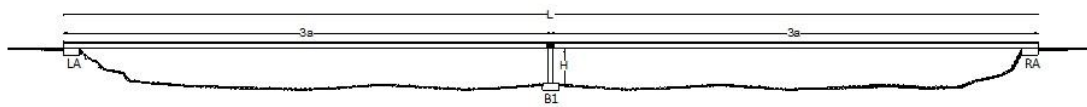
(a) Bridge 4S6a



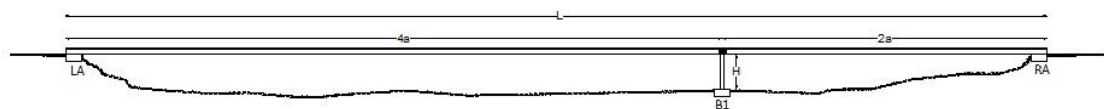
(b) Bridge 3S6aC1



(c) Bridge 3S6aC2



(d) Bridge 2S6aC1

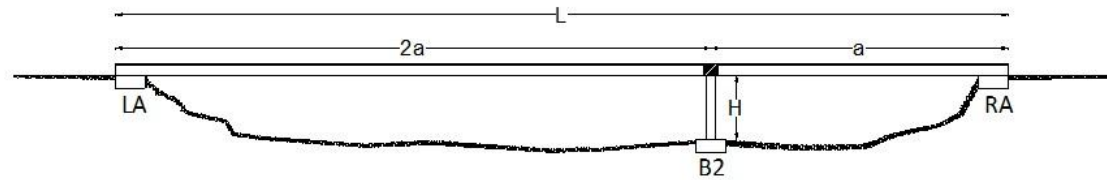


(e) Bridge 2S6aC2

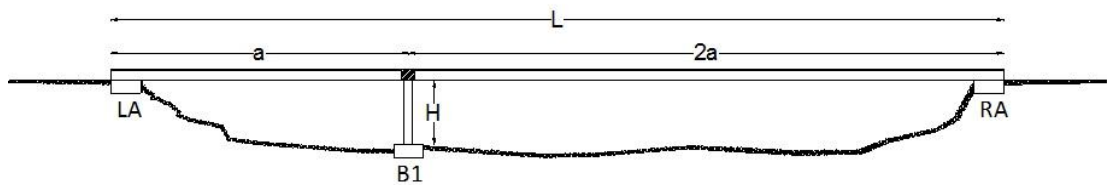


(f) Bridge 2S6aC3

Figure 5.3 Two-Span to Four-Span Bridge Models with Constant Length  $L = 6a$



(a) Bridge 2S3aC1



(b) Bridge 2S3aC2

Figure 5.4 Two-Span Bridge Models with Constant Length  $L = 3a$ 

The same cross section of the bridge shown in Figure 4.2 is assumed to apply to all bridge models shown in Figures 5.1 to 5.4. Although in typical bridge design the cross section of the superstructure, cap beam and piers is expected to change when significant changes in the span length and pier height occur, in this Chapter these cross sections are assumed constant in the understanding that what is being determined are pier ductility indexes, which are response ratios.

The span lengths of all bridge models illustrated in Figures 5.1 to 5.4 were determined as multiples of the span length of the multi-span bridge models shown in Figure 4.1. This was done in order to be able to use the same displacement time history sets ( $D_X$ ,  $D_Y$ ,  $Z \cdot D_Z$ ) generated for the bridge models in Chapter 4 as the spatially varying seismic excitation for the bridge models shown in Figures 5.1 and 5.2. As was the case in Chapter 4, in this Chapter the scaling factor  $Z$  was set to  $Z = 0.67$  in order to consider the



typical ratio of horizontal to vertical seismic acceleration components used in design codes.

As described in Chapter 3 and 4, displacement time history sets were generated at specific points having ground surface spatial coordinates ( $X$ ,  $Y$ ) coinciding with the pier support locations of the multi-span bridge models shown in Figure 4.1. Moreover, soil cases were defined for such bridge models that established the soil type under each pier (see Tables 4.2, 4.3 and 4.4). Therefore, in order to be able to use the same displacement time history sets for other bridge structural configurations, the pier support locations of these bridges had to match the ground spatial coordinates and the soil type of the pier support locations of the bridge models shown in Figure 4.1. In this Chapter, the Hard Soil Case is assumed to apply to all bridge models. From Tables 4.2 to 4.4, it can be seen that the Hard Soil Case implies that all piers are under the same hard soil type and as a result, the applicability of the displacement time history sets can be based only on the ground spatial coordinates of the pier locations.

Since the same bridge cross section is considered in the bridge models shown in Figure 4.1, 5.1 to 5.4, all pier support locations with a given  $X$  coordinate will share the same  $Y$  coordinate. As a result, only the  $X$  coordinate of the pier support location needs to be defined in order to determine the applicable displacement time history set. Given that the relative distance between pier supports in the bridge models shown in Figure 4.1 is constant (that is,  $a = 36.58$  meters, as defined by Table 4.1), then any pier support located at a distance relative to the left abutment location (LA) that happens to be multiple of the distance  $a = 36.58$  m will already have a specific displacement time history set defined at

such location, as long as the length of the bridge does not exceed the length of the long multi-span bridge model [see Figure 4.1(c)]. All bridge models given in Figures 5.1 to 5.4 have pier locations in compliance with the above conditions.

Finally, it should be mentioned that the restrictions of the pier location and the type of soil under such location for the bridge models shown in Figures 5.1 to 5.4 were set only as a matter of convenience. In general, displacement time history sets can be generated for any location on the ground surface having any soil type following the methodology presented in Chapter 3.

### **5.3 Three-Span Bridge Models with Variable Bridge Lengths**

Figure 5.1 shows six different structural arrangements for three-span bridge models. Bridge 3SC1 shown in Figure 5.1(a) is identical to the small multi-span bridge model shown in Figure 4.1(a). The purpose of considering this bridge was to provide a general reference for the average pier ductility index to which the average pier ductility indexes for the other five bridges in Figure 5.1 could be compared too. Except for Bridge 3SC6, where an increase in the pier heights is considered, the rest of the bridges have a constant pier height of  $H = 7.93$  meters, which is the same height used for the multi-span bridge models in Chapter 4.

As can be observed in Figure 5.1, the positions of Bents B1 and B2 with respect to the Left Abutment LA are different among the different bridges, except for Bridges 3SC1 and 3SC6, where both bents share the same position on the ground surface. Therefore, the ground spatial coordinates of Piers 1 to 4 will be different for each bridge

and as a result, the pier ductility index values for each bridge are presented in separate graphs (Figures 5.5 to 5.10) in order to avoid any confusion.

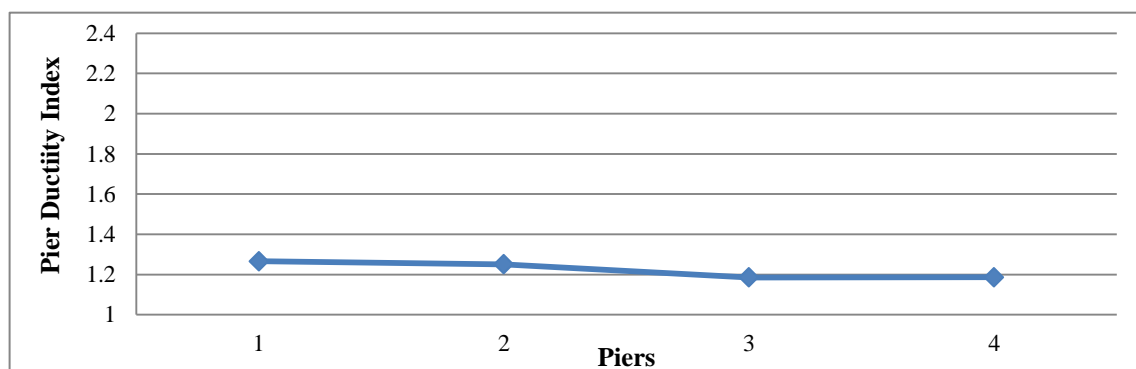


Figure 5.5 Mean Pier Ductility Indexes for Bridge 3SC1

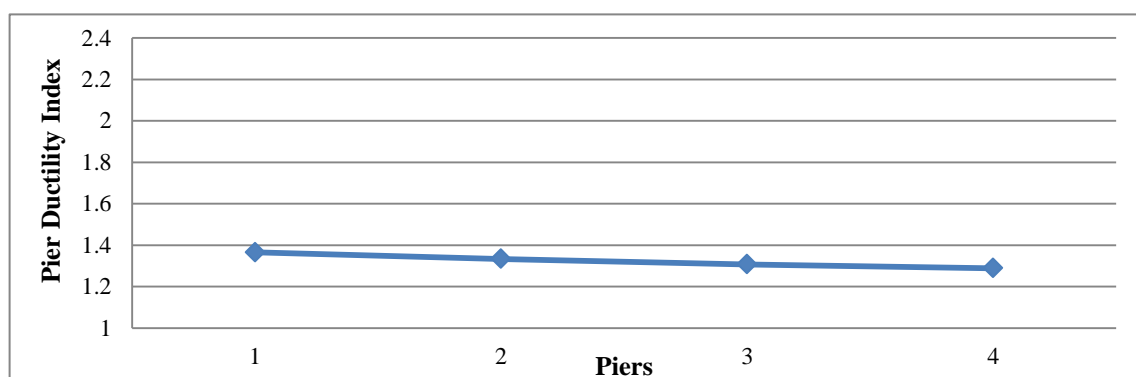


Figure 5.6 Mean Pier Ductility Indexes for Bridge 3SC2

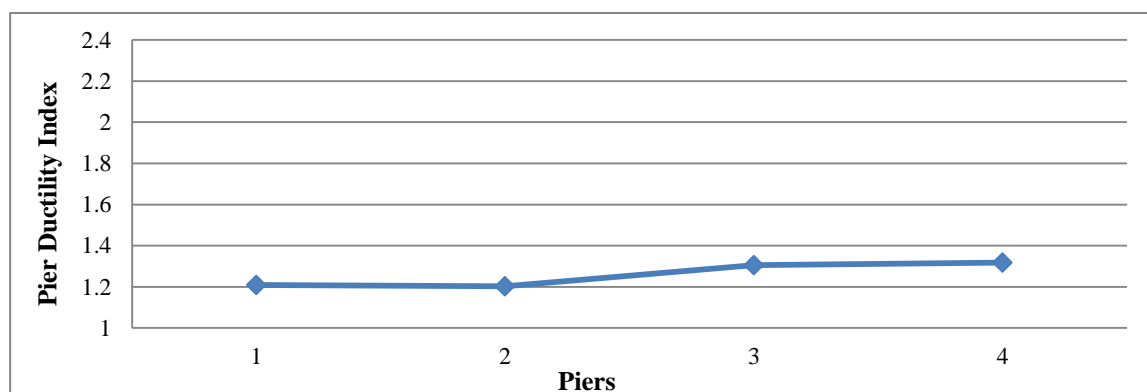


Figure 5.7 Mean Pier Ductility Indexes for Bridge 3SC3

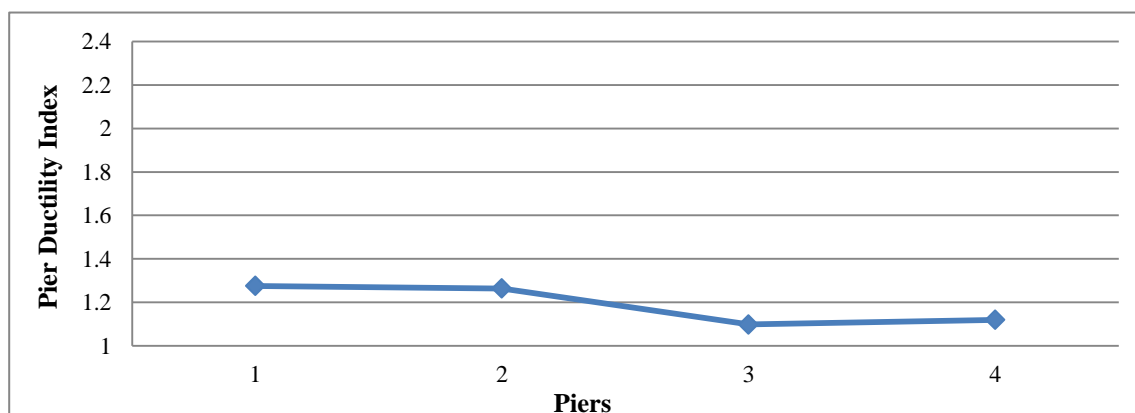


Figure 5.8 Mean Pier Ductility Indexes for Bridge 3SC4

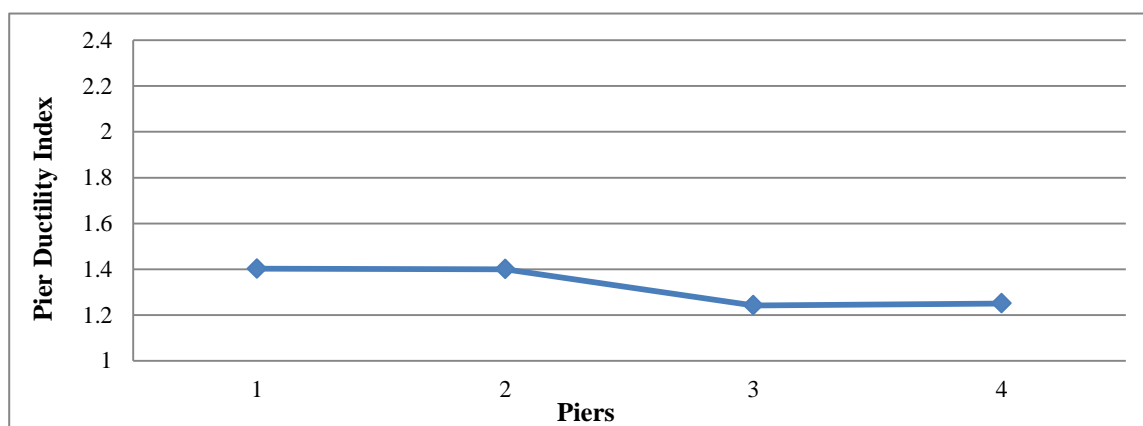


Figure 5.9 Mean Pier Ductility Indexes for Bridges 3SC5

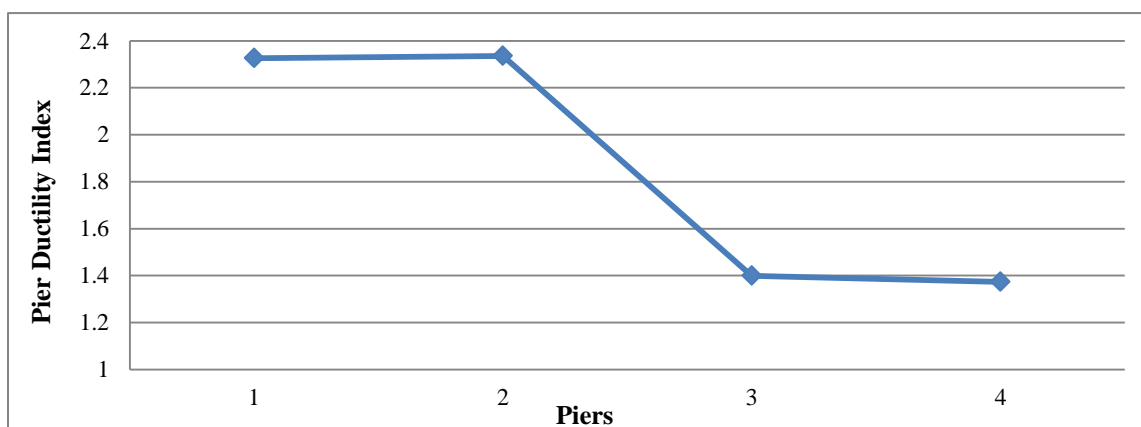


Figure 5.10 Mean Pier Ductility Indexes for Bridge 3SC6

By taking averages of the mean pier ductility indexes observed in each Figure 5.5 to 5.10 the following conclusions can be established:

1. When compared to the average pier ductility index values obtained for the reference bridge (Bridge 3SC1) and span length increases are considered, the average pier ductility index value increases by 8% for Bridges 3SC2 and 3SC5, and 3% for Bridge 3SC3. However, a reduction of about 3% occurs in the average pier ductility index value of Bridge 3SC4.
2. When compared to the average pier ductility index values obtained for the reference bridge (Bridge 3SC1) and pier height increases are considered, the average pier ductility index value increases by 52% for Bridge 3SC6.

Since Piers 1 to 4 of Bridges 3SC1 and 3SC6 have identical ground spatial coordinates, the average pier ductility index values per bent can be compared directly as illustrated in Figure 5.11. It can be observed that Bent B1 of Bridge 3SC6 exhibits an 85% increase in the average pier ductility index with respect to Bent B1 of Bridge 3SC1. However, Bent B2 of Bridge 3SC6 exhibits only a 17% increase in the average pier ductility index with respect to Bent B2 of Bridge 3SC1. The significant difference in average pier ductility index values between adjacent bents shown in Figure 5.10 can be attributed to the increase in pier height, the effect of the spatial variability of the seismic excitation and the rigid body motions of the superstructure. As was explained in Section 4.3.1, short multi-span bridges have significant lateral stiffness in the superstructure and will tend to respond in rigid body motion when the bent frames loose lateral rigidity as the pier plastic hinges activate during strong earthquake excitation. As the pier heights

increase the lateral elastic stiffness of the bent frame decreases proportionally and when the pier plastic hinges activate, the lateral stiffness decreases even more; thus, providing even less resistance to rigid body motions of the superstructure. Since under uniform seismic excitation no differential ground movement is expected between adjacent piers, the rigid body motions will tend to be translational in nature and the flexural demands on the piers will be similar. However, under spatially variable seismic excitation differential ground displacements between adjacent bents are expected to occur, which will tend to generate torsional rigid body motions of the laterally stiff superstructure. As a result, the piers furthest away from the shear center of the superstructure will exhibit the greatest flexural demands, which could explain the significant difference in average ductility index values observed in Figure 5.8 for piers of adjacent bents.

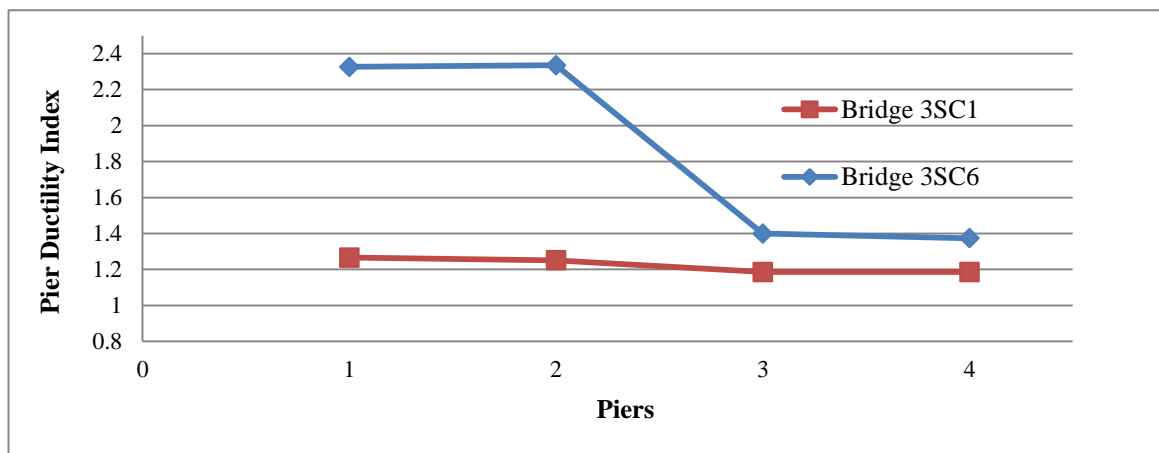


Figure 5.11 Mean Pier Ductility Indexes for Bridges 3SC1 and 3SC6

When compared to the length of Bridge 3SC1 ( $L = 3a$ ), Bridges 3SC2 to 3SC5 have twice the length ( $L = 6a$ ). In fact when using the criteria establishes in Chapter 4, Bridge 3SC1 can be classified as a short multi-span bridge [see Figure 4.1(a)] and Bridges 3SC2 to 3SC5 as medium multi-span bridges [see Figure 4.1(b)]. The average

pier ductility index value for short and medium multi-span bridges can be obtained for the Hard Soil Case from Tables 4.7 and 4.10, respectively as 1.17 and 1.08; thus, a decrease of 8% in the average pier ductility index value is predicted from the results obtained in Chapter 4 when increasing the length of the bridge from  $L = 3a$  to  $L = 6a$ , while keeping the span lengths constant. Such a decrease is most likely caused by the combination of the effects of the spatial variability of the seismic excitation and the reduction in the lateral stiffness of the superstructure as the length of the bridge increases by 100%. Since the superstructure cross section is assumed to remain constant with the increase in bridge length, the decrease in lateral stiffness of the superstructure will be directly proportional to the increase in length. Under this condition, the differential ground movements at the pier supports caused by the spatially variable seismic excitation will tend to generate a translational response from the superstructure in the same direction of the differential ground movement (significantly reducing the rigid body rotational response that is typical of laterally stiffer superstructures). Since uniform seismic excitation will also tend to generate a translational response of the superstructure, then the pier ductility index, which is defined as the ratio of pier responses under spatially variable and uniform seismic excitation, will tend to decrease due to the similarity in the superstructure response.

The results of this Section predict up to 8% increase in the average pier ductility index for bridges that exhibited 100% increase in its length by considering variable increases in span lengths (with the exception of Bridge 3SC4, that exhibited a 3% decrease); this represents up to a 16% increase with respect to the average pier ductility

index value obtained using the results of Chapter 4. Therefore, when considering the same increase in bridge length, the average pier ductility index value is expected to increase by up to 16% when variable span length instead of constant span lengths are used to achieve such an increase. The results of this Section also show that the average pier ductility index increases by 52% when bridges of the same length exhibit increases in pier heights. Therefore, the average pier ductility index of the bridge is more sensible to the effect of changes in pier heights than changes in span lengths.

#### **5.4 Six-Span Bridge Models with Variable Bridge Lengths**

Figure 5.2 shows six different structural arrangements for six-span bridge models. Bridge 6SC1 shown in Figure 5.2(a) is identical to the medium multi-span bridge model shown in Figure 4.1(b). The purpose of considering this bridge was to provide a general reference for the pier average ductility index to which the average pier ductility indexes for the other five bridges in Figure 5.2 could be compared too. Except for Bridge 3SC6, where an increase in the pier heights is considered in piers of Bents B2 to B4, the rest of the bridges have a constant pier height of  $H = 7.93$  meters, which is the same height used for the multi-span bridge models in Chapter 4.

As can be observed in Figure 5.2, the positions of Bents B1 to B5 with respect to the Left Abutment LA are different among the different bridges, except for Bridges 3SC1 and 3SC6, where bents B1 to B5 share the same position on the ground. Therefore, the ground spatial coordinates of Piers 1 to 10 will in general be different ground in each



bridge and as a result, the pier ductility index values for each bridge are presented in separate graphs (Figures 5.12 to 5.17) to avoid any confusion.

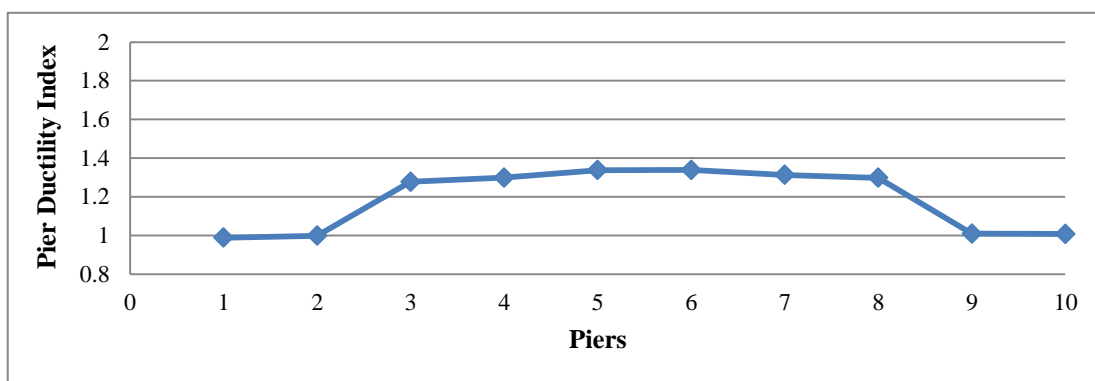


Figure 5.12 Mean Pier Ductility Indexes for Bridge 6SC1

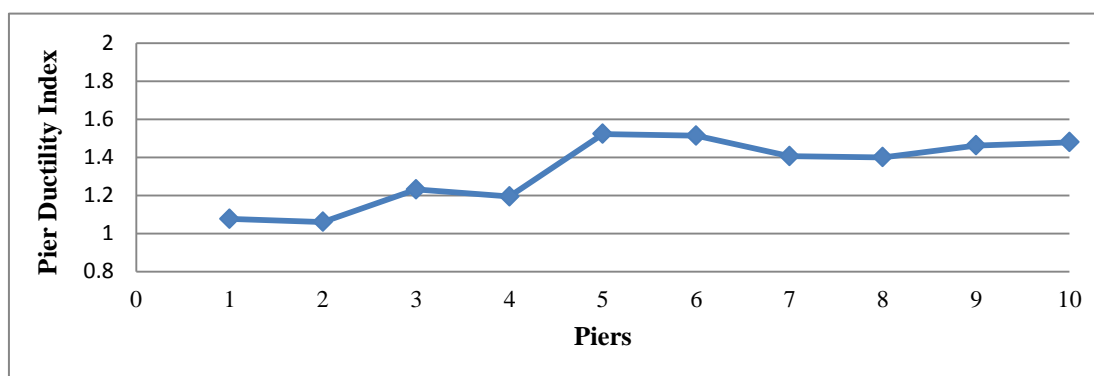


Figure 5.13 Mean Pier Ductility Indexes for Bridge 6SC2

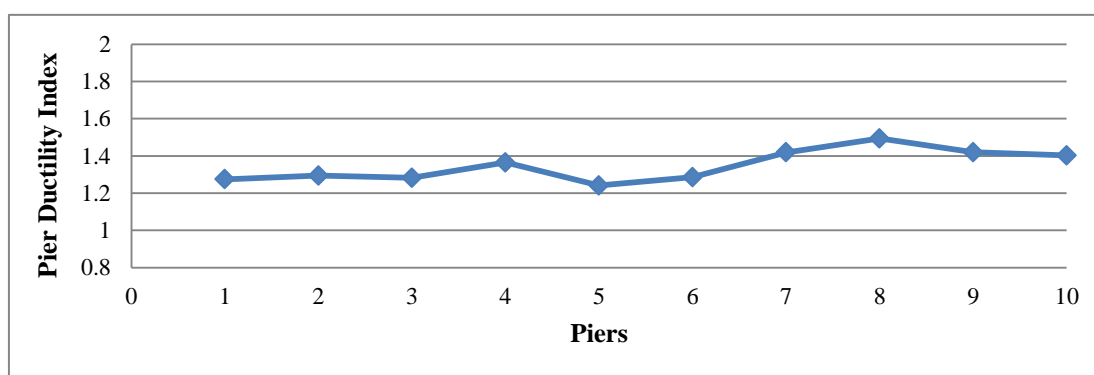


Figure 5.14 Mean Pier Ductility Indexes for Bridge 6SC3

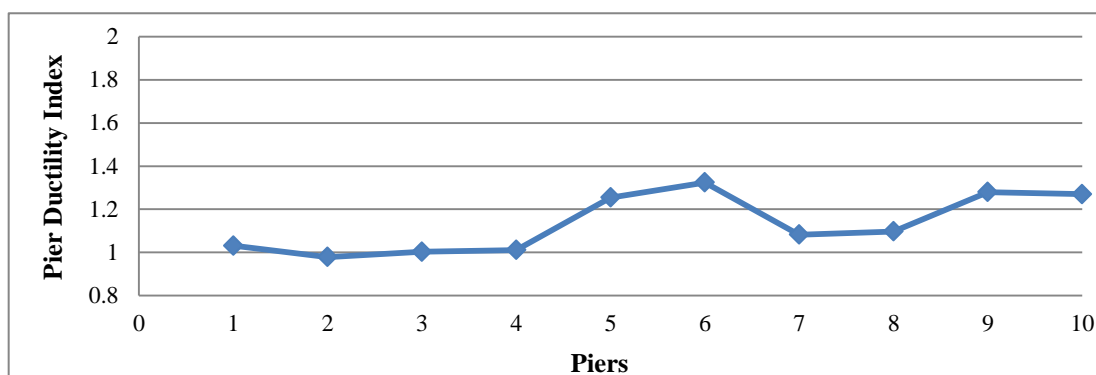


Figure 5.15 Mean Pier Ductility Indexes for Bridge 6SC4

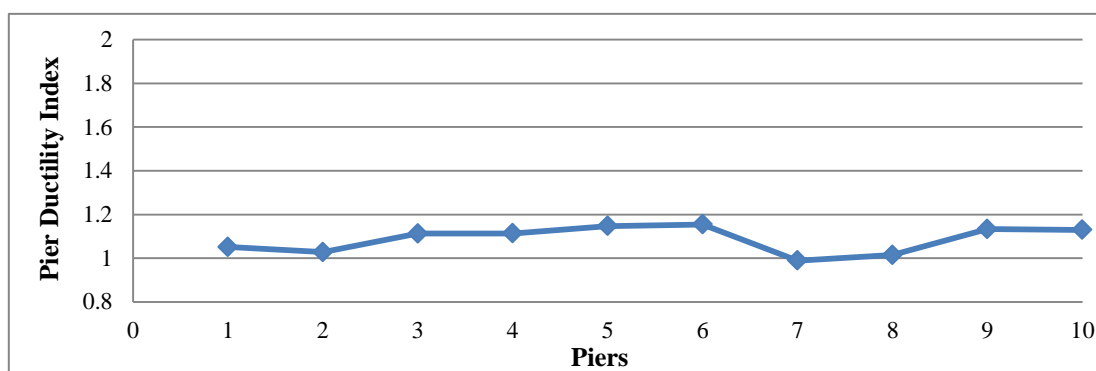


Figure 5.16 Mean Pier Ductility Indexes for Bridge 6SC5

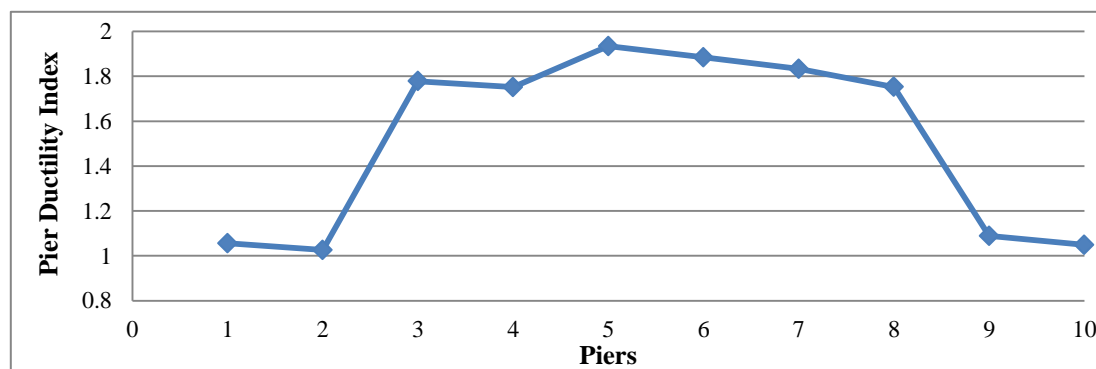


Figure 5.17 Mean Pier Ductility Index for Bridge 6SC6

By taking averages of the pier ductility indexes on each Figure 5.12 to 5.17 the following conclusions can be established:

1. When compared to the average pier ductility index values obtained for the reference bridge (Bridge 6SC1) and span length increases are considered, the average pier ductility index values increase by 14% and 10% for Bridges 6SC2 and 6SC3, respectively. However, the average pier ductility index decreases by 5% and 9% for Bridges 6SC4 and 6SC5, respectively.
2. When compared to the average pier ductility index values obtained for the reference bridge (Bridge 6SC1) and pier height increases are considered, the average pier ductility index value increases by 28% for Bridge 6SC6.

Since Piers 1 to 10 of Bridges 6SC1 and 6SC6 have identical ground spatial coordinates, the average ductility index values per bent can be compared directly as illustrated in Figure 5.18. It can be observed that interior Bent B3 of Bridge 6SC6 exhibits the largest increase (about 43%) in the average pier ductility index value when compared to interior Bent B3 of Bridge 6SC1. It can also be observed that the lowest increase in the average pier ductility index value (about 10%) occurs in the exterior bents (B1 and B5). The reason for the smaller increase in average ductility value in piers of exterior bents is most likely due to the fact that such piers were kept at the same height for both Bridges 6SC1 and 6SC6.

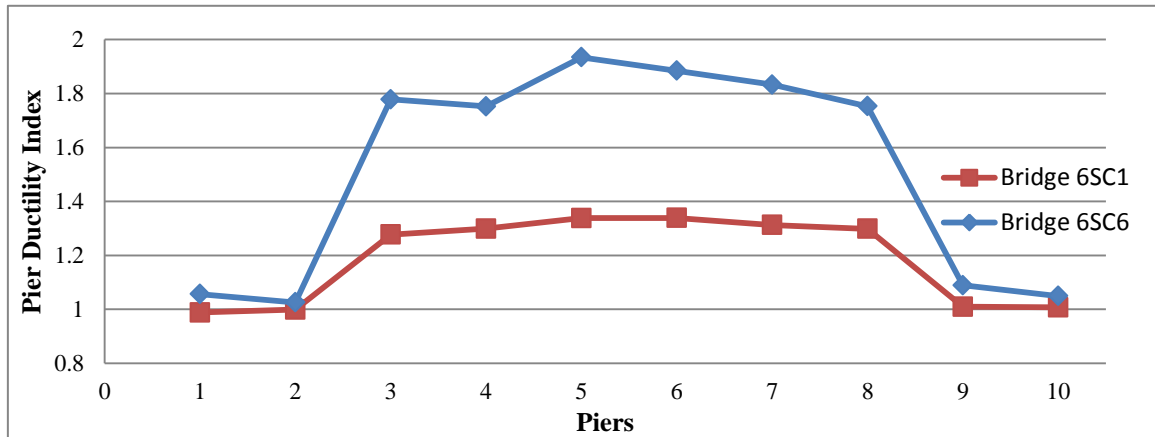


Figure 5.18 Mean Pier Ductility Indexes for Bridges 6SC1 and 6SC6

When comparing the response of Bridges 3SC6 and 6SC6, it can be observed that the interior piers of Bridge 6SC6 don't show significant differences in their ductility index values; however, significant differences in ductility index values occur between piers located on exterior bents compared to piers located on interior bents. Again, this is most likely due to the difference in height between the exterior and interior bents. Moreover, the 52% increase in average pier ductility index values observed in Bridge 3SC6 drops to 28% when considering Bridge 3SC6. Such a drop may be caused by the reduction in the lateral stiffness of the superstructure (as explained in Section 5.3) and the greater lateral stiffness of the exterior bent frames due to their shorter height when compared to the interior bent frames.

When compared to the length of Bridge 6SC1 ( $L = 6a$ ), Bridges 6SC2 to 6SC5 have twice the length ( $L = 12a$ ). In fact using the criteria established in Chapter 4, Bridge 6SC1 can be classified as a medium multi-span bridge [see Figure 4.1(b)] and Bridges 6SC2 to 6SC5 as long multi-span bridges [see Figure 4.1(c)]. From Table 4.10 and 4.13, it can be observed that the average ductility index value for pier on exterior bents is 0.90

and 1.15 for medium and long multi-span bridges, respectively, when supported on Hard Soil Case. Thus, a 28% increase in ductility index for piers on exterior bents can be associated with just the 100% increase in length of the bridge. Practically the same increase in pier ductility index is observed when comparing average ductility indexes for piers in Bents B1 and B5 of Bridges 6SC1 and 6SC3. Therefore, it seems that the increase in ductility index values on piers in exterior bents is due mainly to the increase in length of the bridge and not to a particular arrangement of span length increases. A similar conclusion can be drawn by comparing the average ductility index ranges for all piers in medium and long multi-span bridges. From Tables 4.10 and 4.13 average ductility index values of 1.08 and 1.16 are obtained for medium and long multi-span bridges, respectively, when supported on Hard Soil Case; thus, a 7% increase in the average pier ductility index is predicted from the results of Chapter 4 when the length of the bridge is increased from  $L = 6a$  to  $L = 12a$  considering constant span lengths.

The results of this Section show that the average pier ductility index is expected to increase by 14% and 10% for Bridges 6SC2 and 6SC3, respectively; thus, only net increases of 7% and 3% in the average pier ductility index are expected due to the effect of using variable span length when increasing the length of the bridge by 100% (from  $L = 6a$  to  $L = 12a$ ). For Bridges 6SC4 and 6SC5, the use of variable span lengths to increase the bridge length by 100% generates a decrease in the average pier ductility index. Decreases in the average pier ductility index have little practical value since they represent a reduction of the effect of the spatial variability of the seismic excitation due to the use of a particular arrangement of different span lengths for a given bridge length.

Therefore, the effect of using variable span lengths in six-span bridges on the average pier ductility index value is relatively small and the use of an asymmetric arrangement of different span lengths did not increase the average pier ductility index of the bridge. The results of this Section also show that the average pier ductility index increases by 28% when six-span bridges of the same length exhibit increases in pier heights. Therefore, the average pier ductility index of the bridge is more sensible to the effect of changes in pier heights than changes in span lengths.

### **5.5 Two-Span Bridge Models with Bridge Length $L = 3a$**

The two-span bridge models considered in this section were obtained from the three-span bridge model (Bridge 3SC1) illustrated in Figure 5.1(a). In fact, Bridge 2S3aC1, as illustrated in Figure 5.4(a), is obtained by eliminating Bent B1 from Bridge 3SC1. Similarly, Bridge 2S3aC2, as illustrated in Figure 5.4(b), is obtained by eliminating Bent B2 from Bridge 3SC1. Therefore, Piers 1 to 4 of Bridges 3SC1, 3SC6, 2S3aC1 and 2S3aC2 share the same ground spatial coordinates and all four bridges have the same length. As a result, the mean ductility index values Piers 1 to 4 of all four bridges can be plotted in a single figure (see Figure 5.19).

For the purpose of clarity, the pier ductility index values are plotted in Figure 5.19 for each bent as a ductility index line. For example, for Bent B1, which occurs in Bridges 3SC1, 3SC6 and 2S3aC2, the ductility index line is plotted with the ductility index values of Pier 1 and 2 indicated on the left and right ends of the line, respectively. Similarly, for Bent B2, which occurs in Bridges 3SC1, 3SC6 and 2S3aC1, the ductility index line is

plotted with the ductility index values of Pier 3 and 4 on the left and right ends of the line, respectively. As a reference, the plots illustrated Figure 5.11 can be generated from Figure 5.19 if a line is drawn from the ductility index values of Pier 2 and 3 for Bridges 3SC1 and 3SC6.

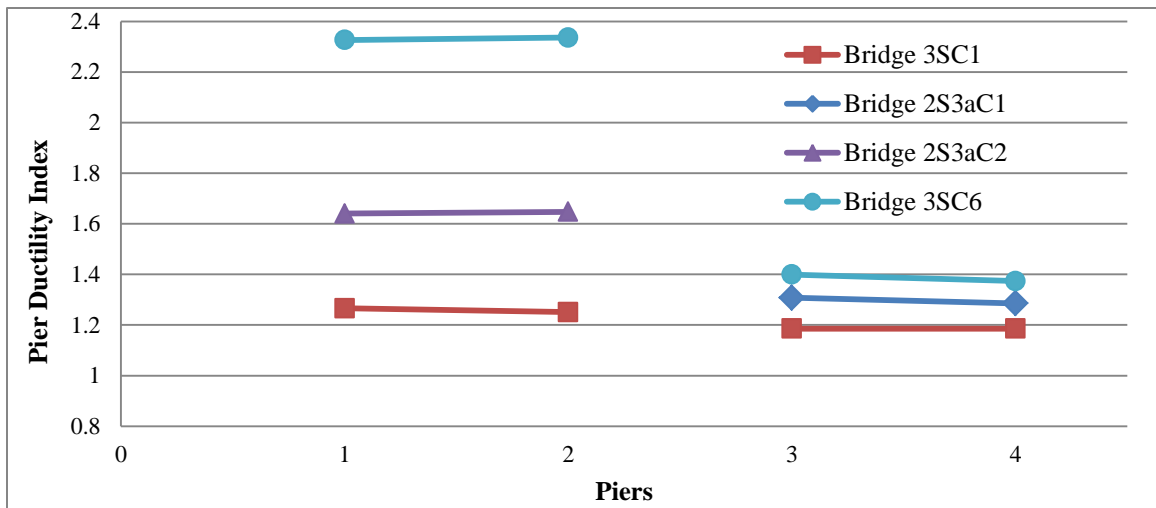


Figure 5.19 Mean Pier Ductility Index Values for Bridges 3SC1, 3SC6, 2S3aC1 and 2S3aC2 Plotted as Bent Ductility Index Lines.

From Figure 5.19, the following conclusions can be drawn by comparing the mean ductility index values of Piers 1 to 4 with the values obtained for Bridge 3SC1 (reference bridge):

1. For Bridges 3SC1 and 3SC6, when comparing the pier ductility index values of the left and right bents, such values are higher for the left bent.
2. For Bridges 2S3aC1 and 2S3aC2, when comparing the pier ductility index values of their single bents, such values are higher for the bent of Bridge 2S3aC2 (which is located to the left side of the bridge).

3. Bridge 3SC6, which is a bridge with variable pier heights and constant span lengths, exhibits the highest pier ductility index values. The increase in the pier ductility index values of this bridge with respect to Bridge 3SC1 is around 42% and 18% for Bents B1 and B2, respectively.
4. Bridge 2S3aC2, which is a bridge with variable span lengths and constant pier heights, shows the second highest ductility index value for Piers 1 and 2 (Bent B1). The increase in the ductility index value of Piers 1 and 2 of this bridge with respect to Bridge 3SC1 is around 32%.
5. Bridge 2S3aC1, which is also a bridge with variable span lengths and constant pier heights, show the second highest ductility index value for Piers 3 and 4 (Bent B2). The increase in the ductility index values of Piers 3 and 4 of this bridge with respect to Bridge 3SC1 is around 10%.

Bridges 2S3aC1 and 2S3aC2 are obtained when a bent frame is taken out of Bridge 3SC1, resulting in bridges with a single bent where one of the spans increased by 100% with respect to the span lengths of Bridge 3SC1. Since a large percentage of the bridge mass is in the superstructure, the lateral inertial forces caused by the seismic excitation on Bridges 3SC1, 2S3aC1 and 2S3aC2 were expected to be similar. In the cases of Bridge 2S3aC1 and 2S3aC2, such forces had to be taken by a single bent frame, which caused an increase in the pier ductility demands of the frame, regardless of whether the seismic excitation was uniform or spatially varying. However, under spatially varying seismic excitation the proportional reduction in the lateral stiffness of the superstructure caused by the 100% increase in length of one of the spans made Bridges 2S3aC1 and



2S3aC2 more susceptible to differential support displacements of bent frame with respect to the abutments. As a result, the pier ductility demands of the bent frame under spatially varying seismic excitation exceeded the values generated under uniform seismic excitation, thus increasing the pier ductility index values.

Since Bridge 3SC1 has two bent frames, the superstructure lateral stiffness value was higher than the value present for Bridges 2S3aC1 and 2S3aC2; thus, smaller differential displacements at the bent frame supports were expected when subjected to spatially varying seismic excitation. As a result, the pier ductility index values of Bridge 2SC1 were smaller than the ductility index values of the corresponding piers of Bridges 2S3aC1 and 2S3aC2.

Finally, the results obtained in this section for two-span and three-span bridges of constant length ( $L = 3a$ ) corroborate the following observation also made in Sections 5.3 and 5.4 for bridges of variable length: the increases in pier ductility index values are more susceptible to increases in pier heights than increases in span lengths. Also, asymmetric arrangements of the span length generate relatively little increase in the pier ductility indexes.

## **5.6 Two-Span to Four-Span Bridge Models with Bridge Length $L = 6a$**

The two-span, three-span and four-span bridge models considered in this section and illustrated in Figure 5.3 were obtained by simply removing 2 to 4 bent frames from Bridge 6SC1. Therefore, all the piers in the remaining bents share the same ground spatial coordinates as the piers in Bridge 6SC1. As a result, the mean ductility index

values of Piers 1 to 10 of all six bridges illustrated in Figure 5.3, along with Bridges 6SC6 and 6SC1 can be plotted in a single figure (see Figure 5.20).

Following the concept introduced in Section 5.4 of expressing the pier ductility index values as bent ductility index lines, the ductility index lines of all eight bridge models that share the same bridge length ( $L = 6a$ ) are plotted in Figure 5.20. As a reference, the plots illustrated Figure 5.18 can be generated from Figure 5.20 if the ductility index lines of Bridges 6SC1 and 6SC6 are joined together by additional lines.

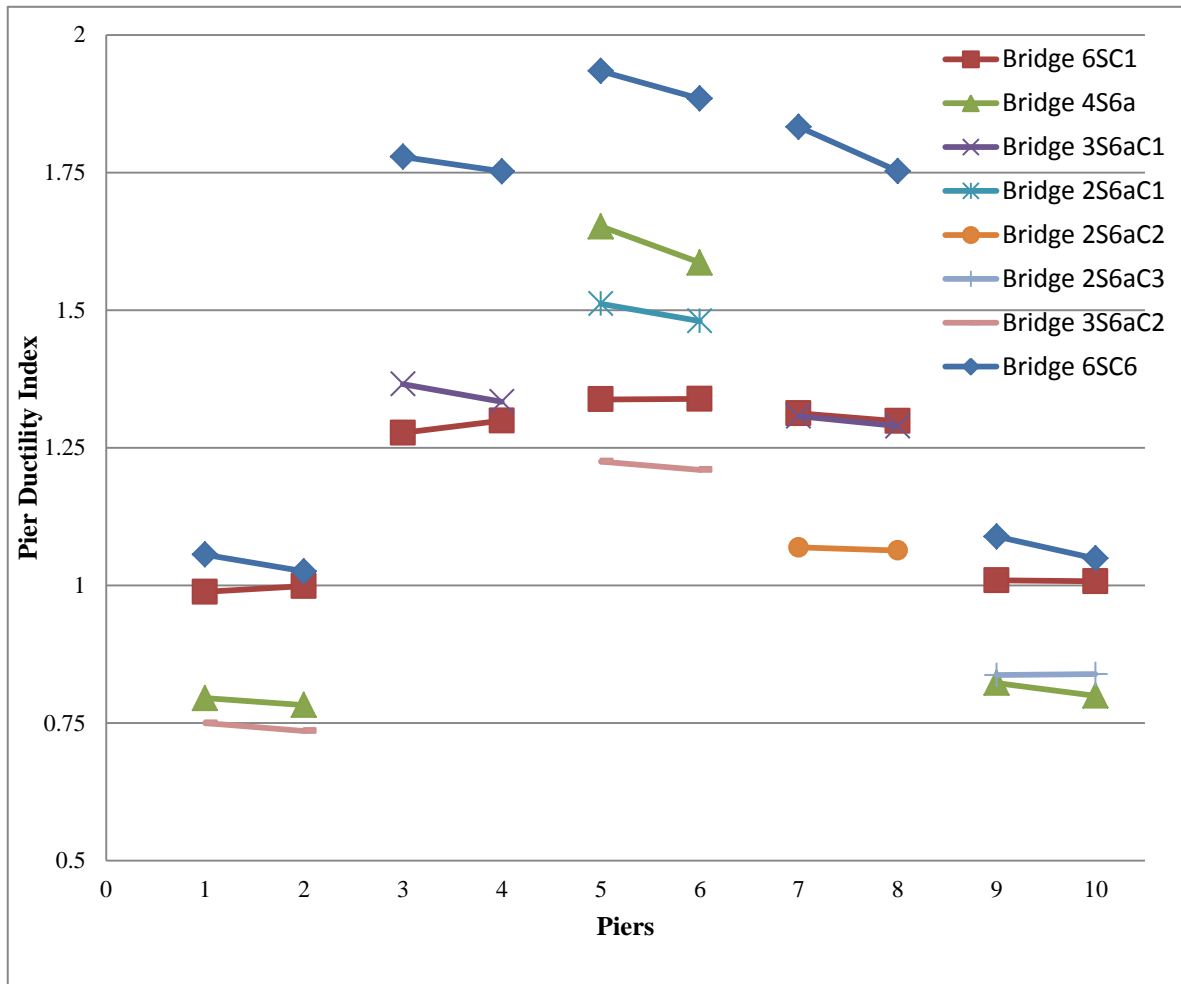


Figure 5.20 Mean Pier Ductility Index Values for Bridges 6SC1, 6SC6, 4S6a, 3S6aC1, 3S6aC2, 3S6aC3, 2S6aC1, 2S6aC2 and 2S6aC3 Plotted as Bent Ductility Index Lines.

From Figure 5.20, the following conclusions can be drawn by comparing the mean ductility index values of all bridges with the values obtained for Bridge 6SC1 (reference bridge):

1. Bridge 6SC6, which is a bridge with variable pier heights and constant span lengths, exhibits the highest pier ductility index increase. The average increase in the ductility index values of piers in interior and exterior bents with respect to Bridge 6SC1 is around 39% and 7%, respectively. The highest increase in ductility index occurs in piers of the midspan bent, where the increase is 43%.
2. Bridge 4S6a, which is a bridge with constant pier heights and variable span lengths, exhibits the second highest pier ductility index increase. The increase in ductility index values of piers in midspan bents with respect to Bridge 6SC1 is around 22%. For piers in exterior bents, the ductility index is less than 1.0.
3. Bridge 2S6aC1, which is a bridge with one bent in the midspan, exhibits the third highest pier ductility index increase. The increase in ductility index values of piers in midspan bent with respect to Bridge 6SC1 is around 12%.
4. Bridge 3S6aC1, which is a bridge with two bents with constant height piers and equal span lengths, exhibits relatively small increases in the pier ductility index values when compared to Bridge 6SC1.
5. Bridge 3S6aC2, which is a bridge with two bents with constant height piers and variable span lengths, exhibits a decrease in the pier ductility index values when compared to Bridge 6SC1.

6. Bridges 2S6aC2 and 2S6aC3, which are bridges with a single bent with constant height piers and variable span lengths with sharp asymmetry, also exhibit a decrease in the pier ductility index values when compared to Bridge 6SC1.

As was previously observed, except for Bridge 6SC6, all other bridges are obtained by taking out bent frames from Bridge 6SC1; thus, these bridges will have one or more span lengths with at least 100% increase in length compared to the span lengths of Bridge 6SC1. As a result, reduction in the lateral stiffness of the superstructure will occur in these bridges, which makes them more susceptible to differential support movement when subjected to spatially varying seismic excitation. Moreover, since all bridges have the same length, the superstructure mass will be the same; however, the decrease in the number of bent frames results in each frame having to take a greater percentage of the lateral inertial force generated by the superstructure mass when subjected to seismic excitation. Therefore, the ductility demand of the piers is expected to increase under spatially varying and uniform seismic excitation.

The compounded effect of the reduction in the lateral stiffness of the superstructure and the reduction in the number of bent frames is expected to generate an increase in the pier ductility indexes of these bridges when compared to Bridge 6SC1. This prediction is corroborated by the pier ductility index values observed in Bridges 4S6a, 3S6aC1 and 2S6aC1, which are all bridges with symmetrical arrangements of span lengths. However, the prediction is not corroborated by the pier ductility index values observed in Bridges 3S6aC2, 2S6aC2 and 2S6aC3, which are all bridges with asymmetrical arrangements in span lengths. Bridges 2S6aC2 and 2S6aC3 have a single

bent frame and since practically all the lateral inertial force generated by the superstructure mass had to be taken by the two piers in this bent, their pier ductility demands exceeded their ductility threshold by more than 500% for both uniform and spatially varying seismic excitation. Since it is highly unlikely that the plastic hinges of these piers will be able to generate that level of plastic rotation required to exceed the ductility threshold by 500%, the resulting state of structural distress will most likely be the destruction of the pier plastic zone for both uniform and spatially varying seismic excitation. Therefore, comparing the ductility index values for these two bridges with the values of Bridge 6SC1 has little practical significance. For the case of Bridge 3S6aC2, although the lateral inertial forces generated by the superstructure mass were distributed among the piers of two bent frames, the resulting pier ductility demands were very close to doubling the ductility threshold for both uniform and spatially varying seismic excitation. Again, the likelihood of the plastic zones of these piers surviving ductility demands close to the 100% of the ductility threshold is low and thus, there is little practical significance in the pier ductility indexes obtained for this bridge.

Finally, the results obtained in this section for two-span to four-span bridges of constant length ( $L = 6a$ ) corroborate the following observation made also in Section 5.5 for two-span bridges of constant length ( $L = 3a$ ) and Sections 5.3 and 5.4 for bridges of variable length: the increases in pier ductility index values are more susceptible to increases in pier heights than increases in span lengths. Also, asymmetrical arrangements of the span lengths did not increase the pier ductility index values mainly because the piers practically failed for both uniform and spatially varying seismic excitation.

## 5.7 Concluding Remarks

When comparing the results of the bridge models considered in this Chapter, it seems that the effects of both the change span length and pier height on the average pier ductility index values are reduced as the length of the bridge increases. In other words, the longer the bridge, the less susceptible the bridge will be to changes in their nonlinear response characteristics under spatially varying seismic excitation caused by changes in the bridge structural geometry. This mainly due to the fact that the increase in length of the bridge generated significant increases in the pier ductility demands and since the pier design was not changed for the longer bridges, the ductility threshold was exceeded sometimes by 500%. Once the ductility threshold is exceeded by a significant amount, the pier plastic zone is likely to sustain unrealistically high plastic rotations and the differences in their response under spatially varying and uniform seismic excitation are reduced. As a result, the pier ductility indexes are reduced.

The asymmetric arrangement of span lengths was observed to generate the highest ductility demands on the piers when compared to symmetrical arrangements, regardless of the bridge length. However, the increase in ductility demand was similar for both uniform and spatially varying seismic excitation, resulting in low values of the pier ductility indexes. As the lengths of the individual spans of the asymmetric bridges were increased, the resulting pier ductility demands also increased to the point of exceeding by more than 100% the ductility threshold. Since that level of ductility demand will most likely cause failure of the pier plastic zone for both spatially varying and uniform seismic excitation, the pier ductility index loses practical significance under those conditions.

Studies of the effect of span length and pier height variability on pier ductility demands of bridges under spatially varying seismic excitation were not found in the published literature. However, Saxena (2000) did consider an existing five-span bridge with an asymmetric pier height arrangement (i.e., all piers had different heights). Although significant differences in the bridge modeling exist when compared to Bridge 6SC6, the behavior of the pier ductility index observed by the piers are similar to the one represented in Figure 5.14, except that the maximum pier ductility index obtained for piers supported on the same soil type was approximately 1.03, which is lower than the value of 1.93 predicted by Figure 5.14. There is very little practical value in comparing both maximums, since the bridges have significant differences in span lengths and pier heights. Lupoi et al (2005) also considered variations in pier heights (with asymmetric and symmetric arrangements) in their parametric studies; however, the results are not presented in terms of pier ductility indexes, but in terms of amplification factors, which are calculated dividing the probability of failure of the bridge due to spatially variable excitation by the probability of failure of the bridge due to uniform seismic excitation. Moreover, they considered variations in the superstructure stiffness in the parametric studies and found such variations more relevant than pier height variations when determining the amplification factors. As was the case with Saxena's bridge models, Lupoi's models also differ significantly with the ones considered in this Chapter.

Finally, it should be mentioned that the sample space of the displacement time history sets used in this Chapter were reduced from 20 to 10 realizations for the spatially varying and uniform seismic excitation. This resulted in relatively small differences in

the pier ductility index values, as can be observed when comparing the Hard Soil Case curve of Figure 4.8 and 4.16 with Figure 5.3 and 5.9, respectively. As was commented in Chapter 3, Saxena (2000) observed that the statistical descriptors of the sample space (mean, standard deviation, etc.) did not change significantly when considering a sample space of 20 or greater realizations. Thus, using 10 realizations did have an effect on the pier ductility index values; however, since the results of this Chapter were presented in terms of relative increases in the pier ductility index of bridges where all bridges considered the 10 realizations, the results presented should not be significantly affected by the reduction of the sample space.



## **6. EFFECT OF SPATIAL VARIABILITY OF SEISMIC EXCITATION WITH A STRONG VERTICAL ACCELERATION COMPONENT AND VARIABILITY OF SOIL CONDITIONS ON PIER DUCTILITY DEMANDS OF MULTI-SPAN BRIDGES**

### **6.1 Introduction**

It is a well-established fact in the technical literature that structures located near the epicenter of a seismic event may be subjected to strong vertical accelerations. Reyes (1997) reported that the ratio of the horizontal to vertical acceleration component (the  $Z$  ratio) may reach 1.10 at distances close to the epicenter. Typical seismic analysis considers  $Z = 0.67$  and the effect of the vertical component is taken indirectly. In Chapters 4 and 5,  $Z = 0.67$  was used to generate the vertical component of a spatially variable seismic excitation and the effect of the increase in the bridge pier axial load generated from such component was determined indirectly from an empirical relationship given in Priestley (1996). Such an empirical relationship was only valid for  $Z = 0.67$  and no empirical relation was found in the literature to account for a variable  $Z$  ratio.

The ideal solution would have been to generate a nonlinear time history algorithm that could instantaneously update the moment-curvature relationships for the piers based on the pier axial load time history variation caused by a three-component spatially varying seismic wave. Once the moment-curvature relationship was updated, then the plastic hinge model could also be updated and a pier ductility demand time history

generated. Such ideal solution is complicated and typically not included in commercially available computer programs such as SAP 2000.

## 6.2 Modeling Methodology

The moment-curvature relationship of the bridge piers depends on the value of the axial load present. Since the plastic hinge model is derived from the moment-curvature relationship of the pier, the plastic hinge properties and hence the ductility range of the piers will also be a function of the axial load. Axial load variations are expected in the piers from the influence of the horizontal seismic components due to bent rigid frame action in the longitudinal and transverse directions, regardless of the magnitude of the vertical seismic component. These variations, along with  $Z = 0.67$ , were accounted for in the bridge piers by performing a plastic analysis procedure on the bridge bent frame, as described in Chapter 3, which resulted in an amplified pier axial load value. The moment-curvature relationship shown in Figure 3.15 was determined based on such an amplified axial load.

In order to investigate the effects on the pier ductility demands of a strong vertical acceleration component in a spatially varying seismic wave, the  $Z$  value was increased from  $0.67$  to  $1.0$ , which represents a typical ratio for seismic waves near the earthquake epicenter, as reported by Reyes (1997). Thus, additional amplification of the pier axial loads would be required to capture the effect of a stronger vertical acceleration component. In this study, a pier axial load amplification factor is generated to account for the  $Z = 1.0$  condition as shown next.

### 6.2.1 Pier Axial Load Amplification Factor

In order to determine the proper amplification factor for the pier axial loads a Monte Carlo Simulation scheme was implemented to study the variations of the pier support vertical reactions as a result of the  $Z$  value changing from  $0.67$  to  $1.0$ . The short, medium and long multi-span bridge models shown in Figure 4.2 were updated by eliminating the plastic hinges and soil spring supports under the pier foundations in order not to bias the vertical reaction values. Such values could be reduced by the energy absorbing capabilities of the plastic hinges and/or the soil spring set; thus, the bridge models were assumed elastic with fixed supports in order to maximize the vertical reaction values. Sets of twenty statistically independent seismic load cases simulating spatially varying three component displacement time histories with  $Z = 0.67$  and  $Z = 1.0$  were generated and time domain analysis was performed the short, medium and long multi-span bridges models illustrated in Figure 4.1 and supported on Hard, Medium and Soft Soil Cases. The pier axial load amplification factor was obtained by dividing the vertical reaction value for  $Z = 1.0$  by the vertical reaction value for  $Z = 0.67$  for each seismic load case. The statistical results for the pier axial load amplification factor are shown in Tables 6.1 to 6.3.

It can be observed in these Tables that except for the case of short multi-span bridge models, the mean and SD values of the pier axial load amplification factor exhibits little variability as the bridge length increases, regardless of the soil case under consideration. Thus, the mean and SD values given in Tables 6.1 to 6.3 were averaged to obtain a global mean and standard deviation. A design value of 1.33 for the pier axial

load amplification factor was obtained by adding the global mean plus twice the global standard deviation. Thus, the axial load value used to obtain the moment-curvature relationship for the bridge piers for  $Z = 0.67$  was multiplied by 1.33 to account for the  $Z = 1.0$  condition. Figure 6.1 shows the calculated and idealized moment curvature relationship for the  $Z = 1.0$  condition and Figure 6.2 show a comparison of the moment-curvature relationships for  $Z = 0.67$  and  $Z = 1.0$ . It can be observed in Figure 6.2 that the difference between both curves is relatively small, except for a 10% reduction in the ultimate curvature for the  $Z = 1.0$  curve with respect to the  $Z = 0.67$  curve; thus, there is a 10% reduction in the ductility range for piers under the  $Z = 1.0$  condition.

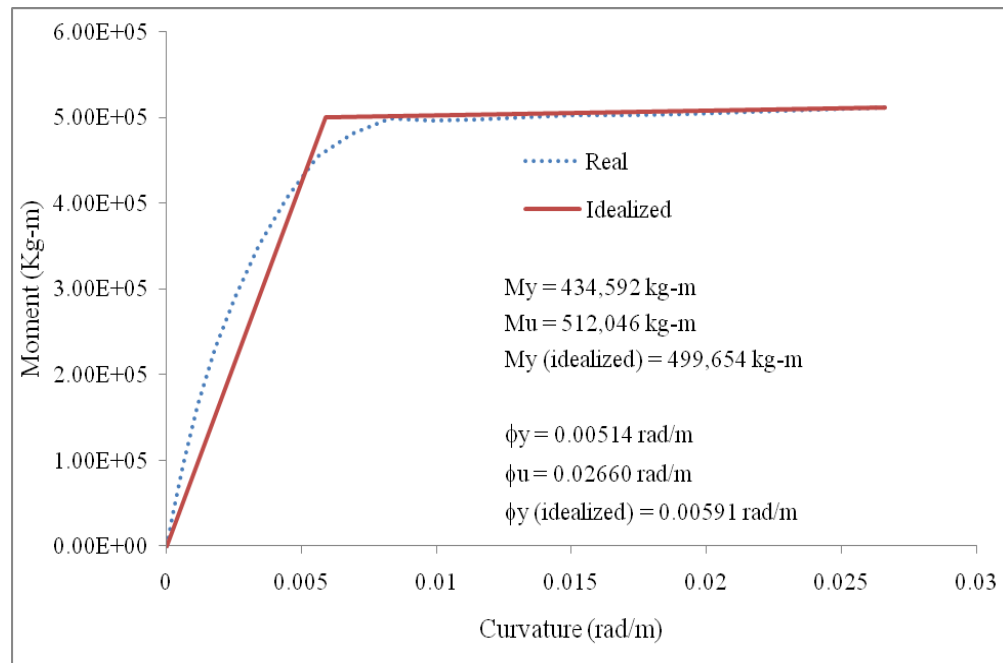


Figure 6.1 Bridge Pier Moment-Curvature Relationship for  $Z = 1.0$

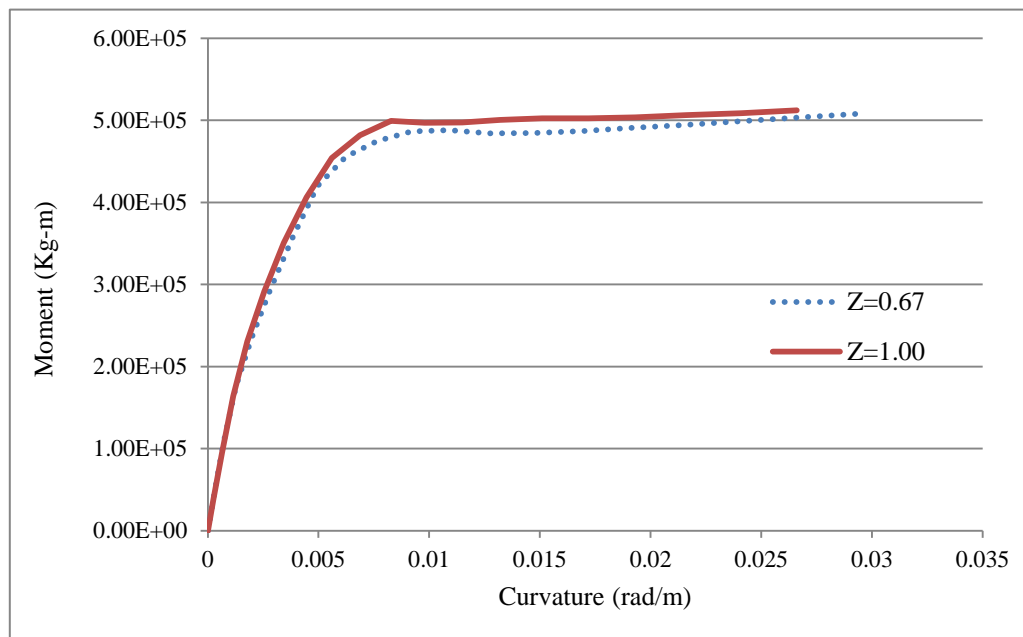


Figure 6.2 Bridge Pier Moment-Curvature Relationships for  $Z = 0.67$  and  $Z = 1.0$

Table 6.1 Pier Axial Load Amplification Factors on Short Multi-Span Bridge Models Subjected to Spatially Varying Seismic Excitation under the  $Z = 1.0$  Condition.

Bent	Pier	Hard Soil Case			Medium Soil Case			Soft Soil Case		
		Mean	SD	COV	Mean	SD	COV	Mean	SD	COV
B1	1	1.07	0.07	0.065	1.09	0.05	0.046	1.15	0.07	0.061
	2	1.07	0.07	0.065	1.09	0.05	0.046	1.17	0.07	0.060
B2	3	1.08	0.06	0.056	1.11	0.08	0.072	1.14	0.12	0.105
	4	1.09	0.05	0.046	1.12	0.07	0.063	1.18	0.10	0.085

Table 6.2 Pier Axial Load Amplification Factors on Medium Multi-Span Bridge Models Subjected to Spatially Varying Seismic Excitation under the  $Z = 1.0$  Condition.

Bent	Pier	Hard Soil Case			Medium Soil Case			Soft Soil Case		
		Mean	SD	COV	Mean	SD	COV	Mean	SD	COV
B1	1	1.12	0.03	0.027	1.14	0.09	0.079	1.14	0.06	0.053
	2	1.12	0.03	0.027	1.14	0.09	0.079	1.17	0.08	0.068
B2	3	1.16	0.06	0.052	1.15	0.07	0.061	1.19	0.10	0.084
	4	1.16	0.08	0.069	1.17	0.10	0.085	1.22	0.13	0.107
B3	5	1.14	0.06	0.053	1.16	0.10	0.086	1.20	0.13	0.108
	6	1.15	0.06	0.052	1.14	0.09	0.079	1.21	0.14	0.116
B4	7	1.14	0.06	0.053	1.15	0.10	0.087	1.19	0.11	0.092
	8	1.15	0.07	0.061	1.16	0.11	0.095	1.21	0.13	0.107
B5	9	1.11	0.03	0.027	1.13	0.06	0.053	1.15	0.11	0.096
	10	1.11	0.04	0.036	1.13	0.09	0.080	1.19	0.13	0.109

The maximum ductility demand that the pier can withstand at the plastic hinge, before reaching the residual flexural strength level (segment DE in Figure 3.5) must be updated for the  $Z = 1.0$  condition. From Figure 6.1, by taking the ratio of the ultimate to idealized yield value of curvature, the maximum ductility demand is calculated as  $0.02660/0.00591 = 4.50$ . As a reference, the maximum ductility demand for the  $Z = 0.67$  condition was calculated as 5.09. Thus, an 11.6% reduction in the maximum ductility value of the plastic hinge model was established to reflect the  $Z = 1.0$  condition.

Table 6.3 Pier Axial Load Amplification Factors on Long Multi-Span Bridge Models Subjected to Spatially Varying Seismic Excitation under the  $Z = 1.0$  Condition.

Bent	Pier	Hard Soil Case			Medium Soil Case			Soft Soil Case		
		Mean	SD	COV	Mean	SD	COV	Mean	SD	COV
B1	1	1.11	0.06	0.054	1.12	0.05	0.045	1.16	0.07	0.060
	2	1.12	0.05	0.045	1.14	0.05	0.044	1.15	0.07	0.061
B2	3	1.13	0.07	0.062	1.16	0.08	0.069	1.17	0.10	0.085
	4	1.14	0.09	0.079	1.14	0.07	0.061	1.18	0.09	0.076
B3	5	1.12	0.08	0.071	1.17	0.09	0.077	1.17	0.08	0.068
	6	1.13	0.09	0.080	1.16	0.08	0.069	1.18	0.09	0.076
B4	7	1.11	0.09	0.081	1.15	0.10	0.087	1.14	0.09	0.079
	8	1.12	0.10	0.089	1.12	0.08	0.071	1.14	0.12	0.105
B5	9	1.11	0.10	0.090	1.15	0.12	0.104	1.16	0.11	0.095
	10	1.11	0.10	0.090	1.12	0.09	0.080	1.16	0.12	0.103
B6	11	1.11	0.09	0.081	1.16	0.12	0.103	1.14	0.10	0.088
	12	1.12	0.11	0.098	1.13	0.11	0.097	1.17	0.12	0.103
B7	13	1.13	0.09	0.080	1.15	0.12	0.104	1.17	0.11	0.094
	14	1.13	0.11	0.097	1.14	0.10	0.088	1.19	0.12	0.101
B8	15	1.12	0.09	0.080	1.18	0.12	0.102	1.17	0.10	0.085
	16	1.13	0.11	0.097	1.15	0.10	0.087	1.20	0.12	0.100
B9	17	1.13	0.09	0.080	1.19	0.10	0.084	1.18	0.09	0.076
	18	1.13	0.10	0.088	1.17	0.09	0.077	1.20	0.10	0.083
B10	19	1.14	0.07	0.061	1.17	0.09	0.077	1.16	0.07	0.060
	20	1.13	0.09	0.080	1.15	0.07	0.061	1.19	0.09	0.076
B11	21	1.10	0.04	0.036	1.15	0.08	0.070	1.15	0.10	0.087
	22	1.10	0.04	0.036	1.15	0.07	0.061	1.17	0.09	0.077

### 6.3 Results for Bridge Pier Ductility Demands

The Monte Carlos Simulation scheme implemented for  $Z = 0.67$  and described in Chapter 4 was repeated using  $Z = 1.0$ . The only relevant update on the bridge models occurred in the plastic hinge model, which was modified to reflect the moment-curvature relationship of the bridge piers given by Figure 6.1. A spatially varying seismic excitation with a strong vertical component was applied to the short, medium and long multi-span bridge models illustrated Figure 4.1 considering the Hard, Medium and Soft Soil Cases given in Tables 4.2 to 4.4 and the pier ductility demands were calculated.

Since the objective of this Chapter is to study the variation of the bridge pier ductility demands when a strong vertical acceleration component is present in a spatially varying seismic wave, a pier ductility index was determined to account for the effect of the strong vertical acceleration component. In this Chapter, this ductility index was renamed the  $Z$  index in order to avoid confusion with the definition of pier ductility index used in Chapters 3 to 5. The  $Z$  index was calculated by dividing the pier ductility values obtained for the spatially varying seismic excitation under the  $Z = 1.0$  condition by the pier ductility values obtained in Chapter 4 for the spatially varying seismic excitation under the  $Z = 0.67$  condition. Thus, the pier ductility demands generated from a uniform seismic excitation under a strong vertical acceleration component was not required in this Chapter.

The general tendencies in the pier ductility demands observed in Chapter 4 for spatially varying seismic waves under the  $Z = 0.67$  were also observed for  $Z = 1.0$  condition. Such tendencies are discussed in depth in Section 4.3 and will not be repeated



here for convenience. Therefore, in order to avoid excessive repetition on the type of graphical and tabular information already presented in Chapter 4, only results that are pertinent to the determination of the  $Z$  index are presented in this Chapter.

### 6.3.1 Short Multi-Span Bridge Models

The statistics for the pier ductility demands for the  $Z = 1.0$  condition in short multi-span bridge models are presented in Table 6.4. Mean values for the  $Z$  index are presented in Table 6.5 and Figure 6.3 shows the same values in graphical form. These values were obtained at each pier location by dividing the ductility demand values for the  $Z = 1.0$  condition by the ductility values for the  $Z = 0.67$  condition for each one of the realizations of the seismic excitation.

Table 6.4 Resultant Pier Ductility Demand on Short Multi-Span Bridge Models Subjected to Spatially Varying Seismic Excitation with a Strong Vertical Acceleration Component ( $Z = 1.0$  Condition).

Bent	Pier	Hard Soil Case			Medium Soil Case			Soft Soil Case		
		Mean	SD	COV	Mean	SD	COV	Mean	SD	COV
B1	1	2.538	0.551	0.217	2.994	0.469	0.157	5.915	0.923	0.156
	2	2.553	0.557	0.218	2.995	0.462	0.154	5.913	0.924	0.156
B2	3	3.895	0.467	0.120	4.443	0.428	0.096	7.581	1.168	0.154
	4	3.865	0.500	0.129	4.433	0.501	0.113	7.525	1.100	0.146

Table 6.5 Mean Z Index Values for Short Multi-Span Bridge Models

Bent	Pier	Hard Soil Case	Medium Soil Case	Soft Soil Case
B1	1	1.018	1.016	1.136
	2	1.022	1.011	1.146
B2	3	0.999	0.990	1.048
	4	0.997	0.986	1.053

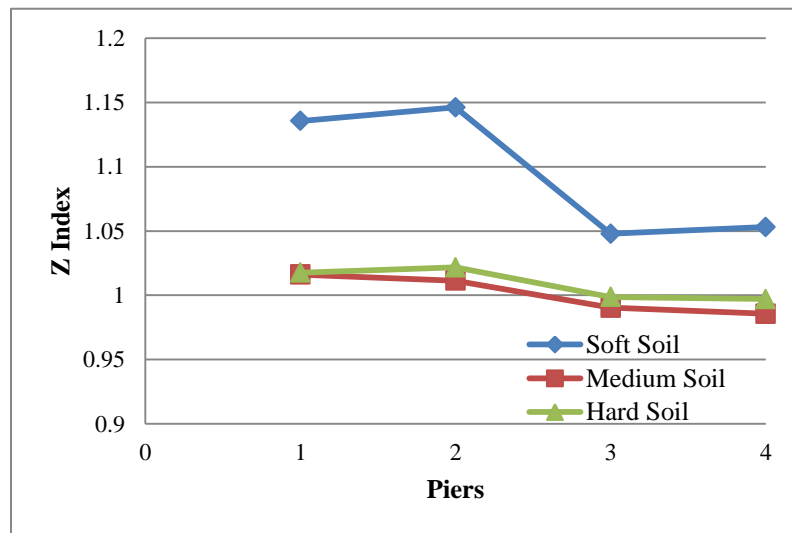


Figure 6.3 Mean Z Indexes for Short Multi-Span Bridge Models

It can be observed in Table 6.4 that the resultant pier ductility demand values exceed the 4.50 threshold only when the short multi-span bridge model is on the Soft Soil Case, thus significant structural distress is predicted at the pier plastic zones for this condition. Such prediction was also made for the  $Z = 0.67$  condition, although a deeper incursion into plastic hinge residual strength zone occurs under the  $Z = 1.0$  condition. For short multi-span bridge models supported on the Medium Soil Case, maximum ductility demand values were very close to the 4.5 threshold, thus some degree of structural

distress at the pier plastic zones is also expected to occur when piers are supported on the Medium Soil Case. This was not the case for the  $Z = 0.67$  condition, where the lower ductility demand coupled with a higher threshold value allowed for a lower structural distress state.

From Table 6.5 and Figure 6.3, it can be observed that for short multi-span bridge models on Hard and Medium Soil Cases, the  $Z$  index is very close to unity for all pier locations, which means that ductility demand values remain practically invariant when changing from the  $Z = 0.67$  to the  $Z = 1.0$  condition. For short multi-span bridge models on the Soft Soil Case, the  $Z$  index values predict a maximum increase of about 15% in the ductility demand when changing from the  $Z = 0.67$  to the  $Z = 1.0$  condition.

Therefore, for short multi-span bridge models, the  $Z$  Index values depend on the type of soil under the piers, but in general the values are close to 1.0 and thus, the strong vertical acceleration component has relatively little effect on the increase in the pier ductility demand. However, the reduction of the pier ductility range, due to the increase in the pier axial load generated by the presence of a strong vertical acceleration component in the seismic wave, can cause a pier to exhibit structural distress at their plastic zone locations even under relatively small increases in the pier ductility demand.

### **6.3.2 Medium Multi-Span Bridge Models**

The statistics for the pier ductility demands for the  $Z = 1.0$  condition in medium multi-span bridges are presented in Table 6.6. Mean values of the  $Z$  Index are presented in Table 6.7 and Figure 6.4 shows the same values in graphical form. It can be observed in Table 6.6 that the ductility demand of all piers supported on the Soft Soil Case and the

piers in exterior bents supported on the Medium Soil Case exceed the 4.50 threshold value and as a result, are subjected to significant structural distress at their plastic zone locations. As a reference, for the  $Z = 0.67$  condition, only piers on exterior bents supported on Soft Soil Case were found to exceed the threshold value. Similar to the  $Z = 0.67$  condition, maximum ductility demands were observed to occur on piers located on exterior bents, regardless of the soil case under consideration.

Table 6.6 Resultant Pier Ductility Demand on Medium Multi-Span Bridge Models Subjected to Spatially Varying Seismic Excitation with a Strong Vertical Acceleration Component ( $Z = 1.0$  Condition).

Bent	Pier	Hard Soil Case			Medium Soil Case			Soft Soil Case		
		Mean	SD	COV	Mean	SD	COV	Mean	SD	COV
B1	1	3.895	0.508	0.130	4.599	0.795	0.173	6.671	1.024	0.154
	2	3.886	0.525	0.135	4.598	0.765	0.166	6.465	1.008	0.156
B2	3	3.671	0.366	0.100	4.312	0.828	0.192	5.899	0.870	0.147
	4	3.653	0.346	0.095	4.306	0.774	0.180	5.82	0.756	0.130
B3	5	3.769	0.365	0.097	4.277	1.226	0.287	5.822	1.047	0.180
	6	3.689	0.405	0.110	4.307	1.326	0.308	5.678	0.927	0.163
B4	7	3.681	0.324	0.088	4.298	0.914	0.213	5.729	1.157	0.202
	8	3.649	0.327	0.090	4.327	0.896	0.207	5.613	1.030	0.184
B5	9	4.028	0.362	0.090	4.590	0.760	0.166	6.447	0.573	0.089
	10	4.006	0.371	0.093	4.624	0.781	0.169	6.322	0.564	0.089

It can be noticed in Table 6.7 and Figure 6.4 that the mean values of the Z Index are close to unity for all pier locations supported on Hard and Medium Soil Cases, which indicates that relatively small increases in the pier ductility demand are predicted when

changing from the  $Z = 0.67$  to the  $Z = 1.0$  condition. For piers supported on the Soft Soil Case, a maximum increase of 13% in the ductility demand is predicted at pier at exterior bent locations when changing from the  $Z = 0.67$  to the  $Z = 1.0$  condition. Also, it can be observed in Figure 6.4 that the degree of variability in the Z Index value along the bridge length is the greatest when piers are supported on the Soft Soil Case, with the maximum values of the Z Index occurring at the piers located at exterior bents. Moreover, as was the case for short multi-span bridge models, the strong vertical acceleration component will generate a reduction in the pier ductility range, causing more piers to exhibit significant structural distress in medium multi-span bridge models, even though the relative increase in the pier ductility demand associated with the strong vertical acceleration component was found to be small.

Table 6.7 Mean Z Indexes Values for Medium Multi-Span Bridges

Bent	Pier	Hard Soil Case	Medium Soil Case	Soft Soil Case
B1	1	1.009	1.011	1.130
	2	1.019	1.014	1.115
B2	3	1.010	1.017	1.007
	4	1.003	1.003	1.032
B3	5	1.016	0.994	1.028
	6	0.998	1.010	1.032
B4	7	1.008	1.002	1.005
	8	1.003	0.992	1.032
B5	9	1.025	1.026	1.097
	10	1.025	1.025	1.096

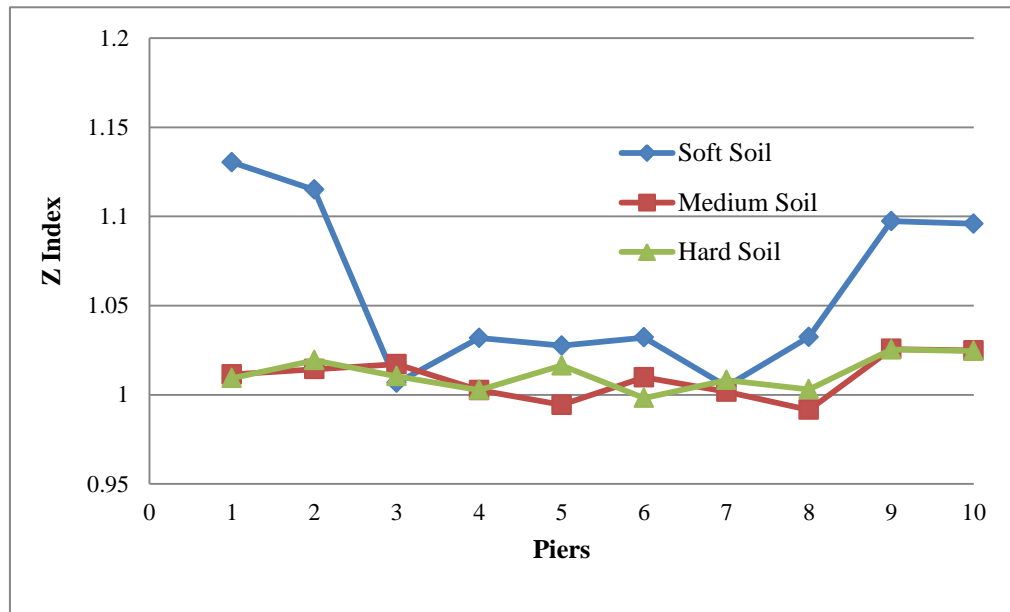


Figure 6.4 Mean Z Indexes for Medium Multi-Span Bridge Models

### 6.3.3 Long Multi-Span Bridge Models

The statistics for the pier ductility demands for the  $Z = 1.0$  condition in long multi-span bridge models are presented in Table 6.8. Mean values of the Z Index are presented in Table 6.9 and Figure 6.5 shows the same values in graphical form. It can be observed in Table 6.8 that the ductility demand of all piers supported on the Soft Soil Case and the piers located on interior bents and supported on Medium and Hard Soil cases exceed the 4.50 threshold value and as a result, their plastic zones are subjected to significant structural distress. As a reference, for the  $Z = 0.67$  condition, only piers supported on the Soft Soil Case were found to exceed the threshold value. Similar to the  $Z = 0.67$  condition, maximum ductility demand values in long multi-span bridge models were observed to occur on piers located on interior bents, regardless of the soil case under consideration, with maximum overall values occurring when piers are supported on the

Soft Soil Case. For medium multi-span bridge models, the maximum ductility demand values were found to occur on piers located on exterior bents, thus the increase in the bridge length does have an effect on the location of the piers that exhibit such values. As discussed in Chapter 4, the probable reason for this fact is the predominance of the transverse seismic response of the bridge due to the reduction in the lateral bending stiffness of the superstructure for the longer length bridges.

It can be observed in Table 6.9 and Figure 6.5 that the degree of variability in the  $Z$  Index value is similar, regardless of the soil case, except for piers located in exterior bents and supported on the Soft Soil Case. For piers supported on Hard and Medium Soil Cases, the increase in the pier ductility demand when changing from the  $Z = 0.67$  to the  $Z = 1.0$  condition was found to be relatively small. The same was found to be true when piers were supported on the Soft Soil Case, except for piers located on exterior bents, where an increase of around 10% was predicted in the ductility demand when changing from the  $Z = 0.67$  to the  $Z = 1.0$  condition.

As was the case for short and medium multi-span bridge models, the number of piers in long multi-span bridge models found to be under significant structural distress increased under a strong vertical acceleration component even though the increase in the ductility demand associated with these components was found to be relatively small. In fact, for the long multi-span bridge models, even when the bridge was supported on the Hard Soil Case, several piers located in interior bents were predicted to exhibit significant structural distress under a strong vertical acceleration scenario.

Table 6.8 Resultant Pier Ductility Demand on Long Multi-Span Bridges Models Subjected to Spatially Varying Seismic Excitation with a Strong Vertical Acceleration Component ( $Z = 1.0$  Condition).

Bent	Pier	Hard Soil Case			Medium Soil Case			Soft Soil Case		
		Mean	SD	COV	Mean	SD	COV	Mean	SD	COV
B1	1	3.898	0.675	0.173	4.302	0.852	0.198	6.779	1.057	0.156
	2	3.907	0.668	0.171	4.355	0.849	0.195	6.605	1.02	0.154
B2	3	3.463	0.651	0.188	3.948	0.656	0.166	4.576	1.208	0.264
	4	3.520	0.690	0.196	3.891	0.599	0.154	4.616	0.997	0.216
B3	5	3.424	0.858	0.251	3.533	0.876	0.248	6.082	1.146	0.188
	6	3.510	0.851	0.242	3.592	0.814	0.227	6.304	1.147	0.182
B4	7	3.875	0.817	0.211	3.995	1.126	0.282	6.775	1.54	0.227
	8	3.976	0.834	0.210	4.088	1.073	0.262	7.212	1.436	0.199
B5	9	4.515	0.667	0.148	4.807	1.255	0.261	7.663	1.538	0.201
	10	4.597	0.830	0.181	4.842	1.265	0.261	8.034	1.497	0.186
B6	11	4.863	1.002	0.206	4.907	1.188	0.242	8.121	1.742	0.215
	12	4.913	0.971	0.198	5.030	1.184	0.235	8.518	1.675	0.197
B7	13	4.847	1.249	0.258	4.633	1.099	0.237	7.902	1.427	0.181
	14	4.911	1.259	0.256	4.695	1.071	0.228	8.223	1.329	0.162
B8	15	3.845	0.825	0.215	4.237	1.569	0.370	6.769	1.632	0.241
	16	3.891	0.856	0.220	4.373	1.562	0.357	7.077	1.474	0.208
B9	17	3.382	0.679	0.201	3.726	1.083	0.291	5.826	1.478	0.254
	18	3.440	0.644	0.187	3.803	1.118	0.294	6.109	1.244	0.204
B10	19	3.396	0.655	0.193	3.833	1.024	0.267	6.137	1.19	0.194
	20	3.363	0.727	0.216	3.892	1.045	0.268	6.166	1.073	0.174
B11	21	4.087	0.708	0.173	4.275	1.128	0.264	7.911	1.179	0.149
	22	4.044	0.699	0.173	4.275	1.110	0.260	7.828	1.011	0.129



Table 6.9 Mean Z Index Values for Long Multi-Span Bridge Models

Bent	Pier	Hard Soil Case	Medium Soil Case	Soft Soil Case
B1	1	1.014	1.006	1.098
	2	1.003	1.012	1.103
B2	3	1.000	1.026	1.002
	4	1.005	0.985	1.014
B3	5	1.012	1.000	1.026
	6	1.005	1.000	1.019
B4	7	0.993	1.004	1.004
	8	0.993	1.023	0.998
B5	9	1.008	1.011	1.000
	10	1.009	1.008	0.998
B6	11	0.995	1.002	1.003
	12	1.003	1.007	1.006
B7	13	1.023	1.016	1.016
	14	1.022	1.005	1.009
B8	15	0.996	0.992	1.006
	16	1.017	0.992	0.999
B9	17	1.010	1.026	1.033
	18	0.998	1.018	1.035
B10	19	1.007	1.014	1.028
	20	0.982	1.012	1.028
B11	21	1.020	1.005	1.091
	22	1.012	0.976	1.096

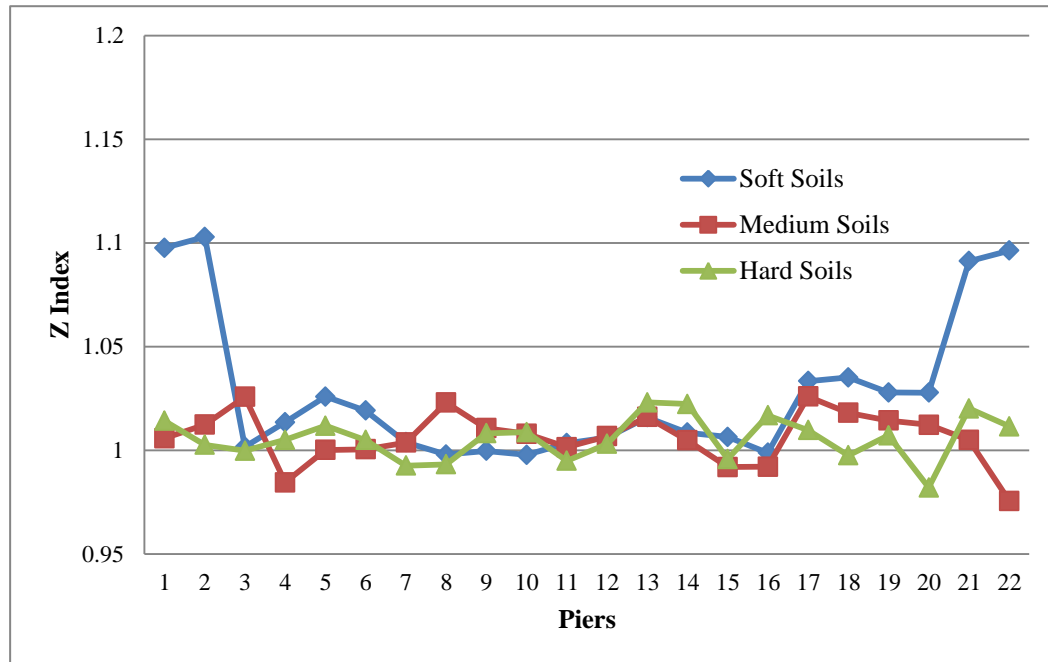


Figure 6.5 Mean Z Indexes for Long Multi-Span Bridge Models

#### 6.4 Concluding Remarks

The presence of a strong vertical acceleration component can be modeled by multiplying the corresponding time history record by an appropriate scaling factor  $Z$ . A value of  $Z = 1.0$  was found to be adequate based on actual seismic records obtained near earthquake epicenters as discussed in Section 6.1. The methodology presented by Priestley et al (1996) to determine pier axial loads that accounts for seismic excitation under the typical  $Z = 0.67$  condition was updated in the Chapter to consider the  $Z = 1.0$  condition using the Monte Carlo Simulation procedure presented in Section 5.2.1. A pier axial load amplification factor of 1.33 was found to be adequate to account for the  $Z = 1.0$  condition.

Based on the results obtained in the Chapter on pier ductility demands for multi-span bridges subjected to spatially varying seismic excitation with a strong vertical acceleration component, the following conclusions can be made:

1. The increase in the pier axial load caused by the increase in the  $Z$  factor reduces the ductility range of the pier as defined by its moment-curvature relationship. For the piers considered in this Chapter, the ductility range was reduced by approximately 12% when increasing the  $Z$  value from 0.67 to 1.0 and the plastic hinge model was updated accordingly.
2. Regardless of the length of the bridge, the  $Z$  Index was found to be in the range of 1.0 to 1.15 for piers supported on the Soft Soil Case. For piers supported on Hard and Medium Soil Cases, the range was found to be 1.0 to 1.03. Thus, up to a 15% increase in pier ductility demand can be expected for piers supported on the Soft Soil Case when increasing the  $Z$  value from 0.67 to 1.0. For piers supported on Hard and Medium Soil Cases, such increase is not expected to exceed 3%.
3. Although the increases in pier ductility demand were found to be relatively small when increasing the  $Z$  value from 0.67 to 1.0, the resulting reduction in the pier ductility range caused more piers to exceed their ductility threshold. Therefore, more piers are expected to experience significant structural damage in their plastic zones as a result of the increase in the  $Z$  value increasing the  $Z$  value from 0.67 to 1.0.

Perhaps the most relevant conclusion that can be drawn from the results of this Chapter is that the presence of a strong vertical acceleration component in the seismic excitation will tend to reduce the flexural ductility of the piers. This will tend to increase the number of piers exhibiting significant structural damage in their plastic zone and thus may reduce the chances of the bridge remaining in service after a strong earthquake. Since the strongest motions often occur near the earthquake epicenter, bridges close to the epicenter will be most likely exposed to strong vertical and horizontal components and their combined effects should be accounted for in the pier design in order to maximize the chances of the bridge remaining in services after the earthquake.

Finally, no published research was found in the literature review on bridge response under spatially varying seismic excitation with a strong vertical acceleration component and as a consequence, none of the results obtained this Chapter could not be compared to results obtained by others.

## 7. SUMMARY, CONCLUSIONS AND RECOMMENDATIONS

### 7.1 Summary

In this study, a methodology is presented to consider the three dimensional dynamic nonlinear response of reinforced concrete bridges subjected to spatially varying seismic ground motion. Multi-component spatially varying acceleration time history records were generated under each bridge pier support location using a stochastic algorithm that accounted for loss of wave coherence, wave passage effects and local soil conditions. Statistical independence of all time histories was assured by changing the seed number in the random number generator of the algorithm. Displacement time histories were obtained from the acceleration time history values by using numerical integration. Post-processing techniques were used to eliminate undesired high and low frequency response, as well as to minimize linear trends and offsets in the displacement time history curves.

Three-dimensional finite element models were generated for short, medium and long multi-span bridges with constant and variable span lengths and pier heights. Nonlinear behavior was restricted at plastic zone locations at the pier ends, which were modeled as bidirectional plastic hinges, allowing the rest of the bridge structure to respond elastically under seismic excitation. Abutments and pier footings were modeled using soil springs sets whose stiffness coefficients were determined based on the dynamic soil stiffness properties, as well as the dimensions and depth of embedment of the footings in accordance with FEMA 356 criteria.

A nonlinear time domain analysis was performed under a Monte Carlo Simulation scheme on short, medium and long multi-span bridge models with constant and variable span lengths and pier heights using seismic load case sets composed of statistically independent displacement time history records. Pier ductility demands and ductility indexes were determined at the plastic hinge locations considering variation in the soil conditions under the piers, variation in the pier axial loads due the presence of a strong vertical acceleration component and variations of the span length and pier height of the multi-span bridge models.

Two plastic hinges were considered per pier, one coinciding with the pier-cap beam interface and the other with the pier-footing interface. Thus, two ductility demand values were obtained per pier. For practical purposes, only the maximum value per pier was reported in this study, although the plastic hinge exhibiting such value was identified. The plastic hinges were modeled using FEMA 356 criteria and the moment-curvature relationship of the pier. In accordance with FEMA 356, a residual bending strength was considered for each plastic hinge to account for the possibility of the plastic rotations exceeding the ultimate rotation predicted from the moment-curvature relationship. This feature of the plastic hinge model allowed for the determination of a threshold value of the pier ductility demand beyond which the pier was predicted to exhibit significant structural distress at the plastic zone locations.

## 7.2 Conclusions

On the basis of the results obtained in this study, several important conclusions can be drawn on the pier ductility demands and pier ductility indexes of bridges subjected to spatially varying seismic excitation.

Some of the major conclusions on pier ductility demands of multi-span bridges with constant span lengths and pier heights supported on variable soil conditions and subjected to a spatially varying and uniform seismic excitation are:

1. The pier ductility demand depends on the length of the bridge and on the type of soil under the pier supports, regardless of whether the seismic excitation is spatially varying or uniform.
2. Consideration of uniform seismic excitation (disregarding the spatially varying nature of the seismic wave) will in general cause an underestimation of the pier ductility demand, regardless of the length of the bridge and the type of soil under the pier supports. The magnitude of the underestimation was found to be in the range of 21% to 64% (i.e., the pier ductility index range was found to be 1.21 to 1.64), depending on the bridge length, on the location of the pier within the bridge length and on the type of soil under the pier supports. The minimum underestimation occurring in short multi-span bridge models supported on Hard Soil Case and the maximum underestimation occurring in long multi-span bridge models supported on Soft Soil Case.
3. The location of the maximum ductility demand within a typical pier depends mainly on the type of soil under the pier support. When supported on hard soils,

the maximum ductility demand occurs on the interface of the pier and foundation (bottom plastic hinge) and when supported on soft soils, the maximum ductility demand occurs on the interface of the pier and cap beam (top plastic hinge). When piers are supported on medium type soils, the location of the maximum ductility demand within the pier will be uncertain and can occur on the top or bottom plastic hinge, depending on the particular seismic load case under consideration.

4. Maximum pier ductility demand values depend on the length of the multi-span bridge and the type of soil under the pier support. For a given bridge length, maximum values occur when piers are supported on soft soils. For a given soil type, maximum values occur in long multi-span bridge models.
5. In general significant pier ductility demand are expected to occur for bridges built on soft soils, regardless of the length of the bridge; thus, consideration should be given to removing the soft soil layer and replacing it with medium to hard soil types prior to the construction of the pier foundations. Another alternative would be to design the pier end zones to be able to withstand the high ductility demands associated with soft soil supports. Practical considerations, such as materials, equipment and labor expenses would have to be evaluated in a case by case basis in order to determine the most convenient alternative.
6. The location of the pier with the maximum pier ductility demand depends mainly on the length of the bridge. For long multi-span bridge models, the piers located



on interior bents exhibit the maximum values, while for medium multi-span bridge models, the piers located on exterior bents exhibit the maximum values.

7. Pier ductility demand values in the transverse and longitudinal direction of the bridge may exhibit significant differences. For short and long multi-span bridge models, maximum values typically occur in the transverse direction. For medium multi-span bridges models, maximum values typically occur in the longitudinal direction. The relative degree of variability along the span of the longitudinal and transverse pier ductility demand values was found to be related to the lateral stiffness of the bridge superstructure, the number of piers in the transverse and longitudinal direction and the type of soil.
8. Two-dimensional simplifications of the bridge structural model may generate unconservative designs of the bridge piers given the fact that in some cases, the maximum ductility demand may be in the out of plane direction. Thus, three-dimensional bridge models are recommended under such scenario, especially if rectangular piers are used, due to their bending strength asymmetry.

Some of the mayor conclusions on pier ductility indexes of multi-span bridges with variable span lengths or pier heights are:

9. The pier ductility index increases more when variations of pier heights are considered than when variations of span lengths are considered, regardless of the length of the bridge. However, the magnitude of the increase seems to be related to the total length of the bridge, where the greatest increase is obtained for the shorter bridges.

10. When considering only pier heights increases, average ductility index increases with respect to constant pier height case of 52% and 28% for three-span and six-span bridges of variable total length, respectively were observed. For two-span and three-span bridges of constant length ( $L = 3a$ ) with variable pier heights, the maximum increase in the pier ductility index was found to be 42%. For two-span to four-span bridges of constant length ( $L = 6a$ ) with variable pier heights, the maximum increase in pier ductility index was found to be 39%.
11. When considering only span lengths increases, average pier ductility index increases with respect to the constant span length case of up to 8% were observed when the span length increases transformed a short multi-span bridge into a medium multi-span bridge. When the span length increases transformed a medium multi-span bridge into a long multi-span bridge, average pier ductility index increases with respect to the constant span length case of up to 14% were observed.
12. For short multi-span bridges becoming medium multi-span bridges due to a 100% increase in length with constant span lengths, the average pier ductility index of the bridge is found to decrease by 8%. The significant loss of superstructure lateral stiffness as the bridge length doubled in magnitude was found to be the most likely cause. Thus, the isolated effect of considering different increments in span lengths to reach the 100% increment in bridge length accounts for a net increase of 16% in the average pier ductility index of the bridge.

13. For medium multi-span bridges becoming long multi-span bridges due to a 100% in length with constant span lengths, the average pier ductility index of the bridge is found to increase by 8%. Thus, the isolated effect of considering different increments in span lengths to reach the 100% increment in bridge length accounts for a net increase of up to 6% in the average pier ductility index of the bridge.
14. The magnitude of the net increase in the average pier ductility index due exclusively to changes in the span length and the pier height is dependent on the length of the bridge; the longer the bridge, the smaller the increase.
15. Asymmetric arrangements of span lengths were found to generate the highest pier ductility demands when compared to symmetric arrangements, regardless of the length of the bridge. In general, pier ductility demands for asymmetric configurations increased with the increase in the length of the bridge. However, the increase in ductility demand was observed to be similar for both spatially varying and uniform seismic excitation, thus generating low values of the pier ductility index.

Some of the mayor conclusions on pier ductility demands of multi-span bridges with constant span lengths and pier heights subjected to spatially varying seismic excitation with a strong vertical acceleration component are:

16. An increase in the pier axial load occurs as a result of an increase in the ratio of magnitude of vertical to the horizontal acceleration component (defined as the  $Z$  ratio). Current design codes assume  $Z = 0.67$ , which was increased to  $Z = 1.0$  to account for the strong vertical acceleration component observed in seismic waves

at close distances to an earthquake epicenter. An amplification factor of 1.33 applied to the pier axial load obtained for the  $Z = 0.67$  was found to be appropriate for the  $Z = 1.0$  condition, based on a Monte Carlos Simulation study.

17. The increase in the axial load reduces the ductility range of the pier, which is defined by the difference between the ultimate and yield curvature values given in the pier moment-curvature relationship. Significant structural distress is predicted at the pier plastic zone locations when the ductility range is exceeded, since the flexural strength of the pier drops to a residual value in accordance with FEMA 356 criteria.
18. The increase of the pier ductility demand due to the presence of the strong acceleration component was found to be relatively small, regardless of the length of the bridge. For multi-span bridges supported on Hard and Medium Soil Cases, the increase did not exceeded 5%. For multi-span bridges supported on Soft Soils Case, the increase did not exceeded 15%.
19. For multi-span bridges supported on the Soft Soil Case, regardless of the length of the bridge, the pier ductility range was exceeded for the  $Z = 1.0$  condition and practically all piers exceeded the ductility range for the  $Z = 0.67$  condition. Thus, such piers are predicted to be in a state of significant structural distress under the seismic event considered in this study, regardless of the value of  $Z$ .
20. For multi-span bridge supported on Medium and Hard Soil Case, regardless of the length of the bridge, none of the pier ductility demands were found to exceed the pier ductility range for the  $Z = 0.67$  condition. However, some ductility demand

values in piers of short, medium and long multi-span bridges supported on Medium Soil Case, and some piers of long multi-span bridges supported on Hard Soil Case, exceeded the pier ductility range for the  $Z = 1.0$  condition. Thus, the presence of strong vertical acceleration components in the spatially varying seismic excitation may increase the number of piers predicted to be in significant structural distress even in cases when such piers are supported on hard or medium soils.

21. The relevant factor for bridges subjected to a strong vertical acceleration component was found to be the reduction of the pier ductility range caused by the increase in the axial load, since this caused an increase in the number of piers predicted to be in significant structural distress, even though the increase in the ductility demand associated with the strong vertical acceleration component was found to be relatively small.

### **7.3 Recommendations for Further Research**

The following recommendations for further research are suggested:

1. The FEMA 356 plastic hinge model does not account for hysteretic damping or strength degradation. More research is needed to determine the effect on the pier ductility demands when plastic hinge models that account for such advanced features are used in evaluating the three-dimensional response of the bridge.
2. Circular piers were used in bridge models to ensure bending strength symmetry and to allow for decoupling of the pier ductility demands in the transverse and

longitudinal direction. Many piers in existing bridges have rectangular, elliptical or other geometrical configurations where bending strength asymmetry is present. More research is needed to determine the effects on the pier ductility demands of piers with these characteristics.

3. The moment-curvature relationships of the piers are a function of the axial load present and in this study it was shown that the reduction in the ductility range of the pier may be the most significant factor when determining their structural performance under spatially varying seismic excitation with a strong vertical component. More research is needed to generate pier ductility demand time histories based on instantaneous updates on the moment-curvature relationships (and thus the plastic hinge model) based on the axial load time history of the pier.
4. The kinetic and kinematic effects of soil-structure interaction (SSI) were disregarded in this study due to the lack of generally accepted methods to incorporate these effects in time history analysis. Since it has been proven by other researchers, such as Sextos (2003) that disregarding the SSI effects may not always lead to conservative results in bridge design, more research is needed in order to properly consider SSI in nonlinear time history analysis. For example, development of nonlinear or bilinear dynamic soil spring stiffness functions that account for reduction of soil stiffness as a function of spring deformations.
5. The lateral stiffness of the bridge superstructure was observed to play an important part in determining the pier ductility demand of short multi-span bridge models. The parametric studies performed by Lupoi et al (2005) also confirm this

fact. Therefore, more research is needed in studying the effects of bending stiffness variations of the superstructure on pier ductility demands of three-dimensional bridge models subjected to spatially varying seismic excitation.

6. Changes in pier heights and span length of bridges under uniform soil conditions can cause increases in the pier ductility index. Since changes in the soil conditions were observed to significantly increase the pier ductility demand of bridges with constant span lengths and pier heights, more research is needed to study the effect on pier ductility demands of bridges with variable geometry under variable soil conditions. Particularly for bridge geometries that involve both asymmetric arrangements of span lengths and pier heights.
7. In this study, the failure limit state for the bridges was assumed to occur when the plastic hinges at the pier end zones reached their residual flexural stress region. More research is needed to study other bridge limit states, such as unseating of superstructure girders, shear and bending failure of cap beams or superstructure, as well as serviceability limit states dealing with allowable bridge deformation.

**APPENDIX A**

**REPRESENTATIVE ACCELERATION, VELOCITY AND DISPLACEMENT**

**TIME HISTORY GRAPHS IN SHORT MULTI-SPAN BRIDGES**

The synthetic spatially varying acceleration time histories generated in this study under each bridge pier support had three components: One in the longitudinal direction  $A_X$ , one in the transverse direction  $A_Y$  and one in the vertical direction  $A_Z$ . In order to avoid excessive repetition of similar graphs, in this appendix only one seismic load case of the longitudinal component  $A_X$  for a short bridge model (see Figure 3.10) supported on hard, medium and soft soil cases (as defined in Table 3.5) are shown. As stated in Chapter 3, regardless of the soil case under consideration, all abutments were assumed supported on hard soil, reflecting the fact that typically these abutments are constructed on bridge approaches, which are made of well graded and compacted engineered soils.

Since SAP2000 requires displacement time histories as the input quantity, each acceleration component had to be numerically integrated to obtain the velocity component and each velocity component had to be numerically integrated once more to obtain the displacement component. The velocity components  $V_X$  and displacement components  $D_X$  integrated from the acceleration components  $A_X$  are also shown here.



### A.1 Time History Graphs for Short Multi-Span Bridge Model Supported on Hard Soil Case.

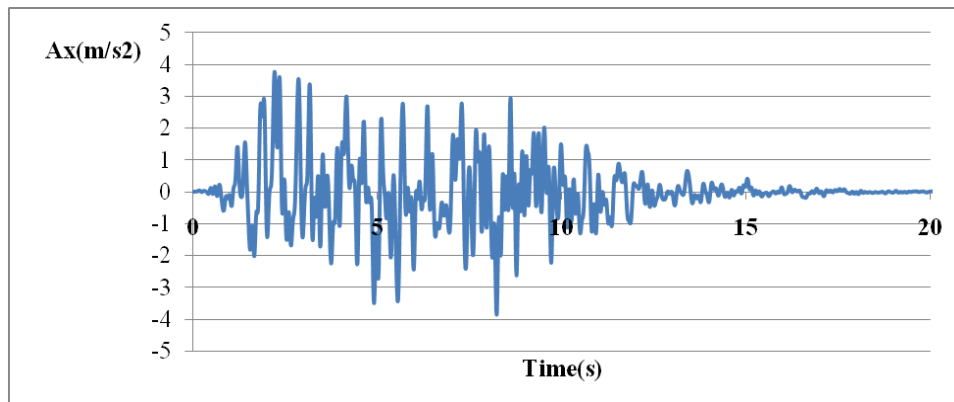


Figure A.1 Left Abutment Acceleration Component Time History for Hard Soils

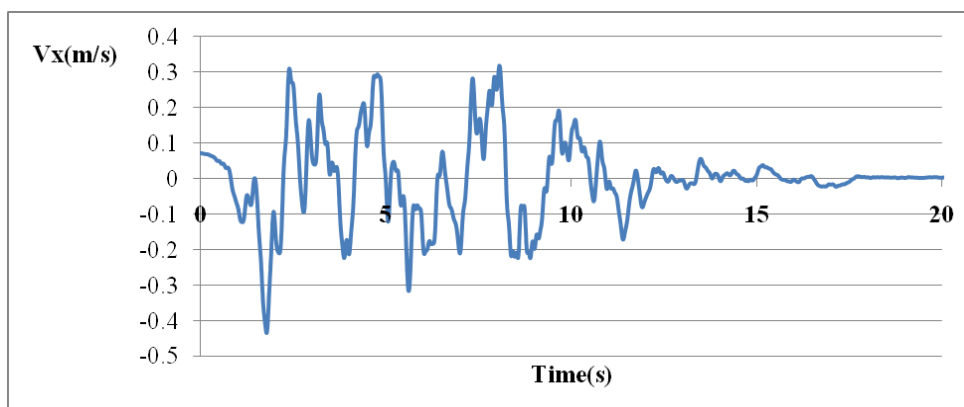


Figure A.2 Left Abutment Velocity Component Time History for Hard Soils

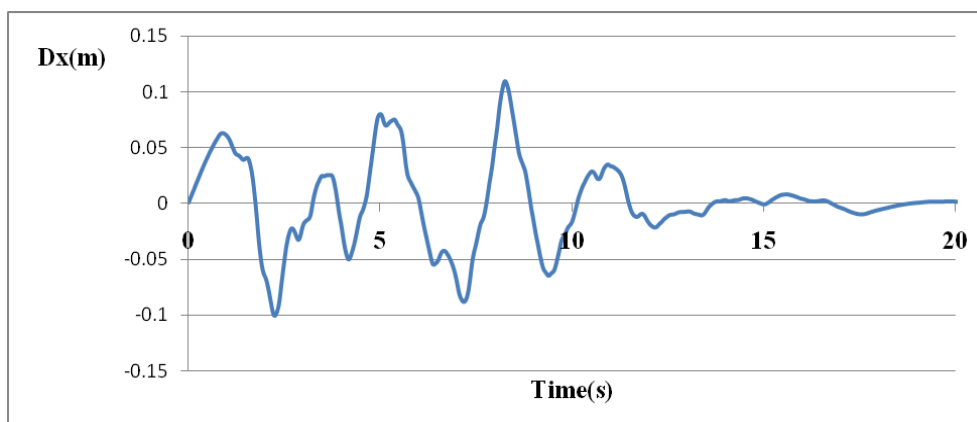


Figure A.3 Left Abutment Displacement Component Time History for Hard Soils

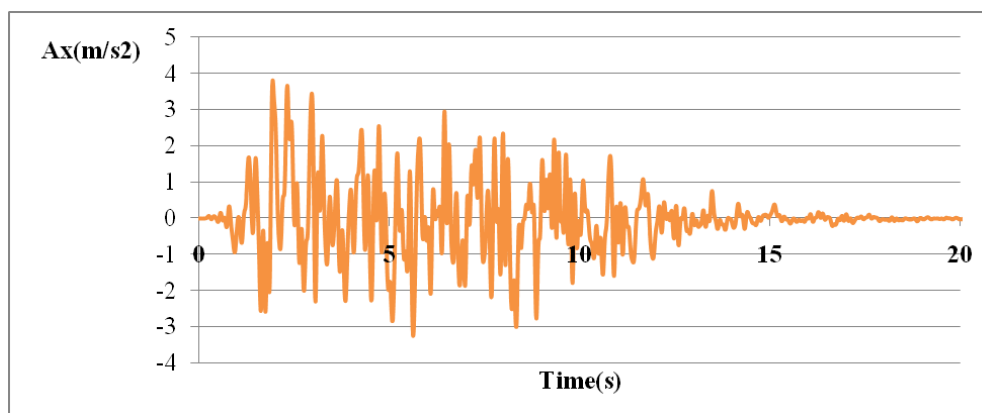


Figure A.4 Bent 1 (Piers 1&2) Acceleration Component Time History for Hard Soils

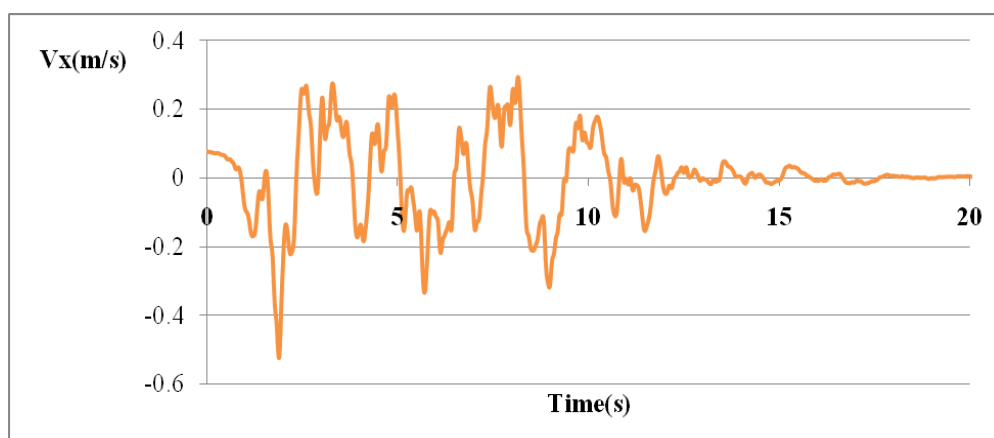


Figure A.5 Bent 1 (Piers 1&2) Velocity Component Time History for Hard Soils

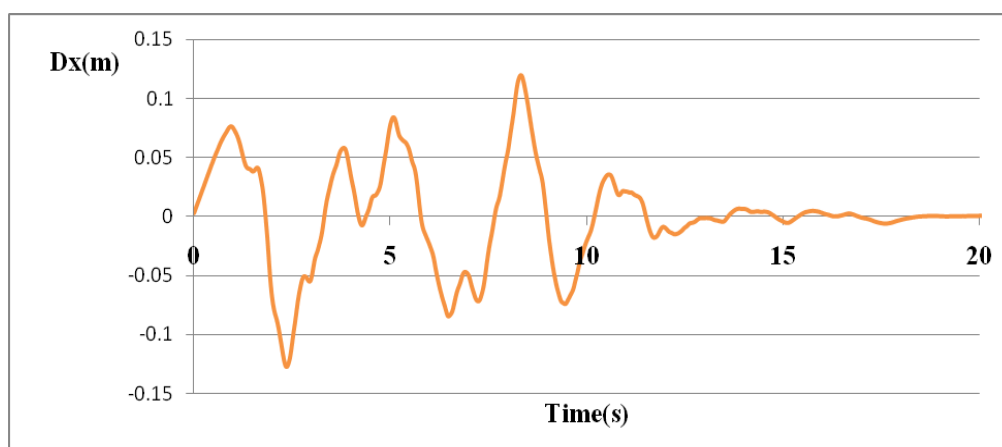


Figure A.6 Bent 1 (Piers 1&2) Displacement Component Time History for Hard Soils

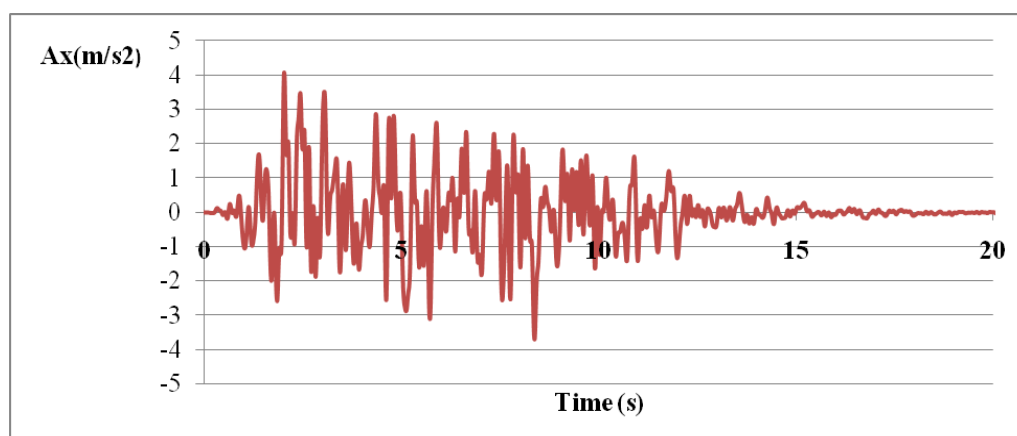


Figure A.7 Bent 2 (Piers 3&4) Acceleration Component Time History for Hard Soils

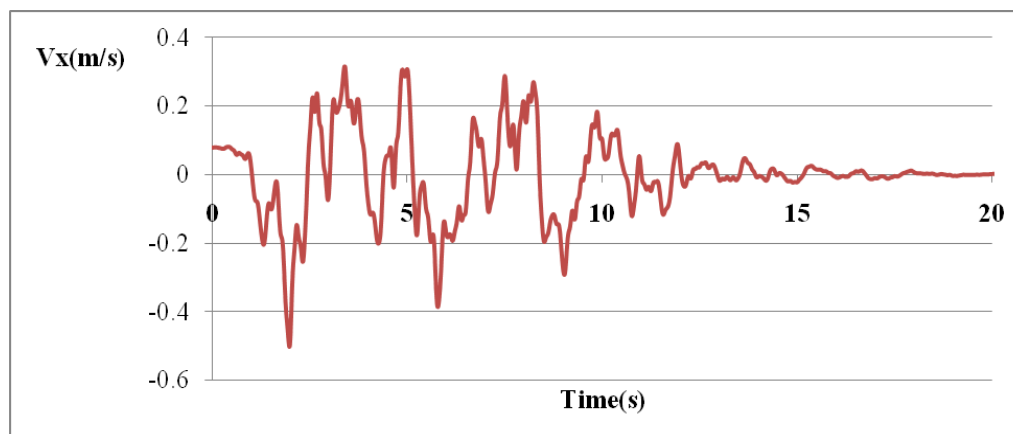


Figure A.8 Bent 2 (Piers 3&4) Velocity Component Time History for Hard Soils

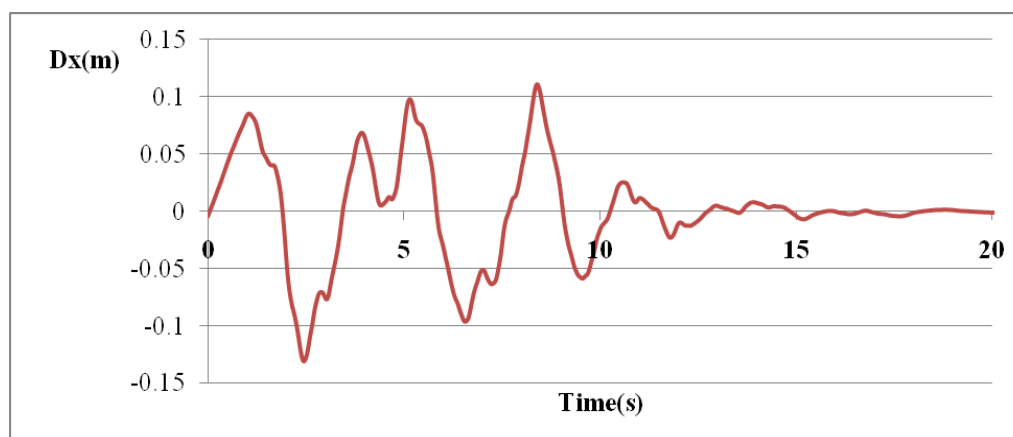


Figure A.9 Bent 2 (Piers 3&4) Displacement Component Time History for Hard Soils

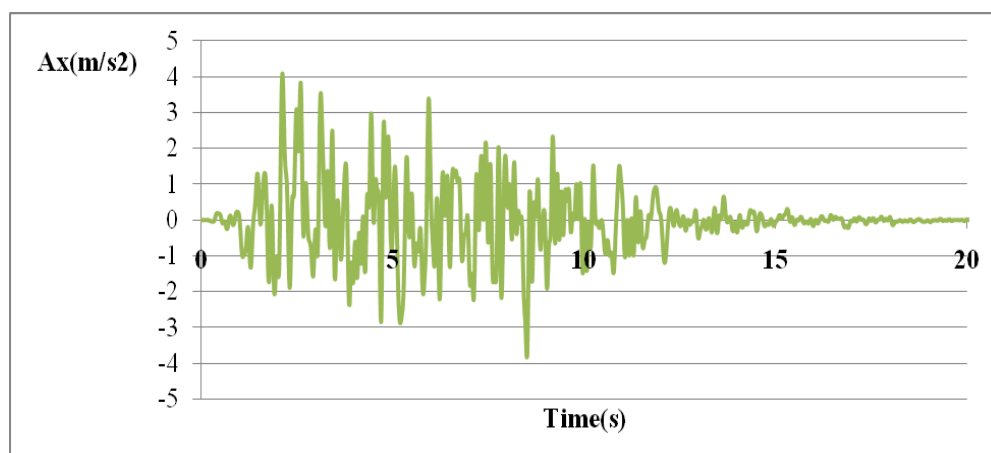


Figure A.10 Right Abutment Acceleration Component Time History for Hard Soils

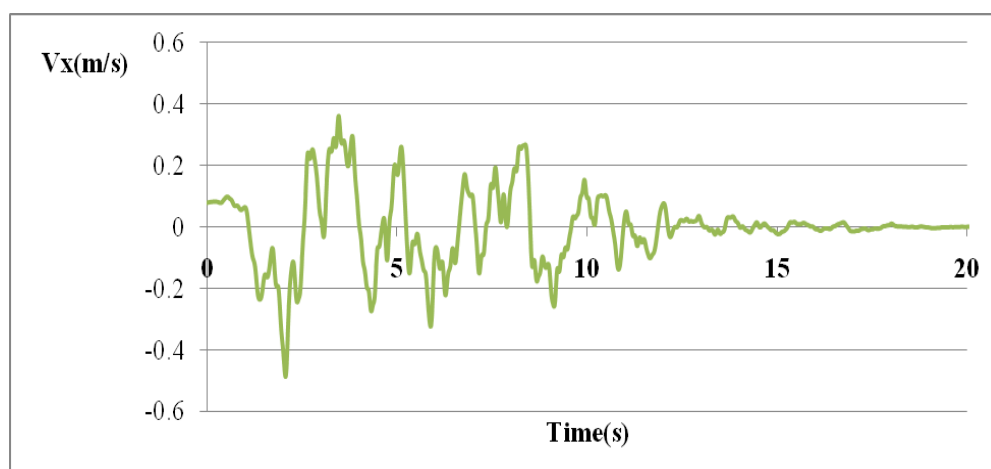


Figure A.11 Right Abutment Velocity Component Time History for Hard Soils

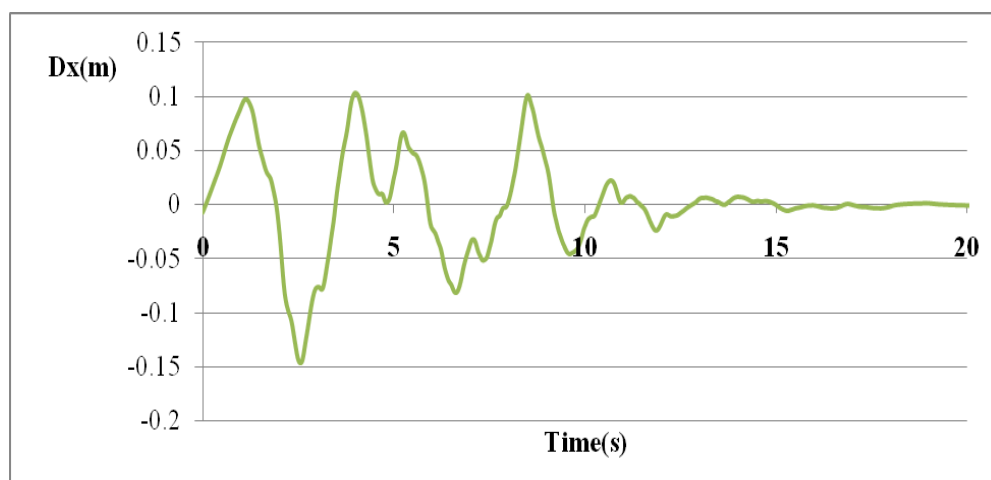


Figure A.12 Right Abutment Displacement Component Time History for Hard Soils

## A.2 Time History Graphs for Short Multi-Span Bridge Model Supported on Medium Soil Case.

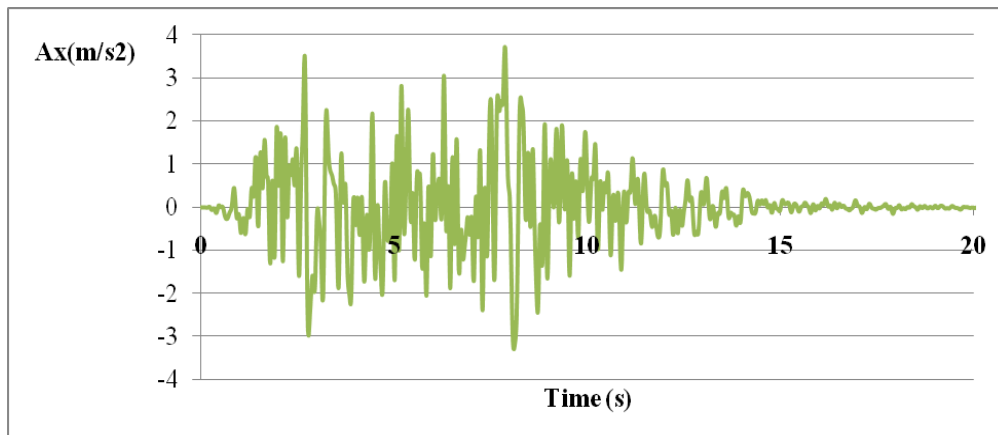


Figure A.13 Left Abutment Acceleration Component Time History for Hard Soil

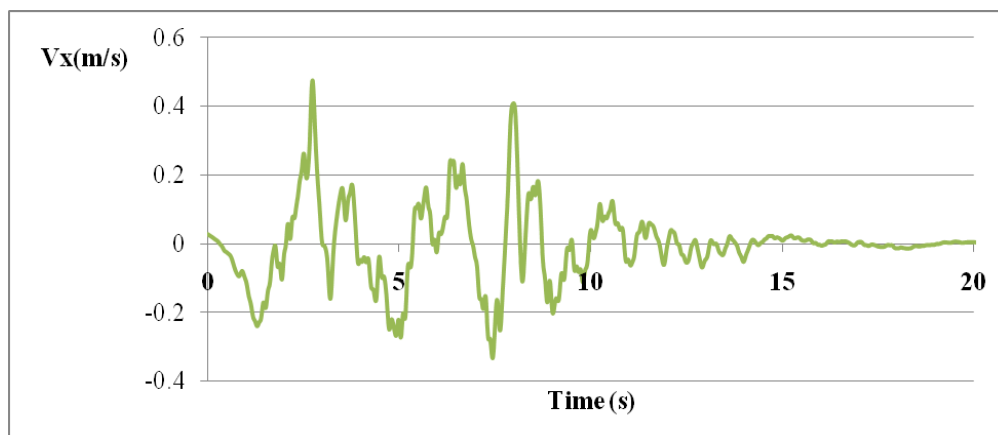


Figure A.14 Left Abutment Velocity Component Time History for Hard Soils

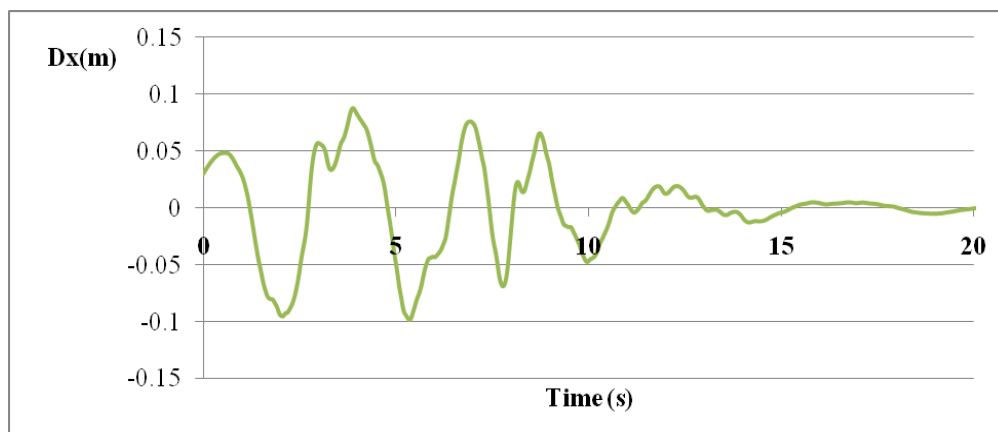


Figure A.15 Left Abutment Displacement Component Time History for Hard Soil

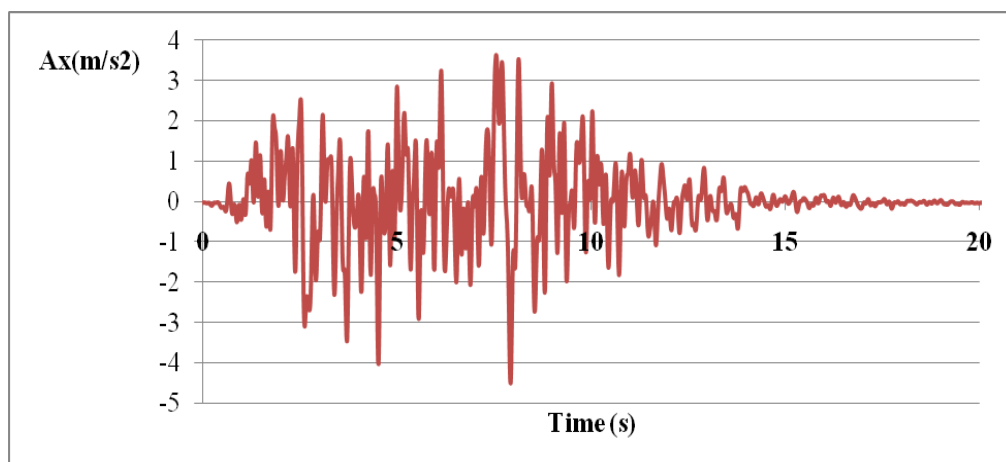


Figure A.16 Bent 1 (Piers 1&2) Acceleration Component Time History for Medium Soil

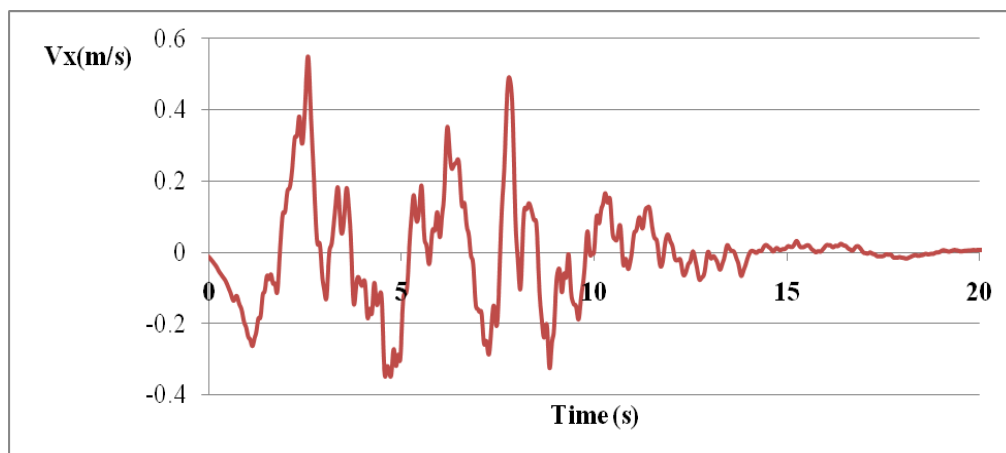


Figure A.17 Bent 1 (Piers 1&2) Velocity Component Time History for Medium Soil

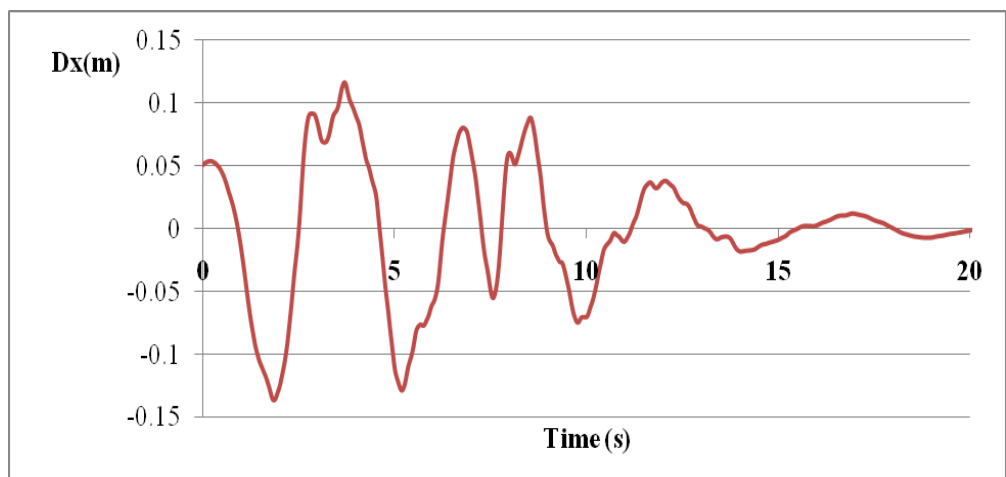


Figure A.18 Bent 1 (Piers 1&2) Displacement Component Time History for Medium Soil.

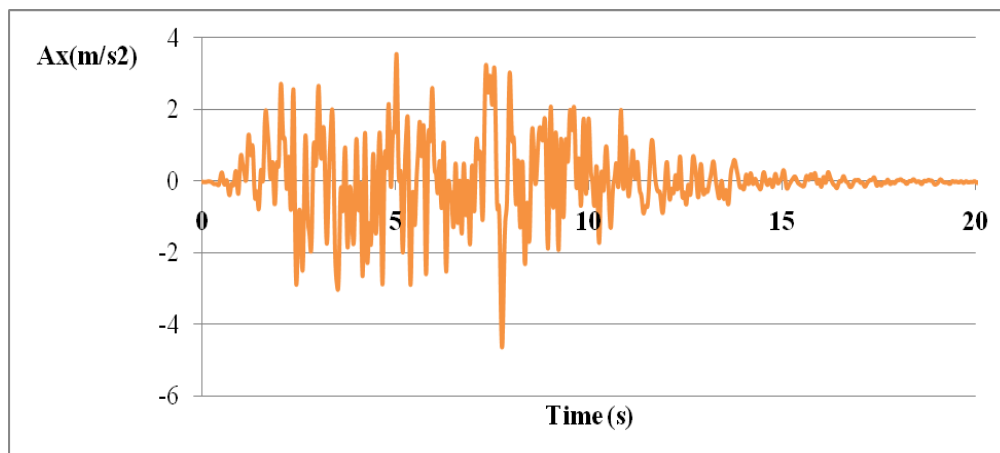


Figure A.19 Bent 2 (Piers 3&4) Acceleration Component Time History for Medium Soil

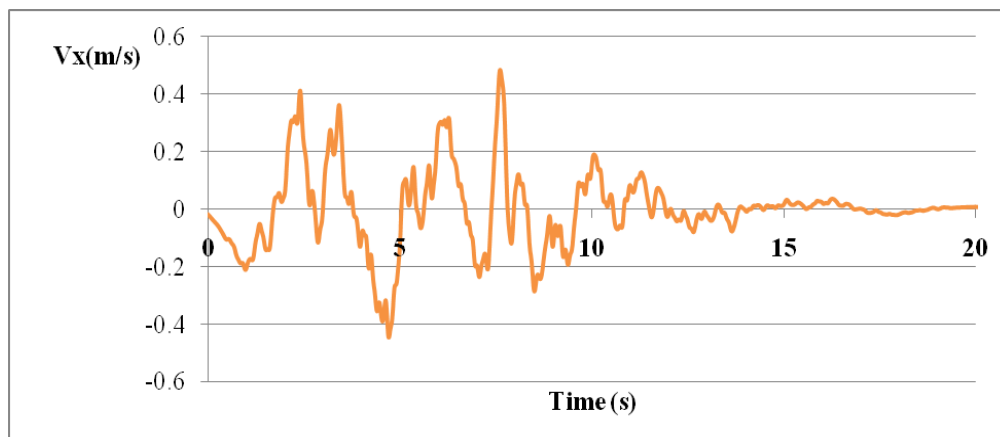


Figure A.20 Bent 2 (Piers 3&4) Velocity Component Time History for Medium Soil

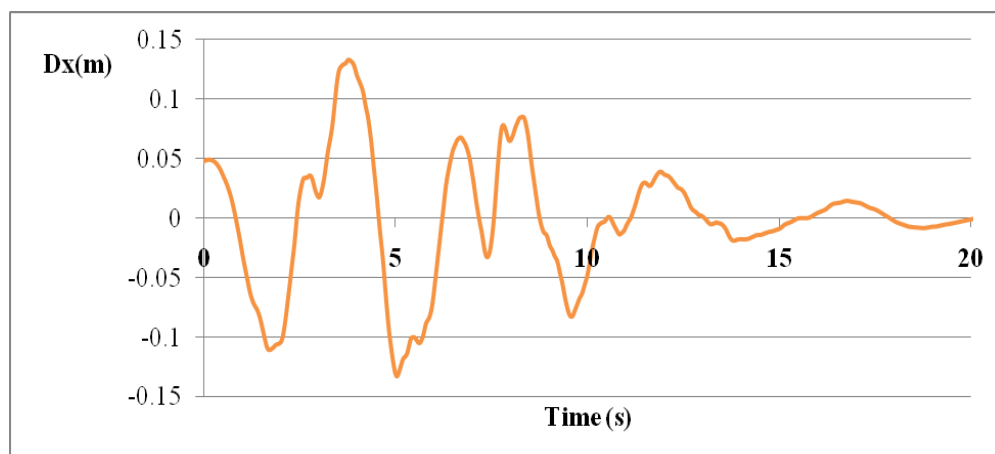


Figure A.21 Bent 2 (Piers 3&4) Displacement Component Time History for Medium Soil.

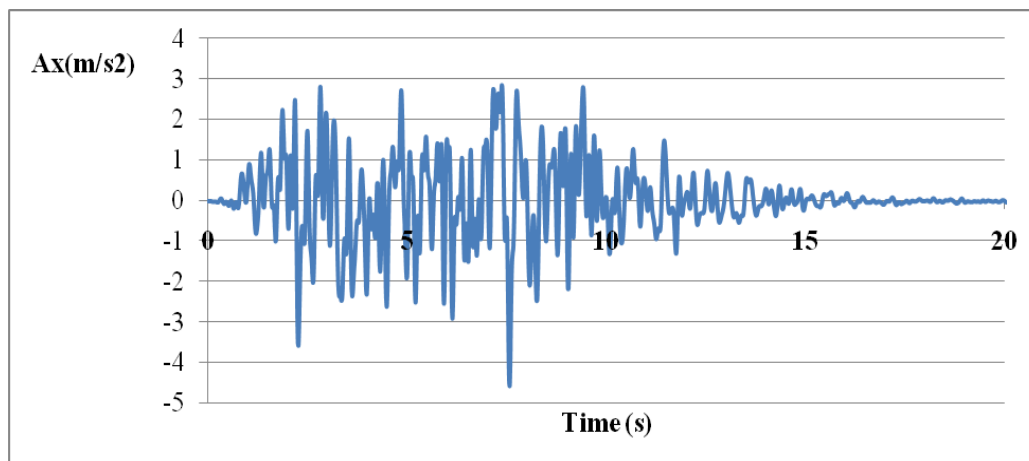


Figure A.22 Right Abutment Acceleration Component Time History for Hard Soil

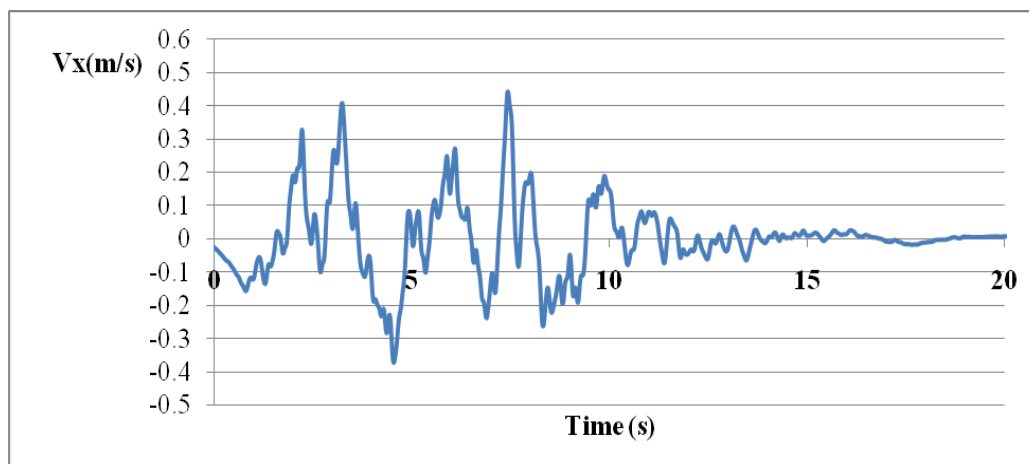


Figure A.23 Right Abutment Velocity Component Time History for Hard Soil

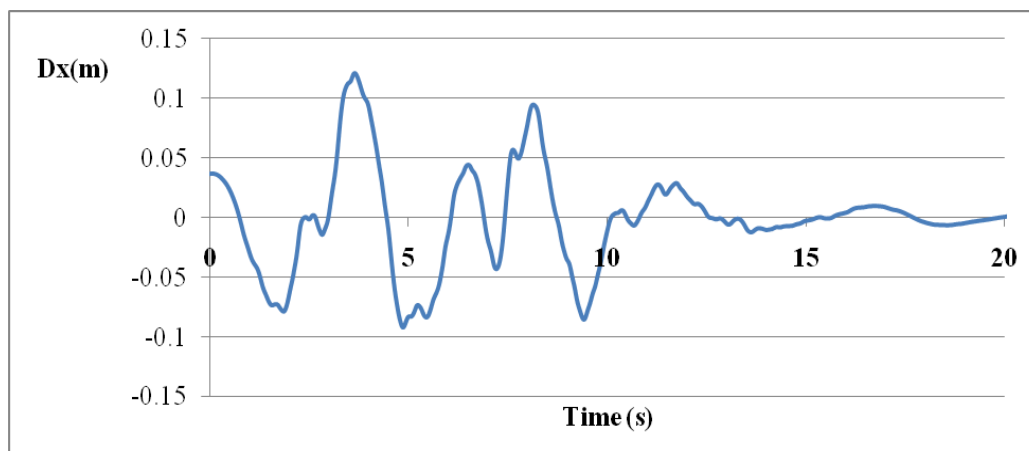


Figure A.24 Right Abutment Displacement Component Time History for Hard Soil



### A.3 Time History Graphs for Short Multi-Span Bridge Model Supported on Soft Soil Case.

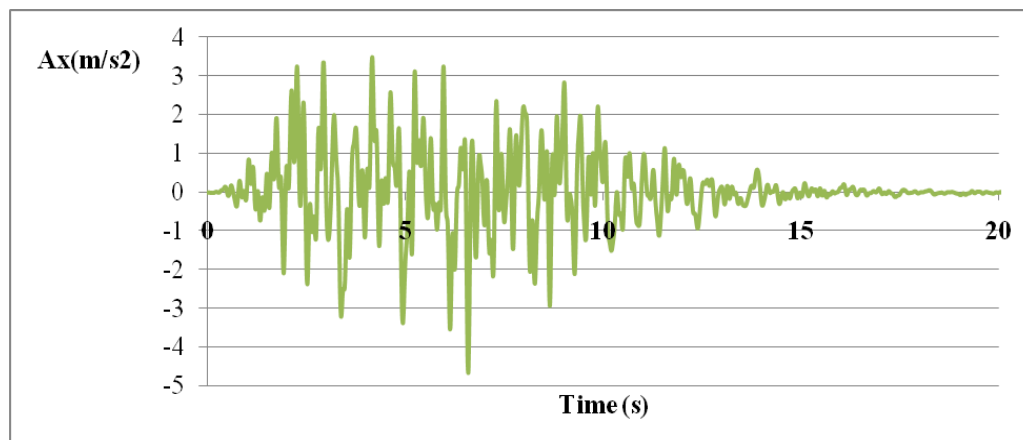


Figure A.25 Left Abutment Acceleration Component Time History for Hard Soil

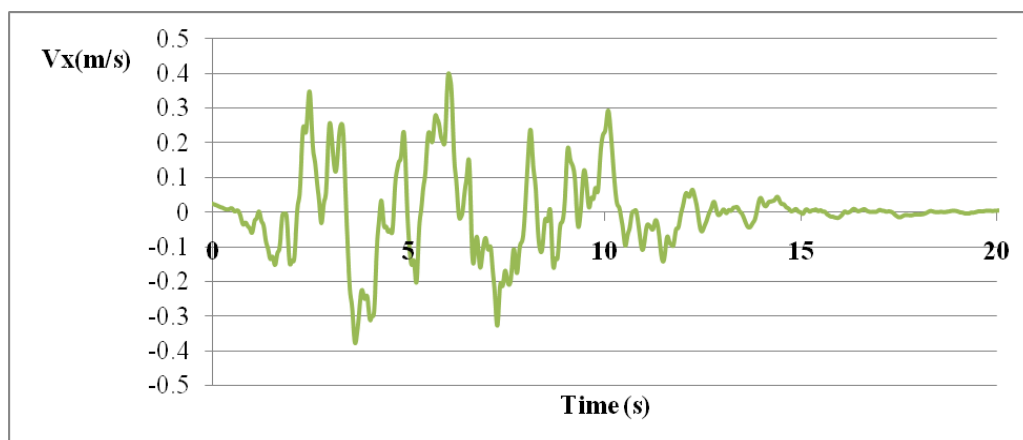


Figure A.26 Left Abutment Velocity Component Time History for Hard Soil

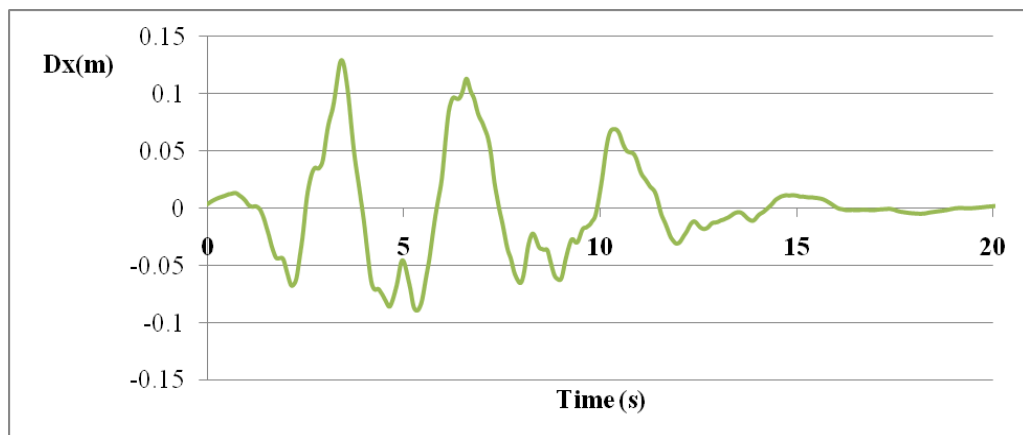


Figure A.27 Left Abutment Displacement Component Time History for Hard Soil

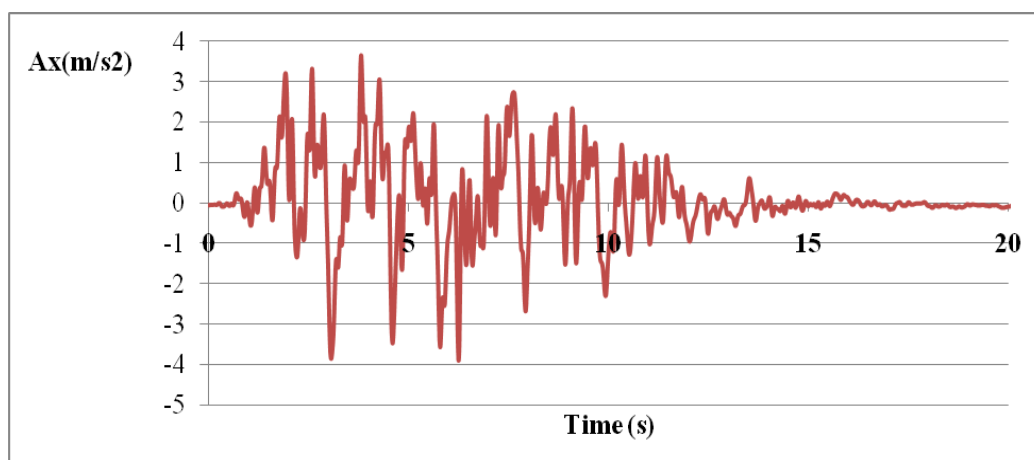


Figure A.28 Bent 1 (Piers 1&2) Acceleration Component Time History for Soft Soil

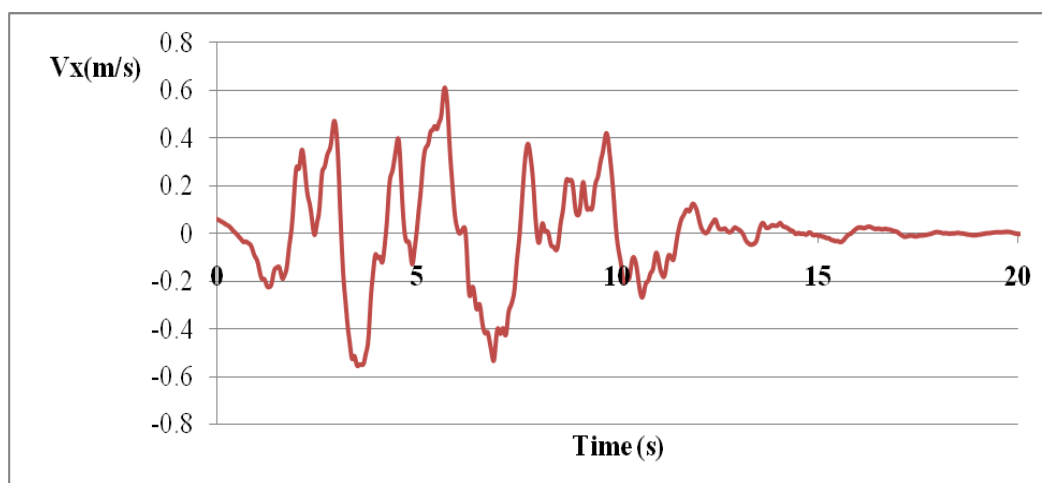


Figure A.29 Bent 1 (Piers 1&2) Velocity Component Time History for Soft Soil

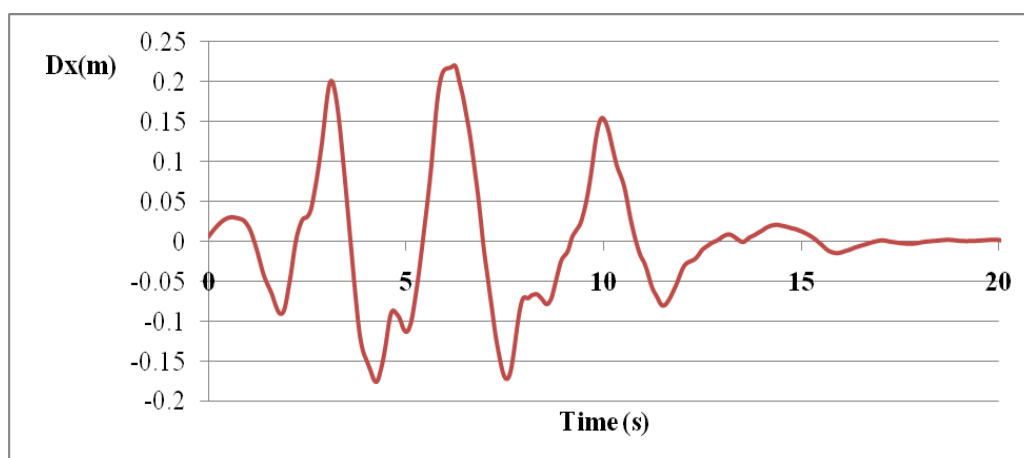


Figure A.30 Bent 1 (Piers 1&2) Displacement Component Time History for Soft Soil

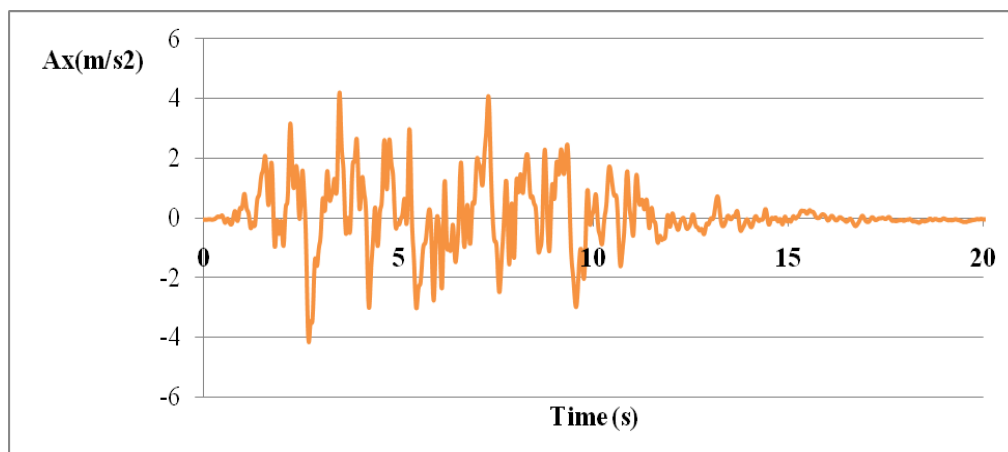


Figure A.31 Bent 2 (Piers 3&4) Acceleration Component Time History for Soft Soil

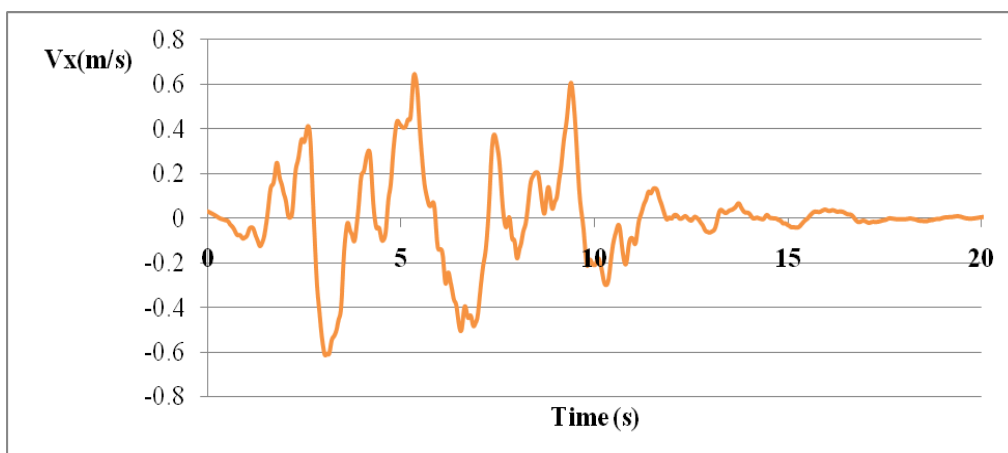


Figure A.32 Bent 2 (Piers 3&4) Velocity Component Time History for Soft Soil

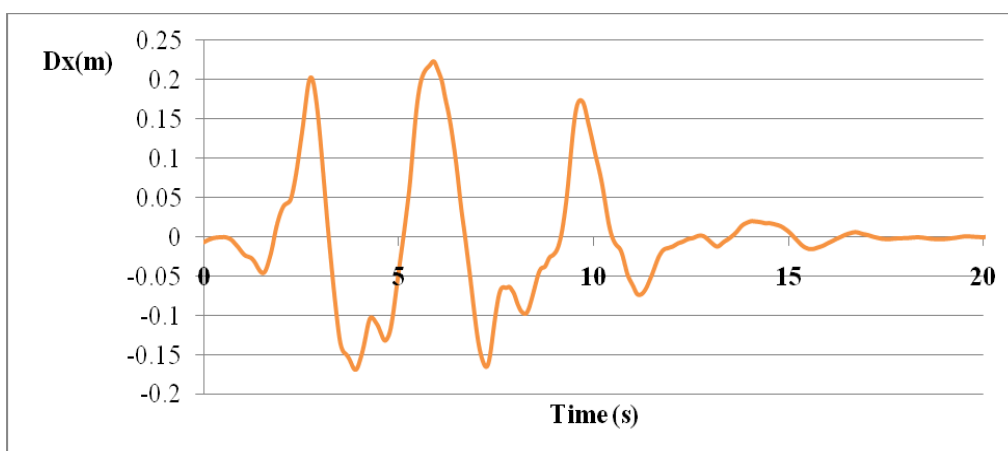


Figure A.33 Bent 2 (Piers 3&4) Displacement Component Time History for Soft Soil

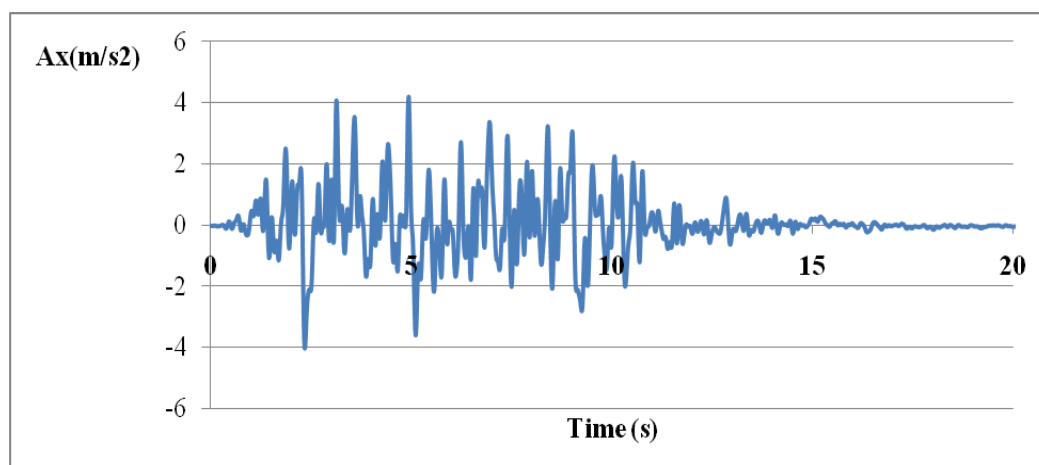


Figure A.34 Right Abutment Acceleration Time History for Hard Soil

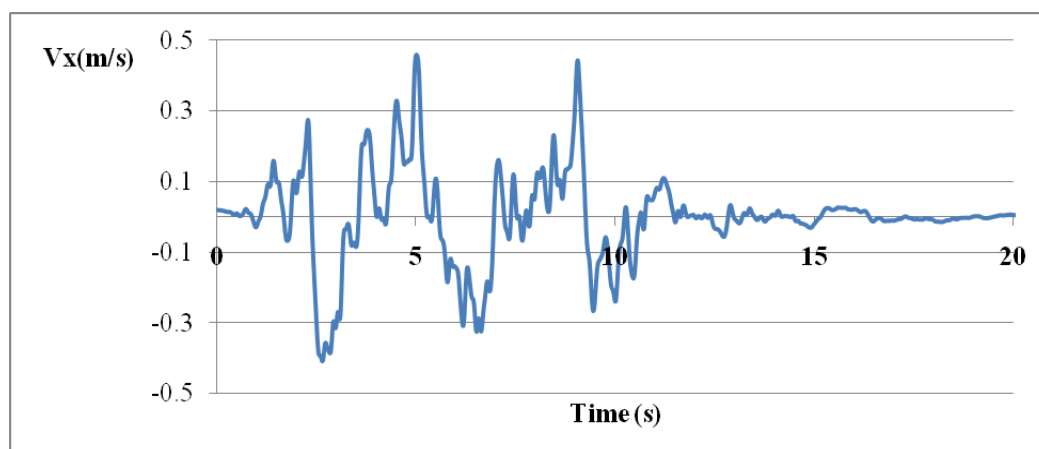


Figure A.35 Right Abutment Velocity Time History for Hard Soil

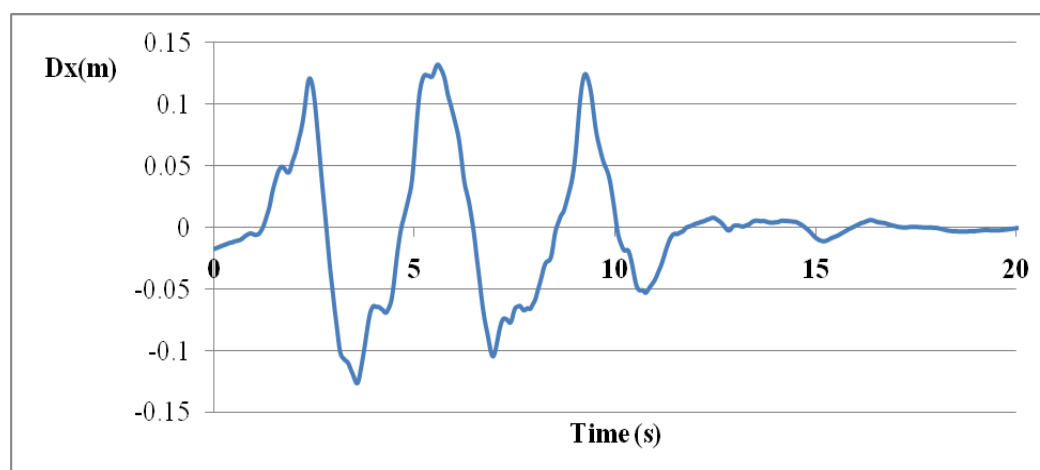


Figure A.36 Right Abutment Displacement Time History for Hard Soil

## APPENDIX B

### BASIC CONCEPTS OF PROBABILITY THEORY AND RANDOM PROCESSES

#### B.1 Basic Concepts of Probability Theory

A variable  $X$  that can assume any value  $x$  from a set containing all possible values is called a random variable. The uncertainty in the value of  $X$  can be treated mathematically using probability theory. A continuous random variable  $X$  can be defined mathematically by its Cumulative Distribution Function (CDF)  $F_X(x)$  and its Probability Density Function (PDF)  $f_X(x)$  given by:

$$F_X(x) = P(X \leq x) \quad (\text{b.1})$$

$$f_X(x) = \frac{\delta F_X(x)}{\delta x} \quad (\text{b.2})$$

Where  $P(X \leq x)$  = probability of  $X \leq x$ . The mean and variance of  $X$  are given by:

$$\mu_X = E(X) = \int_{-\infty}^{+\infty} x f_X(x) dx \quad (\text{b.3})$$

$$\text{var}(X) = \sigma_X^2 = \int_{-\infty}^{+\infty} (x - \mu_X)^2 f_X(x) dx = E(X^2) - \mu_X^2 \quad (\text{b.4})$$

Where  $E$  and  $\sigma_X$  denotes expectation and standard deviation, respectively.

To study the correlation of two random variables  $X$  and  $Y$ , the joint CDF and PDF need to be defined first as follows:

$$F_{X,Y}(x, y) = P(X \leq x, Y \leq y) \quad (\text{b.5})$$

$$f_{X,Y}(x, y) = \frac{\delta^2 F_{X,Y}(x, y)}{\delta x \delta y} \quad (\text{b.6})$$

The covariance of  $X$  and  $Y$  is determined by:

$$\text{cov}(X, Y) = E[(X - \mu_X)(Y - \mu_Y)] = E(XY) - \mu_X \mu_Y \quad (\text{b.7})$$

Where: 
$$E(XY) = \int_{-\infty}^{+\infty} \int_{-\infty}^{+\infty} xy f_{XY}(x, y) dx dy \quad (b.8)$$

and  $\mu_Y$  is the standard deviation of  $Y$ . The correlation between  $X$  and  $Y$  can then be evaluated with the correlation coefficient  $\rho_{XY}$ , which is given by:

$$\rho_{XY} = \frac{cov(X, Y)}{\sigma_X \sigma_Y} \quad (b.9)$$

Where  $\sigma_Y$  is the standard deviation of  $Y$ . If  $\rho_{XY} = \pm 1$ , then  $X$  and  $Y$  are linearly positively or negatively correlated and if  $\rho_{XY} = 0$ , then  $X$  and  $Y$  are uncorrelated.

For most applications of probability theory in the analysis of seismic ground motions, the Gaussian PDF and joint PDF are used and are given by the following expressions:

$$f_X(x) = \frac{1}{\sigma_X \sqrt{2\pi}} \exp \left[ -\frac{1}{2} \left( \frac{x - \mu_X}{\sigma_X} \right)^2 \right] \quad (b.10)$$

$$f_{X,Y}(x, y) = \frac{1}{2\pi \sigma_X \sigma_Y \sqrt{1 - \rho_{XY}^2}} \exp \left[ -\frac{1}{2(1 - \rho_{XY}^2)} \left\{ \left( \frac{x - \mu_X}{\sigma_X} \right)^2 - 2\rho_{XY} \left( \frac{x - \mu_X}{\sigma_X} \right) \left( \frac{y - \mu_Y}{\sigma_Y} \right) + \left( \frac{y - \mu_Y}{\sigma_Y} \right)^2 \right\} \right] \quad (b.11)$$

## B.2 Random Processes

A random process  $x(t)$  is a sequence of an infinite number of random variables,  $X_I(t_I)$ , ...,  $X_n(t_n)$ , where  $t$  represents time. The joint probability function for the random process can be derived from an extension of Eq. b.5; however, such joint probability functions are rarely available. Instead, the random process is usually characterized by its mean value function given by:

$$\mu_x(t) = E[x(t)] = \int_{-\infty}^{+\infty} x f_x(x, t) dx \quad (b.12)$$

and its autocovariance function, which can be derived from Ec. b.7 as:

$$R_x(t_1, t_2) = E[x(t_1)x(t_2)] - \mu_x(t_1)\mu_x(t_2) \quad (\text{b.13})$$

The mean and autocovariance functions are often called the stochastic descriptors of the random process, since they fully describe the stochastic characteristics of the process.

## APPENDIX C

### NOTATION

$A =$	HV coherence function parameter.
$A_X =$	acceleration time history component in the $X$ (longitudinal) direction.
$A_Y =$	acceleration time history component in the $Y$ (transverse) direction.
$A_z =$	acceleration time history component in the $z$ (vertical) direction.
$A_{XZ} =$	vertical acceleration time history component of $S_X$ .
$A_{YZ} =$	vertical acceleration time history component of $S_Y$ .
$A_j(t) =$	simulation of a homogeneous stationary random process.
$a =$	bridge span.
$a_j(t) =$	acceleration random vector.
$\alpha =$	LW coherence function exponential decay parameter.
$b =$	HV coherence function parameter.
$Bb =$	bridge cap beam width.
$Bc =$	bridge superstructure (box girder) cell width.
$Bf =$	bridge footing width.
$\beta =$	angle of incidence of the shear wave.
$\beta_X =$	foundation embedment correction factor for soil spring constant $K_X$ .
$\beta_Y =$	foundation embedment correction factor for soil spring constant $K_Y$ .
$\beta_Z =$	foundation embedment correction factor for soil spring constant $K_Z$ .
$\beta_{XX} =$	foundation embedment correction factor for soil spring constant $K_{XX}$ .



$\beta_{YY} =$	foundation embedment correction factor for soil spring constant $K_{YY}$ .
$\beta_{ZZ} =$	foundation embedment correction factor for soil spring constant $K_{ZZ}$ .
$COV =$	coefficient of variation.
$\Gamma_{jk}(\omega) =$	complex coherence function.
$\gamma =$	unit weight of the soil.
$\gamma_{jk}(\omega) =$	coherence function correlating stations $j$ and $k$ .
$Dp =$	bridge pier diameter.
$D_z =$	displacement time history in the $z$ (vertical) direction.
$D_X =$	displacement time history in the $X$ (longitudinal) direction.
$D_Y =$	displacement time history in the $Y$ (transverse) direction.
$\Delta\omega =$	frequency step.
$\Delta t =$	time step.
$\Delta_{pd} =$	lateral displacement at point of pier moment contraflexure caused by plastic rotation $\theta_{max}$ occurring at the bottom plastic hinge.
$\Delta_{yi} =$	lateral displacement at point of pier moment contraflexure when bottom plastic hinge is activated (i.e., $\theta = \theta_y$ ).
$\delta =$	HV coherence function parameter.
$e =$	natural log constant.
$F_a =$	IBC 2009 code site coefficient.
$F_j(t) =$	simulation of a homogeneous non-stationary random process.
$F_V =$	IBC 2009 code site coefficient.
$f =$	cyclic frequency.
$f'_c =$	compressive strength of concrete.

$f_o =$	HV coherence function parameter.
$f_y =$	yield strength of steel reinforcement.
$G =$	dynamic shear modulus of the soil.
$G_o =$	static shear modulus of the soil.
$g =$	acceleration of gravity.
$H =$	bridge pier height.
$H(\omega) =$	factor matrix of the cross spectral density matrix.
$H_{jj}(\omega) =$	diagonal coefficients of $H(\omega)$ .
$H_{jk}(\omega) =$	off-diagonal coefficients of $H(\omega)$ .
$Hb =$	bridge cap beam depth.
$Hc =$	bridge superstructure (box girder) cell depth.
$Hf =$	bridge footing depth.
$i =$	$\sqrt{-1}$
$\theta =$	rotation of the pier cross section at plastic hinge location.
$\theta_2 =$	rotation of pier cross section at plastic hinge location with respect to local axis 2.
$\theta_{2y} =$	yield rotation of pier cross section at plastic hinge location with respect to local axis 2.
$\theta_3 =$	rotation of pier cross section at plastic hinge location with respect to local axis 3.
$\theta_{3y} =$	yield rotation of pier cross section at plastic hinge location with respect to local axis 3.
$\theta_{max} =$	maximum rotation of the pier cross section at plastic hinge location.
$\theta_R =$	resultant rotation of the pier cross section at plastic hinge location.

$\theta_u =$	ultimate rotation of the pier cross section.
$\theta_y =$	yield rotation of the pier cross section.
$K_X =$	translational soil spring stiffness coefficient in the $X$ direction.
$K_Y =$	translational soil spring stiffness coefficient in the $Y$ direction.
$K_Z =$	translational soil spring stiffness coefficient in the $z$ direction.
$K_{XX} =$	rotational soil spring stiffness coefficient with respect to the $X$ direction.
$K_{YY} =$	rotational soil spring stiffness coefficient with respect to the $Y$ direction.
$K_{ZZ} =$	rotational soil spring stiffness coefficient with respect to the $z$ direction.
$\kappa =$	HV coherence function parameter.
$L =$	bridge length.
$L_p =$	plastic hinge depth.
$L_c =$	length of pier from the maximum moment location to the point of moment contraflexure.
$M_2 =$	applied moment on the pier at plastic hinge location with respect to local axis 2.
$M_3 =$	applied moment on the pier at plastic hinge location with respect to local axis 3.
$M_{2y} =$	yield moment capacity of pier cross section at plastic hinge location with respect to local axis 2.
$M_{3y} =$	yield moment capacity of pier cross section at plastic hinge location with respect to local axis 3.
$M_j(t) =$	modulation function.
$M_R =$	residual moment capacity of the pier cross section.
$M_u =$	ultimate moment capacity of the pier cross section.

$M_y =$	yield moment capacity of the pier cross section.
$\mu_j(t) =$	mean value of a random process.
$Q =$	ductility ratio for seismic forces.
$R =$	pier rotational ductility demand.
$R_2 =$	pier rotational ductility demand with respect to plastic hinge local axis 2.
$R_3 =$	pier rotational ductility demand with respect to plastic hinge local axis 3.
$R_j(t_1, t_2) =$	autocovariance function of a random process.
$RSA_j(\omega) =$	target response spectrum at station $j$ .
$RSA_j^k(\omega) =$	generated response spectrum during $k^{th}$ iteration at station $j$ .
$S =$	seismic shear wave.
$S_j(\omega) =$	power spectral density function.
$S_{jk}(\omega) =$	cross spectral density function.
$S(\omega) =$	cross spectral density matrix.
$S_I =$	IBC 2009 code mapped 1.0 sec. period spectral response acceleration.
$S_{DI} =$	5% damped design spectral response acceleration at 1.0 sec. periods.
$S_{DS} =$	5% damped design spectral response acceleration at short periods.
$S_{MI} =$	maximum considered earthquake response acceleration at short periods.
$S_{MS} =$	IBC 2009 code maximum earthquake spectral response acceleration.
$S_s =$	IBC 2009 code mapped short period (0.2 sec.) spectral response acceleration.
$S_X =$	$X$ (longitudinal) component of $S$ .
$S_Y =$	$Y$ (transverse) component of $S$ .

$SD =$	standard deviation.
$T =$	response spectrum period
$Tb =$	bridge superstructure (box girder) cell thickness.
$Ts =$	bridge superstructure (box girder) overhang thickness.
$t =$	time variable.
$\tau =$	time difference.
$V_X =$	velocity time history in the $X$ (longitudinal) direction.
$v =$	wave velocity.
$v_s =$	shear wave velocity.
$v_X =$	$X$ (longitudinal) component of $v_s$ .
$v_Y =$	$Y$ (transverse) component of $v_s$ .
$\nu =$	Poisson's ratio of the soil.
$\xi =$	distance between stations $j$ and $k$ .
$\phi_2 =$	curvature of the pier cross section at plastic hinge location with respect to local axis 2.
$\phi_{2y} =$	yield curvature of the pier cross section at plastic hinge location with respect to local axis 2.
$\phi_3 =$	curvature of the pier cross section at plastic hinge location with respect to local axis 3.
$\phi_{3y} =$	yield curvature of the pier cross section at plastic hinge location with respect to local axis 3.
$\phi_u =$	ultimate curvature of the pier cross section.
$\phi_y =$	yield curvature of the pier cross section.
$\Phi_{mq} =$	sequence of independent random phase angles.

$\phi_{mq}^{(i)}$	$i^{th}$ realization of $\Phi_{mq}$ .
$W$	bridge superstructure (box girder) width.
$WI$	bridge superstructure (box girder) overhang.
$X$	longitudinal coordinate of the bridge.
$X(\omega)$	Fourier transform variable.
$Y$	transverse coordinate of the bridge.
$Z$	scaling factor of $D_Z$ .
$z$	vertical coordinate of the bridge.
$\omega$	frequency in rad./sec.
$\omega_q$	cut off frequency.

## REFERENCES

1. Abbas, A.M. and Mahonar C.S., "Critically Spatially Varying Earthquake Load Models for Extended Structures". *Journal of Structural Engineering (Madras)*, v29, n1, April/June, 2002, p. 32-52.
2. Abrahamson, N., Scheider J. and Stepp, J., "Empirical Spatial Coherency Functions for Applications to Soil-Structure Interaction Analyses". *Earthquake Spectra*, v7, 1991, p. 1-27.
3. Abdel-Ghaffar A.M. and Rubin L.I., "Suspension Bridge Response to Multiple Support Excitation". *Journal of Engineering Mechanics Division*, v108, 1982.
4. Allam, S. and Data, T., "Response Spectrum Analysis of Suspension Bridges for Random Ground Motions". *Journal of Bridge Engineering*, v7, n6, Nov 2002, p. 325-337.
5. Allam, S., Data, T., "Seismic Response of Cable Stayed Bridge under Multi-component Non-stationary Random Ground Motion". *Earthquake Engineering and Structural Dynamics*, v33, 2004, p. 375-393.
6. American Association of State Highway and Transportation Officials (AASHTO), "Guide Specification for LRFD Seismic Bridge Design", Second Edition, 2011.
7. Berrah, M.K. and Kausel, E., "Modal Combination Rule for Spatially Varying Seismic Motion", *Journal of Earthquake Engineering and Structural Dynamics*, September 1993.
8. Betti, Abdel-Ghaffar, and Niazy, "Kinematic Soil-structure Interaction of Long Span Cable-supported Brigdes", *Journal of Earthquake Engineering and Structural Dynamics*, v22, n5, May 1993, p. 415-430.
9. Berrah M.K. and Kausel E., "Response Spectrum Analysis of Structures Subjected to Spatially Varying Motions", *Journal of Earthquake Engineering and Structural Dynamics*, v21, n6, June 1992, p. 461-470.
10. Behnamfar, F. and Sugimura V., "Dynamic Response of Adjacent Structures Under Spatially Variable Seismic Waves". *Probabilistic Engineering Mechanics*, v14, n1-2, Jan-Apr, 1999, p. 33.44.

11. Bogdanoff, J., Goldberg, J. and Bernard, M., "Response of a Simple Structure to a Random Earthquake-Type Disturbance". Bulletin of the Seismological Society of America, v51, n2, 1961, p. 293-310.
12. California Department of Transportation – Division of Structures. "User Manual for COLx – Column Ductility Program". 1993.
13. Chen, W.F. and Duan, L., "Bridge Engineering Handbook", CRC Press, 2000.
14. Clough R.W. and Penzien J., "Dynamics of Structures", Second Edition, Mc. Graw Hill, 1993.
15. Dameron, Sobash, and Lam., "Nonlinear Seismic Analysis of Bridge Structure Foundation-Soil Representation and Ground Motion Input". Journal of Computers and Structures, v64, n5-6, 1997.
16. Deodatis, G., "Non-stationary Stochastic Vector Processes: Seismic Ground Motion Applications". Probabilistic Engineering Mechanics, v11, n3, 1996, p. 149-167.
17. Deodatis G. and Theoharis, A., "Seismic Ground Motion in a Layered Half-space due to a Haskell-Type Source. Part 1: Theory". Journal of Soil Dynamics and Earthquake Engineering, v13, n4, 1994, p. 281-292.
18. Deodatis G. and Theoharis, A., "Seismic Ground Motion in a Layered Half-space due to a Haskell-Type Source. Part 2: Applications". Journal of Soil Dynamics and Earthquake Engineering, v13, n4, 1994, p. 293-301.
19. Der Kiureghian, A., "Coherence Model for Spatially Varying Ground Motions". Journal of Earthquake Engineering and Structural Dynamics", v25, n1, Jan 1996, p. 99-111.
20. Der Kiureghian, A. and Neuenhofer, A., "Response Spectrum Method for Multi-support Seismic Excitations". Journal of Earthquake Engineering and Structural Dynamics, v21, 1992, p. 747-754.
21. Deb Chaudhury, Amitabha and Gazis, "Response of MDOF Systems to Multiple Support Seismic Excitation", ASCE Journal of Engineering Mechanics, April 1988.
22. Dumanoglu A and Severn R., "Stochastic Response of Suspension Bridges to Earthquake Forces", Journal of Earthquake Engineering and Structural Dynamics, January 1990.



23. Ettouney, M., Hapij, A. and Gajer, R., "Frequency Domain Analysis of Long Span Bridges Subjected to Non-uniform Seismic Motions". *Journal of Bridge Engineering*, v6. n6, Nov/Dic 2001, p. 577-586.
24. Federal Emergency Management Agency and American Society of Civil Engineers. "Pre-standard and Commentary for the Seismic Rehabilitation of Buildings (FEMA 365)". Nov 2000.
25. Halдар, A. and Mahadevan, S., "Reliability Assessment using Stochastic FE Analysis", John Wiley and Sons, Inc., 2000.
26. Halдар A. and Mahadevan, S., "Probability, Reliability and Statistical Methods in Engineering Design, John Wiley and Sons, Inc., 2000.
27. Hao, H, Oliveira, C and Penzien, J., "Multiple-Station Ground Motion Processing and Simulation Based on SMART-1 Array Data". *Nuclear Engineering and Design*, vol. 111, 1989, p. 293-310.
28. Hao, H. and Duan, X., "Seismic Response of Asymmetric Structures to Multiple Ground Motions". *Journal of Structural Engineering*, v121, n11, Nov 1995, p. 1557-1564.
29. Hao, H., "Torsional Response of Building Structures to Spatial Random Ground Excitation". *Engineering Structures*, v19, n2, Feb 1997, p. 105-112.
30. Hao, H., "Ground Motion Spatial Variation Effect on Circular Arch Response". *Journal of Engineering Mechanics*, v120, n11, Nov 1994, p. 2326-2341.
31. Hao, H., "Stability of Simple Beam Subjected to Multiple Support Seismic Excitation". *Journal of Engineering Mechanics*, July 1997.
32. Hao, H., "Response of a Two Way Excentric Building to Non-uniform Base Excitation". *Engineering Structures*, v20, n8, Aug 1998, p. 667-684.
33. Hao H., "A Parametric Study of the Required Seating Length for Bridge Decks During Earthquakes", *Journal of Earthquake Engineering and Structural Dynamics*, v27, 1998, p. 91-103.
34. Hao H. and Zhang, S., "Spatial Ground Motion Effect on Relative Displacements of Adjacent Building Structures", *Journal of Earthquake Engineering and Structural Dynamics*, v28, n4, 1999, p 333-349.

35. Harichandran, R. and Vanmarcke, E., "Stochastic Variation of Earthquake Ground Motion in Space and Time". *Journal of Engineering Mechanics*, v112, n2, 1986, p. 154-174.
36. Harichandran, R. and Wang, W., "Response of Simple Beam to Spatially Varying Earthquake Excitation". *Journal of Engineering Mechanics*, v114, n9, 1988, p. 1526-1541.
37. Harichandran, R. and Wang, W., "Response of Indeterminate Two Span Beam to Spatially Varying Seismic Excitation", *Journal of Earthquake Engineering and Structural Dynamics*, February 1990.
38. Harichandran, R., "Estimating The Spatial Variation of Earthquake Ground Motion from Dense Array Recordings". *Structural Safety*, v10, n1-3, May 1991, p. 219-233.
39. Harichandran, R., Hawwari, A. and Sweidan, B., "Response of Long Span Bridges to Spatially Varying Ground Motion". *Journal of Structural Engineering*, v122, n5, May 1996, p. 476-484.
40. Heredia-Zavoni, E. and Barranco, F., "Torsion of Symmetric Structures due to Ground Motion Spatial Variation". *Journal of Engineering Mechanics*, v122, n9, Sept 1996, p. 834-843.
41. International Code Council, Inc., "International Building Code". 2003 Edition.
42. International Code Council, Inc., "International Building Code". 2009 Edition.
43. Hoshiya, M., "Response Covariance to Multiple Excitations". *Journal of Engineering Mechanics*, April 1986.
44. Kahan, M., Gibert, R. and Bard, P., "Influence of Seismic Wave Spatial Variability on Bridges". *Journal of Earthquake Engineering and Structural Dynamics*, v25, n8, Aug 1996, p. 795-814.
45. Katafygiotis, L., Zerva, A. and Malyarenko, A., "Simulation of Homogeneous and Partially Isotropic Random Fields". *Journal of Engineering Mechanics*, v125, n10, Oct 1999, p. 1180-1189.
46. Kim S.H. and Feng M., "Fragility Analysis of Bridges under Ground Motion and Spatial Variation". *International Journal of Nonlinear Mechanics*, v38, July 2003, p. 705-731.

47. Laouami, N. and Labbe, P., "Analytical Approach for Evaluation of the Seismic Ground Motion Coherency Function". *Journal of Soil Dynamics and Earthquake Engineering*, v21, n8, Dec 2001, p. 727-733.
48. Lin, J., Zhang, Y. and Li, Q., "Seismic Spatial Effects for Long Span Bridges using Pseudo Excitation Method". *Engineering Structures*, v26, n9, July 2004, p. 1207-1216.
49. Lui, X., Ye, J. and Li, A., "Space Coherence Function Model of Vertical Ground Motion". *Gongcheg Lixuel/Engineering Mechanics*, v21, April 2004, p. 140-144.
50. Leger, Ide and Paultre., "Multiple Support Seismic Analysis of Large Structures", *Computers and Structures*, v36, 1990.
51. Loh, C. and Ku, B., "Efficient Analysis of Structural Response of Multiple Support Seismic Excitation". *Engineering Structures*, v17, n1, Jan 1995, p. 15.
52. Loh, C. and Lee, S., "Aseismic Displacement Analysis of Multi-supported Bridges to Multiple Excitations". *Journal of Earthquake Engineering and Structural Dynamics*, v9, n1, Jan 1990, p. 25-33.
53. Loh, C. and Lin, S., "Directionality and Simulation in Spatial Variation of Seismic Waves". *Engineering Structures*, v12, n2, April 1990, p. 134-143.
54. Luco, J. and Wong, H., "Response of a Rigid Foundation to a Spatially Varying Random Ground Motion". *Journal of Earthquake Engineering and Structural Dynamics*, v14, 1986, p. 891-908.
55. Lupoi, A., Franchin, P., Pinto, P. and Monti, G., "Seismic Design of Bridges Accounting for Spatial Variability of Ground Motions". *Earthquake Engineering and Structural Dynamics*, vol 34, Jan 2005, p. 327-348.
56. Monti, G., Nuti, C. and Pinto, P., "Nonlinear Response of Bridges under Multi-support Excitation". *Journal of Structural Engineering*, v122, 1996, p. 1147-1159.
57. Mylonakis, G., Papastratiou, D., Psycharis, J. and Mahmoud, K., "Simplified Modeling of Bridge Response on Soft Soil to Non-uniform Seismic Excitation". *Journal of Bridge Engineering*, v6, n6, Nov/Dic 2001, p. 587-597.
58. Nazmy, A. and Abdel-Ghaffar, A., "Effects of Ground Motions and its Effects on Lifelines". *Engineering Structures*, v16, n7, 1994.

59. Nazmy, A. and Abdel-Ghaffar, A., "Nonlinear Earthquake Response Analysis of Long Span Cable Stayed bridges", *Journal of Earthquake Engineering and Structural Dynamics*, January 1990.
60. Nee K. and Haldar, A., "The Elasto-plastic Nonlinear Seismic Analysis of Partially Restrained Space Structures by the Assumed Stress Method", Technical Report CEEM-89-104. Department of Civil Engineering and Engineering Mechanics, University of Arizona, April 1989.
61. Peña, C. and Haldar, A., "Effect of Spatial Variability of Seismic Excitation and Variability of Soil Conditions on Pier Ductility Demands of Multi-Span Bridges", *Journal of Structural Engineering*, Feb 2012 (Estimated Publication Date).
62. Peña, C. and Haldar, A., "Effect of Spatial Variability of Seismic Excitation on Pier Ductility Demands of Multi-Span Bridges with Uniform Soil Conditions and Variable Span Lengths and Pier Heights", *Journal of Structural Engineering*, March 2012 (Estimated Publication Date).
63. Peña, C. and Haldar, A., "Effect of Spatial Variability of Seismic Excitation with a Strong Vertical Acceleration Component and Variability of Soil Conditions on Pier Ductility Demands of Multi-Span Bridges", *Journal of Structural Engineering*, April 2012 (Estimated Publication Date).
64. Perotti, F., "Structural Response to Non-stationary Multiple Support Excitation", *Journal of Earthquake Engineering and Structural Dynamics*, v19, n4, May 1990, p. 513-527.
65. Price, T. and Eberhard, M., "Effects of Spatially Varying Ground Motions on Short Bridges", *Journal of Structural Engineering*, v124, n8, Aug 1998, p. 948-955.
66. Priestley, M., Seible, F. and Calvi, G., "Seismic Design and Retrofit of Bridges", John Wiley and Sons, Inc. 1996.
67. Ramadan, O. and Novak, M., "Simulation of Multidimensional, Anisotropic Ground Motions", *Journal of Engineering Mechanics*, v120, n8, Aug 1994, p. 1773-1785.
68. Rassem, M., Ghobarah, A. and Heidebrecht, A., "Site Effects on the Seismic Response of Suspension Bridges", *Engineering Structures*, v18, n5, May 1996, p. 363-370.

69. Reyes, A., "Inelastic Nonlinear Seismic Response and Ductility Evaluation of Steel Frames with Fully Restrained, Partially Restrained and Composite Connections", PhD Dissertation, Department of Civil Engineering and Engineering Mechanics, University of Arizona, 1997.
70. Saadeghuaziri, M., Yazdani-Motlagh, A. and Rashidi, S., Effects of Soil-Structure Interaction on Longitudinal Seismic Response of a MSSS Bridges", *Journal of Soil Dynamics and Earthquake Engineering*, v20, n1-4, Oct 2000, p. 231-242.
71. Sarkar, M., "Critical Cross Power Spectral Density Function and the Highest Response of Multi-supported Structures Subjected to Multi-component Earthquake Excitation". *Journal of Earthquake Engineering and Structural Dynamics*, March 1996.
72. Saxena, V., "Spatial Variation of Earthquake Ground Motion and Development of Bridge Fragility Curves", PhD Dissertation, Department of Civil Engineering and Operations Research, Princeton University, 2000.
73. Sextos, A., Kappos, A. and Pitilakis, K., "Inelastic Dynamic Analysis of RC Bridges Accounting for Spatial Variability of Ground Motions, Site Effects and Soil-Structure Interaction Phenomena. Part 1: Methodology and Analytical Tools". *Journal of Earthquake Engineering and Structural Dynamics*, v32, n4, April 2003, p. 607-627.
74. Sextos, A., Kappos, A. and Pitilakis, K., "Inelastic Dynamic Analysis of RC Bridges Accounting for Spatial Variability of Ground Motions, Site Effects and Soil-Structure Interaction Phenomena. Part 2: Parametric Study". *Journal of Earthquake Engineering and Structural Dynamics*, v32, n4, April 2003, p. 629-652.
75. Sextos, A., Kappos, A. and Mergos, P., "Effects of Soil-Structure Interaction and Spatial Variability of Ground Motion on Irregular Bridges: The Case of the Krystallopigi Bridge". 13<sup>th</sup> World Conference in Earthquake Engineering. Vancouver, Canada, Aug 2004, paper No. 2298.
76. Shinozuka, M. and Jan, C., "Digital Simulation of Random Processes and its Applications", *Journal of Sound and Vibration*, v25, 1972, p. 111-128.
77. Shinozuka, M., "Monte Carlo Solution of Structural Dynamics". *Computers and Structures*, v2, 1972, p. 73-85.
78. Shinozuka, M. and Deodatis, G., "Stochastic Process Models for Earthquake Ground Motion". *Probabilistic Engineering Mechanics*, v3, n3, 1988, p. 114-123.

79. Shinozuka, M. and Deodatis, G., "Simulation of Stochastic Processes by Spectral Representation". *Applied Mechanics Review*, ASME, v44, 1991, p. 191-204.
80. Shrikhande and Gupta, "Dynamic Soil-Structure Interaction Effects on the Seismic Response of Suspension Bridges", *Journal of Earthquake Engineering and Structural Dynamics*, November 1999.
81. Soyluk, K. and Dumanoglu, A., "Spatial Variability Effects of Ground Motions on Cable Stayed Bridges". *Soil Dynamics and Earthquake Engineering*, v24, n3, April, 2004, p 241-250.
82. Takeda, T., Sozen, M.A. and Nielsen, N.N., *Reinforced Concrete Response to Simulated Earthquakes*", *Journal of the Structural Division*, ASCE, Vol. 96, ST12, Dec. 1970.
83. Trifunac, M. and Todorovska, M., "Response Spectra for Differential Motion of Columns". *Journal of Earthquake Engineering and Structural Dynamics*, v26, n2, Feb 1997, p. 251-268.
84. Trifunac, M., "Relative Motions of Building Foundations". *Journal of Structural Engineering*, April 1997.
85. Tsai, H.C., "Modal Superposition Method for Dynamic Analysis of Structures Excited by Prescribed Support Displacements". *Journal of Computers and Structures*, v66, 1998.
86. Vo, P.H and Haldar, A., "Post-processing of Linear Accelerometer Data in Structural Identification". *Journal of Structural Engineering*, vol 30, No.2, July-September 2003, pp 123-130.
87. Wang, J., Hu, S. and Wei, X., "Effects of Engineering Geological Conditions on Response of Suspension Bridges". *Soil Dynamics and Earthquake Engineering*, v18, n4, 1999, p. 297-304.
88. Wolf, J.P., "Dynamic Soil-Structure Interaction", Prentice-Hall Inc., 1985.
89. Wolf, J.P., "Soil-Structure Interaction Analysis in the Time Domain", Prentice-Hall, Inc, 1988.
90. Yamamura and Takana, "Response Analysis of Flexible MDOF systems for Multiple Support Seismic Excitation", *Journal of Earthquake Engineering and Structural Dynamics*, April 1990.

91. Yang, Q. and Chen, Y., "Coherence Model for Spatially Varying Ground Motions". *Journal of Earthquake Engineering and Structural Dynamics*, July 2000.
92. Zhanardo, G., "Seismic Response of Multi-span Simply Supported Bridges to Spatially Varying Earthquake Ground Motion". *Journal of Earthquake Engineering and Structural Dynamics*, v31, n6, June 2002, p. 1325-1345.
93. Zendagui, D., Berrah, M. and Kausel, E., "Stochastic De-amplification of Spatially Varying Ground Motions". *Soil Dynamics and Earthquake Engineering*, vol 18, n6, Aug 1999, p. 395-471.
94. Zandagui, D. and Berrah, M., "Spatial Variation of Seismic Motion Induced by Propagation of Body Waves". *Soil Dynamics and Earthquake Engineering*, vol 22, n9-12, Oct/Dec 2002, p. 805-811.
95. Zembaty, Z., "Vibration of Bridge Structure under Kinematic Wave Excitation". *Journal of Structural Engineering*, v123, n4, April 1997, p. 479-488.
96. Zembaty, Z. and Rutemberg., "On the Sensitivity of Bridge Seismic Response with Local Soil Amplification". *Journal of Earthquake Engineering and Structural Dynamics*, v27, 1998, p. 1095-1099.
97. Zerva, A., "Correlation Patterns in Characteristics of Spatially Variable Seismic Ground Motion". *Journal of Earthquake Engineering and Structural Dynamics*, v26, n1, Jan 1997, p. 19-39.
98. Zerva, A., "On the Spatial Variation of Seismic Ground Motions and its Effects on Lifelines". *Engineering Structures*, v16, n7, 1994.
99. Zerva, A. and Zhang, O., "Response of Multi-span Beams to Spatially Incoherent Seismic Ground Motion", *Journal of Earthquake Engineering and Structural Dynamics*, August 1990.
100. Zerva, A., "Spatial Variation of Seismic Ground Motions. Modeling and Engineering Applications", CRC Press, 2009.